

**Synergistic Chemo- and Photodynamic Treatment of Cancer
Cells with C₆₀ Fullerene Nanocomplexes**

**Synergistische chemo- und photodynamische Behandlung von
Krebszellen mit C₆₀-Fulleren-Nanokomplexen**

Dissertation zur Erlangung des
naturwissenschaftlichen Doktorgrades
der Julius-Maximilians-Universität Würzburg

vorgelegt von
Anna Grebinyk

aus
Kyiv, Ukraine

Wildau 2020



Submitted on:

Members of the Promotionskomitee:

Chairperson:

Primary Supervisor: Professor Dr. Thomas Dandekar

Second Supervisor: Professor Dr. Marcus Frohme

Date of Public Defence:

Date of Receipt of Certificates:

**Eidesstattliche Erklärungen nach §7 Abs. 2 Satz 3, 4, 5
der Promotionsordnung der Fakultät für Biologie**

Eidesstattliche Erklärung

Hiermit erkläre ich an Eides statt, die Dissertation: „**Synergistische chemo- und photodynamische Behandlung von Krebszellen mit C₆₀-Fulleren-Nanokomplexen**“, eigenständig, d. h. insbesondere selbständig und ohne Hilfe eines kommerziellen Promotionsberaters, angefertigt und keine anderen, als die von mir angegebenen Quellen und Hilfsmittel verwendet zu haben.

Ich erkläre außerdem, dass die Dissertation weder in gleicher noch in ähnlicher Form bereits in einem anderen Prüfungsverfahren vorgelegen hat.

Weiterhin erkläre ich, dass bei allen Abbildungen und Texten bei denen die Verwertungsrechte (Copyright) nicht bei mir liegen, diese von den Rechtsinhabern eingeholt wurden und die Textstellen bzw. Abbildungen entsprechend den rechtlichen Vorgaben gekennzeichnet sind sowie bei Abbildungen, die dem Internet entnommen wurden, der entsprechende Hypertextlink angegeben wurde.

Affidavit

I hereby declare that my thesis entitled: „**Synergistic Chemo- and Photodynamic Treatment of Cancer Cells with C₆₀ Fullerene Nanocomplexes**” is the result of my own work. I did not receive any help or support from commercial consultants. All sources and / or materials applied are listed and specified in the thesis.

Furthermore I verify that the thesis has not been submitted as part of another examination process neither in identical nor in similar form.

Besides I declare that if I do not hold the copyright for figures and paragraphs, I obtained it from the rights holder and that paragraphs and figures have been marked according to law or for figures taken from the internet the hyperlink has been added accordingly.

Würzburg, den _____

Signature PhD-student

„C₆₀-Buckminsterfullerene: not just a pretty molecule“

Sir Harold Kroto (1998)

ACKNOWLEDGEMENTS

I would like to thank from the bottom of my heart to my primary supervisor *Prof. Dr. Marcus Frohme* for the opportunity to perform the current study at his division Molecular Biotechnology and Functional Genomics at the Technical University of Applied Sciences Wildau. His dynamic personality and open mindset steered the working atmosphere to drive scientific courage forward. His over sky research management sets an exceptional opportunity to learn just observing him in action. The completion of this research was an exciting adventure of one dream that would never have come true without his generous support and brilliant supervision!

I would like to take this opportunity to extend my heartily to my official supervisor *Prof. Dr. Thomas Dandekar* not only for taking the external research under his wings but for raising its quality through his input! His feedback was constantly informative and fruitful, pushing me to go beyond my limits. I am very grateful for his constant 24/7 support and sharp advices during publications preparation as well as for his constant extremely kind attitude!

The presented research was carried under the cooperative guidance of *Prof. Dr. Olga Matyshevska*, my role-model of a female scientist. Her deep grasp of biological logic always makes the obtained data shine. I am deeply indebted to her for her generous help and assessment of the ongoing research and published results.

I want to express my special gratitude to *Prof. Dr. Yuriy Prylutskyy* and *Dr. Svitlana Prylutska* for their constant support in a family-heated attitude as well as for their substantial help not only in battling but in overcoming unexpected scientific challenges. Their hardworking style has set a high standard for me to learn from.

I am grateful to *Prof. Dr. Uwe Ritter* for the continuous supply of C₆₀ fullerene. I also direct my special thanks to *Prof. Dr. Sigurd Schrader* and *Dr. Viachaslau Ksianzou* for the constant support and access to the optics laboratories.

I would like to thank to my working group for everyday company and friendly support. I wish to express my gratitude to *Dr. Lars Radke* and *Disieree Grienetz*, whose kind guidance especially on the beginning of the project became a game-changer; special thanks go to *Dr. Oliver Brödel* and *Chris Schwarz* for advice and technical support on a daily basis, *Dr. Sofia Cortes* and *Dr. Catrin Wernicke* for kind guidance in cell-based techniques, *Dr. Jörn Glökler* for creative ideas, *Liane Kober*, *Dr. Jens Fischbach*, *Dr. Katja Schulze* and *Dr. Ulrich Tillich* for teaching me new techniques, *Wilhelm Gossing*, *Philipp Franke* and *Karolin Keil* for their support, *Juliane Pfeil* for image processing and last but not least, thanks to *Dr. Heike Kagel*, *Benjamin Girke* and *Dr. Oksana Chepurna* for their help with LED light source development. I would like to thank the students involved in the studies *Benjamin Kolp* and *Tobias Hagemann* for their passionate work and delivered results.

I am grateful to the German Academic Exchange Service for the scholarship “The Research Grants – Doctoral Programmes in Germany” 57129429. I would like to express my deep gratitude to *Elena Schmid* for her enormous work with all required documents for my family and *Dr. Thomas Prahl* for his stimulating advice.

I would like to express my gratitude to my family: to my parents *Victoriia* and *Hryhorii Mykhailov* for their endless care and faith; to my uncle *Dr. Konstantin Grytsenko* for refreshing nudges; to my brother-in-law *Dr. Dmytro Grebinyk* for taking care of things in Kyiv, and to my grandparents *Dr. Evgenija Mykhailova* and *Prof. Dr. Vyacheslav Mykhailov* for my inherited curiosity in biological matter and science-oriented life style. I am deeply grateful to my husband *Dr. Sergii Grebinyk* for his limitless patience and unconditional help. And my special thanks go to our son *Artem* for becoming my most efficient personal motivator.

I find myself to be indeed an enormous lucky person to have been working and learning from each of you, my dearest Scientific Family! You will always hold a special place in my heart.

TABLE OF CONTENTS

Erklärungen nach §4 Abs. 3 Satz 3, 5, 8 der Promotionsordnung der Fakultät für Biologie:	I
Eidesstattliche Erklärung	I
Affidavit	I
Acknowledgements	III
Table of Contents	1
Summary	6
Zusammenfassung	7
I. INTRODUCTION	8
I.1 Nanotechnology for cancer treatment	8
I.1.1 What is cancer?	8
I.1.1.1 Origin and statistics	8
I.1.1.2 Difference between the normal and the cancer cell	9
I.1.1.3 Chemotherapy as a common cancer treatment	12
<i>Doxorubicin as an example for a conventional chemotherapeutic anticancer drug</i>	13
<i>Berberine as an example for a natural anticancer drug</i>	14
I.1.2 Cancer nanomedicine	15
I.1.2.1 Arsenal of nanoplatfoms for medical applications	16
I.1.2.2 Cancer physiology-driven design of nanodrugs	19
I.2 C ₆₀ fullerene-based cancer treatment approaches	23
I.2.1 Discovery of fullerenes: from hypotheses to the Nobel prize	23
I.2.2 Structure-determined properties of C ₆₀ fullerene	25
I.2.3 Photodynamic therapy with C ₆₀ fullerene	28
I.2.4 Drug delivery with C ₆₀ fullerene	32

I.3 Carbon nanoparticles-mediated photodynamic chemotherapy	35
II. AIM OF THE THESIS	39
III. MATERIALS AND METHODS	41
III.1 Materials	41
III.1.1 Chemicals	41
III.1.2 Media and buffers	42
III.1.3 Cell lines	42
III.1.4 Assay Kits	43
III.1.5 Special consumable supplies	43
III.1.6 Light sources	43
III.1.7 Equipment	44
III.1.8 Software	45
III.2 Methods	45
III.2.1 C ₆₀ -drug nanocomplex synthesis	45
III.2.2 Analytical methods	46
III.2.2.1 Matrix assisted laser desorption ionization-time of flight mass spectrometry	46
III.2.2.2 High performance liquid chromatography-tandem mass spectrometry	46
III.2.2.2.1 C ₆₀ fullerene quantification	47
III.2.2.2.2 Doxorubicin quantification	49
III.2.2.3 Spectroscopic and fluorometric analysis	50
III.2.2.4 Dynamic light scattering	51
III.2.3 LED light source	51
III.2.4 Cell-based methods	53
III.2.4.1 Cell culture	53
III.2.4.2 C ₆₀ fullerene immunofluorescence staining	53
III.2.4.3 Visualization of drug intracellular accumulation	54
III.2.4.4 C ₆₀ fullerene extraction	54

III.2.4.5 Isolation of mitochondria	55
III.2.4.5.1 Protein concentration assay	55
III.2.4.5.2 Succinate-reductase activity assay	56
III.2.4.6 Photodynamic treatment of cells with C ₆₀ fullerene	56
III.2.4.7 Drug delivery with C ₆₀ fullerene	57
III.2.4.8 Photodynamic treatment of cells with C ₆₀ fullerene-drug nanocomplex	57
III.2.4.9 Cell viability	57
III.2.4.10 Intracellular reactive oxygen species generation	58
III.2.4.11 Intercellular ATP content	58
III.2.4.12 Caspase 3/7 activity	59
III.2.4.13 Flow cytometry	59
III.2.4.13.1 Drug intracellular accumulation	59
III.2.4.13.2 Cell death type differentiation	59
III.2.4.13.3 Cell cycle	60
III.3 Statistics	61
III.3.1 Half-maximal inhibitory concentration	61
III.3.2 Combination index	61
IV. RESULTS	62
IV.1 C ₆₀ fullerene	62
IV.1.1 C ₆₀ uptake by leukemic cells and its intracellular distribution	63
<i>Qualitative analysis</i>	63
<i>Quantitative analysis</i>	64
IV.1.2 Photodynamic treatment of cells with C ₆₀ fullerene	66
IV.1.2.1 Cell viability	66
IV.1.2.2 Intracellular reactive oxygen species generation	68
IV.1.2.3 Apoptosis induction	69
IV.2 C ₆₀ -Drug nanocomplexes	71
IV.2.1 Analyses of C ₆₀ -Doxorubicin nanocomplexes	71

IV.2.1.1 HPLC-ESI-MS/MS analysis	72
IV.2.1.2 Spectroscopic and fluorometric analysis	73
IV.2.1.3 Size distribution analysis by dynamic light scattering	74
IV.2.2 Drug delivery with C ₆₀ nanocomplexes	76
IV.2.2.1 Cellular effects of C ₆₀ -Doxorubicin nanocomplexes	76
IV.2.2.1.1 Intracellular accumulation of C ₆₀ -Doxorubicin nanocomplexes	76
<i>Qualitative analysis</i>	76
<i>Quantitative analysis</i>	77
IV.2.2.1.2 Cell viability	79
IV.2.2.2 Cellular effects of C ₆₀ -Berberine nanocomplexes	82
IV.2.2.2.1 Cellular effects of alkaloid Berberine alone	83
<i>Intracellular accumulation</i>	83
<i>Cell viability</i>	84
<i>Intracellular reactive oxygen species generation</i>	85
<i>Apoptosis induction</i>	86
IV.2.2.2.2 Cellular effects of C ₆₀ -Berberine nanocomplexes	87
<i>Intracellular accumulation</i>	87
<i>Cell viability</i>	89
<i>Apoptosis induction</i>	91
IV.3 Towards photodynamic chemotherapy with C ₆₀ -drug nanocomplexes	92
IV.3.1 C ₆₀ -Doxorubicin nanocomplexes	92
IV.3.1.1 Cell viability	92
IV.3.1.2 Intracellular reactive oxygen species generation	95
IV.3.1.3 Apoptosis induction	96
IV.3.2 C ₆₀ -Berberine nanocomplexes	99
IV.3.2.1 Cell viability	99
V. DISCUSSION	102
V.1 Effects of C ₆₀ fullerene on leukemic cells	103

V.1.1 C ₆₀ fullerene's uptake by leukemic cells	103
V.1.2 Photodynamic treatment of leukemic cells with C ₆₀ fullerene	106
V.2 Effects of C ₆₀ -drug nanocomplexes on leukemic cells	111
V.2.1 Nanocomplexes with a common chemotherapeutic Doxorubicin	112
V. 2.1.1 C ₆₀ -Doxorubicin characterization	112
V. 2.1.2 C ₆₀ -Doxorubicin's uptake by leukemic cells	115
V. 2.1.3 Effects of C ₆₀ -Doxorubicin on leukemic cells	116
V.2.2 C ₆₀ -nanocomplexes with an alternative anticancer drug Berberine	118
V.2.2.1 Herbal alkaloid Berberine's effects on leukemic cells	118
V.2.2.2 Effects of C ₆₀ -Berberine on leukemic cells	120
V.3 Towards photodynamic chemotherapy with C ₆₀ -drug nanocomplexes	122
V.4 Outlook	128
VI. REFERENCES	133
VII. APPENDIX	i
Appendix 1. Red light sources for C ₆₀ photodynamic treatment of cells	i
Appendix 2. Spectroscopic and fluorometric analysis of Berberine	ii
Appendix 3. C ₆₀ sonodynamic treatment of cancer cells	iii
Appendix 4. Berberine (0.5 μM) localization in CCRF-CEM cells	v
Appendix 5. Intracellular reactive oxygen species generation in CCRF-CEM cells treated with photoexcited Berberine	vi
Abbreviations	vii
List of Figures	ix
List of Tables	xii
List of Formulae	xiii
Curriculum Vitae	xiv
Publications	xvi
Original peer-reviewed publications derived from the Thesis	xvi
Other publications derived from the Thesis	xvii
Other peer-reviewed publications	xix

SUMMARY

Recent progress in nanotechnology has attracted interest to a biomedical application of the carbon nanoparticle C₆₀ fullerene (C₆₀) due to its unique structure and versatile biological activity. In the current study the dual functionality of C₆₀ as a photosensitizer and a drug nanocarrier was exploited to improve the efficiency of chemotherapeutic drugs towards human leukemic cells.

Pristine C₆₀ demonstrated time-dependent accumulation with predominant mitochondrial localization in leukemic cells. C₆₀'s effects on leukemic cells irradiated with high power single chip LEDs of different wavelengths were assessed to find out the most effective photoexcitation conditions. A C₆₀-based noncovalent nanosized system as a carrier for an optimized drug delivery to the cells was evaluated in accordance to its physicochemical properties and toxic effects. Finally, nanomolar amounts of C₆₀-drug nanocomplexes in 1:1 and 2:1 molar ratios were explored to improve the efficiency of cell treatment, complementing it with photodynamic approach.

A proposed treatment strategy was developed for C₆₀ nanocomplexes with the common chemotherapeutic drug Doxorubicin, whose intracellular accumulation and localization, cytotoxicity and mechanism of action were investigated. The developed strategy was revealed to be transferable to an alternative potent anticancer drug – the herbal alkaloid Berberine.

Hereafter, a strong synergy of treatments arising from the combination of C₆₀-mediated drug delivery and C₆₀ photoexcitation was revealed. Presented data indicate that a combination of chemo- and photodynamic treatments with C₆₀-drug nanoformulations could provide a promising synergetic approach for cancer treatment.

ZUSAMMENFASSUNG

Kürzliche Fortschritte in der Nanotechnologie haben Interesse an einer biomedizinischen Anwendung des Kohlenstoffnanopartikels C₆₀ Fulleren (C₆₀) aufgrund seiner einzigartigen Struktur und breiten biologischen Aktivität geweckt. In der aktuellen Studie wurde die doppelte Funktionalität von C₆₀ als Photosensibilisator und als Wirkstoff-Nanoträger genutzt, um die Wirkung von Chemotherapeutika auf menschliche Leukämiezellen zu verbessern.

C₆₀ alleine zeigte in den Zellen eine zeitabhängige Akkumulation mit vorherrschender mitochondrialer Lokalisation. Die Wirkung von C₆₀ auf Leukämiezellen, die mit unterschiedlicher Wellenlänge bestrahlt wurden, wurde bewertet, um die effektivsten Photoanregungsbedingungen zu finden. Die physikochemischen Eigenschaften und toxischen Wirkungen von C₆₀ auf die Leukämiezellen wurden nach nicht kovalenter Bindung von Arzneistoffen bewertet. Schließlich wurden nanomolare Mengen von C₆₀-Wirkstoff-Nanokomplexen in Molverhältnissen von 1:1 und 2:1 untersucht, um die Effizienz der Behandlung von Zellen zu verbessern und sie durch photodynamischen Ansatz zu ergänzen.

Mit dem gängigen Chemotherapeutikum Doxorubicin wurde eine Behandlungsstrategie entwickelt und dessen intrazelluläre Akkumulation und Lokalisation, Zytotoxizität und Wirkmechanismus untersucht wurden. Es wurde gezeigt, dass die entwickelte Strategie auch auf ein alternatives Krebsmedikament übertragbar ist – das pflanzliche Alkaloid Berberin.

Die erhaltenen Daten deuten darauf hin, dass eine Kombination von chemo- und photodynamischen Behandlungen mit C₆₀-Nanokomplexen einen vielversprechenden synergetischen Ansatz für die Krebsbehandlung bieten könnte.

I. INTRODUCTION

1.1 Nanotechnology for cancer treatment

Science, engineering and technology merged in the field of nanotechnology to create, investigate and apply nanoparticles (Feynman, 1960). Nanoparticles are generally defined as any particulate material, for which at least one dimension lies in a range of 1-1000 nm. Nanosize grants particles tunable physico-chemico-biological properties that enhance their performance over bulk counterparts. Nanotechnology in medicine involves applications of nanoparticles to develop novel therapies and improve existing approaches. This field has tremendous potential to play a significant role in cancer prevention, detection and treatment (Min et al., 2015; Chen et al., 2016a; Shi et al., 2017).

1.1.1 What is cancer?

1.1.1.1 Origin and statistics

Cancer is usually viewed as an evolutionary process resulted from the accumulation of somatic mutations in the progeny of a normal cell, leading to a selective growth advantage and ultimately to their uncontrolled proliferation. Cancer is a group of noncommunicable diseases responsible for 18.1×10^6 new cases and 9.6×10^6 deaths in 2018 and ranked as the single most important barrier that is revoking an expected increase of life expectancy in 21st century worldwide (Bray et al., 2018). The most frequent human cancers arise in epithelial tissues in lung, breast, prostate, colon, skin and stomach.

The last two decades have seen enormous advances in understanding of cancer disease at the molecular level. However, the main challenge, that limits success to

be achieved with current evolving treatment options, is the high diversity and heterogeneity of tumors (Cleary et al., 2014; Shi et al., 2017; Turajlic et al., 2019). The other aspect could be linked with the majority of funding supports basic research, having less than 5% for translational research (Fang & Casadevall, 2010; Hait, 2010), so the ultimate goal to cure cancer is pending. As the altered genetic and metabolic profiles of cancer cells distinguish them from normal cells, the high-priority pharmacological challenge is to develop new anticancer treatment strategies targeting cancer cells alterations.

1.1.1.2 Difference between the normal and the cancer cell

A fundamental hallmark of the cancer cell is its chronic proliferation (Cooper, 2000; Weinberg, 2007; Hanahan & Weinberg, 2011). The key mechanisms of chronic proliferation include the activation of oncogenes, the rewiring of intracellular signaling pathways, the adaptation of the cellular metabolism and the downregulation of cell sensitivity to factors that inhibit growth or lead to programmed cell death.

Main mechanisms of the oncogenes activation in human neoplasms are genetic alterations such as chromosomal translocation, point mutation deletion, gene amplification and insertion (Hassanpour & Dehghani, 2017). In average, solid tumors display 50 genes with somatic mutations, reaching a maximum of 200 mutations in melanomas and lung tumors (Vogelstein et al., 2013). However, in a typical tumor only from two to eight of these mutations are critical and drive a malignant transformation through alterations in cell fate, cell survival and/or genome maintenance (Weinberg, 2007; Vogelstein et al., 2013). For example, mutation in the gene of the cell cycle guardian protein p53 leads to expression of its mutant form that blocks wild-type p53 and functions as a transcriptional factor of both cell cycle arrest and apoptosis downregulation (Weinberg, 2007; Hassanpour & Dehghani, 2017). Furthermore, there are common alterations in epigenetic regulation, which primarily include DNA hypomethylation and repress the expression of antioncogenes (Hassanpour &

Dehghani, 2017; Weyandt et al., 2017).

For proliferation induction, the cancer cell produces growth factors, stimulates surrounding normal fibroblasts to produce them (Bhowmick et al., 2004; Cheng et al., 2008) and/or alters growth factors receptors (Cooper, 2000; Hanahan & Weinberg, 2011; Sever & Brugge, 2015). Many somatic mutations in the cancer cell genome drive a constitutive activation of proteins in the MAPK/ERK (mitogen-activated protein kinases/originally called extracellular signal-regulated kinases) and the PI3K/AKT/mTOR (phosphoinositide 3-kinases/protein kinase B/mechanistic target of Rapamycin) signaling pathways (Jiang & Liu, 2009; Davies & Samuels, 2010; Hanahan & Weinberg, 2011; Sever & Brugge, 2015) that transmit a constantly activated proliferative signal. Other signaling pathways, that can be altered in a cancer cell and drive proliferation, include JAK/STAT (Janus kinases/signal transducer and activator of transcription proteins) (Sever & Brugge, 2015) and Wnt/ β -catenin (Wingless-related integration site/ β -catenin) (Weinberg, 2007) pathways.

The normal cell responds to mitogens only if it is not restrained by the inhibitory action of cadherin-mediated contact inhibition and is attached to a supportive matrix via integrins (Gumbiner, 1996). In contrast, the cancer cell loses the importance of those connections and becomes insensitive to the contact inhibition (Brücher & Jamall, 2014). Oncoprotein Ras mimics the signal of integrins and growth factor receptors. It functions as a G protein without mechanism to shut it off, that traps the oncoprotein in the active mitogen signal-emitting configuration (Weinberg, 2007).

The cancer cell alters its metabolism to meet needs of excessive proliferation, not excluding the constant maintenance of critical cellular processes. The increased nutrients consumption provides the cancer cell with the required energy and carbon intermediates. While the normal cell relies primarily on aerobic respiration – oxidative phosphorylation in mitochondria, the cancer cell switches to aerobic glycolysis and glutaminolysis (Amoêdo et al., 2013; Sever & Brugge, 2015; Weyandt et al., 2017). The increased dependence on these pathways is commonly known as the Warburg effect, or the loss of the Pasteur effect (Hanahan & Weinberg, 2011; Amoêdo et al.,

2013; Giacotti, 2014; Sever & Brugge, 2015). The PI3K/AKT/mTOR pathway determines overexpression of transporters for glucose and other nutrients, glycolytic and lipogenesis enzymes (Wallace, 2012). This adjustment allows the cancer cell to use glycolytic intermediates for its anabolism and escape the harmful effects of possible high reactive oxygen species (ROS) level at the expense of enhanced aerobic oxidative phosphorylation in mitochondria (Herst et al., 2017). The malfunctioning phosphorylation in mitochondria leads to oxygen accumulation in the cell. Instead of being oxidized to water, oxygen functions as acceptor of electrons, that leak out of disrupted electron transport chain (Schumacker, 2006).

In the majority of cancer cells malfunctioned mitochondria contribute to cancer progression as well. Mitochondria drive malignant transformation, provide building blocks for cancer anabolism, control redox and calcium homeostasis, participate in transcriptional regulation and govern regulated cell death (Wallace, 2012; Herst et al., 2017; Porporato et al., 2018). Cancer-associated alterations in mitochondria include overexpression of antiapoptotic Bcl-2-related proteins, inactivation of p53, methylation of promoters of proapoptotic genes and further upregulation of PI3K/AKT/mTOR pathway (Yang et al., 2016; Porporato et al., 2018). Mitochondrial ROS are important signaling molecules and function as potent cancer mitogens that lead through DNA oxidation to further genomic instability (Gupta et al., 2012; Yang et al., 2016). The balance of intracellular ROS and antioxidants plays a key role in homeostasis maintenance in both normal and cancer cell, whereas imbalance leads to the excessive mitochondrial oxidant stress and the followed inability of the cell to cope with exogenous oxidative attacks, that initiates apoptosis (Kong et al., 2000; Ribeiro et al., 2004). Yet the cancer cell inactivates the apoptotic machinery through multiple mechanisms that hinder apoptosis, otherwise normally induced due to present DNA damage, hypoxia, oxidative stress and loss of anchorage (Cooper, 2000; Weinberg, 2007; Giacotti, 2014). Oncogenic signals, transmitted through Ras and PI3K, promote cell survival by inactivating proapoptotic proteins Bim and Bad as well as by enhancing the expression of antiapoptotic Bcl2-related proteins

and inhibitors of proapoptotic proteins (Weinberg, 2007; Giacotti, 2014). Overexpression of Bcl2-family proteins such as Puma, Noxa, Bid and Bax occurs under a loss of p53 function (Yip & Reed, 2008; Giacotti, 2014).

Cancer cell functions with a heightened basal level of ROS signaling that stimulates proliferation. The escalated oxidant status makes cancer cells more vulnerable to further prooxidant stress (Schumacker, 2006; Fiaschi & Chiarugi, 2012). Modest level of ROS is required for cancer cells to survive, whereas higher level kills them (Kong et al., 2000; Schafer & Buettner, 2001). This paradox provides an opportunity for researchers to exploit oxidant stress for the development of cancer therapies (Wallace, 2012). The central role of the oncogenic mitochondrial ROS in genomic instability and cancer development make mitochondria a promising target for anticancer therapy (Yang et al., 2016). However, the modulation of ROS signaling alone seems not to be an ideal approach, because some cancers can adapt to oxidant stress (Fiaschi & Chiarugi, 2012) and the redundant pathways supporting cancer growth are complex.

Understanding of the genetic and metabolic alterations in cancer cells is a critical initial step towards a successful cancer therapy development. Only with sufficient prognostic knowledge of the specific treatment-cell interactions one can start to design the optimal treatment strategy. Any new treatment approach must be first precisely evaluated at the cellular level *in vitro* before it can be further translated to at the tissue, organ and body levels.

1.1.1.3 Chemotherapy as a common cancer treatment

Chemotherapy (CT), surgery and radiotherapy are the most common types of cancer treatments available nowadays (Arruebo et al., 2011). Surgery is the oldest modality and operates by zero-order kinetics, in which 100% of excised cells are killed (Pollock & Morton, 2003). However, surgery is not able to hinder possible cancer recurrence. With the advent of radiotherapy in the 1920s and CT in the 1940s, cancer

surgery has become conservative (Shewach & Kuchta, 2009; Arruebo et al., 2011). Radiotherapy and CT target a fraction of actively proliferating cells during each treatment. In recent years, immunotherapy developed as an important therapeutic alternative that exploits the patient's immune system to identify the cancer cells as foreign and wipe them out (Guo et al., 2019).

CT aims to slow down the growth of cancer cells that evolve to divide quickly (Chabner & Roberts, 2005; Shewach & Kuchta, 2009). The first generation of anticancer chemotherapeutic agents commonly exploits a single toxic drug such as the anthracycline antibiotic Doxorubicin (Cortés-Funes & Coronado, 2007). A common feature of a large number of cancer chemotherapeutics is the ability to hinder DNA synthesis and therefore cell division (Shewach & Kuchta, 2009).

Doxorubicin as an example for a conventional chemotherapeutic anticancer drug

Doxorubicin – (8*S*-*cis*)-10-[(3-*amino*-2,3,6-*trideoxy*- α -*L*-lyxo-hexopyranosyl)oxy]-7, 8, 9, 10-tetrahydro-6, 8, 11-trihydroxy-8-(hydroxyacetyl)-1-methoxynaphthacene-5, 12-dione hydrochloride, CAS No. 25316-40-9, molecular weight of 580 g/mol – contains a quinone-containing rigid planar aromatic ring bound by a glycosidic bond to an aminosugar daunosamine (Cortés-Funes & Coronado, 2007; Tacar et al., 2013). Doxorubicin, firstly extracted from *Streptomyces peucetius* in the 1970's, continues to be routinely used nowadays in the treatment of many cancers including breast, lung, gastric, ovarian, multiple myeloma, sarcoma, thyroid and pediatric cancers, non-Hodgkin's and Hodgkin's lymphoma (Cortés-Funes & Coronado, 2007; Kizek et al., 2012). The main mechanism of Doxorubicin toxicity against cancer cells is its intercalation into nuclear DNA that is followed by inhibition of topoisomerase activity, DNA transcription, replication and repair (Kizek et al., 2012; Tacar et al., 2013). The main side effects of Doxorubicin target cardiomyocytes and are considered to be determined by another mechanism, mainly, iron-related ROS formation through metal chelation and flavoprotein reductases-associated redox cycling (Kizek et al., 2012; Finn et al., 2011; Thorn et al., 2011). The extended ROS

generation causes serious adverse cardiotoxicity owing to the high content of mitochondria in cardiomyocytes and limits the drug's clinical application (Jung & Reszka, 2001; Tacar et al., 2013).

An efficient clinical practice in cancer CT is challenged with a number of setbacks, including poor specificity, high general toxicity and induction of drug resistance in cancer cells (Chen et al., 2016a; Shi et al., 2017). Therefore, new approaches to improve efficiency and attenuate side effects are urgently needed.

Berberine as an example for a natural anticancer drug

Historically natural products have always provided drugs against a wide variety of diseases, with cancer being no exception (Shewach & Kuchta, 2009). Herbal secondary metabolites exhibit multiple biological and pharmacological properties, representing a natural library of bioactive compounds with potentially high safety, availability, accessibility and low costs. One of the most versatile class of herbal secondary metabolites presents heterocyclic, nitrogen containing, low-molecular-weight molecules – alkaloids. These toxic molecules ensure a defense of plants against herbivores, bacteria, fungi and viruses (Keasling, 2008; Xiao et al., 2012; Ortiz et al., 2014). Representatives of this class often exhibit pharmacological effects and are used as anticancer therapeutics such as Vinblastine, Vincristine, Paclitaxel and Camptothecin (Mann, 2002).

The isoquinoline quaternary alkaloid Berberine – *2,3-methylenedioxy- 9,10-dimethoxyprotoberberine chloride*, CAS No. 633-65-8, molecular weight of 372 g/mol – is a common drug in Ayurvedic, Chinese, Middle-Eastern and native American folk medicines due to its board spectra of biological activities (Pereira et al., 2007; Neag et al., 2018). Applications of Berberine as a low cost therapeutic with anti-inflammatory, antimutagenic, antidiabetic, antimicrobial and antiviral effects seem to be promising (Cernáková et al., 2002; Abd El-Wahab et al., 2013; Cai et al., 2014; Ortiz et al., 2014). In recent years, Berberine has been reported to inhibit proliferation of many cancer cell

lines originated from head and neck squamous carcinoma (Seo et al., 2015), melanoma (Serafim et al., 2008), leukemia (Xiao et al., 2012), oral (Kuo et al., 2005), pancreatic (Park et al., 2015), colon (Zhang et al., 2013), breast (Patil et al., 2010) and prostate (Meeran et al., 2008) cancer. Given the positive charge of nitrogen atom (Gumenyuk et al., 2012), Berberine interacts directly with genomic (Wang et al., 2011b; Li et al., 2012) and telomeric (Franceschin et al., 2006; Arora et al., 2008) DNA, inducing double-strand breaks and telomere stabilization, respectively. The potential intracellular targets of Berberine are DNA topoisomerase I, POT1 (Xiao et al., 2012), Wnt (Albring et al., 2013; Zhang et al., 2013), p53 (Patil et al., 2010; Wang et al., 2014), NF- κ B (Liu et al., 2010b), cyclooxygenase-2, and Mcl-1 (Kuo et al., 2005), nucleophosmin/B23 (Wu et al., 1999), death-domain-associated protein (Zhang et al., 2010). Berberine's anticancer cytotoxicity is associated mainly with oxidative stress escalation and mitochondrial dysfunction (Meeran et al., 2008; Park et al., 2015; Neag et al., 2018), apoptosis activation and cell cycle arrest (Kuo et al., 2005; Patil et al., 2010; Zhang et al., 2010; Cai et al., 2014). However, hormetic effect (Bao et al., 2015), poor water solubility, stability and bioavailability (Mirhadi et al., 2018) limit clinical applications of Berberine.

The advent of nanomedicine and application of biocompatible, bioavailable and nontoxic nanoparticles brought significant advances in the field of cancer therapy offering the customizable and safer treatment option. Delivery nanosystems could pave a way to overcome limitations and improve Doxorubicin and Berberine anticancer efficacy.

1.1.2 Cancer nanomedicine

Nanomedicine, the application of nanotechnology to health and medicine, is a new interdisciplinary science to address various conventional medical shortcomings including but not limited to poor bioavailability, impaired target specificity, systemic and organ toxicity of conventional drugs (Chen et al., 2016a; Shi et al., 2017).

Nanoparticles have made a rapid and broad impact on healthcare (Min et al., 2015; Yingchoncharoen et al., 2016). A wide range of synthetic lipid, protein, polymeric, organic and inorganic nanoparticles have been employed for the development of cancer therapeutics (Senapati et al., 2018).

1.1.2.1 Arsenal of nanoplatforms for medical applications

Nanotechnology has made important contributions to oncology over the past several decades. A large number of nanoscale and nanostructure-based therapeutic and diagnostic agents have been developed, not only for cancer treatment but also for its prevention and detection (Arruebo et al., 2011). The size-dependent tunable electronic, optical, magnetic and mechanical properties are fundamental to the current excitement and growing applications of nanomaterials (Chen et al., 2016a). The most attractive nanomaterials include lipid, polymeric, dendritic, inorganic and organic nanoparticles. Beyond their widely reported use as carriers for chemotherapeutic drugs, nanoparticles have shown potential for the delivery of various new anticancer therapeutic agents, including molecularly targeted agents, antisense oligonucleotides, small interfering RNA (siRNA), mRNA and DNA inhibitor oligonucleotides (Shi et al., 2017). Most commonly classification organizes nanoparticles into three material-based categories: inorganic-, organic- and carbon-based.

Inorganic nanomaterial includes nanoparticles made of metal, its oxide and semiconductor (Jeevanandam et al., 2018). Inorganic nanoparticles as carriers offer the advantage of being extremely robust, and thus very stable and resistant to enzymatic degradation (Chen et al., 2016a). Furthermore, their intrinsic electronic, optical and magnetic properties can be tailored by judicious control of their crystal phase, size, shape, composition and surface characteristics to make them truly multifunctional for imaging and therapy. However, toxicity is a major concern with inorganic nanocarriers containing heavy metal atoms, which requires a biocompatible coating. Magnetic nanoparticles, usually consist of a magnetic core (e.g. magnetite or maghemite), have

been widely used in drug and gene delivery, where they are used as nanocarriers for magnetic-field-directed targeting to the site of interest (Price et al., 2018). Compared to the conventional gadolinium chelates, magnetic nanoparticles-based contrast agents offer excellent image enhancement for magnetic resonance imaging due to their large magnetic moment as well as improved cellular internalization and slower clearance from the target site (Cheng et al., 2014; Issa & Obaidat, 2019). Gold nanoparticles found various applications in diagnostics due to their functionality as indicator and detection probe. Those nanoparticles are attractive candidates for biological imaging as they can be visualized based on their interaction with light (Capek, 2017). Silver nanoparticles have excellent antimicrobial activity against viruses, bacteria and other eukaryotic microorganisms (Akter et al., 2018; Tang & Zheng, 2018). Semiconductor silica nanoparticles can be classified into solid or non-porous and mesoporous. Silica nanoparticles became common platforms for various catalytic and chemical reactions, bioimaging, drug and gene delivery owing to the straightforward and size-controlled synthesis, chemical and physical stabilities, large surface area, hydrophilic surface and well-defined surface chemistry (Jeelani et al., 2019).

Organic nanoparticles are made mostly from organic matter, excluding carbon-based nanomaterial. The utilization of noncovalent (weak) interactions for the self-assembly and design of molecules helps to transform the organic material into desired nanostructures such as liposomes and micelles, polymeric and dendritic nanoparticles. Liposomes are small lipid vesicles of one or several lipid bilayers with a polar aqueous “core”, a lipophilic bilayer compartment and a hydrophilic exterior (Chen et al., 2016a). Therefore, liposomes can deliver both hydrophobic and hydrophilic cargo. Phospholipid bilayer nanoliposome is the first anticancer drug delivery nanosystem translated into real-time clinical application as Doxil® was approved in 1995 by the U.S. Food and Drug Administration (FDA). Anticancer drug Doxil® is a liposomal nanoformulation of Doxorubicin with size of 80-100 nm (Barenholz, 2012) that along with other lipid-based nanoparticles still represent a large proportion of clinical stage nanotherapeutics (Shi et al., 2017). The major problems associated with liposomes are

their stability, poor batch to batch reproducibility, difficulty in sterilization and low drug loading capacity. Polymeric nanocarriers offer a great deal of flexibility in tailoring of chemical composition, size, biodegradability, morphology and surface functionality (Uhrich et al., 1999). As a result, they serve as excellent drug carriers for a range of applications in sensing, imaging and therapeutics (Chen et al., 2016a). Hydrophilic polymers, such as polyethylene glycol (PEG), chitosan and dextran, are widely used as coating agents on other nanoparticles to enhance their aqueous dispersibility, bioavailability and targeting efficacy. Dendrimers are a class of repeatedly hyperbranched polymeric macromolecules with well-defined organic units extending from a center (Bharali et al., 2009). The advantage of dendrimers is that they can be synthesized and designed for specific applications. Dendritic scaffolds as delivery carriers for Doxorubicin improved drug-loading capacity and stabilized such systems in the body (Lai et al., 2007; Bharali et al., 2009).

The variety of natural and artificial carbon allotropes is astounding and many of these carbon structural formations have interesting electronic, mechanical and physicochemical properties at the nanoscale. Carbon nanoparticles include fullerenes, carbon nanotubes, graphene and graphene oxide nanoparticles, carbon and graphene dots, nanohorns and nanodiamonds, that have a great versatility in terms of loading and easy functionalization (Mendes et al., 2012; Iannazzo et al., 2013; Slepíčka et al., 2013). Although these nanoparticles mainly consist of one element carbon, its different structures show versatile properties. Graphene is considered as the fundamental building block for carbon-based nanomaterials that is wrapped up into round fullerenes, rolled into nanotubes or stacked into graphite (Choudhary et al., 2014). Of the various strategies used in nanomedicine, carbon-based nanomaterial has been on the rise due to its high surface area, multifunctional surface chemistry, mechanical strength (Schrand et al., 2009; Hu & Lu, 2014), high chemical stability (Cheng & Xue, 2016) and biocompatibility (Zuckerman & Kao, 2009). Moreover, the existence of the high band gap is responsible for a variety of unique optical properties (Dong & Cao, 2018), based on which carbon nanoparticles have found many interesting applications in

biomedical imaging and therapeutics. Given an intrinsic strong absorption and photodependent toxicities, carbon nanoparticles have attracted attention as possible therapeutics agents for the cancer phototherapy, that exhibited advantages in terms of enhancing cancer killing specificity and reducing side effects in comparison to conventional cancer therapies (Dong & Cao, 2018).

1.1.2.2 Cancer physiology-driven design of nanodrugs

Nanomaterials offer several key advantages for therapeutic applications compared to conventional molecular probes. A tunable size, shape and the surface properties of the nanoparticles enable to precisely address the alterations in cancer pathophysiology of the tumor microenvironment. In that way, nanoparticles provide a platform for a targeted drug delivery to tumors with minimal systemic biodistribution.

Nanoparticles are selectively accumulated and preferentially remained at the tumor site (Yingchoncharoen et al., 2016; Shi et al., 2017; Tran et al., 2017). It happens because tumor blood vessels are characterized by abnormalities, such as high proportions of proliferating endothelial cells, pericyte deficiency and aberrant basement membrane formation (Danhier et al., 2010). As a result, the tumor blood vessels are leaky and cause the higher extravasation of macromolecules and hydrophobic particles in a size range between 10 and 500 nm (Yingchoncharoen et al., 2016; Fan et al., 2017; Perry et al., 2017; Shi et al., 2017). From another side, a nonfunctional lymphatic drainage with the high interstitial fluid pressure causes nanoparticles' retention in tumors (Fan et al., 2017; Perry et al., 2017; Golombek et al., 2018). These two alterations contribute to a phenomenon referred as the enhanced permeability and retention effect (Matsumura & Maeda, 1986) that plays a central role in the passive cancer targeting with nanoparticles.

The nanocarrier protects drug from its fast degradation by endogenous defenses including enzymatic degradation and rapid clearance (Biju, 2014; Chen et al., 2016a; Senapati et al., 2018), prolongs drug's plasma half-life in the systemic circulation

(Maeda et al., 2001; Sun et al., 2014) and promotes the attenuation of premature drug leakage in healthy tissues and side effects; that taken together improve drug's bioavailability. As a particle's size gets smaller, its surface area/volume ratio gets larger. The larger the ratio is, the higher the payloads of therapeutic molecules could be entrapped by the carrier (Biju, 2014; Tran et al., 2017). From another point, being at the surface of the nanocarrier determines a faster drug release (Buzea et al., 2007; Rizvi & Saleh, 2018). The shape of the drug delivery nanosystem impacts fluid dynamics in blood, which influences nanoparticles' circulation time and cellular uptake. Currently, the use of spherical nanocarriers appears to be most common than that of the nonspherical alternatives due to the higher stability in the blood flow pattern (Sun et al., 2014) and absence of challenges in synthesis and testing (Truong et al., 2015).

The nanoparticle's surface properties, such as surface charge and hydrophilicity/hydrophobicity, influence the stability of the system as well as its interactions with the surrounding environment as they affect the hydrodynamic radius, plasma reactivity and interactions with cell plasma membrane (Sun et al., 2014). An electrical zeta potential of a particle determines its stability, thus, when the surface charge of nanoparticle is close to neutral, the colloidal system is usually unstable and massive agglomeration takes place (Moore et al., 2015). A slightly negative or positive charge is suggested to be the optimum with minimal self to self and self to non-self interactions (Yingchoncharoen et al., 2016). Thus, for stable nanoformulations the zeta potential should be above ± 30 mV (Sun et al., 2014; Chitkara, 2018). Due to large surface area/volume ratios, nanoparticles tend to adsorb blood proteins that form a protein complex "corona" and are faster cleared by macrophages (Honary & Zahir, 2013). Negative charge and higher hydrophilicity shown less protein adsorption and, therefore, favor elongated circulation time (Kou et al., 2013; Chitkara, 2018). On the other hand, nanomaterials also have immunomodulatory effects that can promote the adaptive immune response against malignancy (Zhu et al., 2014). The blood proteins adsorbed onto the nanoparticles include immunoglobulins, apolipoproteins and

proteins of the complement system that induce signals for immune response and shape nanoparticles interaction with immune cells (Hussain et al., 2012; Jiao et al., 2014). Inflammation is evidenced by the production of cytokines or chemokines as the main downstream event of the oxidative stress induced by nanoparticles (Jiao et al., 2014).

Nanocarrier surface properties define its interaction with the cancer cell and the rate of its internalization. Nanoparticles with positively charged surfaces interact rapidly with the negatively charged cell plasma membrane through electro-static interactions and internalize through the clathrin-mediated endocytosis (Harush-Frenkel et al., 2007; Wang et al., 2011a; Tran et al., 2017), negatively charged nanoparticles are more likely to take advantage of caveolae-mediated pathway (Perumal et al., 2008; Sahay et al., 2010), when the neutral nanoparticles show no clear preference for specific routes (Kou et al., 2013). Otherwise, higher lipophilicity promotes faster diffusion of molecule across the plasma membrane and relocation to other cellular membranes, thus facilitating intracellular uptake (Castano et al., 2004). Hydrophobic drugs are shown to attack cancer cells mainly by direct interactions, whereas hydrophilic agents act indirectly by damaging blood vessels (Luksiene, 2003). Thus, once an iron oxide nanoparticle was coated with pullan, the increased hydrophilicity caused a reduction of its cellular uptake via endocytosis (Gupta & Gupta, 2005; Sun et al., 2014); and vice versa, an increased lipophilicity of neocarzinostatin conjugated with copolymers appears to be responsible for its escalated cell surface affinity and ≤ 30 folds intensification of endocytosis rate (Maeda et al., 2001).

Assessing the efficient drug intracellular level, the intracellular drug escape should be considered as well. An upregulation of the P-glycoprotein-mediated efflux system, identified as a primary cause of multidrug resistance to chemotherapy and molecularly targeted therapies, presents a major setback in current cancer handling (Holohan et al., 2013; Sun et al., 2014). However, P-glycoprotein does not operate with polymeric nanodrugs (Maeda et al., 2001) or carbon nanoparticle C₆₀ fullerene (Xu et al., 2012) that can result in reduced efflux, an increased intracellular delivered drug concentration and reduction of cancer drug resistance (Xu et al., 2012). On top of it,

the rapid development of nanotechnology determined the possibility to assemble several types of therapeutic agents on the basis of one nanosystem through physical adsorption and chemical binding forces, providing a unique opportunity to develop a multimodal cancer therapy (Sun et al., 2014; Fan et al., 2017), which may substantially improve the therapeutic effectiveness and treat those malignant tumors that harbor resistance to monotherapy.

Given a determination of a nanoparticles biological fate by its physico-chemical properties, the design of the anticancer drug-loaded nanosystems should be developed based on the main optimal characteristics in order to achieve a highest level of safety with better functionality, sensitivity, efficiency and specificity (Tab. 1). The particle's shape, size and surface chemistry are significant for determining important pharmacokinetic criteria, such as adsorption, cellular uptake, accumulation and biodistribution patterns. Filtering and clearance of foreign molecules in the organism should be considered since ≥ 200 nm nanoparticles tend to activate the lymphatic system and are removed from circulation quicker (Rizvi & Saleh, 2018), whereas 100-200 nm nanomaterials are able to escape renal, hepatic and lymphatic clearance (Spencer et al., 2015). Thus, from literature evaluation and discussion so far, the optimum size and charge for a nanoparticle is approximately 100-200 nm and $\geq \pm 30$ mV, respectively.

Table 1. The rational design for nanosystem as a carrier of anticancer drug

<i>Characteristic</i>	<i>Advantageous value</i>
size	100-200 nm
charge	$\geq \pm 30$ mV
solubility	hydrophilicity for prolonged circulation hydrophobicity for higher cellular uptake

The advent of nanomedicine brought significant advances in the field of cancer medicine offering the customizable and safer treatment options. Nanoparticle-based treatment represents a promising strategy to enhance therapeutic outcomes and attenuate off-target side effects. The intermolecular interactions in the pair of drug-

nanoparticle should be considered as well depending on the defined molecular structures. For nanoparticles to have a clinical translation potential, the complexity in the design and development needs to be minimized to create a nanosystem that can be reproducibly prepared and characterized. Clinical impact of nanotechnology for cancer treatment will strongly benefit from customized nanoparticle-based therapies, designed to overcome physiological context of varying disease states.

1.2 C₆₀ fullerene-based cancer treatment approaches

The constantly increasing interest in novel nanotechnology platforms for biomedical applications stimulated the investigation of carbon nanomaterials. Fullerenes, graphene and their derivatives have shown good biocompatibility, which makes them attractive candidates for biomedical applications (Navya & Daima, 2016). The most prominent representative of the fullerenes is a C₆₀ fullerene (Kroto et al., 1985) (here consistently abbreviated “C₆₀”, CAS No. 99685-96-8, molecular weight of 720.7 g/mol). C₆₀ not only exhibits unique physico-chemical properties, biological activity and antioxidant behavior, but also possesses a significant potential to serve as a nanocarrier for drug delivery into cancer cells (Gharbi et al., 2005; Scharff et al., 2008; Chaudhuri et al., 2009; Liu et al., 2010a; Delgado et al., 2014; Huang et al., 2014; Magoulas et al., 2015; Prylutska et al., 2015; Prylutsky et al., 2015; Goodarzi et al., 2017; Kumar & Raza, 2017).

1.2.1 Discovery of fullerenes: from hypotheses to the Nobel prize

The discovery of fullerenes, as the third allotrope from of carbon after graphite and diamond, is a quit fascinating example of a new scientific idea to raise above common skepticism and disbelief.

In 1970 Eiji Osawa (Toyohashi University of Technology, Japan) conjectured the existence of fullerenes in the form of icosahedron consisting sixty atoms (Osawa,

1970). At the same year Robert Henson (Atomic Energy Research Establishment, UK) predicted and modeled the molecular structure of C_{60} , whose idea faced huge skepticism and was never published (acknowledged in 1999 (Thrower, 1999)). Independently Dmitry Bochvar and Elena Gal'pern (Elementoorganic Chemistry Institute of the Academy of Sciences, USSR) calculated the electronic structure of the closed C_{60} molecule in 1973 (Bochvar, D. A. & E. G. Galpern, 1973), that was repeated later by Robert Davidson (Dow Chemical Company, USA), predicting its high chemical stability (Davidson, 1981). In 1980 Sumio Iijima (Arizona State University, USA) observed so-called "bucky onions" of less than 10 nm in diameter in amorphous carbon films (Iijima, 1980). The next hint could be found in the work by Eric Rohlfing (Corporate Research Science Laboratory, USA), who analyzed carbon clusters C_{20-90} vaporized from graphite with UV laser ionization (Rohlfing et al., 1984).

In 1984 Harold Kroto (University of Sussex, UK) was preoccupied with carbon chains formation in the interstellar space and found the way to Richard Smalley's laboratory through his connection to Robert Curl (Rice University, USA) with a very similar graphite laser vaporization set-up as used by Eric Rohlfing (Rohlfing et al., 1984). The time of flight mass spectra of carbon clusters prepared by graphite laser vaporization had two dominant peaks that were attributed to previously unknown molecules of pure carbon. In 1985 Harold Kroto et al. identified C_{60} molecule as buckminsterfullerene (Fig. 1; know as well as buckyball or fullerene, named after the designer/inventor of the geodesic domes Buckminster Fuller) and proposed its special structure as a hollow closed sphere consisting of 12 pentagons and 20 hexagons with the exact same symmetry of a soccer ball (Kroto et al., 1985).

That groundbreaking *Nature* letter (Kroto et al., 1985) was evidence-based and logical, but did not convince all scientific community in the discovery of a new carbon allotrope at that time. During followed years, the authors managed to obtain a wide range of circumstantial evidence to support the proposed structure (Zhang et al., 1986; Yang et al., 1987; Curl & Smalley, 1988; Kroto, 1988, 1993). In 1990 Wolfgang Krätschmer et al. (Max Planck Institute for Nuclear Physics, Germany and University

of Arizona, USA) developed a procedure of burning an arc between two graphite rods in a helium atmosphere (Kratschmer et al., 1990) that enabled to synthesize large quantities of C_{60} for full structural characterization.

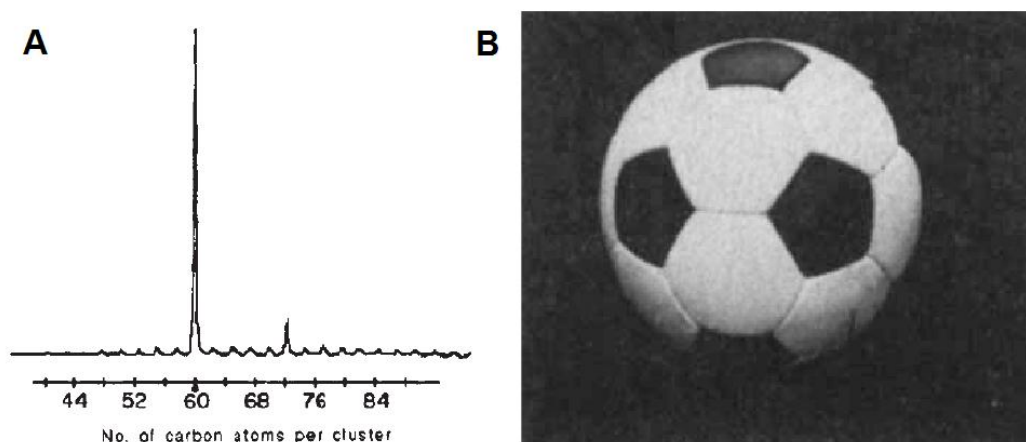


Figure 1. Discovery of C_{60} fullerene: A – time of flight mass spectra of carbon clusters prepared by graphite laser vaporization with 2 predominant peaks corresponding to C_{60} and C_{70} ; B – the suggested truncated icosahedral structure of C_{60} formed by replacing each vertex on the seams of a soccer ball by a carbon atom; Images by Harold Kroto et al. (Kroto et al., 1985).

The journal *Science* named C_{60} „Molecule of the Year” in 1991, describing it as “the discovery most likely to shape the course of scientific research in the years ahead” (Koshland, 1991). In 1996 the Nobel Prize in Chemistry was awarded to Robert Curl, Harold Kroto and Richard Smalley for their discovery of fullerenes that had implications for all natural sciences.

Fullerene science, born in astronomy, expanded in chemistry and physics, has found versatile applications in biology and medicine, inspiring a new branch of research fields. The unique physicochemical properties of C_{60} are important for a better understanding of its versatile biomedical effects.

1.2.2 Structure-determined properties of C_{60} fullerene

Pristine non-modified C_{60} is a lipophilic, spheroidal-shaped and symmetrical molecule with 0.72 nm in diameter (Scharff et al., 2008; Montellano et al., 2011). C_{60} 's structure is stable with decomposition appearing only at $> 1000^{\circ}\text{C}$ (Goodarzi et al., 2017). Sixty carbon atoms with $sp^{2.3}$ -hybridized valence shells form 12 pentagons with C5–C5 single bonds and 20 hexagons with C5–C6 double bonds, bend together in a

ball-like closed atom-cage with a common conjugated π -electron system (Kroto et al., 1985; Kroto, 1993; Yadav & Kumar, 2008; Montellano et al., 2011; Goodarzi et al., 2017). Due to that specific packing the surface of C_{60} is three times smaller than expected for biological molecules with the same molecular weight of 720.7 Da. The presence of 120 symmetry operations, like rotations around an axis or reflections in a plane, which map the molecule onto itself, has made C_{60} the most symmetrical molecule that follows the Golden Mean rule (Koruga et al., 2002; Yadav & Kumar, 2008). The unusual structure of C_{60} determines its unique physico-chemical properties and biological activity (Nielsen et al., 2008; Scharff et al., 2008; Li et al., 2010b; Montellano et al., 2011) (Fig. 2).

C_{60} behaves as an electron deficient alkene and reacts readily with electron rich species (Yadav & Kumar, 2008). Due to its exceptional capacity for radical scavenging C_{60} is often called “radical sponge” (Chen et al., 2004; Gharbi et al., 2005; Piotrovsky, 2006; Scharff et al., 2008; Iuga et al., 2011; Castro et al., 2017). C_{60} reacts with such ROS as superoxide, hydroxyl and hydrogen peroxide without being consumed (Goodarzi et al., 2017). Antioxidant activity of C_{60} was shown *in vitro*, *in vivo* and in the clinical studies (Chen et al., 2004; Gharbi et al., 2005; Inui et al., 2011). Since oxidative stress is the cause and/or mechanism of many diseases, C_{60} 's antioxidant activity determines its strong anti-aging (Gao et al., 2011; Baati et al., 2012), anti-inflammatory (Ryan et al., 2007; Dellinger et al., 2015), cardiovascular- (Thompson et al., 2014) and neuro-protective (Lee et al., 2011; Tong et al., 2011) effects.

From the other point, given extra energy input antioxidant and protective C_{60} 's nature turns to prooxidant and toxic. Under UV-vis light irradiation C_{60} absorbs photon energy and promotes intracellular ROS production that consequently stimulates oxidative stress progression and cell death induction (Akiyama et al., 2008; Nielsen et al., 2008; Scharff et al., 2008; Otake et al., 2010; Prylutska et al., 2010; Sharma et al., 2011; Orlova, 2013; Li et al., 2014). The mechanism of ROS generation is discussed in details in the following chapter dedicated to C_{60} -based cancer photodynamic therapy (PDT) that is defined as a non-surgical approach aimed on the selective elimination of

cancer cells. C₆₀-based PDT has been explored to suppress bacterial infections as well (Mizuno et al., 2011; Huang et al., 2014; Grinholc et al., 2015; Spesia et al., 2017) becoming an alternative strategy for microorganisms destroying with absence of multi-drug resistance development (Huang et al., 2014).

Given its spherical structure, nanosize and high hydrophobicity, C₆₀ is able to translocate through the lipid plasma membrane, localize in intracellular membranes and interact with active sites of enzymes. C₆₀ blocks a hydrophobic cavity of the active site in carbonic anhydrases (Innocenti et al., 2010) and protease of human immunodeficiency viruses (HIV) (Friedman et al., 1993; Martinez et al., 2016). C₆₀ significantly inhibits HIV replication and with additional UV-vis light irradiation leads to its complete degradation (Tanimoto et al., 2012).

The C₆₀'s hydrophobic nature challenges its solubility in polar solvents. Colloid solutions and derivatization are two main methods to boost C₆₀'s solubility in aqueous solutions that is critical for biological application (Goodarzi et al., 2017). Pristine C₆₀ forms stable colloid solutions in water (Labille et al., 2009; Prylutska et al., 2009; Prylutsky et al., 2014b). Functionalization of C₆₀ improves its water solubility and increases its biocompatibility by decreasing the aggregate size (Nielsen et al., 2008), but on the other hand, inhibits its interaction with cellular lipid membranes and changes the pattern of cellular uptake (Luksiene, 2003; Yamakoshi et al., 2003; Nielsen et al., 2008; Santos et al., 2014; Stueckle et al., 2016). C₆₀ diffuses through bilayer membrane from six (Santos et al., 2014) to nine (Qiao et al., 2007) orders of magnitude faster as compared with its hydrophilic derivatives, which interact with polar groups on the membrane surface instead of entering the cell. Moreover, the presence of functional groups on C₆₀ surface decreases the quantum yield of singlet oxygen production after molecule photoexcitation (Orlova, 2013; Spesia et al., 2017). Thus, the cellular uptake and further biological effects of pristine C₆₀ and its derivatives could differ.

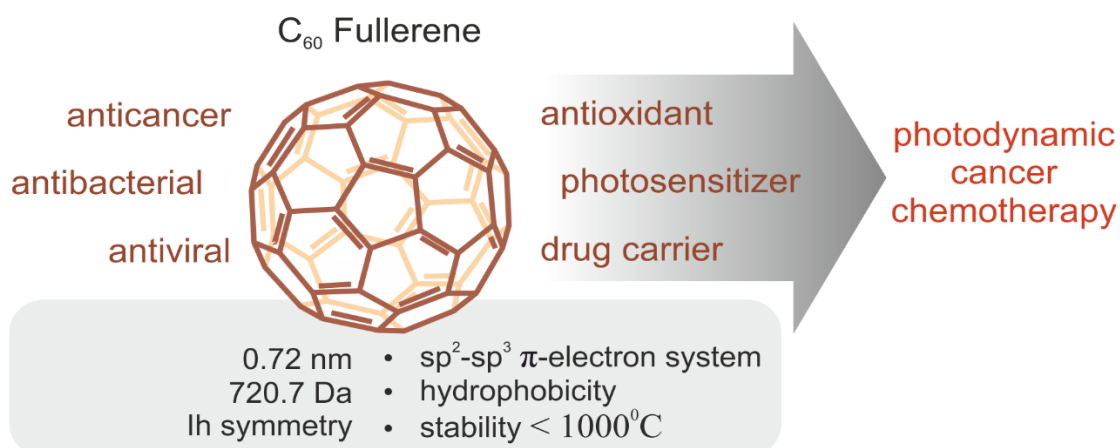


Figure 2. Structure-determined properties of C₆₀: nanosize, stability, symmetry, sp^{2,3}-hybridization and hydrophobicity of C₆₀ shape its anticancer, antibacterial and antiviral effects, as well as antioxidant, photosensitizing and drug-carrier functions that can contribute towards development of the photodynamic cancer chemotherapy.

C₆₀ unique properties at the nanoscale give rise to several possible anticancer therapeutic applications including such functionalities as antioxidant, photosensitizer and drug carrier (Fig. 2). As a key role, a C₆₀ anti- and prooxidant bivalent nature provides opportunity to modulate the oxidant balance differently in cells exposed to dark and light, respectively. ROS production or alteration of the redox conditions in specific subcellular compartments such as mitochondria in combination with other complementary agents has a potential to result in a synergistic toxicity towards cancer cells, while still minimizing the effects on normal (Schumacker, 2006).

1.2.3 Photodynamic therapy with C₆₀ fullerene

PDT that targets important cancer cell's survival adaptation of escalated oxidant status was introduced in 1972 by Tom Dougherty, who used a fluorescent dye fluorescein as a photosensitizer to treat cancer in mice under blue light irradiation (Dougherty, 1974, 1996). The main idea of PDT is to combine two non-toxic components – a photosensitizing molecule and visible light – which in the presence of oxygen gain a pronounced toxicity (Dolmans et al., 2003; Ribeiro et al., 2004; Sharma et al., 2011). Anticancer PDT effects are realized directly through the induction of cancer cell death and/or indirectly when damage of the vascular system and activation of the immune response are provoked (Agostinis et al., 2011; Saini & Poh, 2013).

Rapid development of endoscopic fiber optic devices (Flusberg et al., 2005; Keahey et al., 2016) allows to test PDT in treatment not only for skin malignancies, but for brain, lung, esophagus, colon, pancreas, liver, bile duct, breast, bladder, prostate and neck cancers as well (Dolmans et al., 2003; Agostinis et al., 2011; Keahey et al., 2016). Over the past decade, the application of nanoparticulate agents has been established both in pharmaceutical research and in clinical settings (Li et al., 2010a; Agostinis et al., 2011). In particular, a nanoliposomal photosensitizer formulation of Verteporfin, Visudyne®, which has been approved by FDA in 2000 for treatment of age-related macular degeneration, is now in several clinical trials for PDT of skin, breast, pancreatic and brain cancer according to database “clinicaltrials.gov”.

Today considerable attention is devoted to C_{60} as a potential regulator of oxidative balance in biological systems. Since a C_{60} molecule consists of $sp^{2.3}$ -hybridized carbon atoms, it is able to generate ROS after UV-vis light irradiation with a quantum yield of 1.0 (Spesia et al., 2017). Advantages of C_{60} compared to conventional photosensitizing molecules are higher photostability and lesser photobleaching (Sharma et al., 2011).

There are two ways of ROS production by photoexcited C_{60} : by energy (type I) or electron (type II) transfer from photoexcited C_{60} to oxygen (Fig. 3) (Luksiene, 2003; Yamakoshi et al., 2003; Castano et al., 2004; Sharma et al., 2011; Orlova, 2013; Huang et al., 2014; Spesia et al., 2017). In the ground singlet state all electrons of a C_{60} molecule are paired at the low energy molecular orbital (S_0). Following the absorption of a photon, its energy is transferred to an electron (e^-), boosting it to a higher energy level (S_1). As a result, an excited singlet state of $^1C_{60}^*$ is formed with the unchanged spin orientation of the excited e^- (Castano et al., 2004). This short-lived (nanoseconds) unstable species is readily converted to its triplet state $^3C_{60}$ via intersystem crossing with inversion of the excited e^- spin orientation (Luksiene, 2003; Castano et al., 2004; Orlova, 2013). Since direct conversion from triple (T_1) to the initial ground singlet state is a “spin-forbidden” process, C_{60} triplet is long-lived (microseconds) and loses energy, resulting in either type I or type II ROS generation (Castano et al., 2004). The highly

energetic triplet $^3\text{C}_{60}$ appears to be an excellent acceptor and, in the presence of electron donors, is easily reduced to the radical form $\cdot\text{C}_{60}$ (Sharma et al., 2011; Goodarzi et al., 2017). This intermediate transfers an electron to the oxygen (type I), with production of a superoxide anion radical $\text{O}_2^{\cdot-}$. The superoxide anion radical initiates free radical chain reactions with formation of toxic hydroxyl radical, hydrogen peroxide and peroxynitrite (Yamakoshi et al., 2003; Sharma et al., 2011). On the other hand, C_{60} can decay from its triplet to the ground state transferring its energy directly to O_2 generating singlet oxygen $^1\text{O}_2$ (type II) (Sharma et al., 2011; Spesia et al., 2017).

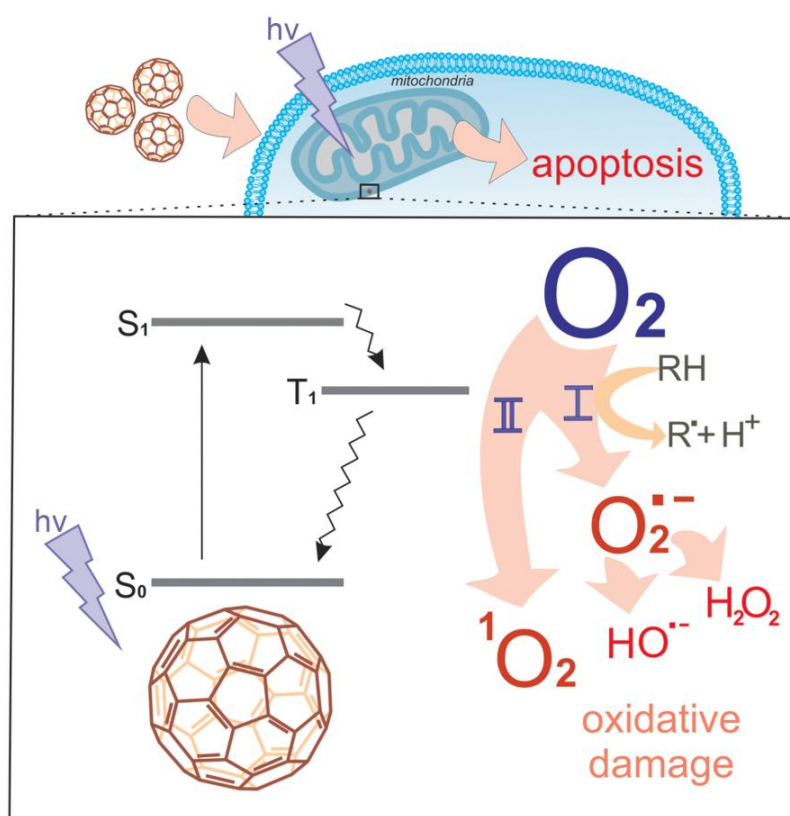


Figure 3. Schematic mechanism of photodynamic treatment of cancer cells with C_{60} : an absorbed photon excites C_{60} to the excited singlet state S_1 that relaxes to the longer lived triplet state T_1 ; the C_{60} triplet interacts with oxygen either through type I or type II, resulting in the intensification of reactive oxygen species generation and induction of apoptotic cell death.

The produced ROS are excellent oxidizing agents that react with a wide range of biological targets such as proteins and lipids, generating photoproducts. Oxidative stress, which occurs when ROS generation overwhelms the cell antioxidant defense system can lead to cell death by apoptosis (Luksiene, 2003; Castano et al., 2004; Orlova, 2013). Mitochondria have been found to be an important subcellular target for many photosensitizing drugs due to its direct role in apoptosis induction (Castano et

al., 2004; Ribeiro et al., 2004b).

C₆₀-mediated PDT efficiency *in vitro* and *in vivo* was shown to a large extent with its hydrophilic derivatives hydroxy- (Castano et al., 2004; Nielsen et al., 2008; Otake et al., 2010), carboxy- (Orlova, 2013), PEG- (Castano et al., 2004; Montellano et al., 2011) -C₆₀ and C₆₀ with various organic substitutes (Luksiene, 2003; Otake et al., 2010; Li et al., 2014; Santos et al., 2014; Stueckle et al., 2016; Spesia et al., 2017). Pristine C₆₀ may be applied in PDT in the form of liposome-based delivery systems (Akiyama et al., 2008; Kato et al., 2010; Sharma et al., 2011; Yano et al., 2011) or water colloidal C₆₀ solutions (Burlaka et al., 2004; Prylutska et al., 2007, 2010; Scharff et al., 2008). Previously, a negligible dark toxicity of pristine C₆₀ (Levi et al., 2006) and its colloid solution (Prylutska et al., 2007, 2009, 2019) against normal cells was shown. Considerable concentrations (277 μ M) had no effect on epithelial cell's morphology, cytoskeletal organization, cell cycle dynamics nor on cell proliferation (Levi et al., 2006). Water colloidal C₆₀ solution, explored in the current thesis, demonstrated low toxicity against human embryonic kidney cells with a high IC₅₀ value (555 μ M at 24 h) (Prylutska et al., 2019).

In contrast, a pronounced proapoptotic effect was detected in leukemic cells treated with ≤ 20 μ M C₆₀ and irradiated with UV-vis light in the range of 320-600 nm (Burlaka et al., 2004; Scharff et al., 2008; Palyvoda et al., 2010; Prylutska et al., 2010; Grebinyk et al., 2012; Grynyuk et al., 2013). A continuous intensification of ROS production and inhibition of the glutathione-dependent antioxidant system testified a subsequent intense induction of oxidative stress (Grynyuk et al., 2013). As a result, store-operated Ca²⁺ entry and cytochrome *c* release from mitochondria induced Ca²⁺-dependent apoptosis induction of leukemic cells, followed by caspase-3 activation and DNA fragmentation (Palyvoda et al., 2010; Grebinyk et al., 2012). The obtained data promise an application of photoexcited C₆₀ as a powerful agent for PDT against leukemic cells and indicate the potential of C₆₀ as an effective photosensitizer in cancer therapy.

One of the chief attractions of PDT is the concept of dual selectivity (Castano et

al., 2004). Collateral damage to normal tissue can be minimized by increasing the selective accumulation of the photosensitizer in the tumor and by delivering the light in a spatially confined and focused manner. Photosensitizing effects of C_{60} and its derivatives are induced by different visible light sources including broadband mercury-vapor (Burlaka et al., 2004; Scharff et al., 2008; Grebinyk et al., 2012; Grynyuk et al., 2013), halogen (Tabata et al., 1997; Yamakoshi et al., 2003; Liao et al., 2011; Sharma et al., 2011), tungsten-xenon (Mroz et al., 2011b; Sperandio et al., 2013) and fluorescent (Yu et al., 2016) lamps as well as sharp band lasers (Sharma et al., 2011; Orlova, 2013; Yu et al., 2016). Lasers provide a monochromatic and powerful illumination but possess a limited irradiation area. Alternative convenient lamps can be spectrally filtered to meet requirements for treatment of large areas, however, that leads to significant fluence rate reductions. A recent study (Franskevych et al., 2017) demonstrates C_{60} photoinduced cytotoxic effects against leukemic cells after irradiation with a white light-emitting diode (LED) lamp with the broad emission spectrum (420-700 nm). LEDs as a light-source for PDT have been explored previously and were shown to be more cost-effective and serviceable as clinical lamps or lasers (Yu et al., 2009; Hempstead et al., 2015; Erkiert-Polguj et al., 2016). Performance tests have proven that an LED-system can provide an adjustable, stable, wavelength-specific, homogeneous and large-area illumination for *in vitro* and *in vivo* studies.

1.2.4 Drug delivery with C_{60} fullerene

The novel rapidly evolving trend in anticancer drug research is the alteration of the drug's chemical structure and the design of multicomponent nanosystems, accounting for 25% of all drugs (Dutta, 2007). To date, more than 50 nanopharmaceuticals have been approved and are available for clinical practice, and much more are being studied in clinical trials (Ventola, 2017). A common practice in the development of nanodrugs is the complexation or encapsulation of a therapeutically active agent with nanoparticles to alter its pharmacokinetic and/or pharmacodynamic

properties. Doxorubicin is one of the first candidates for a targeted nanodelivery due to life-threatening cardiotoxicity and other serious side effects (Tacar et al., 2013; Kumar & Raza, 2017). Complexation of Doxorubicin with nanostructures increases the drug's size, both improving its retention in the organism and prolonging the therapeutic activity (Patil et al., 2010; Fojtu et al., 2017). To develop an applicable nanosystem for a successful anticancer drug delivery, previous studies focused on aspects regarding stability, biocompatibility, biodistribution and functionality (Schütz et al., 2013; Fojtu et al., 2017).

The combination of C_{60} 's antioxidant potential (Gharbi et al., 2005; Delgado et al., 2014; Castro et al., 2017) and its ability for drug delivery makes the nanostructure very attractive for anticancer therapy. A coupling of Doxorubicin and C_{60} for a passive targeting of cancer cells can be achieved by covalent linkage (Chaudhuri et al., 2009; Liu et al., 2010a; Magoulas et al., 2015) or by noncovalent interactions (Blazkova et al., 2014; Panchuk et al., 2015). A nanocomplex of C_{60} with two amide-linked Doxorubicin molecules showed the same cytotoxicity against human breast cancer MCF-7 cells as the free drug (Lu et al., 2009). When Doxorubicin was bound to C_{60} through a carbamate linker it exhibited no change in antitumor efficacy but had no systemic toxicity in a murine tumor model (Chaudhuri et al., 2009). When one or two Doxorubicin molecules were anchored on pegylated C_{60} particles through a urethane type bond the nanocomplex exhibited a delayed antiproliferative effect on MCF-7 cells (Magoulas et al., 2015).

π - π stacking interactions between unsaturated (poly)cyclic molecules determine supramolecular nanosized self-assemblies, commonly used for fast, easy and cost effective coupling of the cargo molecules with carbon nanoparticles (Li et al., 2014; Pérez & Martín, 2015), improving the stability and drug-loading capacity (Yang et al., 2018). A spherical polyene molecule of C_{60} predicts its π - π stacking interactions with aromatic moieties of proteins, nucleic acid bases, aromatic vitamins and antibiotics. The interaction of C_{60} and C_{70} with the planar π surface of a tetraphenylporphyrin presented a new recognition element in supramolecular chemistry (Boyd et al., 1999).

The noncovalent interactions in a C₆₀ model nanocomplex with benzene (Li et al., 2016) and hexabenzocoronenes (Sepúlveda et al., 2017) were estimated to form due attractive π - π stacking with the energy -4.8 and from -14.1 to -75.8 kcal/mol, respectively. C₆₀ nanocomplexes with four antiglioblastoma aromatic drugs, aimed on penetration of the brain blood barrier, were estimated to form noncovalent nanocomplexes (Samanta & Das, 2017). Host-guest C₆₀ chemistry with calixarenes is based on allying of the concave surfaces and affects C₆₀ separations, modifies its redox behavior and entraps C₆₀ in a container (Georghiou, 2016). C₆₀ noncovalently-loaded with 5-Aminolevulinic acid showed no dark toxicity and higher PDT efficiency both *in vitro* and *in vivo* in comparison with the free compound (Li et al., 2014).

For noncovalent complexation of the aromatic Doxorubicin molecule with the surface of C₆₀ the π - π stacking effect is responsible as well. In a pioneering attempt (Evstigneev et al., 2013) showed a simple and fast method of C₆₀ noncovalent complexation with Doxorubicin in water and later in physiological solution (Prylutsky et al., 2015). Molecular modeling, spectroscopy, atomic-force microscopy, dynamic light and small-angle X-ray scattering evidenced C₆₀-Doxorubicin nanocomplex (C₆₀-Dox) formation with an energy of -6.3 kcal/mol (Evstigneev et al., 2013; Prylutsky et al., 2015). The proposed nanosystem was shown to have higher toxicity compared to the free drug against various human tumor cell lines *in vitro* and mice Lewis lung carcinoma *in vivo* (Panchuk et al., 2015; Prylutska et al., 2015). In another approach an antimicrobial effect and the applicability of noncovalent C₆₀-Dox for *in vivo* imaging was shown (Blazkova et al., 2014).

As Doxorubicin is a representative or model substance for many anticancer drugs, the strategy was shown to be transferable to other drugs (Evstigneev et al., 2013) including cisplatin (Prylutska et al., 2017a,b) and an experimental angucycline antibiotic Landomycin A (Prylutsky et al., 2016). The toxicity and number of apoptotic cells were increased after cisplatin complexation with C₆₀ (Evstigneev et al., 2013; Prylutska et al., 2017a,b). C₆₀-Landomycin A nanocomplex showed higher toxicity towards cancer cells and lower toxicity towards normal cells in contrast to a

drug alone (Evstigneev et al., 2013; Bilobrov et al., 2019). The increase of the anticancer drugs' efficiency after its noncovalent complexation with C₆₀ nanostructure points towards a promising cancer treatment strategy that has a potential to improve the chemotherapy outcome.

1.3 Carbon nanoparticles-mediated photodynamic chemotherapy

A complex nature of cancer disease evolves to withstand commonly implemented cancer therapies. The multimodal combination of therapies with distinct anticancer mechanisms offers a potential advantage and enhanced efficiency over monotherapy approaches (Li et al., 2010a; Fan et al., 2017). Once combined, different cancer therapies confront cancer cells with distinct attack strategies, gaining a stronger therapeutic potential. The nanotechnology platform enables the merging of different active agents on the molecular level complementing the strategy with an option of nanodelivery.

Photodynamic chemotherapy exploits two anticancer agents – a photosensitizing molecule and a chemotherapeutic drug (Peng et al., 2009; Wang et al., 2016; Ke et al., 2017; Lee & Ma, 2017; Zhang et al., 2017; Candido et al., 2018; Khaliq et al., 2018; Sun et al., 2018). The former is harmless itself, but being illuminated with visible light in the presence of oxygen induces cell death through ROS-mediated compact apoptosis (Ribeiro et al., 2004; Agostinis et al., 2011). Once combined, PDT and CT confront cancer cells with two different “swords”, resulting in a stronger therapeutic potential in comparison with the corresponding therapies apart or their theoretical sum.

Photosensitizers and Doxorubicin were applied either separately as a co-treatment (Chen & Xu, 2015; Aniogo et al., 2017) or bound on the nanocarrier platform (Peng et al., 2009; Wang et al., 2016; Ke et al., 2017; Lee & Ma, 2017; Zhang et al., 2017; Candido et al., 2018; Khaliq et al., 2018; Sun et al., 2018). The enhanced efficiency of Doxorubicin included into nanoplatfoms together with such photosensitizers as chlorin 6 (Peng et al., 2009; Zhang et al., 2017; Sun et al., 2018),

phthalocyanines (Wu et al., 2014; Ke et al., 2017; Candido et al., 2018), indocyanine green (Li et al., 2018), merocyanine (Wang et al., 2016), methylene blue (Khaliq et al., 2018) and perfluorocarbon (Lee & Ma, 2017) was recently reported.

Carbon-based nanomaterials can serve as a smart material for phototherapies and anticancer drug delivery. The table 2 demonstrates carbon-based nanodelivery platforms developed for combined photodynamic cancer chemotherapy. Thus, Doxorubicin and protoporphyrin IX bound to a carbon dot led to ROS generation and drug release (Kumari et al., 2018). Moreover, since, the absorption spectra of the protoporphyrin IX overlaps with the fluorescence spectra of carbon dot, those two molecules formed a fluorescence resonance energy transfer (FRET) pair. In another approach, Doxorubicin and phthalocyanine were assembled on the biocompatible poly-L-lysine-grafted graphene, providing together strong synergistic effects against three different cancer cell lines (Wu et al., 2014). Graphene oxide was explored to deliver photosensitive hypocrellin A and hydroxycamptothecin, that had a higher antiproliferative effect towards A549 cells compared with each drug alone (Zhou et al., 2014).

Table 2. Nanocarbon-mediated photodynamic cancer chemotherapy

<i>Nano-carbon</i>	<i>Therapeutic system, size (reference)</i>	<i>Experimental in vitro / in vivo model</i>	<i>Light fluence</i>	<i>Results</i>
dot	Protoporphyrin IX – carbon dot – Doxorubicin, - (Kumari et al., 2018)	n/a	UV lamp, λ_{\max} = 302 nm	<i>in vitro</i> drug release and ROS generation through FRET
graphene	Zn(II)phthalocyanine – poly-L-lysine – graphene – Doxorubicin, 200 nm (Wu et al., 2014)	HeLa, MCF-7 & B16 cells	660 nm laser, 0.15 W/cm ² , 10 min	pH-triggered drug release, \uparrow cellular uptake, synergistic therapies combination
	graphene oxide – hypocrellin A – hydroxycamptothecin, - (Zhou et al., 2014)	A549 cells	470 nm LED 25 mW, 5 min	synergistic therapies combination

C_{60}	C_{60} fullereneol–hydrazone – Doxorubicin with PEG shell, 135 nm (Fan et al., 2013)	HeLa, L929 & A549 cells	460–485 nm, 30 min	active targeting, pH-triggered drug release, ↑ cellular uptake, synergistic therapies combination
	polyethyleneimined C_{60} – hydrazone – Doxorubicin, 100-200 nm (Shi et al., 2014)	B16-F10 cells / melanoma B16-F10 in C57 mice	532 nm laser, 100 mW/cm ² , 5 min	active targeting, pH-triggered drug release, ↑ cellular uptake, ↓ side effects synergistic therapies combination,
	C_{60} fullereneol–thioketal linker – Doxorubicin, 130 nm (Shi et al., 2016)	4T1 cells / 4T1 tumor in BALB/c mice	532 nm laser, 100 mW/cm ² , 10 min	ROS-triggered drug release, ↑ cellular uptake, synergistic therapies combination
	diadduct malonic acid- C_{60} – Docetaxel in micelles, 109 nm (Guo et al., 2014)	HeLa cells / S180 tumor in KM mice	532 nm laser, 100 mW/cm ² , 3 min	↑ time in blood, ↑ intratumoral uptake, ↓ side effects, synergistic therapies combination

C_{60} nanostructure is the most often used due to the dual nanocarrier/photosensitizer behavior. Polyhydroxylated (Fan et al., 2013; Shi et al., 2016) and polyethyleneimined (Shi et al., 2014) C_{60} delivered Doxorubicin with the high ratio of drug release and increased toxicity both *in vitro* and *in vivo*. These approaches required sophisticated chemical synthesis of covalently bound cargo to the C_{60} molecule. A diadduct of malonic acid- C_{60} and Docetaxel was co-entrapped in micelles that prolonged the blood circulation time and increased drug intratumoral distribution and anticancer effect (Guo et al., 2014).

The advantageous synergistic effect is primarily attributed to the heterogeneity of cancer cell resistance to each of the monotherapies and finally aims to apply lower clinical dosage of the chemotherapeutics (Fan et al., 2017). Co-delivered chemotherapeutic and photosensitizer commonly have distinct intracellular targets that

activate different signaling pathways. The observed synergism in treatment efficiency of those anticancer agents combined on one nanoplatform involves the oxidative stress propagation (Fan et al., 2017). Photosensitizer-mediated ROS generation leads to a higher tumor permeability and intracellular drug uptake that significantly enhanced drug's therapeutic efficacy (Sano et al., 2013; Golombek et al., 2018). The combination of the C_{60} prooxidant properties and its drug delivery capability (Montellano et al., 2011; Goodarzi et al., 2017; Kumar & Raza, 2017) makes this nanostructure attractive for the cancer photodynamic chemotherapy.

The C_{60} abilities to increase the intracellular concentration of co-delivered cargo, to produce cytotoxic ROS under photoexcitation and to decrease systemic toxicity of the therapeutic agent can result in a higher therapeutic index for the co-delivered anticancer drug (Fig. 4). So, the double hit strategy towards cancer cell can be realized by the means of single double nanosystem C_{60} -drug.

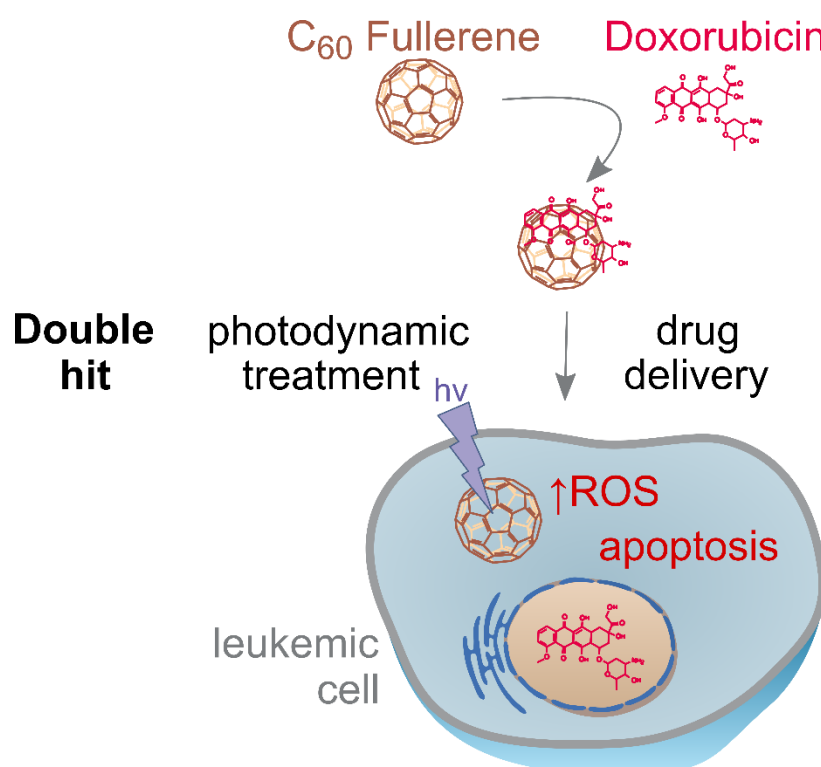


Figure 4. C_{60} -Dox nanocomplex for photodynamic cancer chemotherapy: the approach is realized by treating cancer cells with a C_{60} -Dox nanocomplex to facilitate anticancer drug delivery; on the next step, cancer cells are irradiated with visible light in order to photoexcite C_{60} . As a result, cancer cells are exposed to the double hit by both photoexcited C_{60} and Doxorubicin anticancer actions through oxidative stress-mediated apoptosis induction.

II. AIM OF THESIS

The aim of the presented research is to develop a photodynamic and chemotherapeutic treatment strategy for human leukemic cell with C_{60} fullerene-based nanocomplexes. The aim is divided into three objectives that include investigation of C_{60} nanostructure applications as 1) a photosensitizer, 2) an anticancer drug nanocarrier and 3) their combination (Fig. 5). The dual functionality of C_{60} is hypothesized to result in a significant synergy of treatment efficiency and a decreased efficient dose of the co-delivered chemotherapeutic drug.

1) photodynamic treatment



- C_{60} as a photosensitizer
- LED as a light source

2) drug delivery



- C_{60} -based delivery of anticancer drugs

3) combined



- C_{60} as a photosensitizer
- C_{60} -based delivery anticancer drugs
- LED as a light source

Figure 5. The workflow plan for the development of C_{60} -based photodynamic treatment and drug delivery to cancer cells.

Three key milestones are determined for tracking the project progress.

The first part is dedicated to detection and optimization of the C_{60} photosensitizing activity *in vitro*. C_{60} 's intracellular accumulation, localization and phototoxic effects on leukemic cells are studied in the combination with high power single chip light-emitting diodes (LEDs) of different wavelengths. The obtained data

should provide a reliable description of C₆₀'s cellular effects under the conditions of the light exposure with the developed LED light source (milestone 1).

The second part is focused on the C₆₀-based drug delivery into leukemic cells. Nanocomplexation of C₆₀ with the common anticancer drug Doxorubicin forms the main model nanocomplex. The research will assess the physicochemical properties of C₆₀-drug nanocomplex formed after noncovalent interaction of the components, its intracellular accumulation and cytotoxic potential against leukemic cells. The possibility of the delivery for the herbal alkaloid Berberine as an alternative drug with C₆₀ nanocomplex will be clarified as well. The second dataset should define the toxic effects of C₆₀-drug nanocomplexes on leukemic cells (milestone 2).

Two first milestones (set specific light exposure conditions as well as established C₆₀-drug active dose) enable an investigation of the combinative chemo- and photodynamic treatment strategy of human leukemic cell. The final part will study cellular effects of the C₆₀-Doxorubicin nanocomplex in combination with the LED light irradiation. The toxicity of photodynamic treatment of leukemic cells will be studied with C₆₀-Berberine nanocomplex as well. In that way, the main hypothesis will be tested with a quantitative analysis of the toxicities' synergy during combinative chemo- and photodynamic therapeutic treatment of leukemic cells with C₆₀ nanocomplexes (milestone 3).

III. MATERIALS AND METHODS

III.1 Materials

III.1.1 Chemicals

Standard chemicals were from Carl Roth GmbH + Co. KG (Karlsruhe, Germany) or Sigma Aldrich Co. (St-Louis, USA).

Table 3. Chemicals used in the work
(if not otherwise described chemicals were of p.a. grade)

<i>Chemical</i>	<i>Supplier</i>	<i>Location</i>
Aqueous colloid solution of pristine C ₆₀ fullerene (C ₆₀), 200 µM, 99% purity, 12 months stability and homogeneity with an average nanoparticle's size of 100 nm	Prof. Dr. Uwe Ritter, University of Technology Ilmenau	Ilmenau, Germany
Berberine	Sigma-Aldrich Co.	St-Louis, USA
Bovine Serum Albumin (BSA)	Sigma-Aldrich Co.	St-Louis, USA
CO ₂	Air Liquide	Paris, France
4',6-Diamidine-2'-phenylindole dihydrochloride (DAPI)	Sigma-Aldrich Co.	St-Louis, USA
3-(4,5-dimethylthiazol-2-yl)-2,5-diphenyl tetrazolium bromide (MTT)	Sigma-Aldrich Co.	St-Louis, USA
Doxorubicin	Sigma-Aldrich Co.	St-Louis, USA
Ethyl acetate	Acros Organics	New Jersey, USA
Fetal Bovine Serum (FBS)	Biochrom	Berlin, Germany
Fluorescein isothiocyanate (FITC)-labeled polyclonal antibody against mouse IgG, F7506	Sigma-Aldrich Co.	St-Louis, USA
Hoechst 33342	Sigma-Aldrich Co.	St-Louis, USA
L-glutamin, K0283	Biochrom	Berlin, Germany

MitoTracker Orange FM	Invitrogen Molecular Probes	Carlsbad, USA
3-(<i>N</i> -morpholino)propanesulphonic acid (MOPS)	ICN Biomed Inc.	Ohio, USA
2-(4-iodophenyl)-3-(4-nitrophenyl)-5-phenyl-2H-tetrazolium (INT)	Acros Organics	New Jersey, USA
Penicillin/Streptomycin	Biochrom	Berlin, Germany
Poly-D-lysine hydrobromide	Sigma-Aldrich Co.	St-Louis, USA
P-Phenylenediamine	Sigma-Aldrich Co.	St-Louis, USA
Primary monoclonal antibody IgG against C ₆₀ , 1-10F-A8	Santa Cruz Biotech Inc.	Santa Cruz, USA
Sodium succinate	Acros Organics	New Jersey, USA

III.1.2 Media and buffers

Table 4. Media and buffers used in the work

<i>Media and buffers</i>	<i>Supplier</i>	<i>Location</i>
Roswell Park Memorial Institute medium (RPMI 1640, F1215)	Biochrom	Berlin, Germany
Dulbecco's Modified Eagle medium (DMEM, F0435)		
Trypsin, L2153		
Phosphate buffered saline (PBS)		

III.1.3 Cell lines

Table 5. Cell lines used in the work

<i>Cell line</i>	<i>Supplier</i>
CCRF-CEM (ACC 240)	Leibniz Institute DSMZ-German Collection of Microorganisms and Cell Cultures (Deutsche Sammlung von Mikroorganismen und Zellkulturen), Germany
Jurkat (ACC 282)	
Molt-16 (ACC 29)	
THP1	Dr. Sofia Cortes, New University of Lisbon, Portugal
HeLa	Dr. Müller, Department of Gastroenterology, Infectiology and Rheumatology and Division of Hepatology, Germany

III.1.4 Assay Kits

Table 6. Kits used in the work

<i>Kit</i>	<i>Supplier</i>	<i>Location</i>
Apoptosis Detection Kit	eBioscience™	San Diego, USA
Caspase-Glo® 3/7 Activity assay Kit	Promega	Madison, USA
Mitochondrial ToxGlo™ assay Kit		
ProteoMass Peptide&Protein MALDI-MS Calibration Kit	Sigma-Aldrich Co.	St-Louis, USA

III.1.5 Special consumable supplies

Table 7. Consumables used in the work

<i>Consumable</i>	<i>Supplier</i>	<i>Location</i>
Cell culture flask 25 and 75 cm ²	Sarstedt	Nürnberg, Germany
Transparent microtiter plate with 6-, 12-, 96- and 384-wells		
Cedex Smart Slides	Roche	Basel, Switzerland
Centrifuge filters Amicon Ultra-0.5 3 K	Sigma-Aldrich Co.	St-Louis, USA
Fast-Read 102® counting chamber	Biosigma	Cona, Italy
Glass cover slips	Carl Roth	Karlsruhe, Germany
Eclipse XDV-C8 150 × 4.6 mm, 5 μm	Agilent	Santa Clara, USA
Eclipse XDB-C18 100 × 4.6 mm, 3 μm		

III.1.6 Light sources

Table 8. Light sources used in the work

<i>Light source</i>	<i>Supplier</i>	<i>Location</i>
365 nm Nichia SMD LED UV NCSU275	LUMITRONIX LED-Technik	Hechingen, Germany
405 nm high power single chip LED VL400-EMITTER	Roithner Lasertechnik	Vienna, Austria
515 nm high power single chip LED APG2C1-515	GmbH	
650 nm LED ELD-650-523		
632 nm helium-neon 30 mW laser	Melles Griot	New York, USA

III.1.7 Equipment

Table 9. Equipment used in the work

<i>Equipment</i>	<i>Supplier</i>	<i>Location</i>
Airstream Biological Safety Cabinet, class II	Esco	Portland, USA
BZ-9000E Fluorescence Microscope	Keyence	Osaka, Japan
Cedex XS Analyzer	Roche	Basel, Switzerland
Centrifuge 5810 R	Eppendorf	Berlin, Germany
CO ₂ humidified incubator	Binder	Tuttlingen, Germany
Flow cytometer BD FACSJazz™	BD Biosciences	Singapore
Laboratory power supply DIGI 35 CPU	Conrad Electronic	Hirschau, Germany
Light microscope IX2-SLP	Olympus	Tokyo, Japan
Multimode microplate spectrometer Infinite M200 Pro	Tecan	Männedorf, Switzerland
Nexera HPLC system	Shimadzu	Kyoto, Japan
LCMS-8040 Tandem Quadrupole Mass Spectrometer, equipped with an Electro Spray Ionization (ESI) source		
MALDI-TOF Axima Confidence mass spectrometer		
UV-Spectrophotometer UV-1800		
Plate shaker MTS 2/4 digital	IKA	Staufen, Germany
Thermo Savant UVS 400A SpeedVac	Thermo Fisher Scientific Inc.	Berlin, Germany
Ultrasonic generator 68101 and MH2 transducer, 1MHz	Kaijo	Tokyo, Japan
Ultrasonic bath RK 31, 35 kHz	BANDELIN electronic	Berlin, Germany
Zetasizer Nano S	Malvern Instruments	UK

III.1.8 Software

Table 10. Software used in the work

<i>Software</i>	<i>Supplier</i>	<i>Location</i>
BD FACS™	BD Biosciences	Singapore
BZ-II Analyzer	Keyence	Osaka, Japan
BZ-II Viewer		
ComboSyn	ComboSyn, Inc.	Paramus, USA
CorelDraw	Corel	Ottawa, Canada
Inkscape	Inkscape	California, USA
GraphPad Prism 7.0	GraphPad software	La Jolla, USA
LabSolutions LCMS	Shimadzu	Kyoto, Japan
Launchpad™ v.2.9		
Microsoft Office 2013	Microsoft	Redmond, USA
SOLIDWorks	Dassault Systems	Massachusetts, USA

III.2 Methods

III.2.1 C₆₀-drug nanocomplex synthesis

Doxorubicin and Berberine were dissolved in water at initial concentration in 18.5 and 2.8 mM respectively. A nanocomplex with C₆₀ was prepared according to the protocol (Prylutskyy et al., 2015). Briefly, the Doxorubicin and Berberine solutions were mixed with C₆₀ colloid solution in 1:2, 1:1 or 2:1 molar ratio of the components (Tab. 11). The mixtures were treated in an ultrasonic disperser for 30 min, stirred magnetically for 24 h at room temperature (RT) and centrifuged at 4000 g for 15 min with the use of centrifuge filters Amicon Ultra-0.5 3 K for sample purification.

Table 11. Stock concentrations of C₆₀ and Doxorubicin/Berberine in nanocomplexes

<i>Molar ratio</i>	<i>[C₆₀], μM</i>	<i>[drug], μM</i>
1:2 (only for Berberine)	100	200
1:1	100	100
2:1	200	100

The stability (optical spectra and size distribution) of nanocomplexes was systematically controlled and shown to be practically unchanged after 6 months of

storage in physiological saline solution. The working concentration of C₆₀-Doxorubicin (C₆₀-Dox) and C₆₀-Berberine (C₆₀-Ber) nanocomplexes in the samples was presented according to drug-equivalent concentration purposely to compare the effect of the nanocomplexes with the effect of free drug in the same concentration.

III.2.2 Analytical methods

III.2.2.1 Matrix assisted laser desorption ionization-time of flight mass spectrometry

A Matrix Assisted Laser Desorption Ionization – Time of Flight – Mass Spectrometry (MALDI-TOF-MS) Axima Confidence mass spectrometer was used to measure the mass of molecular species in C₆₀ colloid solution. Samples (1 µL) were mixed with equal volume of saturated matrix solution (6.5 mM 2,5-dihydrobenzoic acid in 0.1% trifluoroacetic acid, 50% acetonitrile) and spotted on the stainless steel target plate and dried. Desorption and ionization were achieved using a 337 nm nitrogen laser. Mass spectra were obtained at maximal laser repetition rate of 50 Hz within a mass range from 0 to 3000 Da.

The MALDI-TOF mass spectrometer was calibrated externally using a mixture of standard peptides: Bradykinin fragment 1-7 (757.40 Da), Angiotensin II (human, 1 046.54 Da), P₁₄R (synthetic peptide), 1 533.86 Da and ACTH fragment 18-39 (human, 2 465.20 Da) from ProteoMass Peptide&Protein MALDI-MS Calibration Kit. A total of 600 laser shots were accumulated and averaged for each sample to generate representative profiles. MALDI-TOF-MS data processing was performed using the Launchpad™ v.2.9 software.

III.2.2.2 High performance liquid chromatography-tandem mass spectrometry

Chromatographic separation and mass spectrometric detection were achieved by employing the Nexera High Performance Liquid Chromatography (HPLC) system

coupled to the LCMS-8040 Tandem Quadrupole Mass Spectrometer, equipped with an electro spray ionization (ESI) source.

The instrument response y related linearly to the standard concentration of the investigated agent x for a limited range of concentration was expressed in a linear regression model ($y = a + b \times x$).

The validation of the analytical methods was done with calculation of limit of detection (LoD) and limit of quantification (LoQ) according to (Shrivastava & Gupta, 2011):

$$LoD = 3 \times S_a/b \text{ and } LoQ = 10 \times S_a/b, \quad (1)$$

where S_a is the standard deviation of the regression line and b is the slope of calibration curve. For data processing the software LabSolutions HPLC-MS/MS was used.

III.2.2.2.1 C₆₀ fullerene quantification

Chromatographic separation of C₆₀ was performed using the column Eclipse XDV-C8 under isocratic elution conditions with a mobile phase of toluene and methanol. Chromatographic conditions and optimized MS parameters are presented in the table 12. MS chromatograms of C₆₀ were acquired using single ion monitoring (SIM) mode in positive regime with target molecular ion 720 [M]⁺ m/z (Fig. 6).

C₆₀ calibration standards from 0.05 to 5 μM were prepared from a 200 μM water stock solution. Quantification was achieved using regression curve, the linear regression equation was:

$$y = (4e + 06)x + 116614 \quad (2)$$

MS chromatograms of C₆₀ had a retention time in 3.21 min. The good linearity ranges were achieved by the analysis of linear correlation coefficient for C₆₀ $r = 0.999863$.

All analyses were performed in triplicates and the peak areas were measured.

Table 12. HPLC-ESI-MS conditions for analysis of C₆₀

<i>Chromatographic conditions</i>	
Column, its temperature	Agilent Eclipse XDB-C8, 40°C
Mobile phase	methanol:toluene (45:55, v:v)
Flow rate	0.7 mL/ min
Run time	5 min
Injection volume	3 µL
<i>MS conditions</i>	
Desolvation line temperature	250°C
Heat block temperature	400°C
Target molecular ion	720 [M] ⁺ m/z
Time window	0-5 min
Dwell time	0.2 s
Interface voltage	4.5 kV
Nebulizing gas flow	3 L/min
Drying gas flow	15 L/min

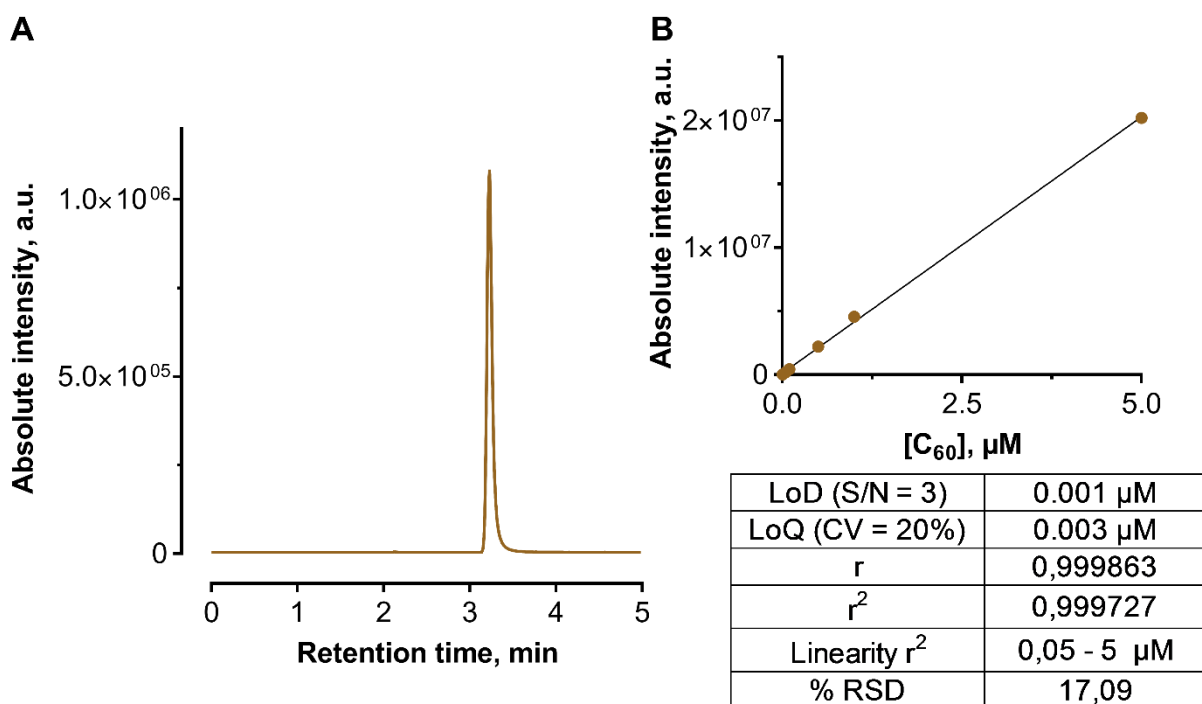


Figure 6. Developed HPLC-ESI-MS method for C₆₀ detection and quantification: A – representative SIM-chromatogram of C₆₀, B – calibration curve with method's performance characteristics used for nanoparticle content quantification.

III.2.2.2.2 Doxorubicin quantification

Elution and separation of Doxorubicin was performed using the Eclipse XDB-C18 column under isocratic conditions with a mobile phase of acetonitrile and 0.1% formic acid water solution. The chromatographic reverse phase conditions and optimized MS/MS parameters are presented in the table 13. For identification and quantification, the molecular ion of Doxorubicin was chosen. HPLC-ESI-MS/MS analysis was performed in positive mode with using the multiple reactions monitoring (MRM) mode that provides high sensitivity and accuracy of measurements. After MS/MS-optimization a unique MRM-transition that includes precursor and characteristic product ions was acquired and used for further identification and quantification. The protonated Doxorubicin ($[M+H]^+$, 544.2 m/z) was used as a precursor ion with the most abundant fragment ions of 130.2 and 361.1 m/z.

Table 13. HPLC-ESI-MS/MS conditions for analysis of Doxorubicin

<i>Chromatographic conditions</i>	
Column, its temperature	Agilent Eclipse XDB-C18, 40°C
Mobile phase	Acetonitrile:0.1% formic acid in H ₂ O (80:20, v:v)
Flow rate	0.3 mL/min
Run time	17 min
Injection volume	3 µL
<i>MS/MS conditions</i>	
Desolvation line temperature	250°C
Heat block temperature	400°C
Target molecular ion	544.2 [M] ⁺ m/z
Product ions	130.2, 361.1 m/z
Time window	0-17 min
Dwell time	0.2 s
Interface voltage	4.5 kV
Nebulizing gas flow	3 L/min
Drying gas flow	15 L/min

Doxorubicin calibration standards from 0.02 to 20 μM were prepared from a 1.85 mM water stock solution. The standards were stored in the dark at 4 $^{\circ}\text{C}$. Quantification was achieved using the regression curve (Fig. 7) according to the linear regression equation:

$$y = (1.21030e + 006)x + 104963 \quad (3)$$

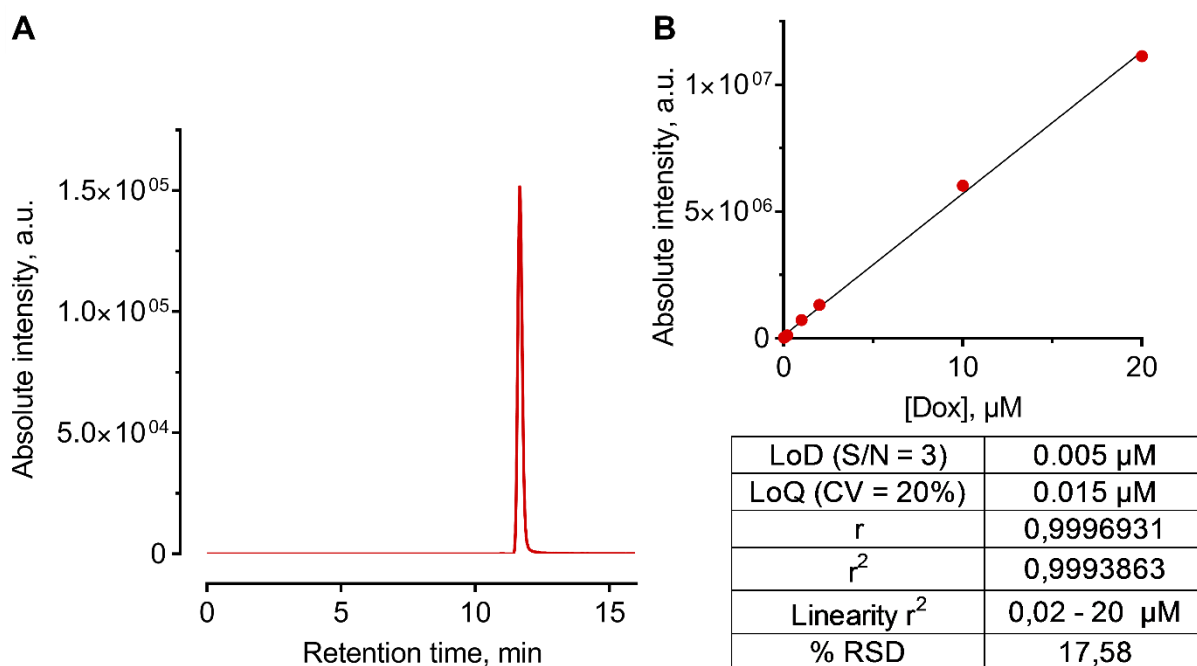


Figure 7. Developed HPLC-ESI-MS method for Doxorubicin detection and quantification: A – representative MRM-chromatogram of Doxorubicin, B – calibration curve with method's performance characteristics used for drug content quantification.

III.2.2.3 Spectroscopic and fluorometric analysis

C_{60} samples (100 μL) were placed into a 96-well plate Sarstedt and the absorption spectrum was measured with a multimode microplate spectrometer Tecan infinite M200 PRO with following parameters – wavelength range: 200-900 nm, wavelength step size: 2 nm, number of flashes per well: 10.

The absorption and fluorescence spectra of free Doxorubicin and C_{60} -Dox (100 μL in 96-well plate Sarstedt) were measured with a multimode microplate spectrometer Tecan Infinite M200 Pro at the following parameters: 1. Absorption – wavelength range: 400-550 nm, wavelength step size: 5 nm, number of flashes per

well: 25; 2. Fluorescence – $\lambda_{\text{ex}} = 470$ nm, wavelength range: 500-800 nm, wavelength step size: 2 nm, number of flashes per well: 25.

III.2.2.4 Dynamic light scattering

Short ultrasonication (30 s, 35 kHz) was applied to remove air bubbles. C₆₀-Dox size distribution was evaluated with a Zetasizer Nano S equipped with a He-Ne laser (633 nm). Data were recorded at 37°C in backscattering mode at a scattering angle of 173°. C₆₀-Dox (1 mL of 1 µM) were placed in disposable polystyrene cuvettes. The same sample was measured 10 times to establish average diameters and intensity distributions. The autocorrelation function of the scattered light intensity was analyzed by the Malvern Zetasizer software with the Smoluchowski approximation.

III.2.3 LED light source

For cell treatment in well plates a LED-based system was developed (Fig. 8 and 9). The light source system consists of control and irradiation units. Taking the demands from experiments into account the irradiation unit was set up with a high power single chip 405 nm LED VL400-EMITTER on a cylindrical heat sink (Fig. 9 A). The cascade of lenses was designed to ensure high irradiation power density and even illumination over the irradiated area (Fig. 9 A).

For the development of the optical cascade an aspherical lens was used for reducing the divergence angle of the beam ($D = 13.0$ mm, $h = 7.1$ mm from Cree Inc., North Carolina, USA), which allowed to focus all light to a second spherical lens with 35° angle ($D = 16.4$ mm, $h = 5.0$ mm from Cree Inc., North Carolina, USA) to increase radiation density. The diameter of the collimated beam was determined by the distance between two lenses. The light system provides the same power density at any point of irradiation. The maximum diameter of the beam was 35 mm and minimum 25 mm with 130 mW power. The light fluence was used at either 5 or 10 J/cm² for comparison of

cells treatment effects. The mounting carcass was built in SOLIDWorks from Dassault Systems (Massachusetts, USA) (Fig. 8).

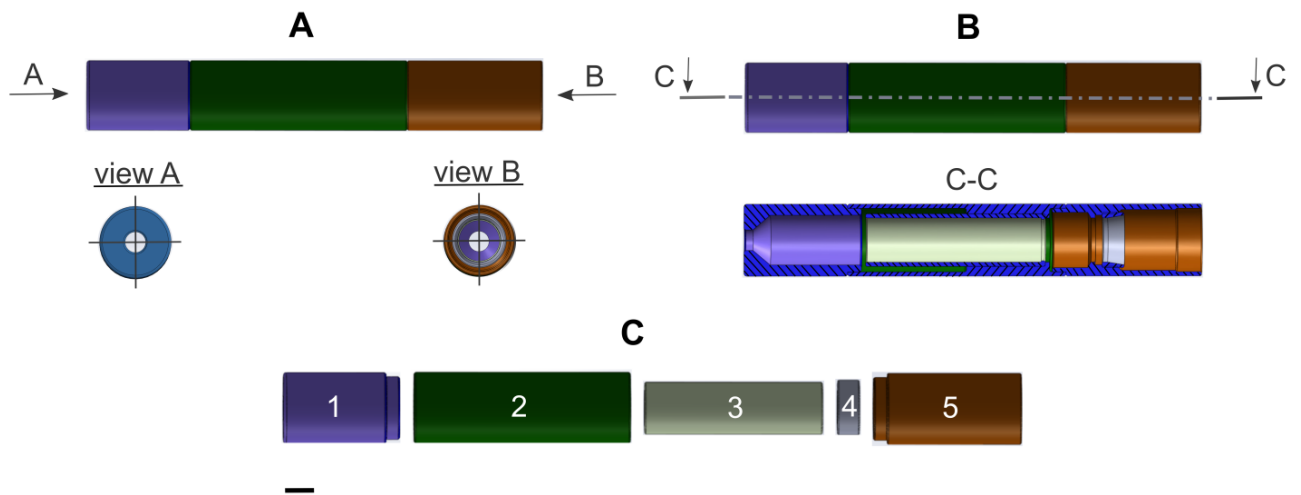


Figure 8. Parts of LED light source designed in 3D software SOLIDWorks: A – main views, B – cross section, C – extended view, scale bar 10 mm.

The parts have been 3D-printed with polylactic acid at Ultimaker 2+ (Utrecht, Netherlands). The plastic mounting carcass is composed of five parts that have been assembled according to the figure 8. The final light system was constructed with a metal turning and assembled at the Fotonika Plus Co. (Cherkasy, Ukraine) (Fig. 9 C).

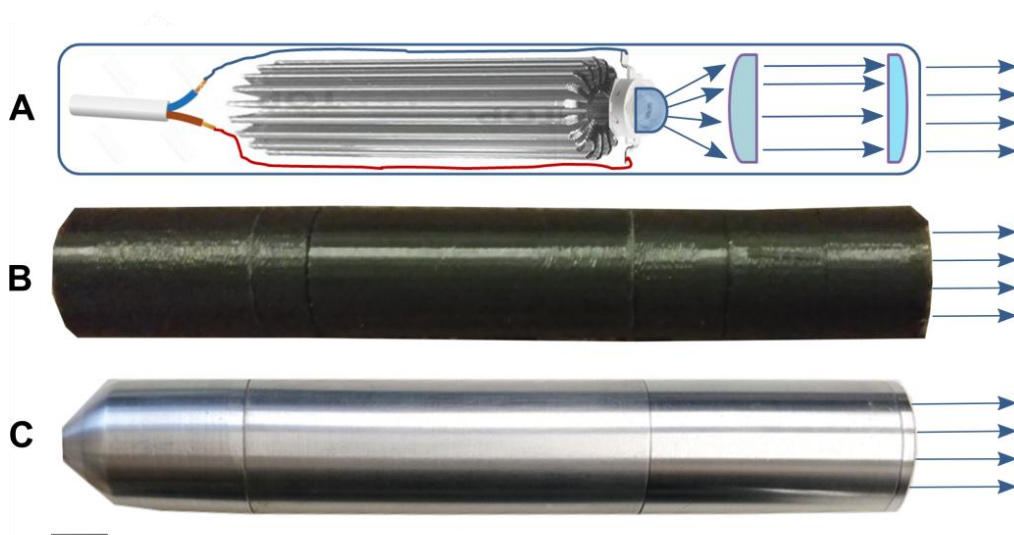


Figure 9. LED light system scheme: A – electrical part, LED and optical system, B – 3D printed plastic mounting carcass, C – final metal model, scale bar 10 mm.

III.2.4 Cell-based methods

III.2.4.1 Cell culture

The human cancer T-cell lines of leucosis origin (CCRF-CEM, Jurkat, THP1 and Molt-16) were maintained in RPMI 1640 medium. The cancer lines of carcinoma origin (HeLa) were maintained in DMEM medium. Both media were supplemented with 10% Fetal Bovine Serum, 1% Penicillin/Streptomycin and 2 mM Glutamine. Cells were cultured in 25 or 75 cm² culture flasks at a 37⁰C with 5% CO₂ in a humidified incubator Binder. The passaging was performed once cells reached ≈ 80%. Treatment with trypsin (1:10 in PBS) was used to detach adherent cells. The number of viable cells was counted upon 0.1% trypan blue staining with a Roche Cedex XS Analyzer.

III.2.4.2 C₆₀ fullerene immunofluorescence staining

CCRF-CEM cells (2×10⁵/mL) were seeded in 6-well plates on cover slips, previously coated with poly-D-Lysine, and incubated for 24 h. Cells were treated with 20 μM C₆₀ colloid solution for further 24 h or 1 μM free Doxorubicin and C₆₀-Dox for 1, 3 and 6 h. Then cells were washed with PBS, stained with MitoTracker Orange FM for 30 min at 37⁰C and then fixed with 4% paraformaldehyde for 15 min at RT in the dark. After washing with PBS, cells were permeabilized with 0.2% Triton X100 for 10 min at RT and washed again with PBS. Blocking was performed using 10% BSA for 20 min with following washing in PBS. The primary monoclonal antibody IgG against C₆₀ conjugated to thyroglobulin of bovine origin (dilution ratio of 1:30 in PBS/1.5% BSA) was added to the CCRF-CEM cells and incubated overnight at 4⁰C in a humidified chamber. Then CCRF-CEM cells were incubated for 3 h at RT with a FITC-labeled polyclonal antibody against mouse IgG developed in rabbit (dilution ratio of 1:200 in PBS/1.5% BSA). Slides were washed after each step in three shifts of PBS for 15 min each. The coverslips were rinsed with dH₂O, incubated with nucleus

staining antifade solution (0.6 μM DAPI, 90 mM p-Phenylenediamine in glycerol/PBS) for 2 h in the dark and sealed with slides.

CCRF-CEM cells were observed using a Fluorescence Microscope Keyence BZ-9000 BIOREVO equipped with blue ($\lambda_{\text{ex}} = 377 \text{ nm}$, $\lambda_{\text{em}} = 447 \text{ nm}$), green ($\lambda_{\text{ex}} = 472 \text{ nm}$, $\lambda_{\text{em}} = 520 \text{ nm}$) and red ($\lambda_{\text{ex}} = 543 \text{ nm}$, $\lambda_{\text{em}} = 593 \text{ nm}$) filters with the acquisition software Keyence BZ-II Viewer. The merged images and single cell fluorescence intensity profiles were processed with the Keyence BZ-II Analyzer software.

III.2.4.3 Visualization of drug intracellular accumulation

CCRF-CEM cells were seeded in 6-well plates Sarstedt at a cell density of 2×10^5 cells/well in 2 mL of culture medium and incubated for 24 h. Then, cells were treated with 1 μM free Doxorubicin and C_{60} -Dox or 10 μM free Berberine and C_{60} -Ber during 1, 3 and 6 h. In the preliminary investigation of Berberine intracellular accumulation, CCRF-CEM cells were treated with 50 μM Berberine for 4 h. Cells were washed with PBS.

Visualization was performed with a Fluorescence Microscope Keyence BZ-9000 BIOREVO equipped with red (for Doxorubicin, $\lambda_{\text{ex}} = 480 \text{ nm}$, $\lambda_{\text{em}} = 600 \text{ nm}$) or green (for Berberine, $\lambda_{\text{ex}} = 435 \text{ nm}$, $\lambda_{\text{em}} > 515 \text{ nm}$) filter and a respective acquisition software Keyence BZ-II Viewer. The merged images were processed with the Keyence BZ-II Analyzer software.

III.2.4.4 C_{60} fullerene extraction

CCRF-CEM cells ($2 \times 10^5/\text{mL}$) were seeded in 6-well plate Sarstedt. After 24 h cells were incubated for 0-48 h in the presence of 20 μM C_{60} , washed with PBS three times and transferred to the distilled H_2O . The freeze-thawing cycle was repeated three times. The probes were dried at 80°C under reduced pressure. Toluene/2-isopropanol

(6:1, v/v) was added in the final volume 0.5 mL, the mixture was sonicated for 1 h and centrifuged (70 min, 20 238 g). The toluene layer was analyzed with HPLC-ESI-MS.

III.2.4.5 Isolation of mitochondria

CCRF-CEM cells were incubated for 24 h in the presence of 20 μ M C₆₀ and the mitochondria fraction was isolated accordingly to (Frezza et al., 2007). Briefly, cell suspension ($5 \times 10^6/4$ mL) was centrifuged at 600 g at 4°C for 10 min, cells were resuspended in 3 mL of ice cold isolation buffer (IB: 0.01 M Tris-MOPS, 1 mM EGTA/Tris, 0.2 M sucrose, pH 7.4) and homogenized in the teflon-glass potter on ice. The homogenate was centrifuged at 600 g at 4°C for 10 min. The collected supernatant (S1) was centrifuged at 7000 g at 4°C for 10 min. The pellet (P2) was resuspended in 200 μ L ice-cold IB and centrifuged at 7000 g at 4°C for 10 min. The mitochondrial fraction obtained in pellet (P3) was used for extraction of C₆₀ as well as for measurements of protein concentration and succinate-reductase activity as mitochondrial marker.

III.2.4.5.1 Protein concentration assay

The protein concentration colorimetric assay is based on the proportional change of the dye Coomassie's color from brown to blue upon its binding with proteins (Bradford, 1976). Aliquots of both homogenate and all fractions after differential centrifugation were used to determine the protein concentration. After incubation with 0.01% Coomassie working solution in 4.7% ethanol and 8.5% phosphoric acid for 5 min, protein concentration was estimated by absorption at $\lambda = 595$ nm with a multimode microplate spectrometer Tecan Infinite M200 Pro, using BSA as a protein standard for calibration.

III.2.4.5.2 Succinate-reductase activity assay

Succinate-reductase (SR) activity colorimetric assay is based on the reduction of a tetrazolium salt 2-(4-iodophenyl)-3-(4-nitrophenyl)-5-phenyl-2H-tetrazolium (INT) to cyan farmazan (Pennington, 1961). Aliquots of homogenate (50 μ L) as well as of fractions after differential centrifugation were shaken for 15 min at 37°C in 0.5 mL of the working solution (0.1% INT, 50 mM sodium succinate, 25 mM sucrose in 50 mM potassiumphosphat buffer, pH 7.4). To stop the reaction, the proteins were precipitated with 0.5 mL 25% trichloroacetic acid. The farmazan was extracted with 2 mL ethyl acetate. The absorption of organic colored layer was analyzed at $\lambda = 492$ nm with UV-Spectrophotometer UV-1800. The succinate-reductase activity was calculated using extinction coefficient (ΔE) by the following formula:

$$SRActivityUnits \left[\frac{\mu M}{h \times mg \text{ protein}} \right] = \frac{4 \times \Delta E}{20.1 \times \text{protein concentration} \in mg} \quad (4)$$

III.2.4.6 Photodynamic treatment of cells with C₆₀ fullerene

CCRF-CEM cells (10⁴/well) were cultured in 96-well cell culture plates at for 24 h and then incubated for 24 h with 20 μ M C₆₀ and washed with PBS. Light irradiation was applied at the following wavelengths: UV – 365 nm LED lamp, 140.6 mW/cm²; violet – 405 nm high power single chip LED, 108.3 mW/cm²; green – 515 nm high power single chip LED, 50.9 mW/cm²; red – 650 nm single chip LED, 5.1 mW/cm²; red – 632 nm helium-neon 30 mW laser, 90 mW/cm². For *in vitro* screening LED were coupled three in a row on the aluminum heatsink and powered with the power supply module DIGI 35 CPU. The light fluence was used in the range of 1-8 J/cm² for UV, 5-20 J/cm² for violet and green light and 1-80 J/cm² for red light. PBS was replaced with fresh medium immediately after irradiation. Control cells were not exposed to C₆₀ treatment or light irradiation.

III.2.4.7 Drug delivery with C₆₀ fullerene

Leukemic cells (10⁴/well) were cultured in 96-well cell culture plates for 24 h. The cell culture medium was replaced by medium supplemented with drug. Cells were incubated for 24, 48 and 72 h in the presence of free drug or C₆₀-drug nanocomplexes in drug equivalent concentrations (5-100 nM Doxorubicin, 1.3-20 μM Berberine).

The working concentrations of the nanocomplexes used for cells treatment are presented with drug equivalent concentrations to compare the effect of the nanocomplexes with the effect of the free drug in the same concentration.

III.2.4.8 Photodynamic treatment of cells with C₆₀ fullerene-drug nanocomplex

CCRF-CEM cells were cultured as described in the previous section.

After 24 h incubation with nanocomplexes cells were washed with PBS and irradiated with the 405 nm high power single chip LED. The light fluence was used at either 5 or 10 J/cm². PBS was replaced with the fresh medium immediately after irradiation and cells were incubated for up to 24 h. Control cells were incubated without any treatment or light irradiation.

III.2.4.9 Cell viability

Cell viability was determined with the MTT reduction assay (Carmichael et al., 1987), based on the reduction of a yellow tetrazolium salt (3-(4,5-dimethylthiazol-2-yl)-2,5-diphenyltetrazolium bromide, MTT) to purple formazan crystals by metabolically active cells that contain NAD(P)H-dependent oxidoreductase enzymes.

Briefly, 10 μL of MTT solution (5 mg/mL in PBS) was added to each well and cells were incubated for 2 h at 37°C. The culture medium was then replaced with 100 μL of DMSO and diformazan formation was determined by measuring absorption at $\lambda = 570$ nm with the microplate reader Tecan Infinite M200 Pro.

III.2.4.10 Intracellular reactive oxygen species generation

To determine ROS production 2',7'-dichlorodihydrofluorescein diacetate (DCFH-DA) was applied. DCFH-DA is able to penetrate inside the cell, where it is deacylated by esterases to its nonfluorescent form DCFH. Upon interaction with intracellular ROS DCFH is oxidized to DCF, which is characterized by a high green fluorescence. DCFH is mostly sensitive to hydroxyl radical, peroxonitrite and H₂O₂ (Myhre et al., 2003). A stock solution of DCFH-DA (5 mM) was prepared in DMSO, stored at -20⁰C and diluted with PBS immediately before use. CCRF-CEM cells (10⁴/well) were treated as indicated above and washed once with PBS at 1 h and 3 h of further incubation. DCF-DA (5 μM) was added and the fluorescence ($\lambda_{\text{ex}} = 488 \text{ nm}$, $\lambda_{\text{em}} = 520 \text{ nm}$) was recorded every 5 min during 50 min with the microplate reader Tecan Infinite M200 Pro. After 60 min incubation fluorescent images of cells were obtained with the Fluorescence Microscope Keyence BZ-9000 BIOREVO, equipped with a green filter ($\lambda_{\text{ex}} = 472 \text{ nm}$, $\lambda_{\text{em}} = 520 \text{ nm}$).

III.2.4.11 Intercellular ATP content

CCRF-CEM cells were treated as indicated above and transferred to 50 μL glucose-free RPMI. Three hours after light exposure the cellular ATP levels were estimated with the Mitochondrial ToxGlo™ assay Kit according to the manufacturer's instructions. The plates were equilibrated to RT for 10 min and 50 μL of the ATP Detection Reagent was added to each well. ATP Detection Reagent consists of ATP detection containing luciferin, ATPase inhibitors and thermostable luciferase. After shaking at 600 rpm for 1 min the luminescence intensity was measured with the microplate reader Tecan Infinite M200 Pro.

III.2.4.12 Caspase 3/7 activity

The CCRF-CEM cells were treated as described above. The measurements of caspase 3/7 activity are enabled by luminogenic substrate with the respective tetrapeptide sequence Asp-Glu-Val-Asp. After cell lysis and caspase 3/7 cleavage of the luminogenic substrate, the “glow-type” luminescent signal is generated by luciferase. Observed luminescence is proportional to the amount of caspase 3/7 activity present in the sample.

Activity of caspases 3/7 was determined during 6 h period after light exposure using the Promega Caspase-Glo® 3/7 Activity assay Kit according to the manufacturer’s instructions. Briefly, the plates were removed from the incubator and allowed to equilibrate to RT for 30 min. After treatment, an equal volume of Caspase-Glo 3/7 reagent was added followed by gentle mixing with a plate shaker at 300 rpm for 1 min. The plate was then incubated at RT for 2 h. The luminescence of each sample was measured with the microplate reader Tecan Infinite M200 Pro.

III.2.4.13 Flow cytometry

III.2.4.13.1 Drug intracellular accumulation

CCRF-CEM cells (2×10^5 /well) were seeded in 6-well plates, incubated for 24 h, then treated with 1 μ M free and C₆₀ bound Doxorubicin or 10 μ M free and C₆₀ bound Berberine. After 1, 3 and 6 h incubation the cells were harvested, washed with PBS and analyzed with the flow cytometer BD FACSJazz™. A minimum of 2×10^4 cells per sample were acquired and analyzed with the BD FACST™ software.

III 2.2.4.13.2 Cell death type differentiation

CCRF-CEM cells were treated as indicated above. After 6 and 24 h (for C₆₀), 6 h (for C₆₀-Dox) and 24 h (C₆₀-Ber) incubation period the cells were harvested. Apoptosis

was detected by Annexin V-fluorescein isothiocyanate/propidium iodide (Annexin V-FITC/PI) apoptosis detection Kit according to the manufacturer's instructions. Briefly, cells were harvested and washed with Binding buffer. After addition of FITC-conjugated Annexin V cells were incubated for 15 min at RT in the dark. Cells were washed with Binding buffer and 10 min after propidium iodide addition were analyzed with the BD FACSJazz™. A minimum of 2×10^4 cells per sample were acquired and analyzed with the BD FACS™ software.

Based on the fluorescence signal of apoptosis positive control cells stained separately with Annexin V or PI, cells were gated into four main populations and fluorescence overlap between Annexin V and PI was compensated. On histograms of flow cytometry cells are differentiated according to green (Annexin V-FITC) and red (PI) fluorescence intensities: viable (Annexin V-FITC negative, PI negative), early apoptotic (Annexin V-FITC positive, PI negative), late apoptotic (Annexin V-FITC positive, PI positive) and necrotic (Annexin V-FITC negative, PI positive) cells.

III.2.4.13.3 Cell cycle

CCRF-CEM cells (2×10^5 /well) were seeded in 6-well plates, incubated for 24 h, then treated with 10 μ M free and C₆₀ bound Berberine. After 12 h incubation the cells were harvested, washed with PBS, fixed by adding the cell solution dropwise to ice-cold 70% ethanol/PBS, mixed and stored at -20°C overnight. Then cells were washed with ice-cold PBS and treated with the working buffer containing 100 μ g/mL RNase A (in water, preboiled at 95°C for 15 min), 0.1% triton X-100 and 10 μ g/mL propidium iodide for 20 min. Consequently, the DNA content of cells was analyzed with the flow cytometer BD FACSJazz™. A minimum of 2×10^4 events per sample were acquired and analyzed at $\lambda_{\text{ex}} = 488$ nm, $\lambda_{\text{em}} = 692/40$ nm with the BD FACS™ software.

III.3 Statistics

All experiments were carried out with a minimum of four replicates. Data analysis was performed with the use of the GraphPad Prism 7. Data are presented as Mean \pm Standard Deviation. Student's t-test for two samples (one-way analysis of variance) was pursued to detect significant variances between treatments (McDonald & University of Delaware, 2009). Differences values $p < 0.05$ were considered to be significant.

III.3.1 Half-maximal inhibitory concentration

Cell viability curves and half-maximal inhibitory concentration (IC_{50}) values were assessed using the software GraphPad Prism 7. Briefly, individual concentration-effect curves were generated by fitting the logarithm of the tested compound concentrations versus corresponding normalized percentages of cell viability values using nonlinear regression.

III.3.2 Combination index

The combination index (CI), calculated according to Chou-Talalay method (Chou, 2006) with ComboSyn software, was used to evaluate pharmacodynamic interactions between drug and photoexcited C_{60} in cells treated with C_{60} -drug and irradiated with 5 and 10 J/cm^2 LED light. The following equation was used:

$$CI = \frac{(D)_1}{(D_x)_1} + \frac{(D)_2}{(D_x)_2} \quad (5)$$

where $(D_x)_1$ is the concentration of free drug that inhibited cell viability to x%; $(D_x)_2$ is the concentration of free C_{60} that inhibited cell viability to x% after photoexcitation; $(D)_1$ and $(D)_2$ are the concentrations of drug and C_{60} in the C_{60} -drug which inhibited cell viability to x% after photoexcitation. The CI value < 1 , $= 1$ and > 1 indicates on synergistic, additive or antagonistic interaction, respectively.

IV. RESULTS

The current research starts with the development and investigation of the C_{60} -based monotherapeutic anticancer treatment strategies – (1) photodynamic treatment of leukemic cells with C_{60} as a photosensitizer and (2) treatment of leukemic cells with chemotherapeutic drugs through the C_{60} -mediated delivery (Fig. 5). The final step exploits those monotherapeutic treatment strategies combination (3) in the frame of the photodynamic treatment of leukemic cells with C_{60} -drug nanocomplexes using C_{60} both as a photosensitizer and as a drug nanocarrier.

IV.1 C_{60} fullerene

In the first part of the research, pristine C_{60} in the combination with light irradiation with different LEDs sources was explored for photodynamic treatment of human leukemic cells.

In order to elucidate the most abundant presented molecular ions in used C_{60} aqueous solution, MALDI-TOF-MS instrumentation was utilized. This method allows to ascertain that preparation of C_{60} in water has not introduced any modifications to the fullerene structure. The MALDI-TOF-MS analysis of C_{60} samples revealed sharply defined peaks for a predominant molecular mass of 720 Da (Fig. 10). The obtained spectrum confirms the presence of naturally occurring stable isotopes of common element carbon resulted in the gradual triplication of the peak. Only 98.89% of naturally occurring carbon atoms are in the form of ^{12}C ; most of the remaining 1.11% consists of atoms of ^{13}C and trace amount of ^{14}C (Wagner et al., 2018). The presence of one ^{13}C atom in C_{60} molecule shifted mass to 721 Da and 722 Da molecule had two ^{13}C atoms in the cage, respectively.

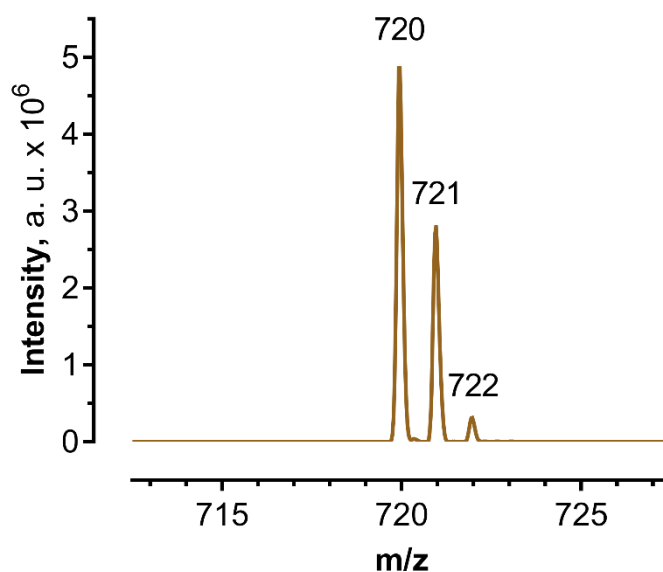


Figure 10. MALDI-TOF-MS spectrum of C₆₀ colloid solution, a.u. = arbitrary units.

IV.1.1 C₆₀ uptake by leukemic cells and its intracellular distribution

The first requirement for any photosensitizing agent is an extensive penetration into the cancer cells since otherwise extracellular ROS generation could be not sufficient to induce cell death. Though the intracellular accumulation of C₆₀ was proved already (Levi et al., 2006; Porter et al., 2007; Horie et al., 2010; Russ et al., 2016), still little is known about its subcellular localization, its ability to relocate and to realize effects at this level in different cell types.

Qualitative analysis

The intracellular uptake and distribution of C₆₀ was studied by fluorescence immunostaining of human leukemic CCRF-CEM cells using primary antibody against C₆₀ and FITC-labeled secondary antibody. The DNA-binding dye DAPI was used as a cell nucleus marker and the membrane potential-sensitive dye MitoTracker Orange as a mitochondrial marker. No significant unspecific green FITC-fluorescence was observed in the control cells incubated in the absence of C₆₀ (Fig. 11 A). After 24 h incubation with C₆₀ no change in nucleus fluorescence as compared with controls was

found, whereas green punctuated dots surrounding the nucleus were detected. The data showed that C_{60} could diffuse through the plasma membrane and locate in the extranuclear region.

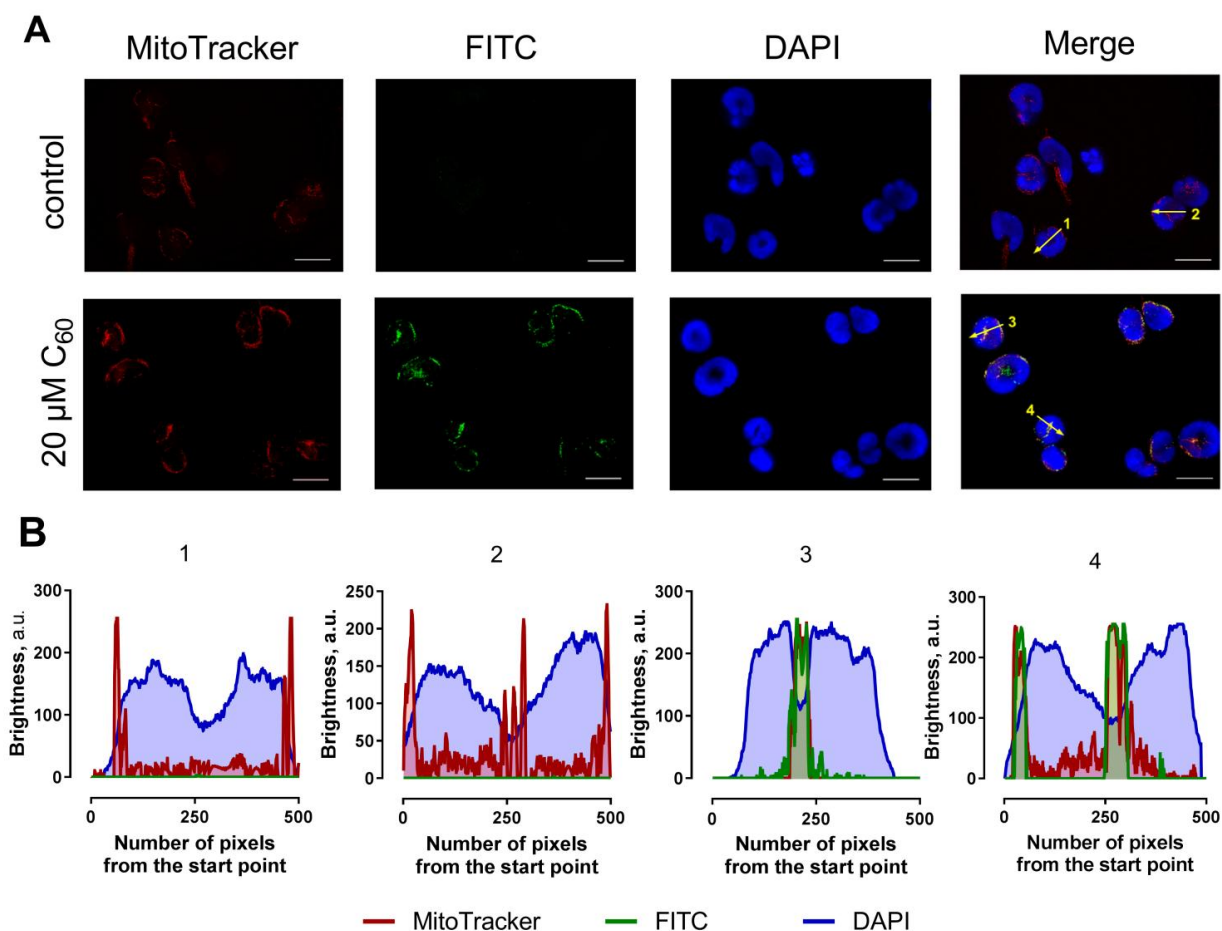


Figure 11. Intracellular localization of C_{60} in CCRF-CEM cells: A – Fluorescence microscopy images of CCRF-CEM cells, incubated for 24 h with 20 μM C_{60} and stained with DAPI (blue), MitoTracker (red) and FITC-labeling of C_{60} (green), scale bar 20 μm ; B – Linear fluorescence profiles of cells along the yellow arrows, indicated on the Merge images: 1, 2 – control cells, 3, 4 – cells incubated for 24 h in the presence of 20 μM C_{60} .

Next, the ability of C_{60} to localize in the mitochondria membranes was evaluated. Fluorescence microscopy showed a partial co-localization of C_{60} antibodies and the mitochondrial marker with an overlap of the green C_{60} and the red mitochondria signals (Fig. 11 B), that suggested C_{60} localization in mitochondria of human leukemic cells.

Quantitative analysis

To study the accumulation dynamics, C_{60} was extracted from the cell

homogenate as well as from the mitochondrial fraction and subjected to high-performance liquid chromatography mass-spectrometry analysis.

The developed HPLC-ESI-MS method (Tab. 12, Fig. 6) enabled the quantitative analysis of C_{60} concentration in toluene extracts of CCRF-CEM cells. The intracellular uptake of C_{60} was time-dependent reaching its maximum of < 250 ng/ 10^6 cells at 24 h of incubation (Fig. 12). The minor decrease at 48 h could be explained by C_{60} partial efflux.

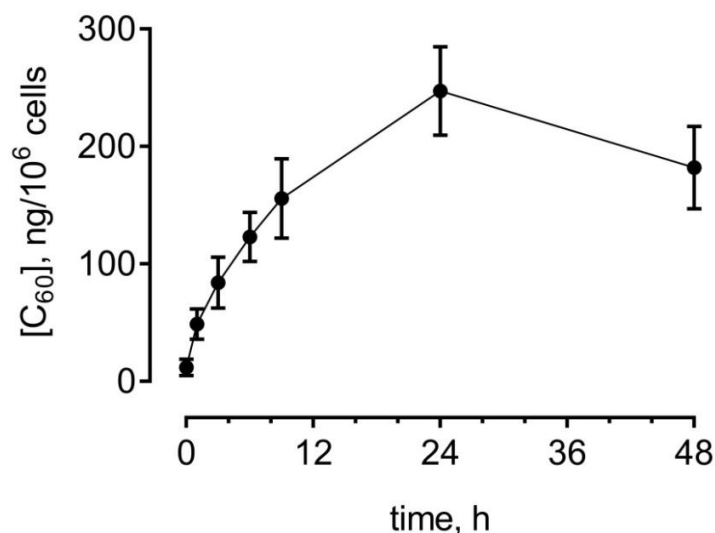


Figure 12. Intracellular uptake of C_{60} in CCRF-CEM cells. HPLC-ESI-MS analysis of C_{60} content in toluene extract of leukemic cells incubated in the presence of $20 \mu\text{M}$ C_{60} during 0-48 h.

The next step was to quantify C_{60} in the mitochondrial fraction using HPLC-ESI-MS method. For that, CCRF-CEM cells were incubated in the presence of C_{60} for 24 h and subjected to homogenization and differential centrifugation. Succinate-reductase activity was used as a mitochondrial marker. The increased succinate-reductase activity of the mitochondrial fraction evidenced enrichment and purity of the obtained fraction (Fig. 13 A). Finally, C_{60} concentration was estimated in cellular fractions (Fig. 13 B).

HPLC-ESI-MS analysis of C_{60} content in the mitochondria fraction showed accumulation at a level of < 180 ng/ 10^6 cells at 24 h that amounted to 72% of its overall content in cell extract. This data demonstrate that C_{60} predominantly accumulates within mitochondria of CCRF-CEM cells.

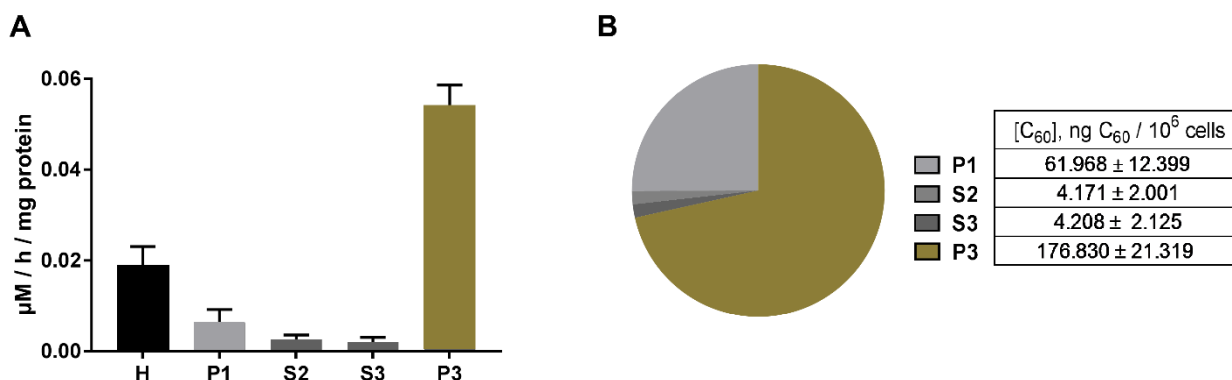


Figure 13. Quantitative analysis of C₆₀ content in mitochondria of leukemic cells: A – Succinate-reductase activity of homogenate (H) and obtained cellular fractions; B – C₆₀ distribution among cellular fractions. Cellular fractions include supernatant 2 and 3 (S2 and S3), pallet 1 and 3 (P2 and P3) according to III.2.4.5 *Isolation of mitochondria*, where P3 corresponds to mitochondrial fraction.

IV.1.2 Photodynamic treatment of cells with C₆₀ fullerene

IV.1.2.1 Cell viability

The efficiency of light-induced excitation of photosensitizing agent substantially depends on its relative optical absorption extinction coefficients. The UV-vis absorption spectrum (200-900 nm) of pristine C₆₀ aqueous colloidal solution (Fig. 14 A) has three intense absorption bands typical for C₆₀ with maxima at 220, 265 and 350 nm and a long broad tail up to the red region of the visible light (Ritter et al., 2015). The figure 14 A demonstrates that the absorption spectrum of C₆₀ and the spectra of the used LEDs are overlapping, suggesting that they could be applied for C₆₀ photoexcitation.

After 24 h treatment with C₆₀ the cells were irradiated and at 48 h their viability was estimated with the MTT assay. As shown in the figure 14 B, the effect of light irradiation itself on CCRF-CEM cell viability depends on light wavelength. Irradiation of cells in the ultraviolet light at 365 nm was followed by a decrease of the viability. The effect became stronger with the increase of the light fluence. After irradiation with 8 J/cm² the viability was only 32 ± 4% compared to viability of control cells kept in the dark.

Irradiation with visible light was followed by smaller cytotoxicity in comparison with UV irradiation even at higher fluences. Only after irradiation with violet light at

405 nm at a maximal dose (20 J/cm^2) cell viability was decreased on $16 \pm 5\%$ of the control level (Fig. 14 B). Light irradiation at 405 nm is used in practice for the sterilization of both clinical and nonclinical environments due to its strong bactericidal activity (McKenzie et al., 2016; Ramakrishnan et al., 2016), but its inactivating effect against mammalian cells is slight (Ramakrishnan et al., 2014, 2016). No significant toxic effect was observed after cells irradiation with green light at 515 nm and red light at 650 nm with fluence rate of 20 J/cm^2 , the cell viability was $90 \pm 5\%$ and $95 \pm 4\%$ accordingly as compared with control (Fig. 14 B and Appendix 1 Fig. 1).

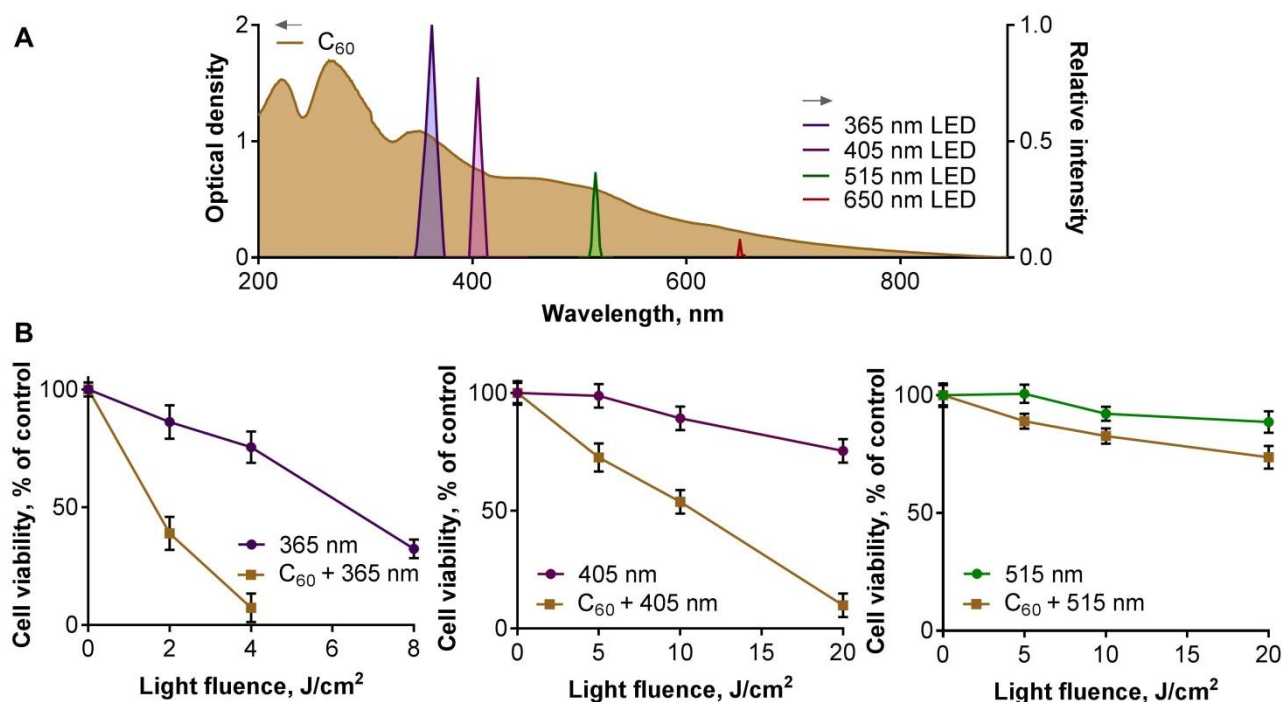


Figure 14. *In vitro* C₆₀ photodynamic treatment of human leukemic cells: A – Absorption spectrum of C₆₀ and spectra of 365, 405, 515 and 650 nm LEDs; B – Viability of CCRF-CEM cells, incubated for 24 h in absence or presence of $20 \mu\text{M}$ C₆₀ and irradiated with 365, 405 and 515 nm LEDs at different light fluences.

Next, cell viability was studied after treatment with C₆₀ and photoexcitation of accumulated nanostructures. No effect was detected when cells were treated with C₆₀ and kept in the dark, but after incubation for 24 h with $20 \mu\text{M}$ C₆₀ and irradiation with 365 nm or 405 nm LEDs a substantial decrease of cell viability was observed (Fig. 14 B). Combined treatment with C₆₀ and UV 365 nm light at the doses of 2 and 4 J/cm^2 decreased the viability down to $39 \pm 6\%$ and $7 \pm 5\%$, respectively, whereas at 8 J/cm^2 almost cells were dead. Photoexcitation of accumulated C₆₀ with violet 405 nm light at

5, 10 and 20 J/cm² light fluence caused a viability decrease to 73 ± 6%, 54 ± 5% and 10 ± 4%, respectively. C₆₀ exhibited lower cytotoxicity under green 515 nm LED light irradiation. Treatment with C₆₀ for 24 h and green light irradiation at 5 and 10 J/cm² resulted in viability around 85 ± 3% with a further 10 ± 3% decrease at 20 J/cm² (Fig. 14 B). No effect was observed at the further shift of the light wavelength into the red region of visible spectrum (Appendix 1 Fig. 1). Even when intensities reached 80 J/cm² using a 632 nm helium-neon 30 mW laser no cytotoxic effect was observed that can be linked with low absorption of longwavelength light by C₆₀.

The obtained results indicated on high output single chip 405 nm LED as the most favorable light source for C₆₀ photodynamic treatment of human leukemic cells. Therefore, 10 J/cm² 405 nm light fluence was used during following assessments of C₆₀'s photocytotoxicity mechanism.

IV.1.2.2 Intracellular reactive oxygen species generation

The efficient and continuous intracellular ROS production is a critical step for realization of a photoexcited C₆₀ anticancer effect. ROS generation was estimated with the use of the fluorescence dye DCFH-DA (Myhre et al., 2003; Eruslanov & Kusmartsev, 2010). CCRF-CEM cells, treated with 10 and 20 μM C₆₀ for 24 h were irradiated at 10 J/cm² 405 nm. The ROS production was studied at 1 and 3 h after light exposure.

When DCFH-DA was added to untreated cells a slight continuous increase of fluorescence was detected (Fig. 15). Neither C₆₀ nor light exposure alone caused significant changes in ROS generation in comparison with control, while at combined treatment with C₆₀ and 405 nm light, ROS production in CCRF-CEM cells was shown to be increased dramatically. Cells treated with 10 μM C₆₀ and irradiated (405 nm, 10 J/cm²) exhibited a 4-fold while cells treated with 20 μM C₆₀ – an 8- and 10-fold increase of ROS level was detected at 1 and 3 h, correspondingly (Fig. 15 A).

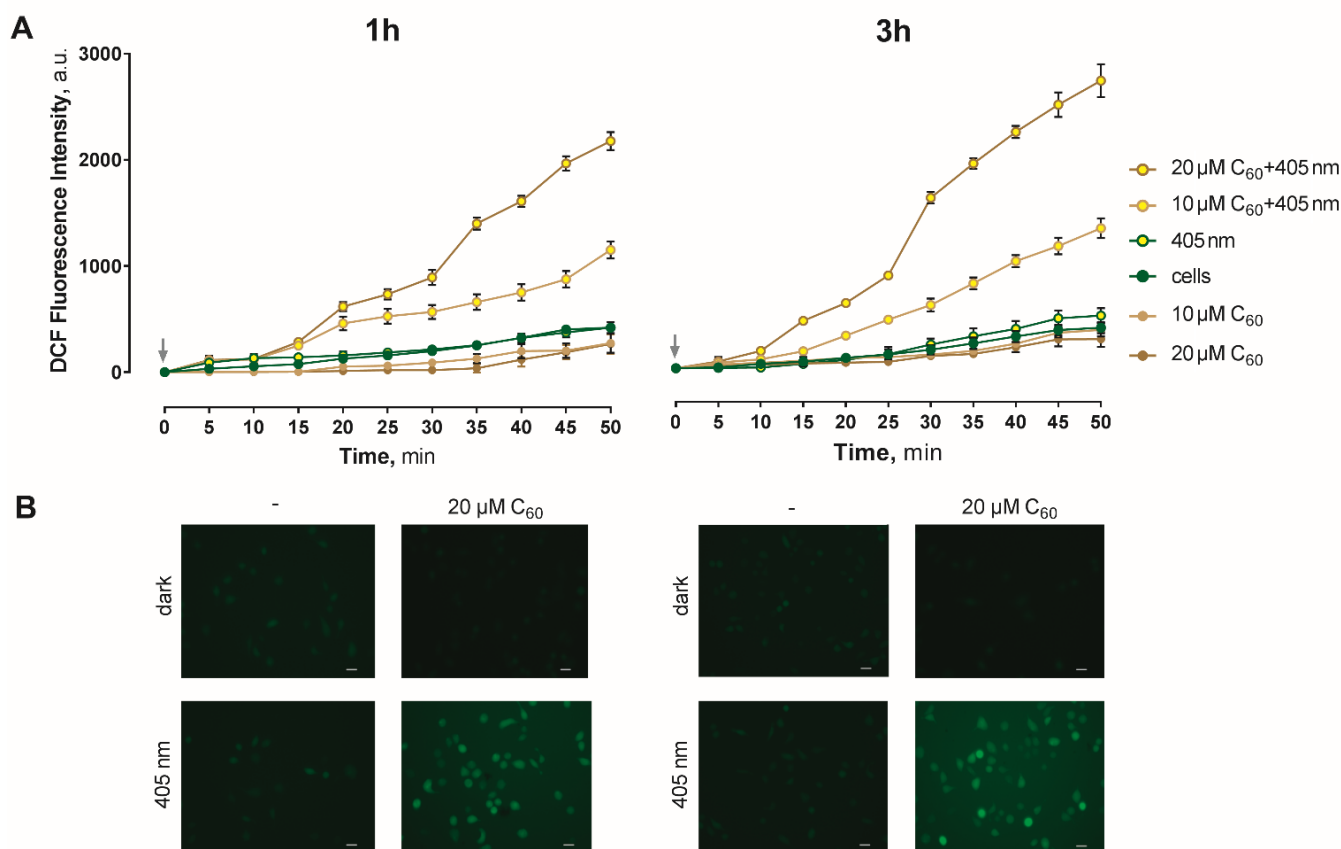


Figure 15. Reactive oxygen species generation in CCRF-CEM cells (A) and fluorescence microscopy images (B) at 1 h and 3 h after treatment with either C₆₀ or irradiation at 405 nm 10 J/cm² alone or their combination, a.u. = arbitrary units, scale bar 20 μm .

The microscopy analysis of cells, presented on the figure 15 B, confirmed DCF fluorescence measurement data, thus, indicating that photoexcitation of accumulated C₆₀ with 405 nm LED was followed by oxidative stress in leukemic cells.

IV.1.2.3 Apoptosis induction

Mitochondria play a leading role in apoptosis induction and progression and are an important subcellular target for many photosensitizing drugs (Castano et al., 2004; Ribeiro et al., 2004). Cytotoxic effects of C₆₀ are considered to be realized particularly through the mitochondrial oxidative damage (Scharff et al., 2008; Grebinyk et al., 2012). Therefore, ATP level was assessed as a main marker of mitochondrial phosphorylation function.

Neither C₆₀ in concentrations $\leq 20 \mu\text{M}$ (Fig. 16 A) nor 10 J/cm² 405 nm light

(Fig. 16 B) had any effect on the ATP level in CCRF-CEM cells. In contrast, the irradiation of cells treated with 20 μM C_{60} caused a gradual decrease of ATP levels that was found to remain at app. 30% following 4-6 h after light exposure (Fig. 16 B).

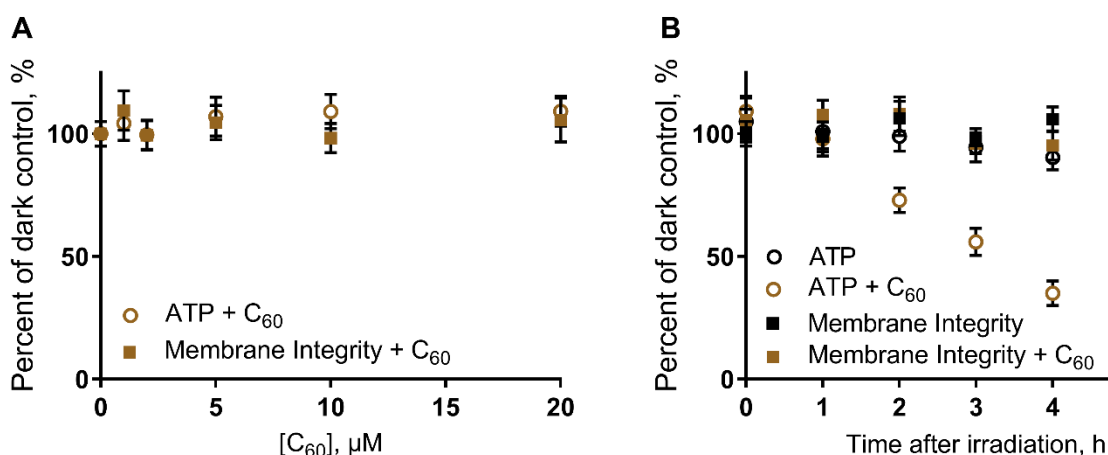


Figure 16. ATP level in CCRF-CEM cells under treatment with 20 μM C_{60} in dark (A) or after irradiation with 10 J/cm^2 405 nm light (B).

The photosensitizing potential of intracellular accumulated C_{60} irradiated with 405 nm light was further studied by evaluation of the caspase 3/7 activity and plasma membrane phosphatidylserine translocation as primary markers of apoptosis.

CCRF-CEM cells were incubated for 24 h with C_{60} , irradiated with 405 nm and caspase 3/7 activity was measured during further 6 h of incubation. It was shown that light irradiation alone had no effect on caspase 3/7 activity of controls, while C_{60} photoexcitation was followed by 4-fold increase of caspase 3/7 activity at 3 h (Fig. 17 A).

Exposure of phosphatidylserine on cell surface is proven to be an “eat me” signal, which facilitates phagocytic recognition of apoptotic cells and their destruction (Suzuki et al., 2013). CCRF-CEM cells, treated with C_{60} and either kept in the dark or irradiated with 405 nm light, were subjected to double staining with phosphatidylserine-binding Annexin V-FITC and DNA-binding dye propidium iodide (Fig. 17 B). Neither treatment with 20 μM C_{60} nor with 405 nm light irradiation alone had significant effect on cells distribution profiles, demonstrating a viability rate around $95 \pm 4\%$. However, under combined action of C_{60} and light a time-dependent increase in the content of apoptotic CCRF-CEM cells was detected that reached a level

of $18 \pm 3\%$ and $50 \pm 3\%$ at 6 and 24 h after light exposure, respectively, compared to $4 \pm 1\%$ of control cells, treated with C_{60} and kept in the dark (Fig. 17 B and C).

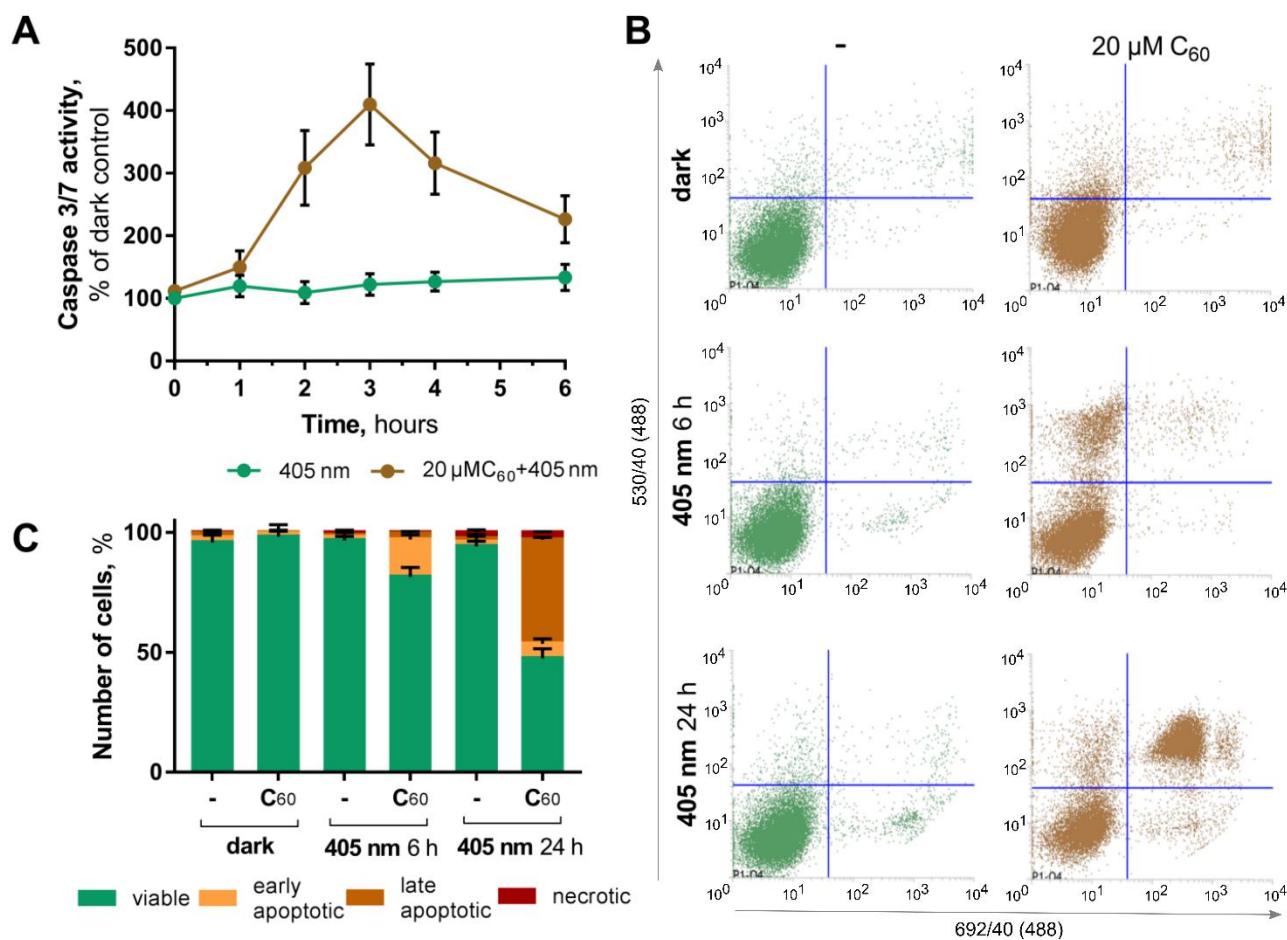


Figure 17. Induction of leukemic cells apoptosis by light irradiation of accumulated C_{60} : Caspase 3/7 activity in CCRF-CEM cells (A); Cell populations content, differentiated with flow cytometry after Annexin-FITC/PI staining at 6 and 24 h after 405 nm light irradiation of CCRF-CEM cells treated with or without 20 μ M C_{60} : FACS histograms (B) and quantitative analysis (C) (FACS histograms: in each panel the lower left quadrant shows the content of viable, upper left quadrant – early apoptotic, upper right quadrant – late apoptotic, lower right quadrant – necrotic cells populations).

The data allow to conclude that the toxic effect of C_{60} against CCRF-CEM cells after photoexcitation is realized by apoptosis induction.

IV.2 C_{60} -Drug nanocomplexes

IV.2.1 Analyses of C_{60} -Doxorubicin nanocomplexes

C_{60} -Doxorubicin nanocomplexes (C_{60} -Dox) were routinely synthesized according to (Prylutsky et al., 2015) and systematically checked with high performance liquid chromatography-electrospray ionization-tandem mass

spectrometry, UV-vis spectrometry and dynamic light scattering to ensure the complexes stability as well as robustness of its synthesis.

IV.2.1.1 HPLC-ESI-MS/MS analysis

To confirm presence of the complex in solution a concentration of 1 μM Doxorubicin was chosen to be optimal for analytical analysis (Fig. 18). The optimum concentration was chosen within linear dynamic range of calibration curve (the range of concentrations where the signals are directly proportional to the concentration of the analyte in the sample) to assure that the method gives results with acceptable uncertainty. It was expected that during the separation process under reverse-phase conditions hydrophobic C_{60} molecules are retained on the column much stronger than those of the more polar Doxorubicin (Dorsey & Dill, 1989).

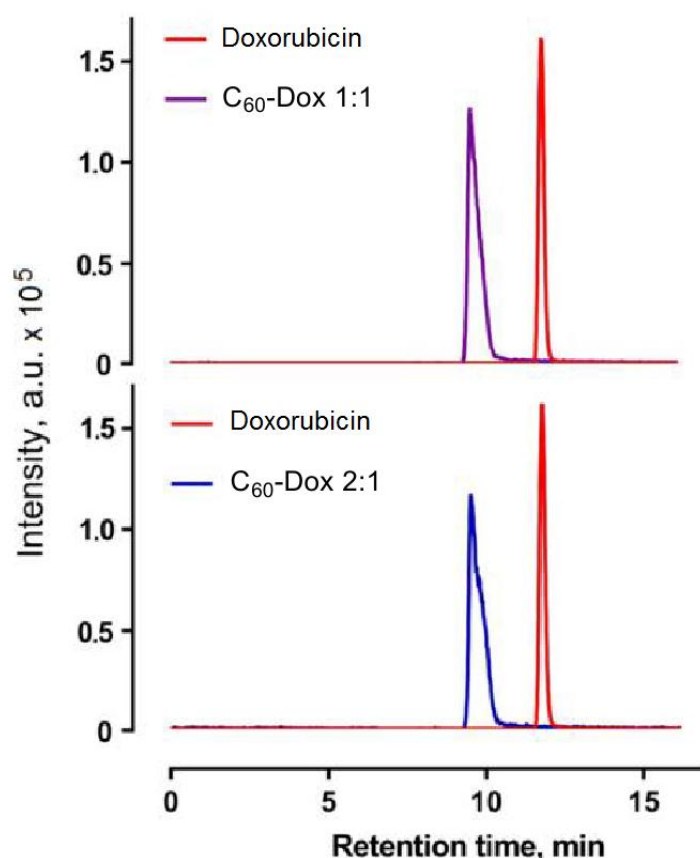


Figure 18. Multiple reaction monitoring chromatograms of free Doxorubicin, C_{60} -Dox 1:1 and 2:1 (1 μM Doxorubicin-equivalent concentration) under isocratic flow (acetonitrile, 0.1% formic acid in H_2O , 80:20, v:v), precursor – product ions transition: 544.2 \rightarrow 130.2 and 361.1 m/z; a.u. = arbitrary units.

Elution with the polar mobile phase will evidently cause decomposition of nanocomplex and release of free Doxorubicin that possesses higher affinity to mobile phase and can be detected by mass spectrometry. Under isocratic flow conditions the retention time for free Doxorubicin and Doxorubicin as a component of nanocomplexes with C_{60} was different – 11.66 and 9.44 min, respectively (Fig. 18). In addition, the chromatography peaks of Doxorubicin released from nanocomplexes were broader and with observed “peak tailing”. The observed changes in chromatograms of the free Doxorubicin and those released from nanocomplexes pointed out on the presence of C_{60} -Dox in solution.

IV.2.1.2 Spectroscopic and fluorometric analysis

The optical properties of Doxorubicin are determined by electron transition in π -complexed system of its aromatic rings and ketone groups (Changenet-Barret et al., 2013). The typical absorption spectrum of Doxorubicin lies in the wavelengths of $\lambda < 600$ nm with a broad band at 480 nm (Fig. 19 A). Since UV-vis absorption spectrum of pristine C_{60} water colloidal solution has three UV absorption bands and a long broad tail up to the red region of the visible light (Fig. 14 A) (Ritter et al., 2015), the respective control spectra of free C_{60} were subtracted from nanocomplex's spectra. The observed absorption spectra of both 50 μ M nanocomplexes were similar to those of free 50 μ M Doxorubicin, but a 30% hypochromic effect was observed (Fig. 19 A) indicating a Doxorubicin fixation on the C_{60} surface due to π - π stacking interactions.

The fluorescence spectrum of Doxorubicin exhibits one broad band that consists of three peaks at 560, 594 and 638 nm with a maximum around 594 nm (Fig. 19 B) (Changenet-Barret et al., 2013), whereas C_{60} has no detectable fluorescence at this spectral band. C_{60} -Dox fluorescence was estimated in a series of dilutions with 3-50 μ M Doxorubicin-equivalent concentration. Regardless of dilution the fluorescence of Doxorubicin ($\lambda_{\text{ex}} = 480$ nm, $\lambda_{\text{em}} = 594$ nm) in nanocomplexes was quenched by C_{60} moieties (Fig. 19 B). Thus, the fluorescence of Doxorubicin in both nanocomplexes at 3 μ M Doxorubicin-equivalent concentration appeared to be quenched by 50%.

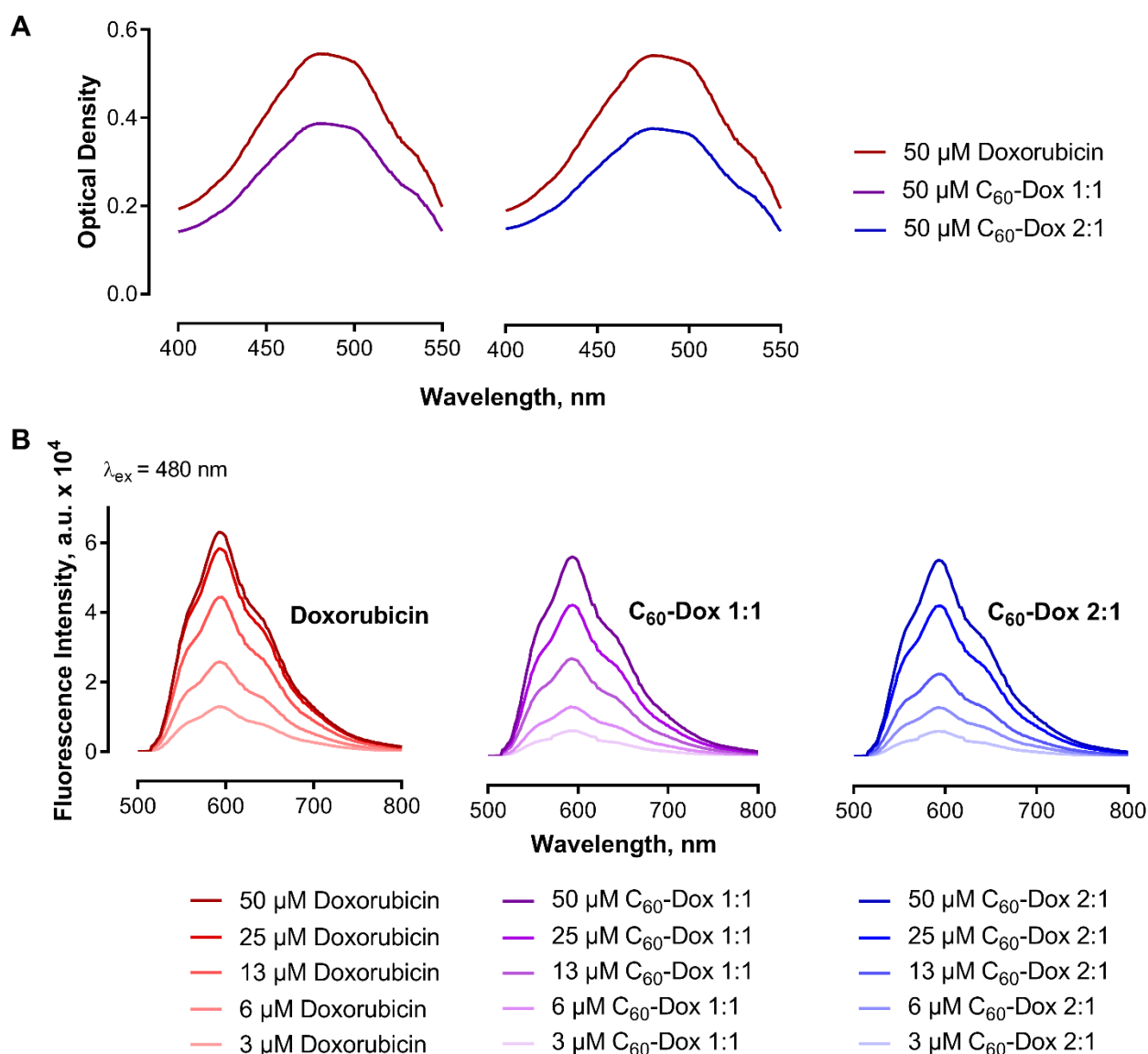


Figure 19. Optical characterization of C_{60} -Dox nanocomplexes: A – Optical density spectra of free Doxorubicin and C_{60} -Dox; B – Fluorescence emission spectra of free Doxorubicin and C_{60} -Dox at Doxorubicin-equivalent concentration from 3 to 50 μM , a.u. = arbitrary units.

The observed Doxorubicin fluorescence quenching is attributed to the strong electron-accepting capability of C_{60} (Liu & Troisi, 2013) and intramolecular excited-state energy transfer typical for noncovalent Doxorubicin complexes (Blazkova et al., 2014; Husseini et al., 2016).

IV.2.1.3 Size distribution analysis by dynamic light scattering

The size and stability of a nanoparticulate anticancer drug is substantially dependent on the cell culture medium composition, ionic strength and protein

concentration. By dynamic light scattering the average hydrodynamic diameter of C₆₀-Dox 1:1 and 2:1 (1 μM) in physiological saline solution (0.9% NaCl) was found to be 135 ± 5 nm and 134 ± 6 nm, respectively, matching the data of previous investigations (Prylutskyy et al., 2015). To estimate the stability in cell culture medium C₆₀-Dox were incubated at 37°C for 72 h in RPMI supplemented with 10% FBS. The pattern of particles size distribution in this medium (Fig. 20) is attributed to the high protein content as well as its probable aggregation (Sabuncu et al., 2012; Gollwitzer et al., 2016).

The dynamic light scattering data on hydrodynamic diameter distribution of 1 μM C₆₀-Dox 1:1 and 2:1 in FBS-supplemented cell culture medium showed that their size was 138 ± 6 nm and 139 ± 5 nm when measured immediately (Fig. 20 A) and 146 ± 4 nm and 144 ± 5 nm after 72 h incubation (Fig. 20 B), correspondingly.

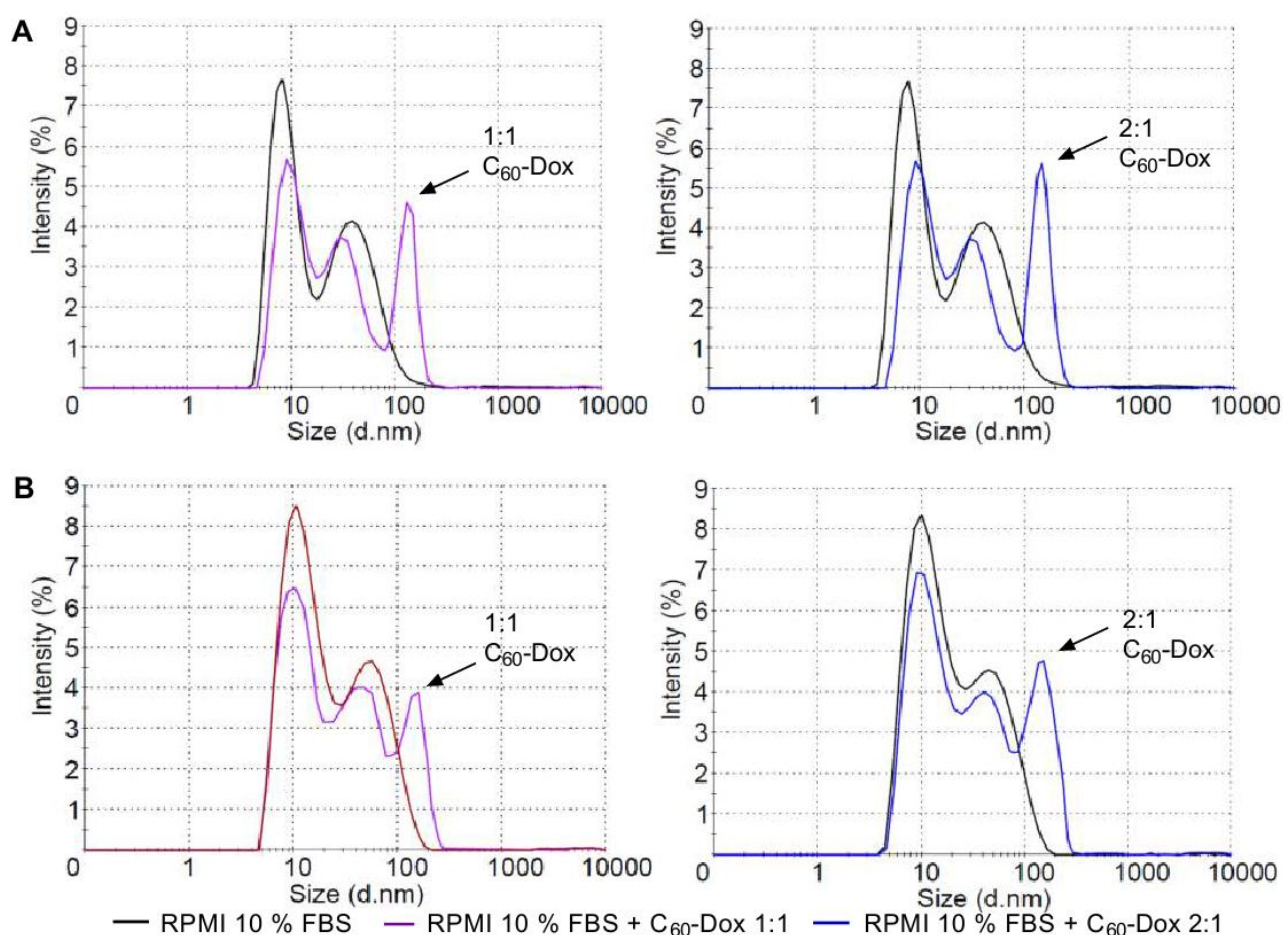


Figure 20. Hydrodynamic size (diameter, nm) of C₆₀-Dox in RPMI cell culture medium supplemented with 10% FBS at 0 (A) and 72 h (B) incubation; Intensity (%): percentage of all scattered light intensity.

The detected stability of the maximum (around 140 nm) indicated that there was no additional aggregation of the C₆₀-Dox during a prolonged incubation in FBS-supplemented cell culture medium which confirmed their suitability for *in vitro* studies.

IV.2.2 Drug delivery with C₆₀ nanocomplexes

IV.2.2.1 Cellular effects of C₆₀-Doxorubicin nanocomplexes

IV.2.2.1.1 Intracellular accumulation of C₆₀-Doxorubicin nanocomplexes

With the use of fluorescence based techniques intracellular localization of C₆₀ and Doxorubicin was studied after CCRF-CEM cells' treatment with C₆₀-Dox in the 1:1 and 2:1 nanomolar ratio. Since Doxorubicin possesses a strong absorption and fluorescence in the visible spectral region (Fig. 19) (Changenet-Barret et al., 2013; Motlagh et al., 2016) the direct tracking of this molecule is possible, whereas C₆₀ monitoring requires additional immunofluorescence staining (Ali et al., 2004; Chirico et al., 2007).

Qualitative analysis

CCRF-CEM cells were incubated for 24 h with the agents under study, subjected to staining and examined with fluorescence microscopy. The overlap of the Doxorubicin red signal with the nuclear marker DAPI blue signal confirmed drug's nuclear localization (Fig. 21). Substantially enhanced Doxorubicin levels were detected in cells treated with C₆₀-Dox as compared with cells treated with the free Doxorubicin. Monitoring of the C₆₀ distribution by immunofluorescence green signal confirmed the intracellular accumulation of the nanostructure and pointed on its extranuclear localization. The observed intracellular allocation of Doxorubicin and C₆₀ evidenced the effective drug release from nanocomplexes.

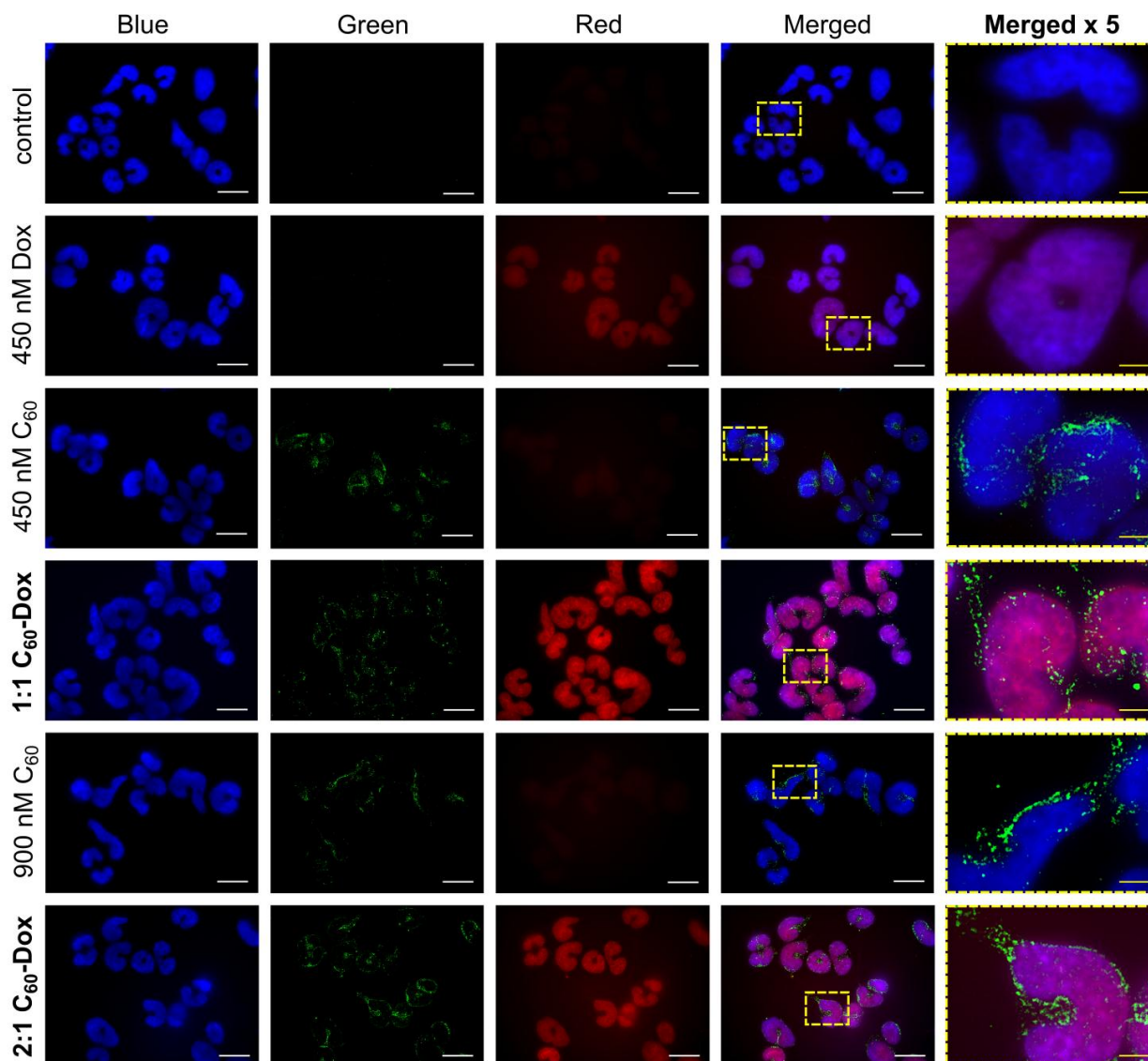


Figure 21. Fluorescence microscopy images of CCRF-CEM cells, stained with DAPI (Blue), FITC-based immunostaining for C₆₀ (Green) and Doxorubicin (Red) after treatment with: 450 and 900 nM C₆₀, 450 nM Doxorubicin (Dox), 1:1 or 2:1 C₆₀-Dox. The white scale bar corresponds to 20 μm , the yellow scale bar on images in the column “Merged x5” corresponds to 4 μm .

Quantitative analysis

CCRF-CEM cells were incubated in the presence of 1 μM Doxorubicin or C₆₀-Dox in a drug-equivalent concentration, examined with fluorescence microscopy and subjected to flow cytometry to quantify the intracellular level of accumulated drug after 1, 3 and 6 h treatment (Fig. 22).

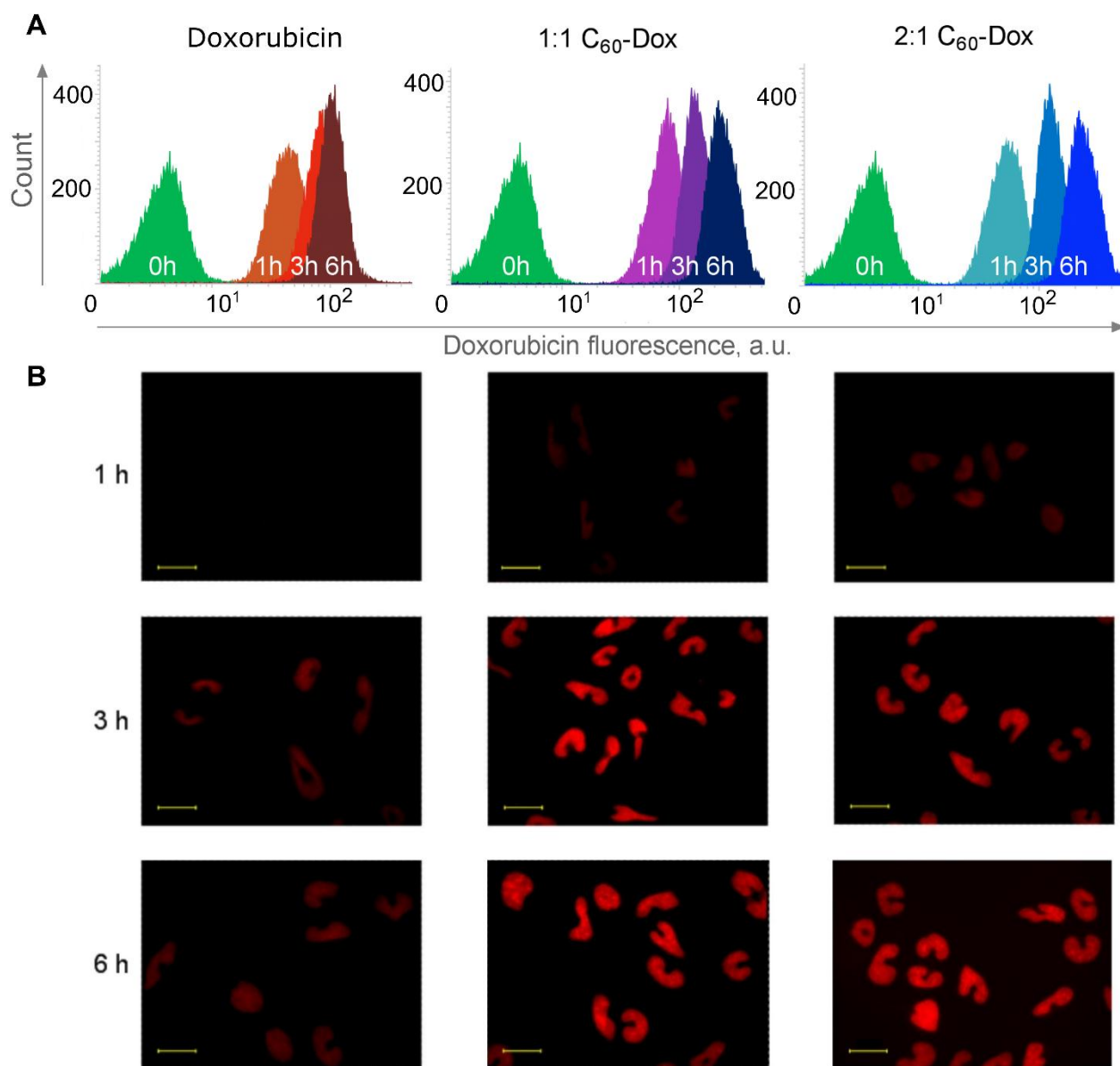


Figure 22. Intracellular uptake of 1 μM free or C₆₀-complexetaed Doxorubicin in a drug-equivalent concentration: flow cytometry (A) and fluorescence microscopy images (B) of CCRF-CEM cells incubated with Doxorubicin and C₆₀-Dox at the ratio 1:1 and 2:1 for 1, 3 and 6 h, scale bar 20 μm .

The mean fluorescence intensity of each sample was calculated from logarithmic FACS histograms by the value of respective Doxorubicin red fluorescence signal ($\lambda_{\text{ex}} = 488 \text{ nm}$, $\lambda_{\text{em}} = 585/29 \text{ nm}$) and presented in the table 14. Autofluorescence of untreated cells was used as a negative control.

Time-dependent accumulation of 1 μM Doxorubicin was demonstrated with the enhanced fluorescence intensity (Fig. 22, Tab. 14). The fluorescence microscopy images illustrate that C₆₀-Dox were internalized faster than free drug as evidenced by

detected much brighter intracellular red fluorescence (Fig. 22). The mean fluorescence intensities of the CCRF-CEM cells, treated with 1:1 C₆₀-Dox at 1 μM Doxorubicin-equivalent concentration, were increased in 1.5, 1.7 and 2.2 times compared to free Doxorubicin at 1, 3 and 6 h, respectively. Delayed intracellular drug accumulation was found for 2:1 C₆₀-Dox, however, at 6 h it reached the same level as 1:1 nanocomplex (Fig. 22, Table 14).

Table 14. Mean fluorescence intensity (FI) of intracellular accumulated Doxorubicin estimated by FACS histograms

<i>FI, arbitrary units</i>	<i>1 h</i>	<i>3 h</i>	<i>6 h</i>
Doxorubicin	45 ± 7	85 ± 9	107 ± 11
1:1 C ₆₀ -Dox	68 ± 9 *	145 ± 12 *	236 ± 22 *
2:1 C ₆₀ -Dox	57 ± 8 *	131 ± 21 *	234 ± 23 *

*p ≤ 0.01 in comparison with the free Doxorubicin

The obtained data demonstrated that Doxorubicin complexation with C₆₀ promoted its entry into the leukemic cells but did not affect the localization.

IV.2.2.1.2 Cell viability

The viability of different human leukemic cell lines was estimated with the MTT assay at 24, 48 and 72 h incubation with C₆₀-Dox or free Doxorubicin separately at drug-equivalent concentrations. C₆₀ alone at concentrations equivalent to those in the nanocomplexes had no effect (data not shown).

The figure 23 presents time- and concentration-dependent decrease of leukemic cells viability during Doxorubicin treatment. The drug exhibited toxicity in the nM range following the order CCRF-CEM > Jurkat > THP1 > Molt-16 (most toxic). Under action of 100 nM Doxorubicin the viability of CCRF-CEM cells was decreased to 84 ± 7, 50 ± 4 and 34 ± 7 % compared to the control at 24, 48 and 72 h, respectively. The comparable pattern of 100 nM Doxorubicin toxic effect was found in Jurkat cells. The viability of THP1 cells after treatment with 100 nM Doxorubicin cells was found to be

50 ± 4, 47 ± 5 and 13 ± 4% at 24, 48 and 72 h, respectively. Half-maximal inhibitory Doxorubicin concentrations (IC₅₀) at 72 h incubation were found to be 80 ± 9, 43 ± 5 and 38 ± 6 nM for CCRF-CEM, THP1 and Jurkat cells, respectively. Molt-16 cells were determined as the most sensitive to the drug since its toxic effect was detected in the range from 1 to 25 nM within all periods of cells incubation. The viability of Molt-16 cells treated with 5 nM Doxorubicin was decreased to 75 ± 4, 28 ± 4 and 18 ± 4% of that of control at 24, 48 and 72 h, respectively, and the value of IC₅₀ at 72 h was equal to only 2.0 nM.

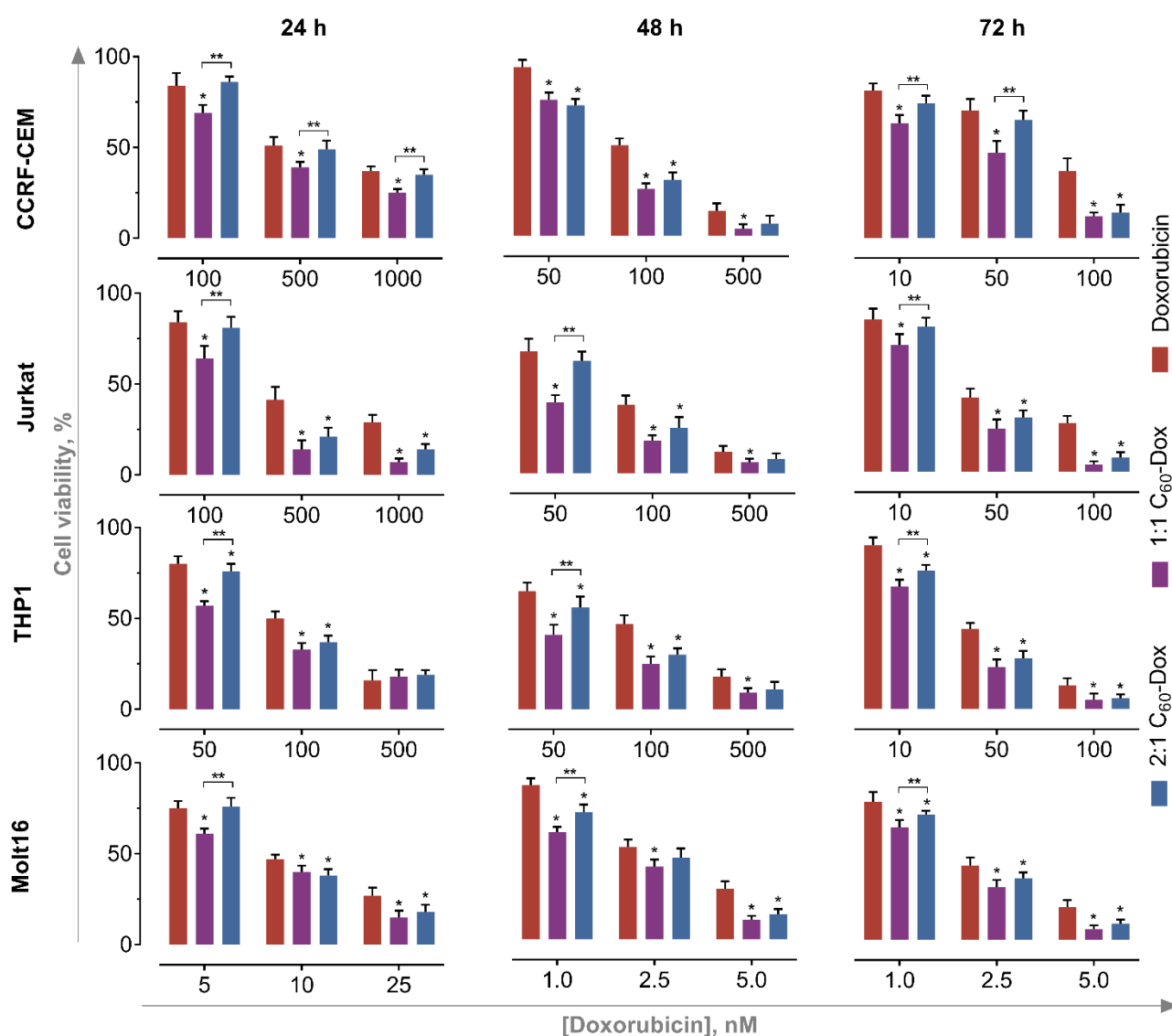


Figure 23. Viability of leukemic cells after treatment with Doxorubicin or its C₆₀-nanocomplexes: CCRF-CEM, Jurkat, THP1 and Molt16 cells were treated with equal doses of free Doxorubicin or C₆₀-Dox 1:1 and 2:1 for 24, 48 and 72 h (* – $p \leq 0.05$ in comparison with the free Doxorubicin, ** – $p \leq 0.05$ in comparison with the C₆₀-Dox 1:1).

Cells treated with free Doxorubicin were used as a control to assess the viability under action of C₆₀-Dox at the equivalent doses of the drug. The value of IC₅₀ for the free Doxorubicin and its C₆₀-nanocomplexes was calculated for each time point and cell line and listed in the table 15.

Table 15. Half-maximal inhibitory concentration (IC₅₀, nM) of free and C₆₀-bound Doxorubicin in human leukemic cell lines

<i>Cell line</i>	<i>Agent</i>	24 h	48 h	72 h
CCRF-CEM	<i>Doxorubicin</i>	579 ± 51	98 ± 7	80 ± 9
	<i>1:1 C₆₀-Dox</i>	299 ± 54	71 ± 4 *	23 ± 8 *
	<i>2:1 C₆₀-Dox</i>	543 ± 48	72 ± 5 *	32 ± 7 *
Jurkat	<i>Doxorubicin</i>	419 ± 50	75 ± 9	38 ± 6
	<i>1:1 C₆₀-Dox</i>	148 ± 19 *	35 ± 7 *	19 ± 3 *
	<i>2:1 C₆₀-Dox</i>	236 ± 33 ***	60 ± 5 *	26 ± 3 ***
THP1	<i>Doxorubicin</i>	113 ± 16	93 ± 13	43 ± 5
	<i>1:1 C₆₀-Dox</i>	57 ± 11 *	33 ± 7 *	20 ± 3 *
	<i>2:1 C₆₀-Dox</i>	77 ± 9 ***	56 ± 8 ***	21 ± 3 *
Molt-16	<i>Doxorubicin</i>	23 ± 2	2.7 ± 0.2	2.0 ± 0.1
	<i>1:1 C₆₀-Dox</i>	16 ± 2 *	1.5 ± 0.2 *	1.3 ± 0.2 *
	<i>2:1 C₆₀-Dox</i>	19 ± 2 ***	1.9 ± 0.1 ***	1.6 ± 0.1 ***

* – p ≤ 0.05 in comparison with the free Doxorubicin

** – p ≤ 0.05 in comparison with the C₆₀-Dox 1:1 nanocomplex

It was shown that both studied nanocomplexes possessed higher toxic potential compared to the free Doxorubicin against human leukemic cell lines (Fig. 23).

Thus, 100 nM C₆₀-Dox 1:1 exhibited 1.2, 1.9 and 3.1-fold enhanced toxicity against CCRF-CEM cells in comparison with the free drug at 24, 48 and 72 h, respectively. Under the treatment with 100 nM C₆₀-Dox 2:1 the decrease of CCRF-

CEM cells' viability was estimated to be on the level of 1.3 and 2.6-fold as compared with the effect of free drug at 48 and 72 h, correspondingly. The similar pattern of the drug toxicity enhancement after its complexation with C₆₀ was found in other leukemic cell lines as well (Fig. 23, Tab. 15). Thus, under the treatment with 100 nM 1:1 C₆₀-Dox the viability of Jurkat cells was further decreased on 1.3, 2.1 and 6.8 times and the viability of THP1 cells on 1.5, 1.9 and 2.6-times at 24, 48 and 72 h, respectively. Under the treatment with 100 nM C₆₀-Dox 2:1 the Jurkat cells' viability was decreased on 1.5 and 3.4 times at 48 and 72 h and the viability of THP1 cells on 1.4, 1.6 and 2.2 at 24, 48 and 72 h, respectively. The enhancement of Doxorubicin toxicity due to complexation with C₆₀ nanostructure was confirmed in experiments with Molt16 cells as well. C₆₀-Dox 1:1 (5 nM) decreased the viability on 1.2, 2.5 and 3.0 times at 24, 48 and 72 h, respectively, whereas 5 nM C₆₀-Dox 2:1 on 2.0 times at both 48 and 72 h in comparison with free 5 nM Doxorubicin.

In summary, at 72 h incubation of cells the value of IC₅₀ for 1:1 and 2:1 nanocomplexes was decreased on ≤ 3.5 and ≤ 2.5 times, correspondingly, in comparison with IC₅₀ for the free drug.

IV.2.2.2 Cellular effects of C₆₀-Berberine nanocomplexes

A wide chemical diversity of natural products presents an important source for discovery of new drugs that are potentially simple, safe, eco-friendly and low-cost in production (Shewach & Kuchta, 2009). Medicinal herbs have attracted increasing attention in the field of cancer treatment due to their potential anticancer effects. The isoquinoline quaternary alkaloid Berberine has board biological activities and potency for the application as an anticancer drug. Owing to aromatic structure of Berberine's molecule, it can be predicted that noncovalent nanocomplexes with C₆₀ would self-assemble due to π - π stacking interactions similar to Doxorubicin. To verify that idea, firstly it was important to define effects of free Berberine on the studied cellular model.

IV.2.2.2.1 Cellular effects of alkaloid Berberine alone

Intracellular accumulation

The innate green fluorescence of Berberine (Appendix 2 Figure 1) (Gumenyuk et al., 2012) enabled the assessment of its intracellular accumulation with direct fluorescence microscopy. Exposure of CCRF-CEM cells to 50 μM Ber for 4 h resulted in intracellular green fluorescence (Fig. 24 A), suggesting its effective intracellular accumulation. Simultaneously cells were subjected to live-staining with the blue-fluorescent DNA-binding dye Hoechst 33342. The single cell fluorescence intensity profiles were estimated for 150 pixels along the yellow lines, pointed on the image “Merged” of CCRF-CEM cells, treated with 50 μM Berberine for 4 h (Fig. 24 A).

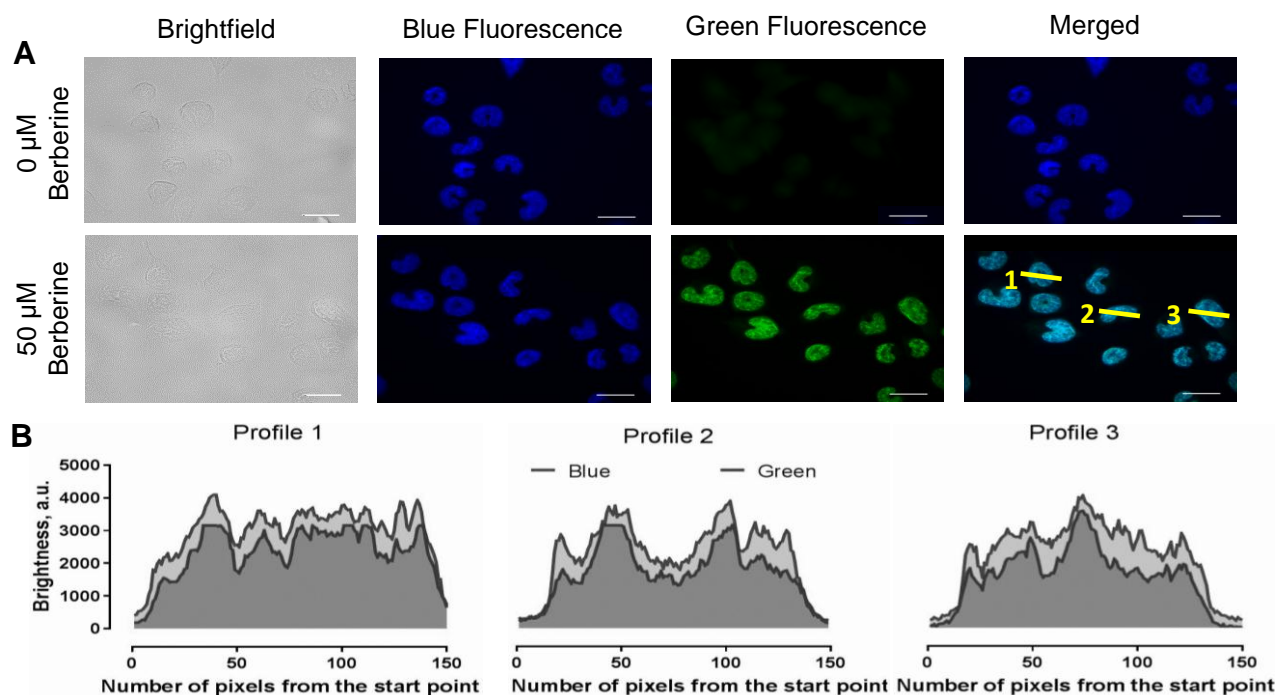


Figure 24. Berberine intracellular localization: A – bright field and fluorescence images of CCRF-CEM cells, incubated for 4 h with 50 μM Berberine, scale bar 20 μm ; B – Single cell fluorescence profile along yellow lines 1, 2 and 3, pointed on the “Merged” fluorescence image, a.u. = arbitrary units.

The fluorescence intensity profiles showed that the green fluorescence signal from Berberine entirely mimicked Hoechst 33342 blue signal distribution (Fig. 24 B), demonstrating that Berberine was concentrated in the cell nucleus. The data suggest that 50 μM Berberine binds DNA of CCRF-CEM cells upon *in vitro* conditions, what

could be linked with its anticancer activity (Franceschin et al. 2006, Arora et al. 2008, Wang et al. 2011b, Li et al. 2013, Ortiz et al. 2014).

Cell viability

The viability of CCRF-CEM cells, exposed to Berberine at concentrations ranging from 0 to 200 μM , was monitored within 72 h of incubation. Cell viability was estimated with the MTT assay and expressed as % of untreated control cells (Fig. 25). Berberine has shown a dose- and time-dependent toxicity against CCRF-CEM cells. Berberine concentration of 10-50 μM induced cytotoxicity, proportional to the incubation time. CCRF-CEM cells under action of 20 μM Berberine showed the viability in $86 \pm 6\%$, $69 \pm 7\%$ and $60 \pm 6\%$ of untreated control cells at 24, 48 and 72 h, respectively. The highest tested Berberine concentration (200 μM) had an acute cytotoxic effect at all time-points with almost no detectable cell viability.

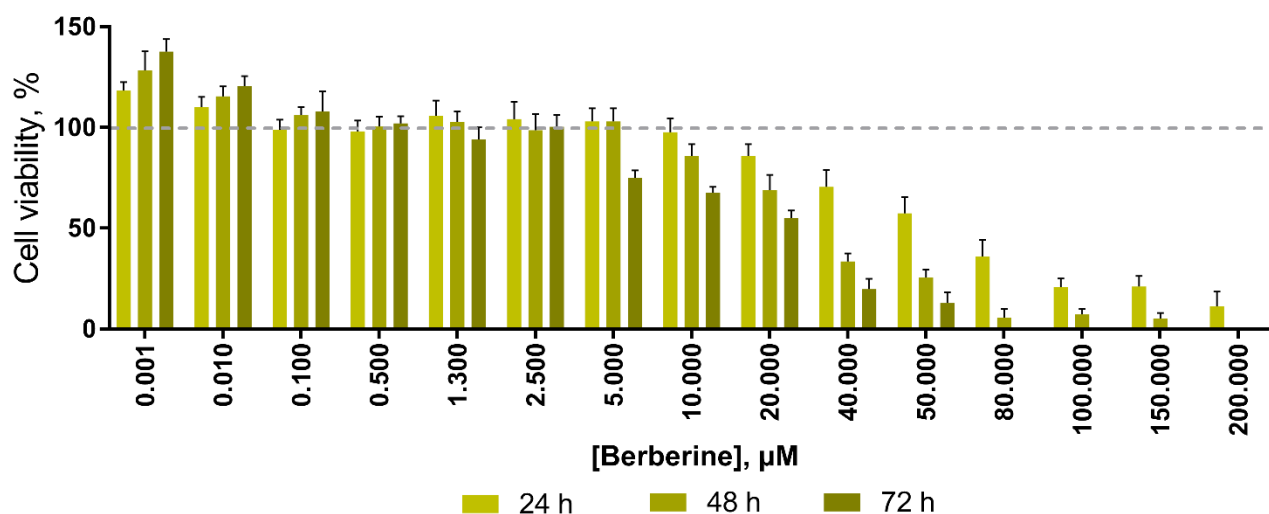


Figure 25. Viability of CCRF-CEM cells, treated with 1-200 μM Berberine during 24, 48 and 72 h.

IC_{50} of Berberine was estimated to be 58 ± 5 , 23 ± 2 and 19 ± 2 μM at 24, 48 and 72 h, respectively. Presented results demonstrate that Berberine exhibits significant cytotoxic effects against human leukemic cells.

Intracellular reactive oxygen species generation

The intracellular level of generated ROS in CCRF-CEM cells after 5 h exposure to 0-25 μM Berberine was estimated by an oxidative-sensitive fluorescence dye DCFH-DA. Increasing concentrations of Berberine administered to the cells provoked an increase of intracellular ROS generation – up to more than double (Fig. 26 A2). In parallel an increase of the green fluorescence, proportionally to Berberine concentration, was observed with fluorescence microscopy (Fig. 26 A1).

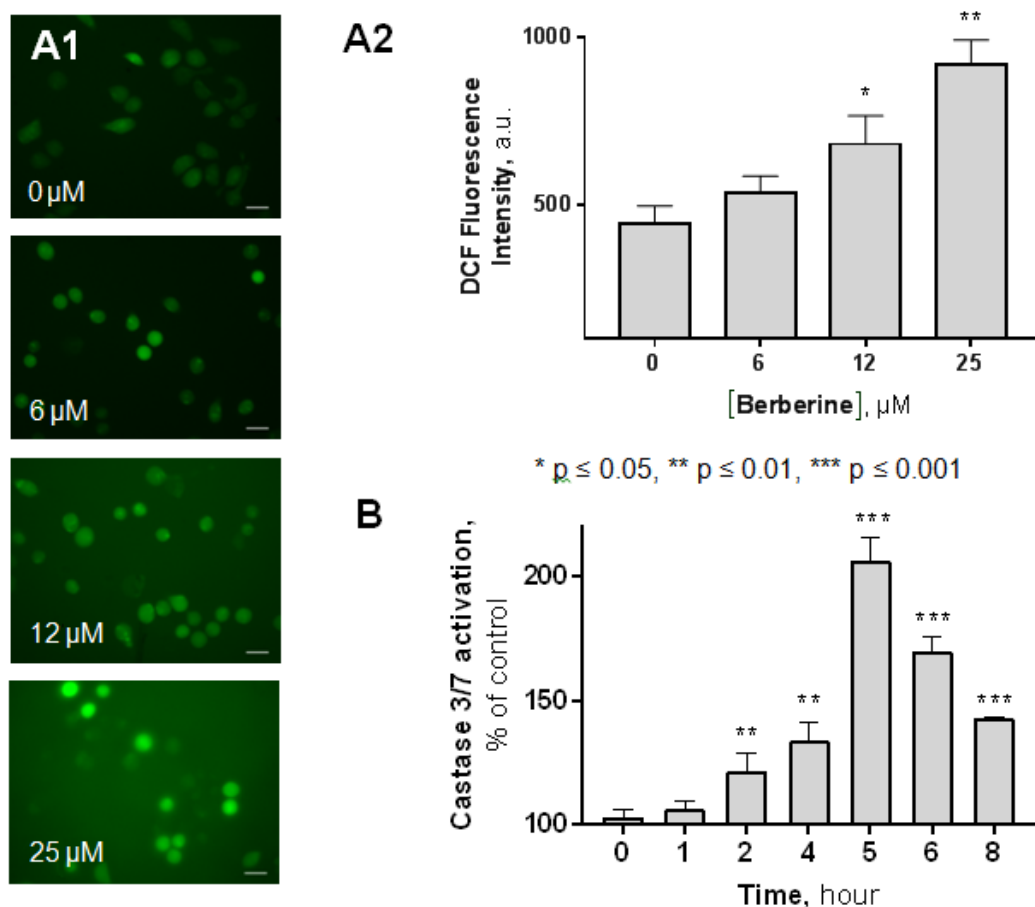


Figure 26. Berberine proapoptotic effects on CCRF-CEM cells. Intracellular ROS generation of CCRF-CEM cells, exposed to 0, 6, 12 and 25 μM Berberine for 5 h: A1 – Fluorescence microscopy of CCRF-CEM cells after 50 min incubation with DCFH-DA, scale bar 20 μm , A2 – Fluorescence intensity of CCRF-CEM cells after 40 min incubation with DCFH-DA, a.u. = arbitrary units; B – Caspase 3/7 activity of CCRF-CEM cells, treated with 25 μM Berberine for 0-8 h.

Apoptosis induction

ROS are increasingly recognized as important initiators and mediators of apoptosis suggesting that Berberine could finally activate the caspase cascade. Therefore, it was determined whether Berberine-induced cell-death is mediated through caspase-3/7. Berberine (25 μM) caused a time-dependent increase of the caspase-3/7 activity (Fig. 26 B), suggesting apoptotic death type mechanisms. Caspase 3/7 activity reached maximum in 210% of control after cells treatment the with 25 μM Berberine for 5 h.

To investigate further a possible proapoptotic effect of Berberine, CCRF-CEM cells were subjected to double staining with Annexin V-FITC/PI (Fig. 27).

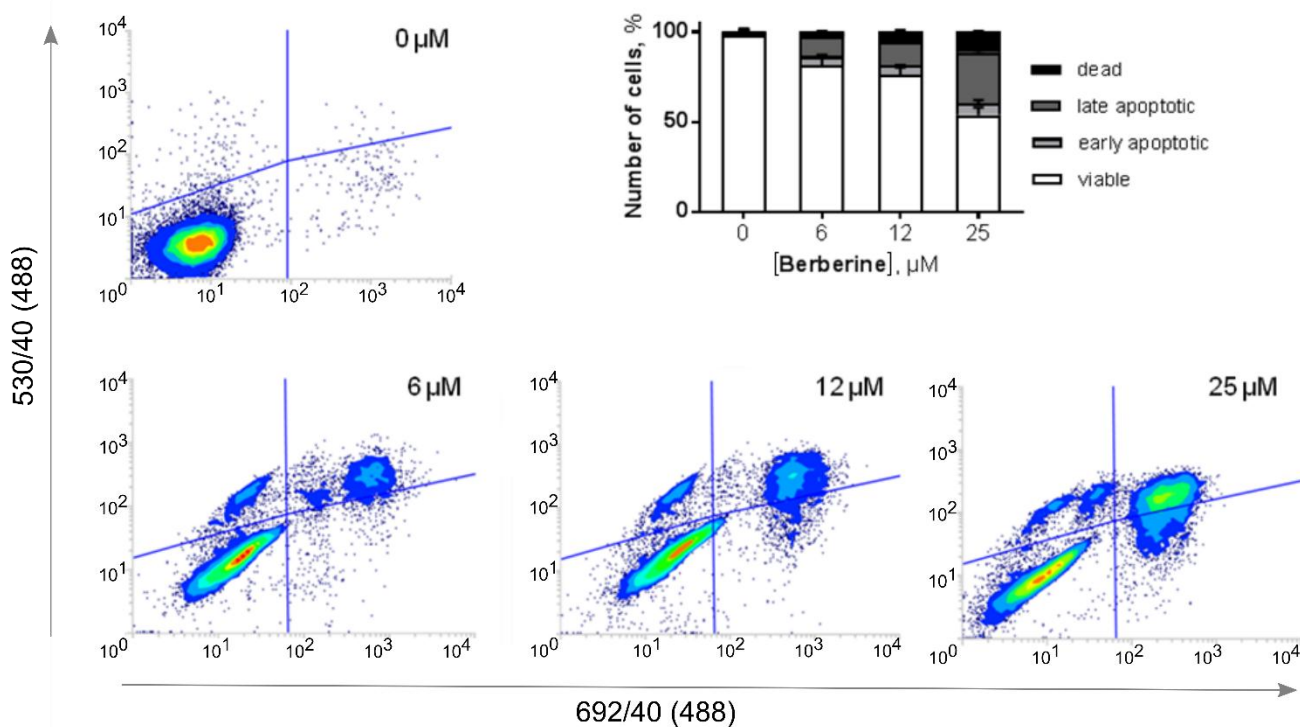


Figure 27. Detection of apoptotic CCRF-CEM cells, treated with Berberine, with Annexin V-FITC/PI double staining: FACS histograms and quantitative analysis of cell populations content, differentiated with Annexin-FITC/PI staining of CCRF-CEM cells treated with 0-25 μM Berberine. (FACS histograms: in each panel the lower left quadrant shows the content of viable, upper left quadrant – early apoptotic, upper right quadrant – late apoptotic, lower right quadrant – necrotic cells populations).

A statistics summary report is illustrated in the figure 27. Untreated control cells showed high viability of $95 \pm 3\%$. Incubation of CCRF-CEM cells with 6 μM

Berberine for 24 h resulted in apoptotic cell population growth up to $16 \pm 2\%$ compared to $4 \pm 1\%$ of control cells. Further Berberine concentration increase caused escalated appearance of both apoptotic and dead cells. The percentage of apoptotic cells treated with 12 and 25 μM Berberine were found to be $18 \pm 2\%$ and $35 \pm 3\%$, and dead cells accounted 6 ± 1 and $11 \pm 2\%$ of the population, respectively.

These findings support the suggested apoptotic cell death induction in leukemic cells under action of herbal alkaloid Berberine.

IV.2.2.2.2 Cellular effects of C₆₀-Berberine nanocomplexes

Taking into account obtained higher IC_{50} and limited water solubility of Berberine as compared with Doxorubicin, C₆₀-Ber nanocomplexes (C₆₀-Ber) were synthesized with one extra molar ratio – 2:1 (on top of 1:1 and 1:2) that provided the opportunity to study a higher Berberine concentrations.

Intracellular accumulation

Strong absorption and fluorescence (Appendix 2 Figure 1) (Gumenyuk et al., 2012) of the Berberine molecule in the visible spectral region enables the tracking of its nanocomplexes with non-invasive direct fluorescence-based techniques. CCRF-CEM cells were incubated in the presence of 10 μM Berberine or C₆₀-Ber for 0, 1, 3 and 6 h and examined with both fluorescence microscopy and flow cytometry to visualize and quantify the intracellular Berberine uptake. Autofluorescence of the untreated cells was used as a negative control. The mean fluorescence intensity of each sample were calculated from logarithmic FACS histograms by the respective value of Berberine green fluorescence signal ($\lambda_{\text{ex}} = 488 \text{ nm}$, $\lambda_{\text{em}} = 530/40 \text{ nm}$) (Tab. 16).

Fluorescence microscopy demonstrated a time-dependent accumulation of 10 μM Berberine in CCRF-CEM cells (Fig. 28 B). According to the literature data Berberine was localized in mitochondria (Pereira et al., 2007) and effectively bound DNA, suggesting its high nuclear affinity (Wang et al., 2011b; Zhang et al., 2013).

Once Berberine was complexed with C_{60} the observed fluorescence intensities were enhanced. Microscopy images demonstrated that C_{60} -Ber were internalized faster and more efficiently in comparison with free Berberine (Fig. 28 B).

Table 16. Mean fluorescence intensity (FI) of the intracellular accumulated Berberine

<i>FI, arbitrary units</i>	<i>1 h</i>	<i>3 h</i>	<i>6 h</i>
<i>Berberine</i>	39 ± 3	45 ± 3	57 ± 5
<i>1:2 C₆₀-Ber</i>	38 ± 2	49 ± 4	80 ± 7 *
<i>1:1 C₆₀-Ber</i>	42 ± 4	59 ± 5 *	79 ± 6 *
<i>2:1 C₆₀-Ber</i>	38 ± 3	57 ± 6 *	81 ± 6 *

* $p \leq 0.01$ in comparison with the free Berberine

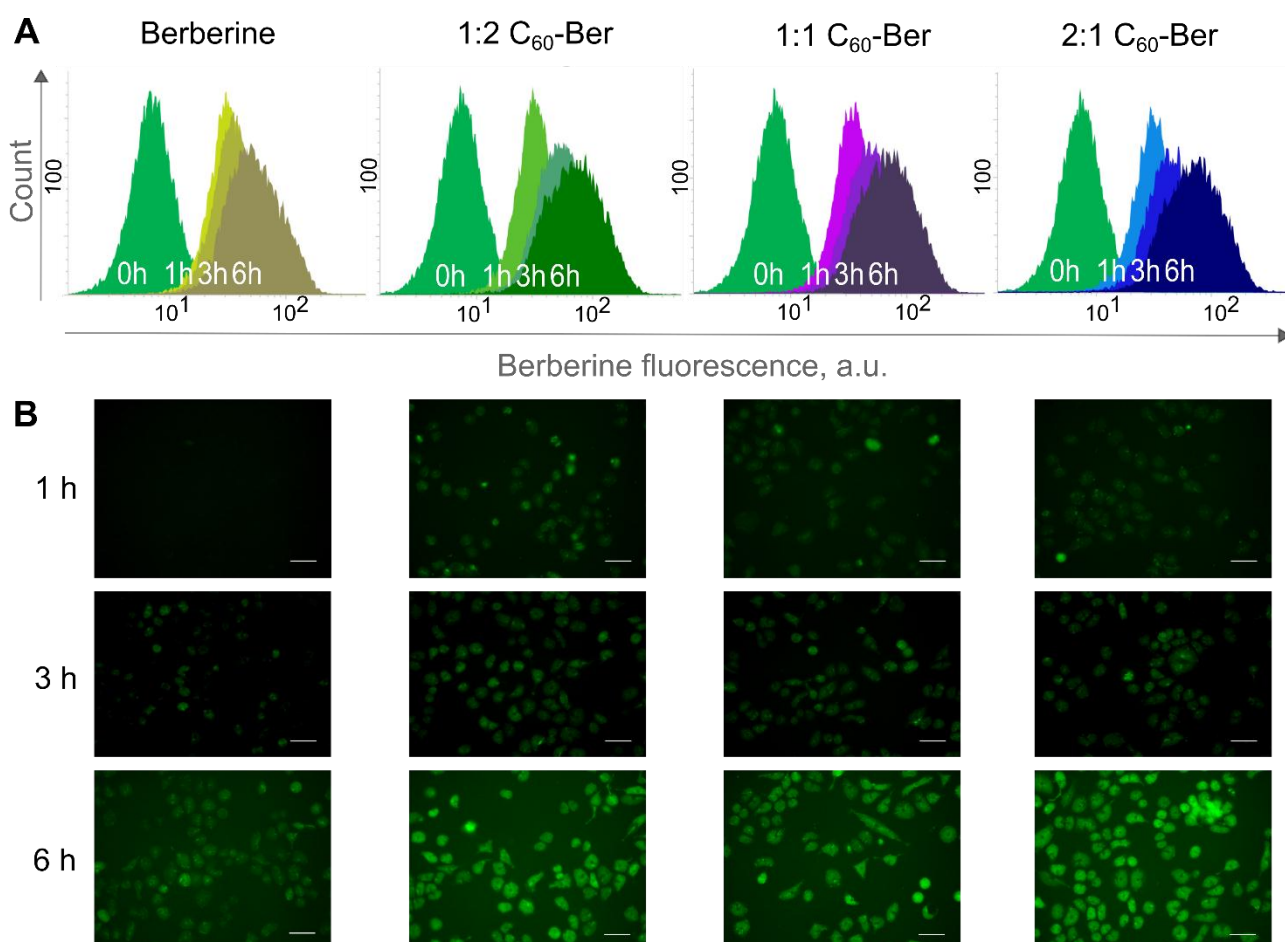


Figure 28. Intracellular accumulation of free Berberine and C_{60} -Ber in a Berberine-equivalent concentration: flow cytometry (A) and fluorescence microscopy (B) of CCRF-CEM cells incubated with 10 μM Berberine and C_{60} -Ber at the molar ratios 1:2, 1:1 and 2:1, scale bar 20 μm .

The mean fluorescence intensity of the CCRF-CEM cells (Fig. 28 A), treated with 1:2 C_{60} -Ber at 10 μM Berberine-equivalent concentration was found to be

increased by 31% at 6 h. In cells treated with C₆₀-Ber at 1:1 and 2:1 molar ratios the fluorescence signal reached the level of 130 and 140% from the control at 3 and 6 h, respectively (Tab. 16). The data obtained showed that Berberine complexation with C₆₀ strongly promoted its cellular uptake.

Cell viability

To evaluate the effect of Berberine on proliferation, CCRF-CEM cells were treated with Berberine and C₆₀-Ber in increasing concentrations for 12, 24 and 72 h; cell viability was evaluated with the MTT assay. Increasing concentrations of Berberine inhibited cell growth in a time- and dose-dependent manner (Fig. 29).

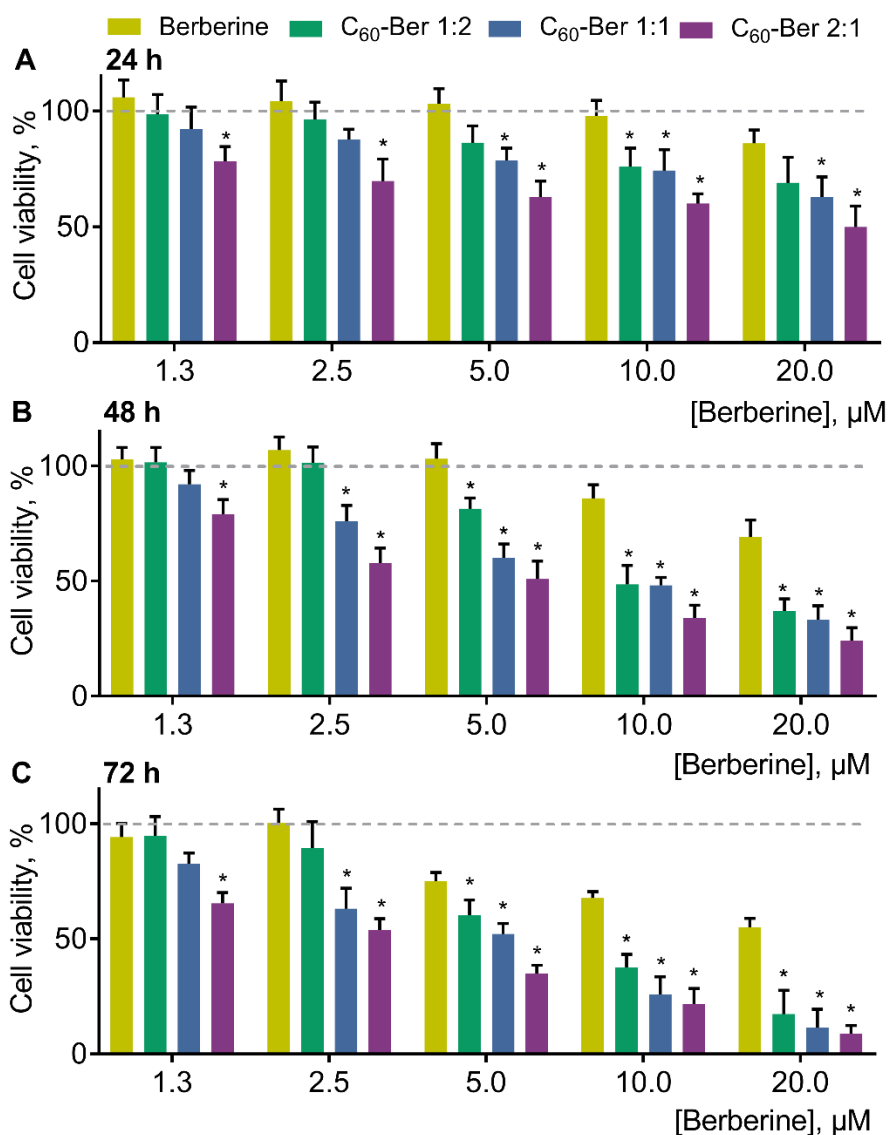


Figure 29. Viability of CCRF-CEM cells, treated with a free or C₆₀-complexed Berberine: for 24 (A), 48 (B) and 72 (C) h (* $p \leq 0.01$ in comparison with the free Berberine).

The number of viable cells gradually decreased under the action of Berberine in the concentration range 1.3-20 μM . Thus, 10 μM Berberine decreased CCRF-CEM cell viability to $71 \pm 9\%$ and $50 \pm 6\%$ of the control at 48 and 72 h, respectively.

All C_{60} -Ber exhibited stronger antiproliferative potential towards CCRF-CEM cells in comparison with the free Berberine. It should be noted, that C_{60} alone at concentrations equivalent to those used in nanocomplexes had no significant effect on cell viability (data not shown). With the increase of C_{60} concentration in C_{60} -Ber a higher toxic potential towards CCRF-CEM cells was observed, following the order $1:2 < 1:1 < 2:1$ (the most toxic). Thus, at 24, 48 and 72 h 10 μM 1:2 C_{60} -Ber decreased cell viability to $76 \pm 8\%$, $49 \pm 8\%$, $26 \pm 7\%$, 1:1 C_{60} -Ber – to $74 \pm 9\%$, $48 \pm 3\%$, $25 \pm 7\%$, and 2:1 C_{60} -Ber – to $60 \pm 4\%$, $34 \pm 6\%$, $22 \pm 7\%$ of the control, respectively (Fig. 29).

The calculated IC_{50} values for the free and C_{60} -complexated Berberine, listed in the table 17, evidenced the C_{60} -dependent enhancement of Berberine cytotoxicity. Thus, at 24 h the IC_{50} value for Berberine after complexation with C_{60} at the molar ratio 1:2, 1:1 and 2:1 was decreased by 1.3, 1.8 and 2.8 times, respectively; at 48 h – by 2.1, 2.9 and 4.6 times, respectively; at 72 h – by 3.2, 4.8 and 6.3 times, respectively (Tab. 17).

Table 17. Half-maximal inhibitory concentration (IC_{50} , μM) of the free Berberine and C_{60} -Ber towards CCRF-CEM cells

	24 h	48 h	72 h
<i>Berberine</i>	58 ± 5	23 ± 2	19 ± 2
<i>1:2 C₆₀-Ber</i>	44 ± 4 *	11.0 ± 1.2 *	6.0 ± 0.4 *
<i>1:1 C₆₀-Ber</i>	33 ± 3 *	8.0 ± 0.7 *	4.0 ± 0.3 *
<i>2:1 C₆₀-Ber</i>	21 ± 2 *	5.0 ± 0.6 *	3.0 ± 0.2 *

* $p \leq 0.01$ in comparison with the free Berberine

Taken together these data indicate that the enhanced cytotoxic effect of C_{60} -Ber can be linked to the increased alkaloid's accumulation in leukemic cells.

Apoptosis induction

To determine whether C₆₀-Ber induced apoptosis, cell cycle distribution and caspase 3/7 activity in CCRF-CEM cells were monitored (Fig. 30 and 31). The analysis of flow cytometric cell cycle distribution indicated on the accumulation of cells in sub G1-phase upon complexation of Berberine with C₆₀. Control cells were characterized with $1.94 \pm 0.51\%$ cells in sub G1-phase. CCRF-CEM cells treated with 10 μM Berberine for 12 h showed slight increase of sub G1-cells to $3.48 \pm 0.89\%$. The treatment of CCRF-CEM cells with 1:2, 1:1 and 2:1 C₆₀-Ber was followed with increase of sub G1-phase to 10.8 ± 1.2 , 10.5 ± 1.9 and $16.3 \pm 1.0\%$, respectively (Fig. 30).

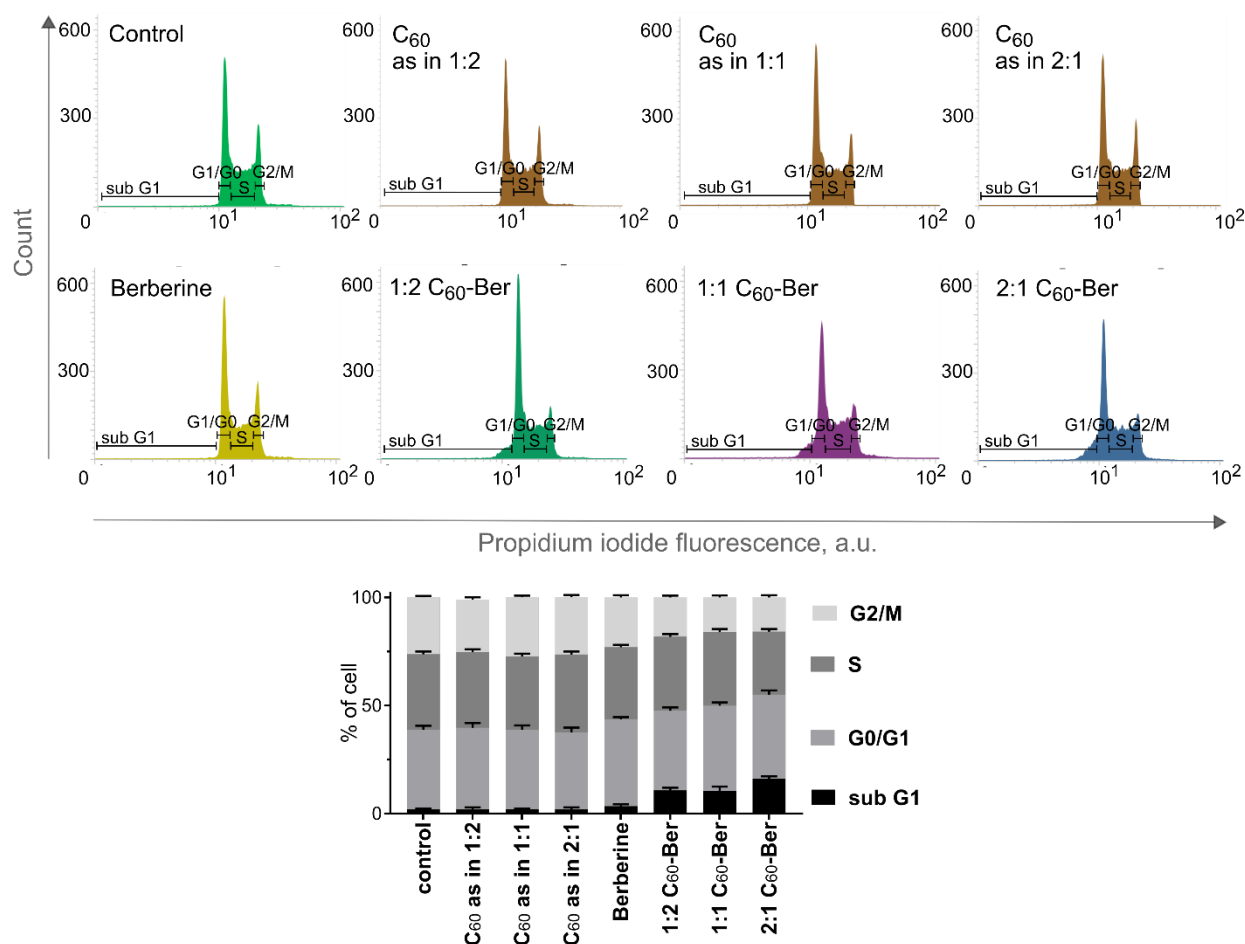


Figure 30. Cell cycle analysis in CCRF-CEM cells, incubated for 24 h after treatment with either free 10 μM Berberine or C₆₀-Ber at Berberine-equivalent concentration. The bar graph depicts the mean percentage of each cell cycle phase.

In cells treated with C₆₀-Ber caspase 3/7 activation was detected starting from 6 h, that reached $170\text{-}178 \pm 11\text{-}14\%$ of control at 24 h (Fig. 31). In contrast cells treated

with the free Berberine were characterized with a delayed caspase 3/7 activation by $35 \pm 8\%$ from the control at 24 h. The activation of caspase 3/7 cells pointed on the induction of apoptotic death of CCRF-CEM cells treated with C₆₀-Ber.

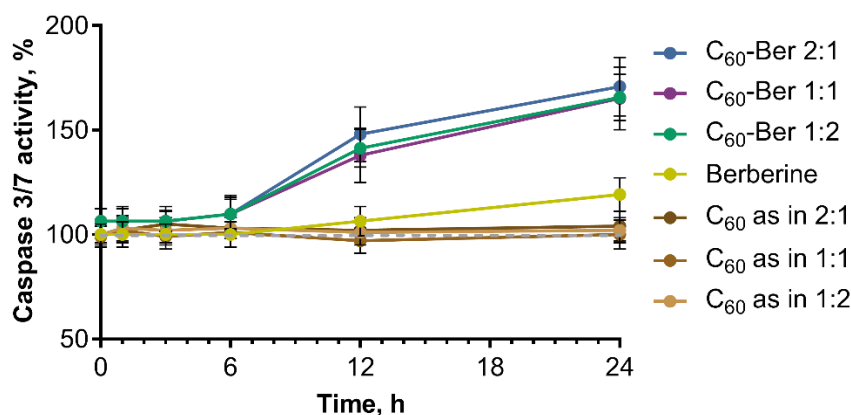


Figure 31. Caspase 3/7 activity in CCRF-CEM cells, incubated for 24 h under treatment with either free or C₆₀-complexated Berberine at 10 μ M equivalent concentration (caspase 3/7 activity of untreated cells is set to 100%).

IV.3 Towards photodynamic chemotherapy with C₆₀-drug nanocomplexes

IV.3.1 C₆₀-Doxorubicin nanocomplexes

IV.3.1.1 Cell viability

For cytotoxicity studies free C₆₀, Doxorubicin or C₆₀-Dox in 50, 150 and 450 nM Doxorubicin-equivalent concentrations were added to the leukemic cells at time point 0 h. At 24 h cells were illuminated with 405 nm LED light and after additional 24 h of incubation cell viability was estimated with the MTT assay. The viability of cells incubated without any treatment was taken as 100% (control).

No effect of C₆₀ introduced alone on leukemic cell viability was detected, while the concentration-dependent toxic effect of the free Doxorubicin was observed. After the treatment with 50, 150 and 450 nM Doxorubicin cell viability was decreased to $81 \pm 5\%$, $70 \pm 3\%$ and $49 \pm 5\%$, correspondingly (Fig. 32). When cells were treated in the dark with the C₆₀-Dox at Doxorubicin-equivalent concentrations the further increase of the Doxorubicin toxicity by 10-20% (Fig. 32) and the decrease of its half-maximal inhibitory concentration (Tab. 18) were observed. These data denote C₆₀'s ability to facilitate intracellular Doxorubicin accumulation (Fig. 22) and, therefore, potentiate its toxic effects. Not any effect of the light irradiation alone on viability of

cells either untreated (data not presented) or treated with free 50, 150 and 450 nM Doxorubicin could be detected (Fig. 32). The phototoxic potential of C_{60} was examined at nanomolar concentrations. The slight statistically valid decrease of cell viability after irradiation of cells treated with C_{60} was observed only at 900 nM and 10 J/cm² light fluence (Fig. 32 B).

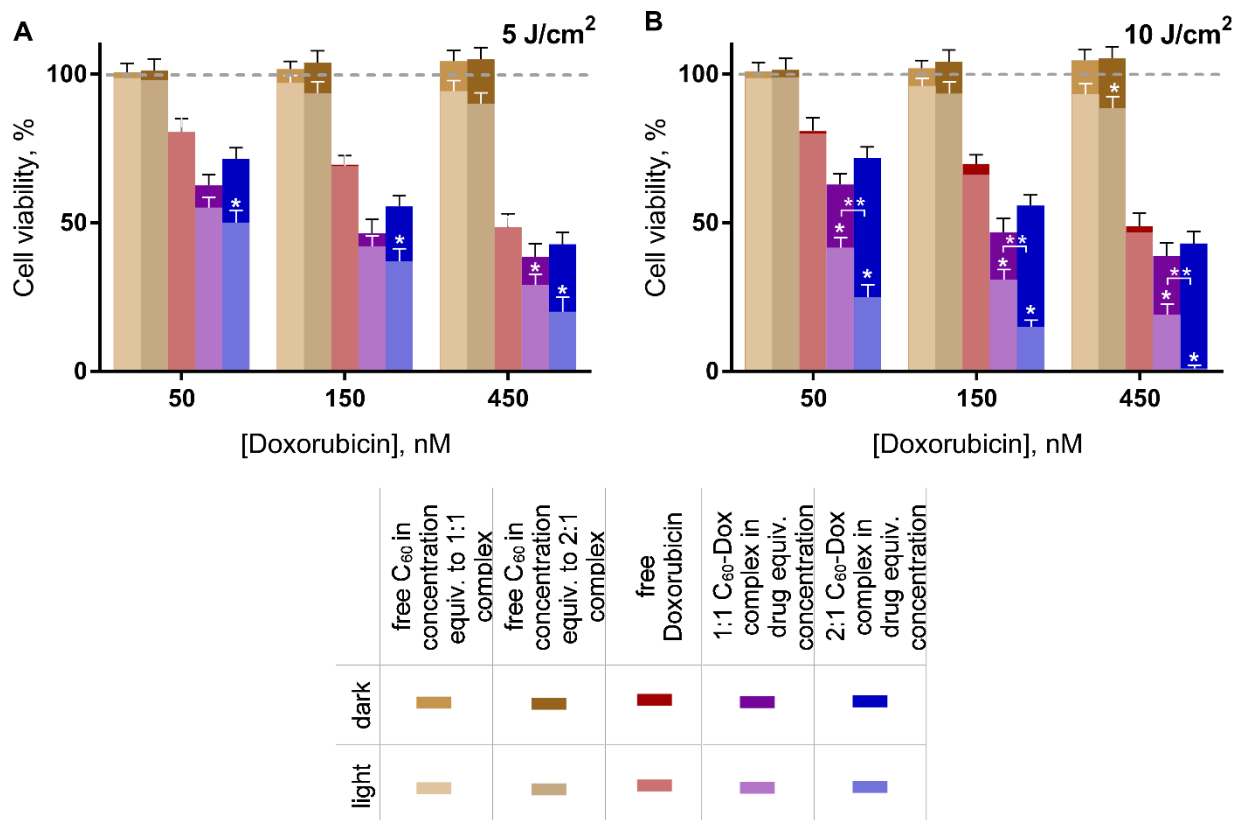


Figure 32. Viability of CCRF-CEM cells under action of photoexcited C_{60} -Dox: cells were treated with either C_{60} and Doxorubicin alone or C_{60} -Dox in Doxorubicin-equivalent concentrations and incubated in dark (dark columns) or after light irradiation with 405 nm LED (pale columns) at 5 J/cm² (A) or 10 J/cm² (B) (* $p \leq 0.01$ in comparison with the respective dark control, ** $p \leq 0.01$ in comparison with the photoexcited 1:1 nanocomplex).

After combined treatment with C_{60} -Dox and light the cells viability as well as the IC_{50} values were considerably decreased. The toxic effect was dependent on the light fluence and C_{60} concentration in the nanocomplex. Thus, the decrease of cell viability after the treatment with 1:1 C_{60} -Dox and 5 J/cm² light was observed only when the nanocomplex was used at 450 nM C_{60} equivalent concentration (Fig. 32 A). When the light fluence was increased up to 10 J/cm² the pronounced phototoxic effect became evident at all studied concentrations of 1:1 C_{60} -Dox (Fig. 32 B) and IC_{50} value appeared to be 3 and 9 times lower as compared with the IC_{50} for non-irradiated 1:1 C_{60} -Dox and for free Doxorubicin, respectively (Tab. 18).

Table 18. IC₅₀ (nM) values for the photoexcited free and C₆₀-complexated Doxorubicin

	<i>dark</i>	<i>5 J/cm²</i>	<i>10 J/cm²</i>
<i>Doxorubicin</i>	390 ± 56	382 ± 53	336 ± 49
<i>1:1 C₆₀-Dox</i>	135 ± 29	86 ± 19	44 ± 7 *
<i>2:1 C₆₀-Dox</i>	225 ± 34 **	64 ± 11 *	25 ± 4 **.*

*p ≤ 0.01 in comparison with the respective dark control, **p ≤ 0.01 in comparison with the 1:1 nanocomplex

The viability of cells treated with 2:1 C₆₀-Dox and irradiated with 5 J/cm² light was decreased substantially in a concentration dependent manner. The most significant toxic effect was observed after the treatment with 2:1 C₆₀-Dox and irradiation with 10 J/cm² light, when the IC₅₀ values was estimated to be 9 and 16 times lower as compared with the IC₅₀ for non-irradiated 2:1 C₆₀-Dox and for the free Doxorubicin, correspondingly (Tab. 18). If to compare with photodependent toxicity of C₆₀ alone towards CCRF-CEM cells at the same conditions, IC₅₀ of photoexcited 2:1 C₆₀-Dox was 7×10³-fold decreased. No signs of appreciable viability were detected when cells were treated with 2:1 C₆₀-Dox at 900 nM C₆₀ equivalent concentration and irradiated with 10 J/cm² light (Fig. 32 B).

To characterize pharmacodynamics interactions between photodynamic treatment and drug delivery with C₆₀ the values of combination index (CI, Tab. 19) were assessed. When cells were co-treated with C₆₀-Dox and 405 nm light at 5 J/cm² fluence the values of CI indicated a synergistic effect. While after co-treatment with 1:1 and 2:1 C₆₀-Dox and light at 10 J/cm² fluence the CI value proved strong and very strong synergistic effect, respectively, of the photoexcited C₆₀ and C₆₀-delivered Doxorubicin in applied bimodal strategy of cells treatment.

Table 19. Combination index of interaction between phototoxic effects of C₆₀ and non-irradiated C₆₀-Dox¹

<i>CI</i>	<i>5 J/cm²</i>	<i>10 J/cm²</i>
<i>1:1 C₆₀-Dox</i>	0.546 (synergism)	0.130 (strong synergism)
<i>2:1 C₆₀-Dox</i>	0.316 (synergism)	0.098 (very strong synergism)

¹This was measured after cells co-treatment with C₆₀-Dox and LED light irradiation. Classification of interaction was determined according to (Chou, 2006)

Next the intracellular ROS generation, ATP level and the markers of apoptotic death were assessed in CCRF-CEM cells after combined treatment with C₆₀-Dox and light.

IV.3.1.2 Intracellular reactive oxygen species generation

The efficient and continuous intracellular ROS production is considered to be a critical step in realization of photoexcited C₆₀ anticancer effect (Fig. 15) (Prylutska et al., 2010; Grynyuk et al., 2013). ROS generation in cells, treated with nanocomplexes, was evaluated with the use of the fluorescence dye DCFH-DA (Myhre et al., 2003; Eruslanov & Kusmartsev, 2010) at 1 and 3 h of incubation in dark or after 405 nm light irradiation at 10 J/cm² fluence. A minor increase of the fluorescence signal was detected during the incubation of the control untreated cells (Fig. 33).

No reliable changes in ROS generation in comparison with the control were observed when 450 or 900 nM C₆₀ was applied alone. Treatment with the free 450 nM Doxorubicin or C₆₀-Dox was followed by a slight increase of ROS generation at 1 h that was attenuated at 3 h (Fig. 33 A). But when cells treated with the free C₆₀ or C₆₀-Dox were irradiated with 405 nm light the ROS production intensified at both 1 and 3 h (Fig. 33 C). In cells treated with 1:1 or 2:1 C₆₀-Dox ROS levels at 3 h after irradiation exceeded the control level by 3.8 and 5.0 times, correspondingly.

The analysis of the fluorescence microscopy images (Fig. 33 B and D) confirmed the obtained quantitative data on intense ROS production in cells after the treatment with photoexcited C₆₀-Dox and supports oxidative stress as a precondition of toxicity of the applied treatment.

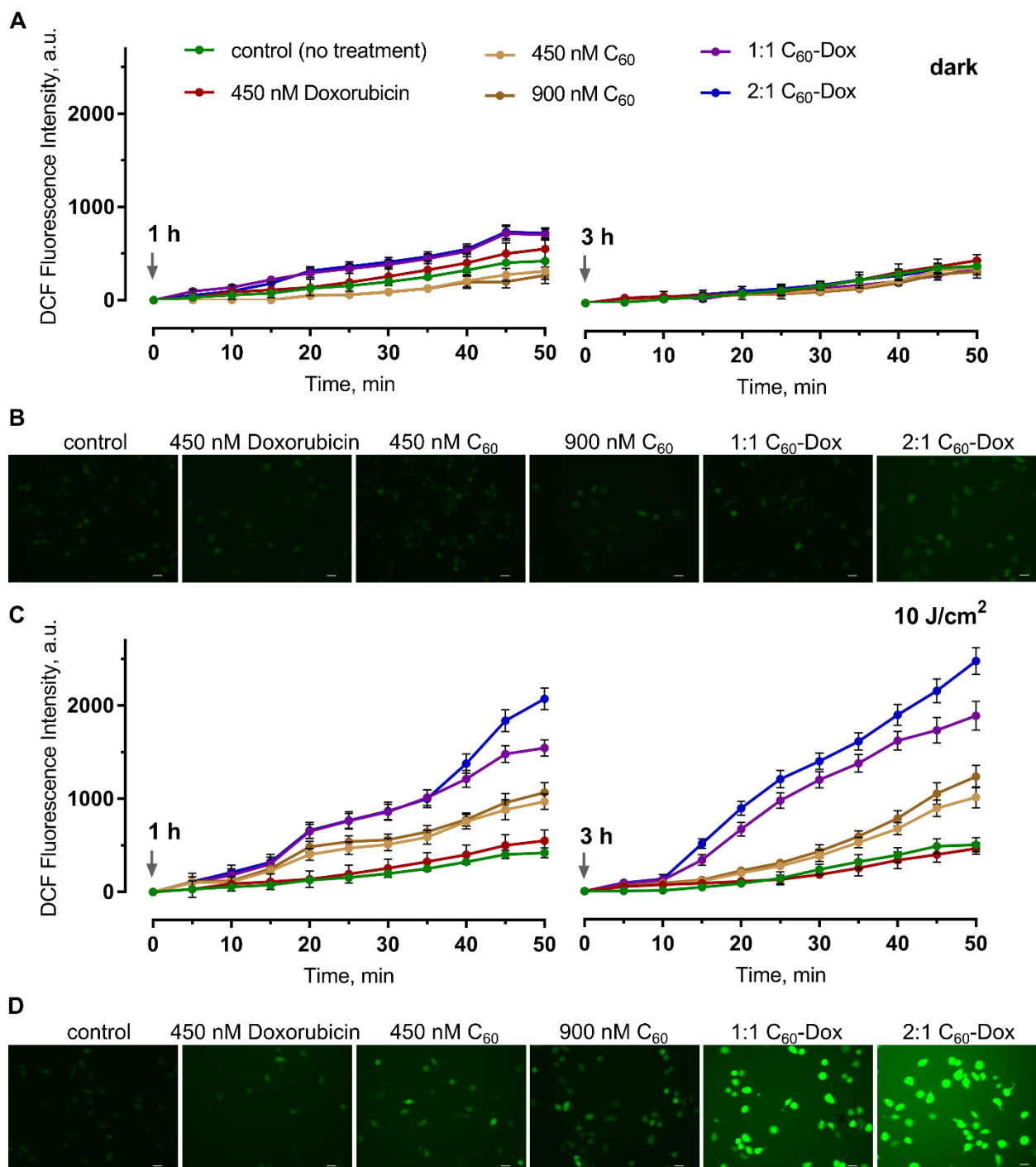


Figure 33. ROS generation in CCRF-CEM cells treated with C_{60} -Dox and light irradiation: the dynamics of ROS generation in cells at 1 and 3 h after the treatment in dark (A) or irradiation with 10 J/cm² 405 nm LED (C), a.u. = arbitrary units; the fluorescence microscopy images of cells at 3 h after the treatment in dark (B) or light irradiation (D) and further 60 min incubation with DCFH-DA, scale bar 20 μ m.

IV.3.1.3 Apoptosis induction

Next it was assessed whether the treatment of cells with C_{60} -Dox and light affected ATP production as the main function of mitochondria. Neither free C_{60} and

Doxorubicin nor light irradiation alone had any effect on the ATP level in CCRF-CEM cells (Fig. 34 A).

In cells treated with 1:1 and 2:1 C₆₀-Dox ATP level was slightly decreased to 84 ± 5% and 87 ± 3% of the control, respectively. The appreciable drop in intracellular ATP level to 30 ± 4% and 28 ± 3% was observed after 10 J/cm² light irradiation of cells treated with 1:1 and 2:1 C₆₀-Dox, respectively (Fig. 34 A), indicating inhibition of mitochondria function that could be attributed to an impaired redox balance.

Apoptotic program execution requires the coordinated activation of multiple subprograms including caspases cascade (Fesik, 2005). The executive caspase 3/7 activation and phosphatidylserine translocation into the outer layer of plasma membrane lipid bilayer were evaluated as markers of apoptotic cell death. No effect of either free C₆₀ or Doxorubicin as well as of light irradiation alone on caspase 3/7 was observed following 3 h of cells incubation. Irradiation of cells treated with 450 or 900 nM C₆₀ was followed by 1.9- fold and 1.6- fold increase of caspase 3/7 activity, respectively, while after irradiation of cells treated with 1:1 or 2:1 C₆₀-Dox a 4.7- and 5.8-fold increase of caspase 3/7 activity was observed (Fig. 34 B).

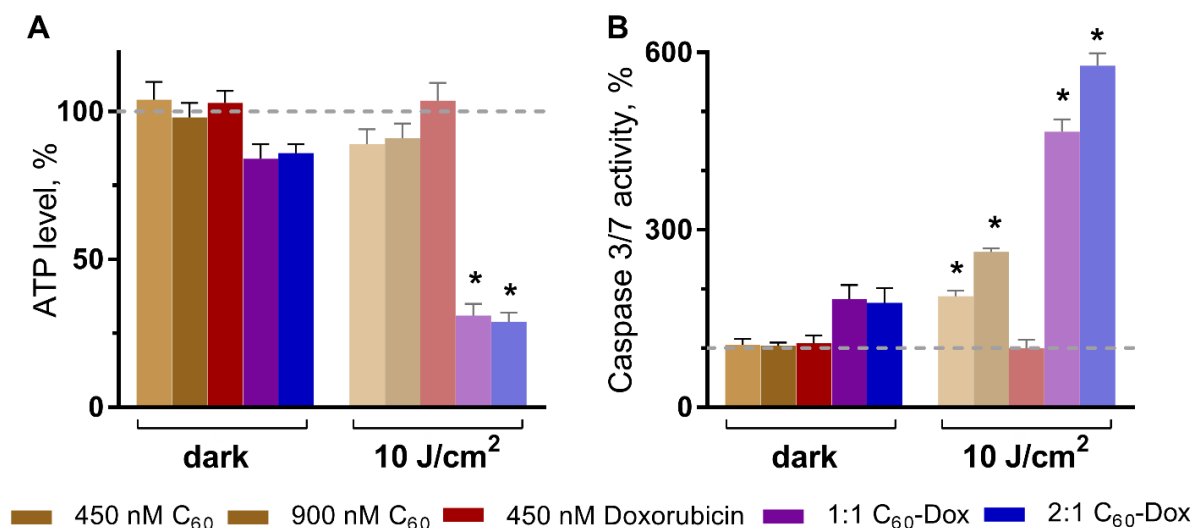


Figure 34. ATP level (A) and caspase 3/7 activity (B) in CCRF-CEM cells at 3 h after treatment. Treatment was done with either free C₆₀ and Doxorubicin or C₆₀-Dox in dark or after irradiation with 10 J/cm² 405 nm LED light (*p ≤ 0.01 in comparison with the respective dark control).

Finally, the exposure of phosphatidylserine on the cell surface was studied. Flow cytometry was used to differentiate the cells stained with Annexin V-FITC and PI. On FACS histograms (Fig. 35 A) cell distribution at 6 h after the treatment with either free

C_{60} and Doxorubicin or C_{60} -Dox is presented according to the green (Annexin V-FITC) and red (PI) fluorescence intensities.

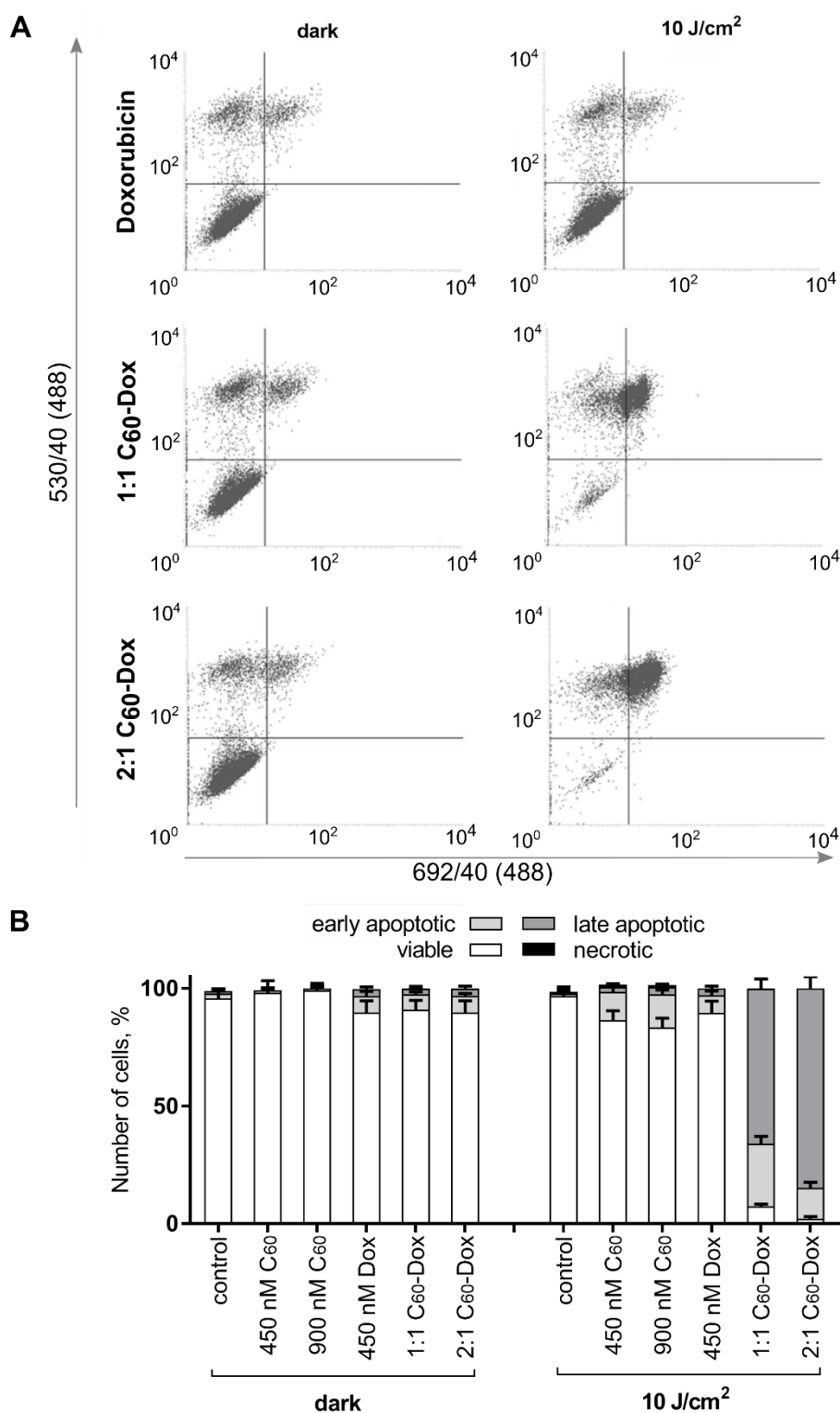


Figure 35. Cell death differentiation in CCRF-CEM treated with C_{60} -Dox and light irradiation: FACS histograms (A) and quantitative analysis (B) of cell populations content, differentiated with Annexin-FITC/PI staining at 6 h after 405 nm light irradiation of CCRF-CEM cells treated with or without free or C_{60} -complexated Doxorubicin (FACS histograms: in each panel the lower left quadrant shows the content of viable, upper left quadrant – early apoptotic, upper right quadrant – late apoptotic, lower right quadrant – necrotic cells populations).

Viable, early apoptotic, late apoptotic and necrotic cells in their quantitative populations analyses are presented in the figure 35 B. Neither treatment with C₆₀ nor 405 nm light irradiation alone had significant effects on cells distribution profiles (FACS histograms are not shown). A slight increase of early apoptotic cells was observed after treatments with free Doxorubicin, C₆₀-Dox or photoexcited C₆₀. When cells treated with C₆₀-Dox were exposed to light a distribution-shift towards late apoptosis was observed. Thus, the content of Annexin V-FITC positive and PI positive cells in population of cells treated with photoexcited 1:1 and 2:1 C₆₀-Dox reached $93 \pm 4\%$ and $96 \pm 4\%$, correspondingly (Fig. 35).

The high prooxidant and proapoptotic efficiency of the C₆₀-Dox treatment and light irradiation of CCRF-CEM cells was confirmed by significant increase of intracellular ROS, decreased ATP levels, caspase 3/7 activation and transition of cells to the late apoptosis stage.

IV.3.2 C₆₀-Berberine nanocomplexes

IV.3.2.1 Cell viability

Finally, the developed dual treatment strategy with photoexcited C₆₀-nanocomplexes was evaluated for an alternative anticancer drug Berberine. CCRF-CEM cells were treated with C₆₀-Ber for 24 h and subjected to 5 or 10 J/cm² 405 nm light irradiation (Fig. 36). The photoinduced toxicities were found in a low nanomolar concentration range of Berberine (≤ 100 nM). Neither free C₆₀, free Berberine nor their nanocomplexes had effect on cell viability if cells were kept at the dark. However, once illuminated free and C₆₀-complexed Berberine exhibited concentration- and light-fluence- dependent toxic effect towards CCRF-CEM cells (Fig. 36).

Free 100 nM Berberine decreased CCRF-CEM cell viability to $66 \pm 4\%$ and $55 \pm 5\%$ under 5 and 10 J/cm² light irradiation, respectively, that pointed on a photosensitizing behavior of free Berberine. C₆₀ alone was previously detected to have phototoxicity towards CCRF-CEM cells starting from 900 nM (Fig. 31). This was re-evaluated here with C₆₀ controls, demonstrating an absence of cell viability changes

under action of ≤ 200 nM photoexcited C_{60} .

C_{60} -Ber induced more pronounced cell viability decline in the combination with 405 nm light irradiation. Thus, 100 nM 1:1 C_{60} -Ber decreased CCRF-CEM cell viability to $28 \pm 4\%$ and $4 \pm 2\%$ under action of 5 and 10 J/cm^2 light irradiation, respectively. CCRF-CEM cell viability upon treatment with 100 nM 2:1 C_{60} -Ber was decreased to $14 \pm 3\%$ and $1 \pm 1\%$ under irradiation with 5 and 10 J/cm^2 405 nm light, respectively. The table 20 presents IC_{50} values calculated for all investigated treatment modalities. Complexation of Berberine with C_{60} in 1:1 and 2:1 molar ratio in combination with 5 J/cm^2 405 nm LED light irradiation caused a decrease in IC_{50} of 4.2 and 17.8 fold, correspondingly, as compared with an action of photoexcited free Berberine. Further light fluence increase up to 10 J/cm^2 was followed by a 10.9 and 21.8 fold decrease of IC_{50} for 1:1 and 2:1 C_{60} -Ber, respectively.

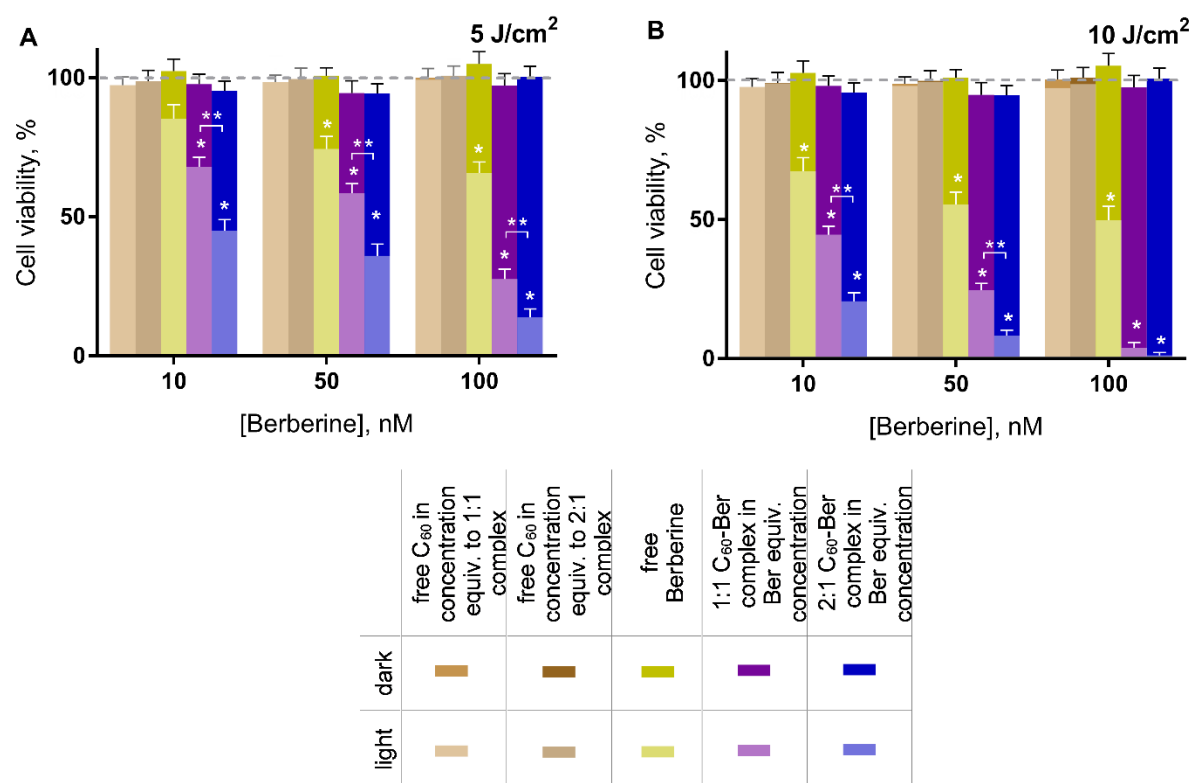


Figure 36. Viability of CCRF-CEM cells under action of photoexcited C_{60} -Ber: cells were treated with either C_{60} and Berberine alone or C_{60} -Ber in Berberine-equivalent concentrations and incubated in dark (A and B, dark columns) or after light irradiation with 405 nm light at 5 J/cm^2 (A, pale columns) or 10 J/cm^2 (B, pale columns), (* $p \leq 0.01$ in comparison with the respective dark control, ** $p \leq 0.01$ in comparison with the photoexcited 1:1 nanocomplex).

The cells treated with respective C_{60} controls had no significant difference in measured viability value either kept in the dark or exposed to the light irradiation. On the graphs dark columns “free C_{60} in concentration equiv. to 1:1/2:1 complex” + “dark” are overlapped with pale columns “free C_{60} in concentration equiv. to 1:1/2:1 complex” + “light”. Therefore, both data sets are seen as “free C_{60} in concentration equiv. to 1:1/2:1 complex” + “light” columns.

Table 20. IC₅₀ (nM) values for the photoexcited free free and C₆₀-complexated Berberine

	<i>dark</i>	<i>5 J/cm²</i>	<i>10 J/cm²</i>
<i>Berberine</i>	$38 \times 10^3 \pm 0.2 \times 10^3$	196 ± 8 *	109 ± 5 *
<i>1:1 C₆₀-Ber</i>	$8 \times 10^3 \pm 0.7 \times 10^3$	47 ± 4 *	10 ± 2 *
<i>2:1 C₆₀-Ber</i>	$5 \times 10^3 \pm 0.6 \times 10^3$	11 ± 3 *, **	5 ± 2 *, **

*p ≤ 0.01 in comparison with the respective dark control, **p ≤ 0.01 in comparison with the 1:1 nanocomplex

The proposed treatment strategies combination shifted the alkaloid's toxicity towards leukemic cells into the nM range. Nanocomplexation with C₆₀ and photoexcitation of the herbal alkaloid Berberine enabled to decrease its IC₅₀ in 3.8×10^3 and 7.6×10^3 times for 1:1 and 2:1 C₆₀-Ber, respectively. The combination index was calculated to assess whether Berberine nanocomplexation with C₆₀ had any synergistic effect with photoexcitation of studied agents (Tab. 21). Independently of the light fluence, CI revealed synergistic effect of the treatment strategy with 1:1 C₆₀-Ber and very strong synergistic effect with 2:1 C₆₀-Ber. Synergism of toxicities arose from the photoexcitation of components and C₆₀-delivery of Berberine was found to be dependent on the C₆₀ amount. Thus, 2:1 C₆₀-Ber was shown to be more efficient in the applied bimodal strategy due to the doubled C₆₀ amount as compared to 1:1 C₆₀-Ber.

Table 21. Combination index of interaction between phototoxic effects of C₆₀ and Berberine and non-irradiated C₆₀-Ber¹

<i>CI</i>	<i>5 J/cm²</i>	<i>10 J/cm²</i>
<i>1:1 C₆₀-Ber</i>	0.548 (synergism)	0.366 (synergism)
<i>2:1 C₆₀-Ber</i>	0.050 (very strong synergism)	0.010 (very strong synergism)

¹This was measured after cells co-treatment with C₆₀-Ber and LED light irradiation. Classification of interaction was determined according to *Chou (Chou, 2006)*

The obtained significant enhancement of drug toxicity towards human leukemic cells upon combination of photodynamic treatment and drug delivery on the basis of nanocomplex with C₆₀ provides a promising synergetic approach for cancer treatment with both classical and alternative chemotherapeutics.

V. DISCUSSION

Sixty carbon atoms arrange 12 penta- and 20 hexagon units to form one lipophilic, spheroidal shaped and symmetrical C₆₀ fullerene molecule in 720,7 Da with an inflected π -electron system (Kroto et al., 1985). The ball-like closed atom-cage determines its unique physico-chemical properties and particular biological activity (Nielsen et al., 2008; Scharff et al., 2008; Montellano et al., 2011). The complex biological effects of C₆₀ can be linked with several main factors including but not limited to: electron deficiency, which allows interaction with free radicals; the ability in the photoexcited state to transfer energy to the oxygen molecule; and lipophilicity that determines membranotropic properties (Emelyantsev et al., 2019). Therefore, recently C₆₀ got a considerable attention as a potential anticancer agent due to its ability to function as an antioxidant, a photosensitizer and a drug carrier (Mroz et al., 2007; Montellano et al., 2011; Goodarzi et al., 2017; Hamblin, 2018). A stable aqueous colloid solution of 100 nm C₆₀ nanoaggregates (Ritter et al., 2015a) was explored in this thesis for the development of a photodynamic chemotherapeutic treatment of cancer cells.

The investigation of any anticancer agent requires a clarification and description of the interactions with its main target: the cancer cell. These interactions determine the intracellular accumulation and localization of the studied molecules. Such knowledge could not only clarify the mechanism of action but also be used to direct the anticancer effects towards specific subcellular targets and optimize cancer therapies' efficiency. The *in vitro* application of any studied agent in the current research followed the investigation of its accumulation and localization in cancer cells. The explored treatment options of cancer cells included investigation of its effects on cell viability, reactive oxygen species generation and apoptosis induction.

Leukemic cell lines are common models for cancer treatment development on cellular level. Leukemia, cancer of the body's blood-forming tissues, including the bone marrow and the lymphatic system, reached 437 033 new diagnosed cases in 2018 (Bray et al., 2018) that accounted in average 14 out of 100,000 persons per year. The human leukemic CCRF-CEM cells were chosen as a main *in vitro* cancer model for the current research.

V.1. Effects of C₆₀ fullerene on leukemic cells

V.1.1 C₆₀ fullerene's uptake by leukemic cells

C₆₀ is a hydrophobic molecule able to penetrate into both lipid bilayer and cell membranes, thus, to penetrate and translocate plasma membranes (Levi et al., 2006; Qiao et al., 2007; Rossi et al., 2013; Santos et al., 2014). However, a low own fluorescence intensity challenged the direct investigation of C₆₀'s intracellular accumulation with fast and reliable fluorescence-based techniques (Kim et al., 1992; Dong & Cao, 2018). First attempts to study intracellular accumulation and pharmacokinetics were done with ¹⁴C-labeled water-soluble C₆₀ derivatives. Thus, accumulation in human keratinocytes (Scrivens et al., 1994) and pharmacokinetics in rats (Yamago et al., 1995) were demonstrated. An alternative technique is a covalent labeling of C₆₀ molecule with fluorescent dyes. Thus, the recent data of our working group evidenced rhodamine B isothiocyanate-C₆₀ (Franskevych et al., 2017) and methylpyridinyl-thiazoloxycarbonylpropylphenyl-C₆₁ (Prylutska et al., 2019) intracellular accumulation in human leukemic Jurkat cells and embryonic kidney HEK293, respectively. However, an attachment of the hydrophilic radioactive or optically active derivative on the C₆₀ hydrophobic molecule could significantly hinder its polarity and change the pattern of its interactions with cellular membranes and whole intracellular distribution. The shift from hydrophobicity to hydrophilicity, even if favorable for C₆₀ solubility in aqueous solutions, was predicted (Luksiene, 2003; Stueckle et al., 2016) and shown (Qiao et al., 2007; Nielsen et al., 2008; Santos et al.,

2014) to hinder its interaction with lipid membranes and cellular uptake.

An expansive and laborious transmission electron microscopy (TEM) enabled visualization of the cellular uptake of unmodified pristine C₆₀ in different cell lines, including human keratinocytes HaCaT and human lung carcinoma cells A549 (Horie et al., 2010), human monocyte-derived macrophage cells (Porter et al., 2007) and mouse macrophages RAW 264.7 (Russ et al., 2016). However, TEM studies provided a little about localization of this molecule at subcellular levels suggesting mainly its intracellular or cytoplasmic accumulation. Some studies contradict each other concerning pristine C₆₀ ability to penetrate the nucleus membrane (Porter et al., 2007; Horie et al., 2010). Therefore, the identification of pristine C₆₀ intracellular localization presented an important scientific task with a potential to add important knowledge to fullerene biology.

The development of a monoclonal IgG antibody against C₆₀ conjugated to bovine serum albumin by Prof. Dr. Bernard Erlanger's group (Chen et al., 1998; Braden et al., 2000) made an immunostaining of pristine C₆₀ molecule possible. So far, C₆₀ antibody visualized the *in vitro* intracellular accumulation of both derivatized and liposome-encapsulated C₆₀ (Ali et al., 2004; Chirico et al., 2007; Kato et al., 2010; Xiao et al., 2010). The antibody-based immunostaining offers an indirect solution for fluorescence labeling of pristine C₆₀ inside the cancer cell. However, this technique could not evaluate C₆₀'s intracellular concentration and accumulation dynamics. In that case, the optimal solution would be utilization of a high-performance liquid chromatography mass-spectrometry – analytical method, that allows a definitive identification and reproducible quantification of the trace-level analyte in a complex sample. This method together with electro-spray ionization was previously reported to be an effective tool for C₆₀ quantification in water samples (van Wezel et al., 2011), zebrafish embryo (Isaacson et al., 2007) and human skin keratinocytes HaCaT (liposome-encapsulated C₆₀) (Kato et al., 2010).

Two identification methods of the intracellular pristine C₆₀ accumulation using the indirect immunostaining and HPCL-ESI-MS were developed and optimized in the

frame of this thesis. The combination of those methods enabled visualization (Fig. 11) and quantification (Fig. 12 and 13) of the intracellular accumulation of pristine C₆₀ in human leukemic cells.

CCRF-CEM cells were shown to take up pristine C₆₀ in a time-dependent manner. The maximum of intracellular C₆₀ level reached < 250 ng/10⁶ cells at 24 h of incubation (Fig. 12). The co-staining with nuclear and mitochondrial markers pointed on the extranuclear preferential mitochondrial localization of C₆₀ in CCRF-CEM cells (Fig. 11) that was further confirmed with differential centrifugation and HPCL-ESI-MS analysis of the C₆₀ content in the mitochondrial fraction. C₆₀ exhibited predominant localization within mitochondria with 72% of its overall content in a cell extract (Fig. 13).

The observed mitochondrial localization of C₆₀ could be linked to its high electronegativity and a resulting affinity to the mitochondria-associated proton pool (Chistyakov et al., 2014; Santos et al., 2014). According to density functional theory simulations, C₆₀ diffuses into the protonated mitochondrial intermembrane space, where it interacts with up to 6 protons, acquiring a positive charge (Chistyakov et al., 2014). A recent study revealed an antioxidant protective effect in *Escherichia coli* aroused from C₆₀-mediated proton transfer and intracellular interaction with free radicals (Emelyantsev et al., 2019). C₆₀'s ability to penetrate the *Escherichia coli* membrane was extrapolated on eukaryote mitochondria, pointing on C₆₀ as a mitochondria-targeting agent.

This phenomenon is common for carboxyfullerenes in human keratinocytes (Chirico et al., 2007) and other negatively charged carbon nanoparticles such as single walled carbon nanotubes— shown to be localized in mitochondria of different cells, too (ASTC-a-1, MCF 7, COS 7, EVC304, and RAW264.7) (Zhou et al., 2010, 2011, 2012). From another point, the direct role of mitochondria in apoptosis induction (Castano et al., 2004; Ribeiro et al., 2004) could explain the proved before high photosensitizing efficiency of C₆₀ molecule (Burlaka et al., 2004; Scharff et al., 2008; Palyvoda et al., 2010; Prylutska et al., 2010; Grebinyk et al., 2012; Grynyuk et al., 2013).

V.1.2 Photodynamic treatment of leukemic cells with C_{60} fullerene

For the optimization of photodynamic treatment of cancer cells the most effective combination of the photosensitizing agent and the light conditions such as light wavelength and fluence has to be evaluated (Dolmans et al., 2003; Sperandio et al., 2013). The use of high power single chip light-emitting diodes is expected to promote photoinduced therapies application, since they have a higher portability and lower cost, compromising the efficiency of lasers (Yu et al., 2009; Erkiert-Polguj et al., 2016). Light fractionation can be realized with the use of sharp spectrum LEDs. The recent advent in the development of LEDs enabled their usage as a light source in various photoinduced (e.g., photodynamic or photothermal) therapies. LED-based equipment has a high potential to simplify PDT's technical part and to reduce its costs (Hempstead et al., 2015).

In this study four LED light sources with maximum at 365, 405, 515 and 650 nm were used to irradiate leukemic cells, previously incubated with 20 μ M C_{60} . The effect of pristine C_{60} and light irradiation combination towards CCRF-CEM cells was shown to be strongly dependent on the light wavelength and fluence. The short wavelength light irradiation was followed by most substantial decrease of leukemic cells viability, loaded with C_{60} . The efficiency of combined effect of C_{60} and light irradiation was proved to follow an expected order 365 nm > 405 nm > 515 nm > 650 nm (no effect) (Fig. 14, Appendix 1 Fig. 1). The detected damaging effects of UV light make its application unfavorable, whereas visible light caused much less cytotoxic effects if any in comparison with UV irradiation, even considering the fact that the visible light was used at higher fluences. The obtained results indicate that a high output single chip 405 nm LED was the optimal light source for C_{60} *in vitro* photodynamic treatment of human leukemic cells at intensities from 5 to 20 J/cm². The application of a 405 nm sharp spectrum high output LED chip for C_{60} photodynamic treatment of cancer cells allowed to decrease the light dose in comparison with broad spectrum light sources used at higher fluence rates of more than 100 J/cm² (Tabata et al., 1997;

Akiyama et al., 2008; Sharma et al., 2011; Jiang & Li, 2012).

However, the use of LED emitters with symmetrical Lambertian emission patterns challenges irradiation reproducibility since LED light fluence distribution is uniform (Moreno & Sun, 2008). The generated light by used LEDs propagates at 140° divergence angle. In order to get uniform illumination at the irradiation spot, the secondary optical modeling of LED light beam was performed with a cascade of the lenses. Aspherical and spherical lenses were used to form, focus and collimate the LED light beam. While LEDs produce a fair amount of heat, an aluminum heatsink was integrated to prevent unstable light output and reduced lifetime. All components of the system were mechanically assembled in a 3D-printed plastic (1st version) and metal turning (final version) mounting carcass and connected to the AC adapter (Fig. 8 and 9). A developed light source reshaped LED light in uniform parallel beam. The possibility to vary the evenly irradiated area is the major advantage of the developed system. It provided the same power density at any irradiation point, allowing for accurate calculation and selection of the irradiation dose. Consequently, the optical elements greatly increased the efficiency of using LED irradiation and collimated it in a narrower beam, that ensured the reproducibility of the irradiation conditions at 405 nm (5 and 10 J/cm²) for further biological investigations.

The required step in cancer PDT is a progression of oxidative stress, which occurs when ROS generation overwhelms the cell antioxidant defense system (Luksiene, 2003; Castano et al., 2004; Sharma et al., 2011; Orlova, 2013).

Intracellular ROS generation can be estimated with the use of redox-sensitive fluorescence dye DCFH-DA (Myhre et al., 2003; Eruslanov & Kusmartsev, 2010). The combinative treatment of CCRF-CEM cells with 20 μ M C₆₀ and 10 J/cm² 405 nm light induced a C₆₀ concentration-dependent oxidative stress at 1 h after light exposure. ROS generation was further intensified at following 3 h, reaching a 10-fold increase (Fig. 15). ROS are excellent oxidizing agents, that directly react with different substrates in a chain reaction during the oxidative damage of fatty acids and other lipids, proteins and DNA (Sharma et al., 2011; Zhou et al., 2016). The oxidation of such important

molecules inside the cell activates different signal pathways of cell injury that, once critical, lead to cell death. Most favorable is an active, programmed process of autonomous cellular dismantling that avoids eliciting inflammation – apoptosis. Apoptotic cell death can be initiated either through the extrinsic pathway with activation of cell-surface death receptors or intrinsic pathway with release of cytochrome *c* from mitochondria (Rustin, 2002). On contrary, necrotic cell death as a violent and quick cell degeneration is caused by chemical damage and has been generally considered as an unprogrammed process. The high dose PDT, delivered either with a high photosensitizer concentration or a high light fluence or both, causes cell death by necrosis, while PDT administered at lower doses tend to predispose cells towards apoptotic cell death (Nagata et al., 2003; Mroz et al., 2011b). The determination of cell death type is important to assess photodynamic treatment efficiency. Among crucial factors, that determine the cell death type, are cell type, state of apoptosis machinery, subcellular localization of primary damage, applied light dose and oxygen partial pressure (Buytaert et al., 2007; Mroz et al., 2011b).

ROS represent a cellular stress factor that, if produced over a certain level of quantity, effectively induces the active mode of a regulated compact destruction of a cell via the mitochondrial apoptotic pathway (Ribeiro et al., 2004). However, high reactivity and short half-life of ROS limits their area of action around their proximal production (Castano et al., 2004). Thus, given its mitochondrial accumulation, C₆₀-mediated ROS production can be predicted to cause the direct damage of mitochondrial membranes after light illumination and to lead to apoptotic cell death induction.

To check whether the treatment of cells with photoexcited C₆₀ affected mitochondria, ATP production was assessed as a main mitochondrial function. A drop of the ATP level in CCRF-CEM cells subjected to treatment with C₆₀ and 405 nm light (Fig. 16) evidenced vulnerability of mitochondria to the progression of C₆₀-mediated oxidative stress.

Proper execution of the apoptotic programme requires the coordination of multiple subprogrammes including the caspase cascade. Caspases are cysteine-aspartic

proteases typically activated in the early stages of apoptosis to cleave key cellular components, including cytoskeleton structural proteins, cleavage of which determines the cell shrinking during apoptosis (Ribeiro et al., 2004; Hassan et al., 2014). The executive caspase 3/7 exhibited a 4-fold activity increase in CCRF-CEM cell treated with C₆₀ and 10 J/cm² 405 nm light (Fig. 17 A) that pointed towards the apoptotic cell death execution. Shrinkage of apoptotic cells enables their removal by phagocytic cells in a clean fashion that avoids many of the problems associated with disruptive necrotic cell death. In order to facilitate their phagocytosis by macrophages, apoptotic cells modify the plasma membrane composition including exposure of phosphatidylserine on the cell surface (Suzuki et al., 2013; Hassan et al., 2014). The detection of a plasma membrane phosphatidylserine externalization in 50% of the cells pointed on a further apoptotic cell death execution in CCRF-CEM cells, treated with C₆₀ and exposed to 10 J/cm² 405 nm light (Fig. 17 B and C).

Taken together the data proved C₆₀'s ability to induce ROS production and apoptosis of leukemic cells after photoexcitation with high power single chip 405 nm LED. The induction of apoptotic cell death underlined the potential for application of the C₆₀ nanostructure as a photosensitizer for an anticancer therapy in combination with an LED as light source.

The obtained data support the common trend in recent years to investigate C₆₀ as a potential photosensitizer to mediate PDT of diverse diseases. Most of these reports have been confined to *in vitro* studies where not only cancer cells but also viruses, bacteria, fungi have been incubated with a diverse functionalized or solubilized C₆₀ followed by illumination with UV-vis light (Sharma et al., 2011; Grinholc et al., 2015; Hamblin, 2018). Light sources usually provided UV, blue, green or white light because the C₆₀ absorption is biased towards lower wavelengths with three intense bands in UV region and a broad tail up to the red light (Fig. 14 A) (Ritter et al., 2015). Since *in vivo* PDT commonly uses red light for its improved tissue penetrating properties, it was unclear whether C₆₀ would mediate effective photodynamic treatment *in vivo*. However, such concerns were addressed in a study of intraperitoneal photodynamic

C₆₀ therapy on a mouse model of abdominal dissemination of colon adenocarcinoma. Mroz et al. detected, that mice suffered toxicity after C₆₀ PDT with red light but exhibited a beneficial therapeutic effect after white light illumination, and suggested that this drawback may actually be an advantage instead (Mroz et al., 2011a).

From another point, a deep penetration of ultrasound (US) waves in biological tissues beyond the reach of external light has aroused the elegant idea to use it an alternative energy source for sensitizer excitation. The sonodynamic therapy (SDT), derived from PDT, recently emerged as a non-invasive cancer treatment modality relying on the activation of certain chemical sensitizers with low intensity high frequency US (Costley et al., 2015). It has been generally accepted that the cavitation effect of US is considered to explain SDT mechanism. The acoustic cavitation is a unique physical phenomenon that includes formation, growth and collapse of bubbles as US wave propagates through liquids. The explosion of bubbles causes a sonoluminescence to release accumulated energy (Putterman & Weninger, 2000). The sonoluminescence spectrum in water is relatively broadband with the UV maximum and a long-wavelength tail (Didenko & Pugach, 1994; Gaitan et al., 1996; Zolfagharpour et al., 2013). On top of turning sound into light, US-generated cavitation bubbles were shown to cause pyrolysis and temperature increase that can be attributed to the induction of toxic effects as well.

Various organic sonosensitizers have been adopted from PDT to SDT including, but not limited to aminolevulinic acid (Ohmura et al., 2011; Li et al., 2015), Rose Bengal (Chen et al., 2016b) and porphyrins (Yumita et al., 2011; Huang et al., 2017; Li et al., 2019; Ma et al., 2019). Compared to organic sonosensitizers, inorganic sonosensitizers such as gold (Gao et al., 2019), silica (Wang et al., 2018) and titanium dioxide (You et al., 2016) nanoparticles offer relatively high chemical and physiological stability and have also been demonstrated to be effective for SDT. The polyethylene glycol- (Tabata et al., 2002), polyhydroxy- (Tziortzioti, 2016) and tris-acid (Iwase et al., 2016) fullerenes have also been shown to efficiently induce ROS-mediated compact apoptotic cancer cell death once used as sonosensitizers. Owing to

the nature of sonoluminescence and its spectrum in particular (Didenko & Pugach, 1994; Gaitan et al., 1996; Zolfagharpour et al., 2013), US seems to be a good matching option for activating pristine C₆₀ to generate ROS.

The follow-up master study of Benjamin Kolp (Kolp, 2018) delivered the first data concerning pristine C₆₀ application as a sonosensitizer for treatment of human cervix carcinoma HeLa cells in combination with high frequency US. For investigation of the combined effect of C₆₀ and high frequency US, HeLa cells were exposed to 5.4 W/cm² 1 MHz US in the absence or presence of 20 μM C₆₀ for different exposure times (≤ 60 s). Cell viability was decreased on $35 \pm 6\%$ at 48 h after US treatment (Appendix 3 Fig. 1) and cell death differentiation analysis distinguished apoptosis in early and late stages under action of sonodynamically excited C₆₀ (Appendix 3 Fig. 2).

The results suggested the promising application of C₆₀ for sonodynamic cancer therapy. Further work is necessary for better understanding of the mechanisms underlying ROS generation and apoptosis induction during SDT. A possible effect of high frequency US on the body homeostasis should be clearly defined. The further strategy of combining sonodynamic and photo-/chemo- therapies has a promising application.

V.2 Effects of C₆₀-drug nanocomplexes on leukemic cells

The advent of nanotechnology presented an opportunity to combine different treatment strategies on the molecular level assembling a few agents on one nanoplatform. Given a board spectrum of C₆₀'s multifunctionalization, C₆₀ can be considered as a promising scaffold for drug delivery (Montellano et al., 2011). C₆₀ as a spherical unsaturated (poly)cyclic molecule predicted adsorption of aromatic molecules via π - π stacking interactions. Comparably, the similar approach was shown before for a coupling of the cargo molecules with carbon nanoparticles that improved the stability and drug-loading capacity (Kar et al., 2008; Li et al., 2014; Pérez & Martín, 2015; Yang et al., 2018). Recently the ability of C₆₀'s polyaromatic surface to adsorb

different therapeutics was exploited to create the C₆₀ nanocomplexes with cargo molecules such as benzene (Li et al., 2016), hexabenzocoronenes (Sepúlveda et al., 2017), anti glioblastoma (Samanta & Das, 2017) and anticancer (Evstigneev et al., 2013; Li et al., 2014) aromatic drugs.

V.2.1 Nanocomplexes with a common chemotherapeutic Doxorubicin

Life-threatening cardiotoxicity and other serious side effects of the anticancer anthracycline chemotherapeutic drug Doxorubicin makes it one of the first candidates for a targeted drug delivery (Tacar et al., 2013; Kumar & Raza, 2017). Moreover, Doxorubicin is a suitable model compound for *in vitro* studies due to its favorable optical properties, determined by electron transition in π -complexed system of its aromatic rings and ketone groups (Changenet-Barret et al., 2013). Evstigneev et al. investigated C₆₀ noncovalent complexation with Doxorubicin in water (Evstigneev et al., 2013) and later in physiological solution (Prylutsky et al., 2015). The developed nanocomplexes exhibited higher toxicity compared with the free drug *in vitro* and *in vivo* (Panchuk et al., 2015; Prylutska et al., 2015). This developed supramolecular self-assembly based on π - π stacking interactions between the unsaturated (poly)cyclic molecules C₆₀ and aromatic drug was further explored in the current research to produce fast, easy, reversible and cost effective nanocomplexes.

The followed *in vitro* study was designed to investigate whether complexation with C₆₀ affected drug intracellular localization and toxicity for human leukemic cells. A C₆₀-Doxorubicin nanocomplex (C₆₀-Dox) was designed in two nanomolar ratios (C₆₀:Dox, Tab. 11) of 1:1 and 2:1 in order to check whether C₆₀'s concentration affected Doxorubicin toxicity.

V.2.1.1 C₆₀-Doxorubicin characterization

The work-flow included a routine synthesis of C₆₀-Dox according to (Prylutsky

et al., 2015). To systematically test the stability of C₆₀-Dox, HPLC-ESI-MS/MS, UV-vis spectrometry and dynamic light scattering analytical procedures were established.

The developed reverse-phase HPLC-ESI-MS/MS method of Doxorubicin's quantification enabled analysis of both free and C₆₀-bound Doxorubicin. It was shown that complexation with C₆₀ resulted in a shift of retention times as well as in different shapes of chromatographic pick in comparison with the free drug (Fig. 18). Observed changes in chromatograms indicated that during decomposition of C₆₀-Dox on the C18 column, C₆₀ molecules, that have a higher affinity to the hydrophobic column, occupied a part of the active binding sites and interfered Doxorubicin's binding to the column properly, thereby, affecting its separation process. That resulted in a shorter retention (reduced time required for Doxorubicin to pass through the column) as well as peak broadening and tailing for Doxorubicin released from the nanocomplex as compared to the free drug. A very similar phenomenon was observed by Liu and Tabata during chromatographic separation of C₆₀ noncovalent nanocomplexes with pullulan (Liu & Tabata, 2010). The differences in chromatograms of free Doxorubicin and those released from nanocomplexes pointed out on the presence of C₆₀-Dox in solution.

The electron transition in the π -complexed system of Doxorubicin's aromatic rings and ketone groups (Changenet-Barret et al., 2013) determines its optical properties, that enable a direct non-invasive optical analysis of the Doxorubicin molecule (Fig. 19). The absorption spectrum of Doxorubicin was recorded in wavelengths of $\lambda < 600$ nm and revealed a broad band around 480 nm. Upon complexation with C₆₀ the Doxorubicin's absorption intensity exhibited 30% hypochromism (Fig. 19 A). The observed data pointed on a Doxorubicin fixation on the C₆₀ surface due to its π - π stacking interactions. The long wavelength absorption maximum of Doxorubicin was used as an excitation wavelength for tracking its fluorescence. The Doxorubicin's fluorescence had a maximum around 594 nm (Changenet-Barret et al., 2013) that was 50% quenched in nanocomplexes by C₆₀ moieties (Fig. 19 B). The observed intense Doxorubicin fluorescence quenching is linked to the typical for C₆₀ strong electron-accepting capability (Liu & Troisi, 2013)

as well as the intramolecular excited-state energy transfer typical for noncovalent Doxorubicin complexes (Blazkova et al., 2014; Husseini et al., 2016). Absorption hypochromism and fluorescence quenching experimentally evidenced the close spatial proximity of the components in C₆₀-Dox.

Further research progress required to assure the stability of nanocomplexes transferred in sophisticated cell culturing media in order to assess its possible biological effects on the human leukemic cells. Such parameters of cell culture medium as its ionic strength and protein concentration as well as elevated temperature and humidity required for cell culturing may affect stability of nanocomplexes. The dynamic light scattering comparative analysis detected nanocomplexes' size to be around 140 nm independent of medium composition, temperature or duration of incubation (Fig. 20). The absence of additional significant aggregation of the C₆₀-Dox in the completed cell culture medium pointed on its suitability for further *in vitro* studies.

The comparison of literature data and results of the current research (Tab. 22) enlightens the congruence between main characteristics of C₆₀-Dox under study with the optimal parameters, defined as “The rational design for nanosystem as a carrier of anticancer drug” in the table 1. Therefore, the proposed noncovalent complexation of Doxorubicin with C₆₀ could be defined as a promising for further investigation.

Table 22. The rational design of C₆₀-Dox nanocomplexes

<i>Characteristic</i>	<i>Advantageous value</i>	<i>Colloid C₆₀</i>	<i>Doxorubicin</i>	<i>C₆₀-Dox</i>
size	10-200 nm	100 nm	1.5 nm	140 nm
charge	$\geq \pm 30$ mV	$- 30$ mV ¹	0 mV ²	$+ 45$ mV ²
solubility	<ul style="list-style-type: none"> •hydrophilicity for prolonged circulation •hydrophobicity for higher cellular uptake 	hydrophobic	hydrophilic	dual

¹(Ritter et al., 2015), ²(Prylutskyy et al., 2014a)

V.2.1.2 *C₆₀-Doxorubicin's uptake by leukemic cells*

The first task of the investigation of C_{60} -complexed Doxorubicin effects in leukemic cells was focused on the assessment of its intracellular accumulation again ideally both qualitatively and quantitatively.

Since Doxorubicin possesses a strong absorption and fluorescence in the visible spectral region (Changenet-Barret et al., 2013; Motlagh et al., 2016) the direct tracking of this molecule is possible, whereas C_{60} monitoring requires additional immunofluorescence staining. With the use of indirect C_{60} immunostaining the intracellular accumulation of the carbon nanostructure was confirmed in cells treated with free nanomolar C_{60} or C_{60} -Dox. When cells were treated with C_{60} -Dox, C_{60} was found in the extranuclear space assumingly in mitochondrial membranes as it was shown for the C_{60} at higher molar concentrations (Fig. 11 and 13). Doxorubicin from both 1:1 and 2:1 nanocomplexes was accumulated in the nucleus and in a higher concentration than after treatment with a free drug, evident by a more intense fluorescence signal. The observed allocation of C_{60} and Doxorubicin inside leukemic cells evidenced the successful drug release from nanocomplexes into intracellular space (Fig. 21). Doxorubicin molecules from C_{60} nanocomplexes as well as free drug entered the nuclei that reflects its antiproliferative impact through DNA damage (Thorn et al., 2011; Kizek et al., 2012; Tacar et al., 2013). A strong red fluorescence of the Doxorubicin molecule with excitation and emission around 480 and 594 nm, respectively (Fig. 19), enabled investigation of its accumulation dynamics with fluorescence-based flow cytometry. Complexation with C_{60} significantly enhanced uptake of Doxorubicin by CCRF-CEM cells. Thus, cells treatment for 6 h with C_{60} -Dox resulted in 2.2-fold increase of drugs intracellular level (Fig. 22).

The intracellular drug accumulation is determined by two independent processes – drug entry into the cell and its efflux from the cell. An increased drug's intracellular uptake upon nanocomplexation with C_{60} points towards the latter functioning as a drug transport promoter. C_{60} was shown to transigrate the cellular

plasma membrane due to passive diffusion (Bedrov et al., 2008), as well as by endocytosis/pinocytosis (Zhang et al., 2009; Russ et al., 2016) and phagocytosis (Asada et al., 2014), while free Doxorubicin permeates only via passive diffusion (Prabhakar & Doble, 2011). C₆₀ could function as a transporter of small aromatic molecules (Borowik et al., 2018), facilitating their intracellular uptake. From the other hand, Doxorubicin was reported to leave a cell via passive and P-glycoprotein-mediated efflux (Wielinga et al., 2000). However, C₆₀ is not recognized by P-glycoprotein (Xu et al., 2012) and is even shown to bind P-glycoproteins (Prylutska et al., 2017a), inhibiting its activity. Multimodal effects of C₆₀ on drug entry into and its efflux from the cell can contribute to the observed enhancement of Doxorubicin's intracellular accumulation in CCRF-CEM cells treated with C₆₀-Dox.

Comparably, a graphene-based triple delivery nanosystem noncovalently loaded with Doxorubicin and phthalocyanine ensured higher cellular drug uptake and effective intracellular drug release (Wu et al., 2014). On the contrary, a covalent bond between carrier and cargo introduces a structural alteration into the drug molecule. Thus, C₆₀ with two Doxorubicin molecules bound through an amide bond was distributed predominantly in the cytoplasm (Liu et al., 2010a). Consequently, the accumulation pattern and interaction with intracellular targets is altered that resulted in complete or partial loss of the drug's function. Taken together, the data on C₆₀-complexated Doxorubicin intracellular distribution evidenced that C₆₀ enhanced the drug's intracellular accumulation but did not affect its nuclear localization in the leukemic cells.

V.2.1.3 Effects C₆₀-Doxorubicin on leukemic cells

The toxic effect of free and C₆₀-complexated Doxorubicin was assessed not only towards not only CCRF-CEM cell line, but also towards additional three human cell lines of leucosis origin – Jurkat, THP1 and Molt16. Viability of leukemic cells was estimated by MTT viability assay at 24, 48 and 72 h incubation in the presence of C₆₀-

Dox as well as of free Doxorubicin separately at equivalent concentrations (Fig. 23).

Free drug showed a common pattern of dose- and time- dependent toxicity against all studied cell lines. The drug was shown to exhibit toxicity against leukemic cells in the nM range. The sensitivity of leukemic cells to Doxorubicin was found to follow the order Molt-16 > THP1 > Jurkat > CCRF-CEM (less sensitive). IC₅₀ for CCRF-CEM, THP1 and Jurkat cells at 72 h incubation were estimated to be 80 ± 9, 43 ± 5 and 38 ± 6 nM, correspondingly (Tab. 15). These data correspond well to literature data (Scott et al., 1986). Molt-16 cells appeared to be the most sensitive to the drug with an IC₅₀ of only 2.0 nM at 72 h incubation. A similar sensitivity of Molt-16 cells with 10-times higher apoptosis induction compared to Jurkat cells under treatment of the anticancer drug Homoharringtonine was previously reported (Cai et al., 2001).

C₆₀-Dox possessed higher cytotoxicity compared to free drug in equivalent concentrations. For the four investigated cell lines the data showed a variety of enhanced toxicities up to 3.5-fold decrease of drug's IC₅₀ under action of the 1:1 C₆₀-Dox. Lower toxicity was detected for 2:1 C₆₀-Dox with IC₅₀ decrease of ≥ 2.5 times compared to free Doxorubicin. Such less pronounced effect of 2:1 C₆₀-Dox can be attributed to the higher concentration of C₆₀ as its component. Due to its antioxidant activity excess of C₆₀ can protect cells against Doxorubicin-associated oxidative stress (Gharbi et al., 2005; Thorn et al., 2011; Castro et al., 2017).

The increased accumulation and cytotoxicity of the C₆₀-complexated Doxorubicin confirmed the function of C₆₀ as a nanocarrier and the perspective of its application for optimization of Doxorubicin efficiency against leukemic cells. As Doxorubicin is only a representative or model substance for many antitumor drugs it was expected that the findings may be transferred to other aromatic drugs. Increasing a drug's uptake into tumor cells and/or its antitumor qualities may point towards new treatment strategies. Complexation of drugs with nanocarriers may serve to reduce their efficacious dose rates and, thus, attenuate the unwanted side effects. Therefore, the ability of C₆₀'s polyaromatic surface to absorb different therapeutics was further

exploited to create C₆₀ drug-carrying nanocomplexes with the experimental angucycline antibiotic Landomycin A (Prylutsky et al., 2016) and Cisplatin (Prylutska et al., 2017a,b), both increased the drugs efficiency towards cancer cells.

V.2.2 C₆₀-nanocomplexes with an alternative anticancer drug Berberine

As an alternative library of potent anticancer drugs natural bioactive compounds offer potentially high safety, availability, accessibility and low costs. Alkaloids, being one of the most versatile class of herbal secondary metabolites, are heterocyclic, nitrogen containing, low-molecular-weight molecules, that provide plants with a defense against herbivores, bacteria, fungi and viruses (Keasling, 2008; Xiao et al., 2012; Ortiz et al., 2014). As a common drug in Ayurvedic, Chinese, Middle-Eastern and native American folk medicines the isoquinoline quaternary alkaloid Berberine exhibits versatile activities including anti-inflammatory, antimutagenic (Cernáková et al., 2002), antidiabetic (Abd El-Wahab et al., 2013), antimicrobial and antiviral (Cai et al., 2014; Ortiz et al., 2014) activities. In recent years, Berberine has been reported to inhibit cell proliferation and to be toxic *in vitro* for many human cancer cell lines including leukemic cells (Xiao et al., 2012).

The antiproliferative properties raise a possibility for the use of Berberine as an anticancer therapeutic, however, its poor water solubility, stability and bioavailability limit its clinical applications (Mirhadi et al., 2018). Furthermore, Berberine's hormetic effect, with low doses strongly stimulating the growth of cancer cells, while high doses having an anticancer effect, challenges a suitable dosage ranging (Bao et al., 2015). The fast and easy strategy of aromatic cargos noncovalent complexation with C₆₀ was predicted to be transferable to deliver the Berberine molecule into leukemic cells.

V. 2.2.1 Herbal alkaloid Berberine's effects on leukemic cells

Given Berberine's promising but not clinically established anticancer function,

firstly a separate study was conducted to evaluate Berberine's mechanism and range of cytotoxicity towards CCRF-CEM cells.

Although, many results show that Berberine effectively binds genomic (Wang et al., 2011b; Li et al., 2012) and telomeric (Franceschin et al., 2006; Arora et al., 2008) DNA, suggesting its high nuclear affinity (Zhang et al. 2013), other data show Berberine's mitochondrial localization (Pereira et al. 2007). To determine the intracellular localization of Berberine is important to explain its anticancer activity since the location could give insights about the drug's impact on cell metabolism.

Berberine's absorption and fluorescence maxima at 424 nm and 560 nm, respectively (Appendix 2 Fig. 1), suggest direct fluorescence microscopy. CCRF-CEM cells incubated for 4 h in the presence of 50 μM Berberine exhibited green fluorescence, the pattern of which mimicked DNA-binding fluorescent dye distribution (Fig. 24). Thus, nuclear localization of free 50 μM Berberine in CCRF-CEM cells was demonstrated. Previously, it was shown that Berberine is transferred into the nucleus via passive diffusion (Zhang et al. 2013), but in concentrations less than 50 μM it also selectively accumulated by mitochondria (Pereira et al. 2007, Serafim et al. 2008). Thus, 0.5 μM Berberine exhibited also both nuclear and extranuclear localization in CCRF-CEM cells (Appendix 4 Fig. 1), pointing out the multiphase model of Berberine accumulation.

A considerable attention has been paid to identify Berberine's inhibiting potential on cancer cell viability (Lin et al. 2007, Meeran et al. 2008, Patil et al. 2010, Zhang et al. 2010, Xiao et al. 2012, Zhang et al. 2013, Park et al. 2015, Seo et al. 2015). A possible Berberine's effect on the viability of CCRF-CEM cells was assessed during 72 h of incubation (Fig. 25). The obtained data determined Berberine to be cytotoxic in the μM range with IC_{50} of 58 ± 5 , 23 ± 2 and 19 ± 2 μM at 24, 48 and 72 h, correspondingly.

Berberine was found to promote oxidative stress in human leukemic cells by doubling the intracellular ROS generation level (Fig. 26 A1 and A2), being in accordance with previous findings (Pereira et al. 2007, Meeran et al. 2008, Park et al.

2015). Treatment of CCRF-CEM cells with Berberine resulted as well in a time-dependent increase to 210% of the caspase-3/7 activity (Fig. 26 B) and plasma membrane phosphatidylserine externalization in 46% of cells (Fig. 27). The observed changes pointed on the oxidative stress and apoptotic cell death induction in leukemic CCRF-CEM cells under action of Berberine.

Thus, the herbal alkaloid Berberine could be defined as a drug candidate for leukemic cancer chemotherapy.

V. 2.2.2 Effects of C₆₀-Berberine on leukemic cells

To overcome limiting factors of Berberine clinical application including but not limited to its hormetic effect, poor water solubility, stability and bioavailability, C₆₀ was explored to deliver Berberine into leukemic cells. Given much higher IC₅₀ and limited water solubility of Berberine in comparison with Doxorubicin, C₆₀-Ber nanocomplexes (C₆₀-Ber) were designed with one extra molar ratio – 1:2 on top of 1:1 and 2:1. The 1:2 C₆₀-Ber provided the opportunity to study a higher Berberine amount. With the use of fluorescence microscopy and flow cytometry the intracellular accumulation of the alkaloid in human leukemic CCRF-CEM cells treated with free Berberine or C₆₀-Ber was confirmed (Fig. 28). Berberine (0.5 μM) was localized both in the cell nucleus and the extranuclear space of CCRF-CEM cells. C₆₀-Ber appeared to be internalized by CCRF-CEM cells faster and more intense than free Berberine (Tab. 16). Comparably to Doxorubicin, the intracellular Berberine accumulation is determined by two independent processes: its entry into and efflux from the cell. A free Berberine permeates the cells through passive diffusion (Prabhakar & Doble, 2011) and is a substrate of P-glycoprotein (Pan et al., 2002), while C₆₀ functions as a transporter of the small aromatic molecules (Borowik et al., 2018) and as an inhibitor of P-glycoproteins (Prylutska et al., 2017a), that increases Berberine intracellular level.

The cell viability assay revealed an enhanced time- and concentration-dependent toxic effect of C₆₀-Ber towards CCRF-CEM cells (Fig. 29). The IC₅₀ of Berberine in

1:2, 1:1 and 2:1 C₆₀-Ber was decreased by 3.2, 4.8 and 6.3 times, respectively compared to the IC₅₀ value of free Berberine at 72 h (Tab. 17). Thus, cytotoxicity was found to follow the order: free Berberine < 1:2 < 1:1 < 2:1 (the most toxic). The earlier activation of caspase 3/7 (Fig. 31) and accumulation in sub-G1 phase (Fig. 30) of CCRF-CEM cells treated with C₆₀-Ber, compared with free Berberine, evidenced apoptosis induction. The enhanced toxic and proapoptotic efficiency of Berberine against leukemic cells upon its complexation with C₆₀ as compared to the free drug is determined by C₆₀'s ability to promote drug accumulation inside cancer cells and potentiate its toxic activity.

It should be noted that complexation with C₆₀ allowed to enhance the Berberine toxicity against leukemic cells more appreciably (≤ 6.3 times decreased IC₅₀) as compared with a C₆₀ complexation with the traditional anticancer therapeutic Doxorubicin (≤ 3.5 -fold decrease of IC₅₀) at the same treatment duration. That can be linked to the higher applied concentration of the components in C₆₀-Ber. Since Berberine was found to be toxic in μM range, it allowed higher C₆₀ and Berberine content in final nanocomplex at the same molar ratios as compared with nM range of Doxorubicin. It could be expected that the drug delivery activity of C₆₀ has a dose-dependent efficiency, thus, explaining the higher toxicity enhancement for Berberine as compared to Doxorubicin. The obtained results encourage the strategy of C₆₀ usage for natural anticancer medicine delivery.

Also, it should be noted that the observed effect on the cytotoxicity of Berberine complexation with C₆₀ nanostructure was found to be opposite in comparison with Doxorubicin. Thus, the C₆₀-Dox with the lower amount of C₆₀ was the most toxic, while the C₆₀-Ber with the higher amount of C₆₀ was found to be the most toxic towards CCRF-CEM cells. That can be attributed to the applied C₆₀ concentration 50-450 nM and 2.5-40 μM in nanocomplexes with Doxorubicin and Berberine, correspondingly. A higher amount of C₆₀ may much better escalate the intracellular accumulation of the delivered cargo molecule than hinder drug-induced ROS-mediated toxic effects.

The nanoparticulation of anticancer drugs expands the scope of their chemical

behavior and pharmacodynamics, as well as reduces efficient doses and unwanted side effects. The explored ability of C₆₀ nanostructure's polyaromatic surface to absorb aromatic molecules was shown to improve drugs' treatment efficiency against human leukemic cells.

V.3 Towards photodynamic chemotherapy with C₆₀-drug nanocomplexes

The combination of the chemotherapeutic and photodynamic treatment strategies was explored on the basis of C₆₀-drug nanocomplexes, exploiting C₆₀ both as a drug carrier and a photosensitizer. The main part of the research focused on the clarification of the effects of photoexcited C₆₀-Dox towards leukemic cells with an assessment of its cytotoxicity mechanism with further brief clarification whether developed strategy works with C₆₀-Ber as well.

The observed allocation of C₆₀ and Doxorubicin inside leukemic cells sets a background for the application of the “two swords” treatment strategy based on improved chemotherapeutic and photodynamic treatments of cancer cells. Thus, nuclear Doxorubicin intercalated into DNA is supposed to block its transcription, replication and repair (Thorn et al., 2011; Kizek et al., 2012; Tacar et al., 2013), whereas photoexcited extranuclear C₆₀ is able to produce ROS and to induce the mitochondrial pathway of apoptosis (Fig. 15-17) (Scharff et al., 2008; Prylutska et al., 2010; Grebinyk et al., 2012; Franskevych et al., 2017).

Nanocomplexes of C₆₀ and Doxorubicin at molar ratios 1:1 and 2:1 and at Doxorubicin equivalent concentrations in a range $\leq IC_{50}$ (150-450 nM) were tested on human leukemic CCRF-CEM cells in combination with 405 nm LED light irradiation (Fig. 32). It should be noted that C₆₀ was used in nanomolar concentrations in contrast to micromolar application in previous studies of our working group (Scharff et al., 2008b; Prylutska et al., 2010; Grebinyk et al., 2012) and by other authors (Mroz et al., 2007; Liao et al., 2011; Lee et al., 2013; Asada et al., 2014; Yin et al., 2014; Yu et al., 2016). Nanomolar C₆₀ was shown to have no dark toxicity and a slight cytotoxic effect

with $11.5 \pm 3.7\%$ decrease of leukemic cell viability after 405 nm light irradiation at 10 J/cm^2 fluence. Free and C_{60} -complexated Doxorubicin exhibited concentration-dependent toxicity towards CCRF-CEM cells. The enhancement of Doxorubicin toxicity upon its complexation with C_{60} corresponds to C_{60} nanocarrier function and was explored in the previous part of the current research.

Compared to dark toxicity, photoexcitation of C_{60} -Dox considerably increased its toxicity towards CCRF-CEM cells. The cytotoxicity was found to be dependent on both concentration and light dose. Light at 5 J/cm^2 fluence had an effect at the highest concentration of 1:1 C_{60} -Dox (450 nM) and all studied concentrations of 2:1 C_{60} -Dox (50, 150 and 450 nM). Once light fluence was applied at 10 J/cm^2 enhancement of nanocomplexes toxicity became evident at all studied combinations of nanocomplexes and light irradiation. The most prominent toxic effect was achieved when leukemic cells were treated with 2:1 C_{60} -Dox and irradiated with 5 or 10 J/cm^2 405 nm light with a 16-fold decrease of IC_{50} as compared with IC_{50} value for the free Doxorubicin ($390 \pm 56 \text{ nM}$, Tab. 18). Phototoxicity of 1:1 C_{60} -Dox occurred to be less pronounced causing a 9-fold decrease of IC_{50} that can be attributed to the lower content of C_{60} as a photosensitizer (Tab. 18).

To estimate the pharmacodynamic interactions of C_{60} 's dual functionality as a drug nanocarrier and a photosensitizer in cells treated with nanocomplexes and light, the value of combination index (CI) was calculated (Tab. 19). CI indicated on a very strong synergy between non-irradiated 2:1 C_{60} -Dox and 10 J/cm^2 photoexcitation of C_{60} . CI value for 1:1 C_{60} -Dox and photoexcitation of C_{60} with 10 J/cm^2 405 nm light evidenced a strong synergy.

In order to clarify the death type of cells exposed to the photodynamic chemotherapeutic treatment with C_{60} -Dox, the similar logic flow and experiments design was applied as in part *V.I.2* dedicated to the explanation of C_{60} phototoxicity mechanism. Thus, cell oxidant balance as well as important markers of apoptotic cell death were studied with one combination of the applied cell treatment conditions – C_{60} -Dox at 450 nM Doxorubicin equivalent concentration and 10 J/cm^2 405 nm LED light

irradiation.

Treatment of CCRF-CEM cells with 1:1 and 2:1 C₆₀-Dox and light resulted in ROS increase by 3.8 and 5.0 fold, correspondingly (Fig. 33). ATP level dropped to $30 \pm 4\%$ and $28 \pm 3\%$ after 10 J/cm^2 light irradiation of cells treated with 1:1 and 2:1 C₆₀-Dox, respectively (Fig. 34 A). Photoexcited 1:1 and 2:1 C₆₀-Dox caused 4.7- and 5.8-fold increase of caspase 3/7 activity (Fig. 34 B) and the exposure of phosphatidylserine on the cell surface in $93 \pm 4\%$ and $96 \pm 4\%$ of cells (Fig. 35), correspondingly. Taken together the obtained data confirmed the prooxidant and proapoptotic effects of combined treatment with C₆₀-Dox and light irradiation on leukemic cells.

The conclusion can be drawn that the main objective of the study was met for the photodynamic chemotherapeutic treatment strategy development on the basis of C₆₀-Dox and 405 nm LED light combination with the proved increase of drug's toxicity and the detected induction of apoptotic cell death in co-treated CCRF-CEM cells.

As a roundup of the current study experiments were conducted to estimate the combination effect of C₆₀-based photodynamic treatment and drug delivery for the alternative anticancer drug herbal alkaloid Berberine. CCRF-CEM cell viability subjected to treatment with photoexcited free or C₆₀-complexated Berberine was studied at identical conditions as Doxorubicin.

Berberine itself was detected to exhibit photosensitizing activity in combination with 405 nm light irradiation. The optical properties of the Berberine molecule, as absorption and fluorescence at 424 nm and 560 nm, respectively (Appendix 2 Fig. 1), explain its photoexcitation under the applied light conditions. Recent studies delivered similar evidence on Berberine's phototoxic effects on glioma (Luiza Andreazza et al., 2016) and cervix carcinoma (Liu et al., 2019) cells exposed to blue light (405 nm and 410 nm, respectively). A progression of oxidative stress detected after 5 J/cm^2 405 nm light irradiation of CCRF-CEM cells, treated with $0.5 \mu\text{M}$ Berberine. Escalated 5-fold ROS level (Appendix 5 Fig. 1) evidenced the photosensitizing activity of Berberine in CCRF-CEM cells under 405 nm light irradiation. The results demonstrated the

presence of two photosensitizers in the proposed C₆₀-Ber, suggesting promising enchantment of nanocomplex toxicity upon light irradiation.

The C₆₀-Ber exhibited a high phototoxicity (Fig. 36). Under the same light exposure (5 and 10 J/cm²) CCRF-CEM cell viabilities were detectable in the range of Berberine concentrations ≤ 100 nM. Free C₆₀ at equivalent concentrations (≤ 200 nM) had no effect on cell viability, independent whether cells were kept at the dark or irradiated at 405 nm. Viabilities of cells treated with increasing concentrations of photoexcited 1:1 and 2:1 C₆₀-Ber were detected to be 16-46% and 38-54% lower compared to the action of free photoexcited Berberine. The IC₅₀ values of photoexcited 1:1 and 2:1 C₆₀-Ber were decreased in ≤ 10.9 and ≤ 21.8 times as compared with free photoexcited Berberine (Tab. 20). The calculated combination index of the photodynamic treatment and drug delivery for Berberine with C₆₀ nanocomplexes evidenced a synergistic effect when using a 1:1 C₆₀-Ber ratio and a very strong synergistic effect with a ratio of 2:1 C₆₀-Ber (Tab. 21).

The Berberine's toxicity enhancement can be explained with multimodal induction of the cell death under the applied combinative treatment conditions. In low concentrations none of the studied agents had any dark toxicity towards cell viability. However, once cells treated with free or C₆₀-complexed Berberine were exposed to 405 nm light, CCRF-CEM cells' viability was significantly decreased. The similar intracellular distribution pattern of free and C₆₀-complexed Berberine pointed on the allocation of C₆₀-Ber components comparably to C₆₀-Dox, favorable for injuring different cell pathways. A higher amount of Berberine, localized in the nucleus, targets DNA (Wang et al., 2011b; Li et al., 2012); C₆₀, localized in mitochondria, targets its membranes (Pereira et al., 2007; Serafim et al., 2008). Lipids and DNA present one of the main targets for photodynamic treatment due to the high reactivity of photoproducts generated after its oxidation (Luksiene, 2003; Castano et al., 2004). Moreover, the extranuclear pool of Berberine in CCRF-CEM cells could be localized in mitochondria as well and take part in induction of the mitochondrial dysfunction (Meeran et al., 2008; Park et al., 2015; Neag et al., 2018). In that way, mitochondria would be exposed to

double cytotoxic hit from both photoexcited C₆₀ and Berberine. The differential effects of C₆₀-Ber on cells under 405 nm light can explain the high efficiency of combined treatment that decreased IC₅₀ of free alkaloid in 3.8×10^3 and 7.6×10^3 times for photoexcited 1:1 and 2:1 C₆₀-Ber, respectively.

As a brief summary of the presented study, the main outcome can be formulated as follows: the combination of LED-based C₆₀-mediated photodynamic treatment of leukemic cells and C₆₀-based drug delivery determined the synergetic toxic efficiency of C₆₀-drug nanocomplexes (Fig. 37).

The data obtained demonstrate the effective combination of chemo- and photodynamic cancer treatment strategies on the basis of the C₆₀-drug nanosystem. C₆₀ nanomolar concentrations were firstly applied for *in vitro* optimization of the drug's chemotherapeutic activity in the frame of photodynamic chemotherapy. According to the recent literature on carbon nanoparticle-mediated photodynamic chemotherapy, the synergistic toxic effect of drug-loaded graphene was achieved at light irradiation of cervix, breast and skin cancer cells treated with Doxorubicin-polylysine graphene-phthalocyanine (Wu et al., 2014) or lung cancer cells treated camptothecin-graphene oxide-hypocrellin A (Zhou et al., 2014), both in μM Doxorubicin concentrations. Used in the current work noncovalent C₆₀-drug nanocomplex synthesis enabled simple and fast preparation of two-component as compared to the mentioned three-component nanosystems, phototoxic in nM Doxorubicin concentrations.

As listed in the table 2, C₆₀ nanostructure is the most common carbon nanoparticle used for photodynamic chemotherapy. Dual functionality of polyhydroxylated C₆₀, as a drug nanocarrier and as a photosensitizer improved Doxorubicin efficiency at in 4-14 μM (Fan et al., 2013) and 19 μM (Shi et al., 2016) drug concentrations. Diadduct malonic acid-C₆₀ was co-entrapped in micelles with 1 μM Docetaxel enhanced its anticancer effect under light irradiation (Guo et al., 2014).

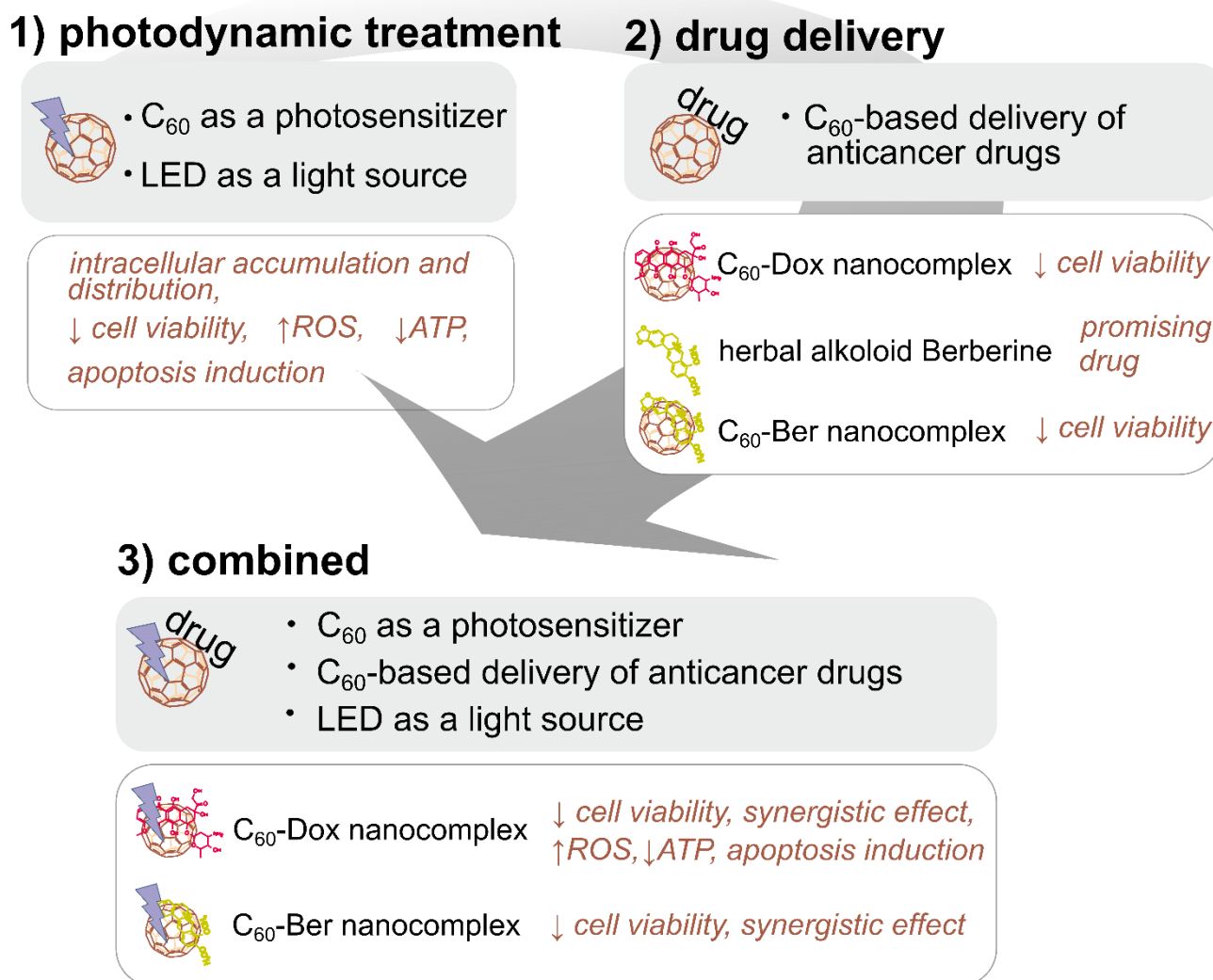


Figure 37. Research workflow with delivered results (in brown) towards C_{60} -drug nanocomplex-based photodynamic cancer chemotherapy: the approach is realized by studying C_{60} -mediated photodynamic treatment of leukemic cells (1) and C_{60} -based drug delivery into leukemic cells (2) and these treatment strategies combination (3).

Chemo- and photodynamic anticancer agents have distinct intracellular targets and, therefore, induce different signaling pathways of cell injury. Earlier studies showed tumor-specific differential effects of agents under the study, thus, Doxorubicin attacked specifically fast proliferating cells (Thorn et al., 2011; Kizek et al., 2012; Tacar et al., 2013), whereas C_{60} mainly targeted the redox state of the cell (Sharma et al., 2011; Orlova, 2013; Goodarzi et al., 2017). The synergistic effect of photodynamic treatment and drug delivery combination is attributed mainly to the further amplification of oxidative stress (Fan et al., 2017). Intensive ROS production promotes apoptosis and assists drug delivery due to ROS-mediated lipid peroxidation of the endosome membranes (Ribeiro

et al., 2004; Fan et al., 2017; Lee & Ma, 2017). The efflux of the drug can be inhibited as well by ROS-mediated oxidation of the intracellular domain of the P-glycoprotein (Khdaïr et al., 2010; Chen et al., 2015; Kalluru et al., 2016). ROS as intracellular signal messengers shift profiles of signaling pathways in treated cells. Carbon nanoparticle were shown to induce ROS-mediated activation of the mitogen-activated protein kinase that increased the vulnerability of lung cancer cells towards Paclitaxel (Arya et al., 2013). The cooperative enhancement interactions between mechanisms of chemo- and photodynamic treatment strategies contribute to the obtained synergistic effect (namely “ $1 + 1 > 2$ ”).

To sum up, the presented research delivers a proof-of-concept, confirming the function of C_{60} as a photosensitizer and a drug carrier and an anticancer drug's activity modulator, that points on its further potent application for optimization of drug's efficiency against cancer cells. One of the major barriers of achieving the transition of nanoparticle-based therapeutics use into clinical practice is the complete understanding of potential toxicological properties of these materials, along with their exact pharmacodynamics and pharmacokinetics (Arruebo et al., 2011).

V.4 Outlook

The fullerene family, and especially C_{60} , has delighted the scientific community with perspective applications in a wide variety of fields, including cancer medicine. In drug discovery a number of specific steps must be accomplished to acquire a compound that is safe and efficacious and also exhibits the complex array of desired drug-like behaviors that warrants advancements to the clinic (Fig. 38). Firstly, the C_{60} nanocomplex with a common anticancer anthracycline chemotherapeutic drug Doxorubicin was designed (1) as a model substance (Evstigneev et al., 2013). The fast and cost-effective synthesis of the complexes in different molecular ratio was established in water and physiological solution (2) (Prylutsky et al., 2014a). The rigorous analytical assessment of stability declared its biological applicability (3)

(Evstigneev et al., 2013, Prylutsky et al., 2014a, 2015). The strategy was expanded with the development of C_{60} nanocomplex with an herbal alkaloid Berberine, firstly proved to be a promising anticancer drug itself. Given its polyaromatic surface, C_{60} nanostructure noncovalently absorbed aromatic drug molecules and improved its efficiency against human leukemic cells (4). The mechanism behind relies on the increased intracellular level of the drug upon C_{60} delivery. C_{60} promotes the passive diffusion of the small molecules and induces endocytosis/pinocytosis preferentially in cancer compared to normal cells (Asada et al., 2014). The reversible π - π stacking of cargo on C_{60} enables the drug release inside leukemic cells. The allocation of C_{60} and drug inside leukemic cells sets suitable conditions for preservation of their each separate anticancer activity mechanism. Thus, Doxorubicin intercalates DNA pairs and blocks its transcription, replication and repair, whereas C_{60} is localized predominantly in mitochondria. Photoexcitation of accumulated C_{60} with visible light induced the mitochondrial pathway of compact cell death apoptosis that boosted its application in cancer photodynamic therapy. The drug delivery and photosensitizing ability of C_{60} supports the combination of the chemo- and photodynamic cancer treatment strategies on the basis of the simple double C_{60} -drug nanosystem.

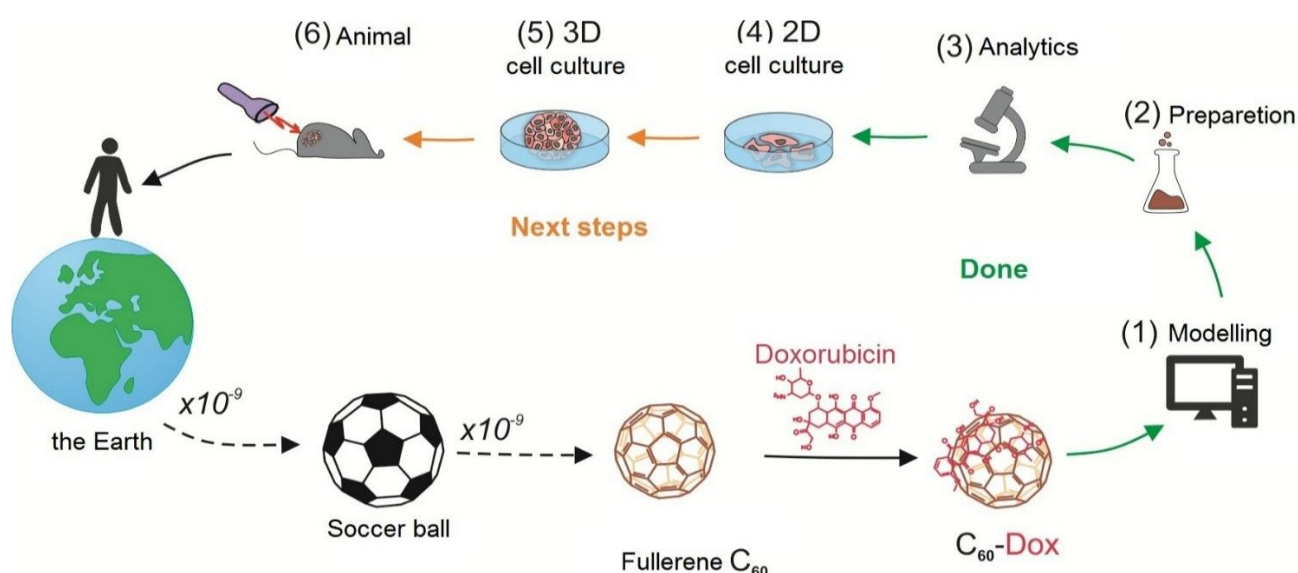


Figure 38. The workflow for studies towards C_{60} -based anticancer photodynamic chemotherapy: computer modeling of the C_{60} -drug (1); the fast and cost-effective preparation of the new nanocomplexes (2); analytical assessment of nanocomplex stability to prove its biological applicability (3); noncovalent complexation of aromatic drug molecule with C_{60} improves its efficiency against human leukemic cells (4); 3D cell culture and *in vivo* study with tumor-bearing mice are planned (5 and 6).

The next research is designed to carry out the next steps of the development of proposed C₆₀-based anticancer treatment strategy (5 and 6). Since tumors are composed of genetically and phenotypically heterogeneous cancer cells, modeling the complexity of human cancers in preclinical testing models is a challenge. The further optimal research strategy flows from monolayer (2D) and three dimensional (3D) cell culture to tumor-bearing animal studies and aims to deliver a preclinical proof-of-concept for the developed cancer treatment strategy.

Cell lines are the most widely used model in cancer research, however, the test of the treatment modalities on normal healthy cells remains to be a burning challenge in cell culture research due to the high difficulty to introduce normal cells in the culture with neither genetic nor physiologic alterations. The biologically relevant and meaningful data concerning the normal healthy cell response to the cancer treatment could be delivered using human primary cell lines. The other aspect of the simplification in the cell culture is the absence of the representation of full heterogeneity along genetic, transcriptomic, epigenetic and/or phenotypic alterations found in the cancer tissue (Dagogo-Jack & Shaw, 2017). A bulk solid tumor is a heterogeneous entity that predominantly consists of drug-sensitive cells, however, the presence of drug-resistant cells drives a disease relapse and further progression after treatment. Thus, the investigation of biochemical activity of developed treatment strategy on drug-resistant cancer cell lines helps to optimize experimental set-up. Taken together with the data of current research with treatment-naïve cell lines, the planned research will provide information for precise dose of the drug and duration for next studies on the tissue level.

Following the biological organization to the next level, the study on the tissue level is enabled using advanced 3D cell culture techniques. The 3D cell culture system takes the actual microenvironment where cells reside in tissues and heterogeneity into account (Edmondson et al., 2014). The core cells of 3D spheroids receive less oxygen, growth factors and nutrients from the medium, therefore, tend to be in a quiescent or hypoxic state. Such cellular heterogeneity resembles *in vivo* tumor tissue environment.

Thus, the behavior of 3D-cultured cells is more reflective of *in vivo* cellular responses and provides more accurate information about pharmacological activity and predict *in vivo* interactions of the designed cancer treatment approach. Based on the data obtained on 3D cells the final drug formulation and light exposure conditions could set a ground for the animal study.

Further work is necessary for a successful transfer of the developed treatment strategy aimed on the investigation effects of C₆₀ nanocomplexes on the animal model. The experimental model of tumor-bearing animals possesses a great opportunity for better understanding of anticancer action mechanisms of C₆₀-drug toxicity. The study on xenografts of human cancer models in immunodeficient mice as the classical model could address the regulators' requirements whether new medicine demonstrates acceptable balance of safety and efficacy. The limited penetration depth of the light in biological tissues could challenge the application the developed C₆₀- and 405 nm LED-based photodynamic treatment strategy in a frame of the photodynamic cancer chemotherapy. For that, the promising approach of using ultrasound instead of light for C₆₀ molecule excitation could be used and was previously discussed in the "V.1.2 *Photodynamic treatment of leukemic cells with C₆₀ fullerene*". Further possible solutions to improve light penetration of biological tissues could include additional skin optical clearing (Hirshburg et al., 2007; Zhu et al., 2013) or coupling of the LED light source with fiber optics for direct and precise light intratissue delivery. The synthesis of new C₆₀ derivatives and nanocomplexes presents another possibility to advance C₆₀-based PDT. For example, in order to increase the red light absorption C₆₀ molecule can be modified with decacationic radicals (Sperandio et al., 2013) and additional red light harvesting chromophores (Lee et al., 2013; Li et al., 2014). Finally, since blue light photon, proven to be the most efficient for C₆₀ excitation, has doubled energy of a red light photon, two red photons could be delivered quasi simultaneously instead of one blue photon by means of nonlinear optics approaches (Sharma et al., 2011; Shen et al., 2016). The essential difference between two-photon and one-photon traditional PDT is the light absorption mechanism, while further photophysical and

photochemical processes are the same, giving ground to rely on the similar high treatment efficiency.

Since the employment of fullerenes for cancer treatment is still at an early stage of development, the high attention should be paid to an identification of possible toxicity and safety of any new C₆₀ formulation. The studies examining the toxicity of fullerenes on human systems are still emerging and the subject of much debate. A number of factors alter C₆₀'s toxicity including but not limited to its chemical structure, surface modifications and preparation procedure. Pristine C₆₀ was shown to have no acute or sub-acute toxicity in a large variety of living organisms, from bacterial and fungal to human cells, and also in drosophila, mice, rats and guinea pigs (Andrievsky et al., 2005; Kolosnjaj et al., 2007; Aschberger et al., 2010, 2010; Kepley, 2012; Emelyantsev et al., 2019; Prylutska et al., 2019). However, pristine C₆₀ has a very long biological half-life that determines its bioaccumulation and long-term effects (Nielsen et al., 2008; Johnston et al., 2010; Stueckle et al., 2016). The pharmacodynamics and pharmacokinetics of any new C₆₀ formulation should certainly be defined that requires further investigations before an effective assessment of possible human health risks can be done.

The potential for using fullerene-based medicines is substantial but concerns of toxicity have slowed the initial enthusiasm that surrounded their discovery. The promising results have emerged in the last years, bringing fullerenes again to the front of interest. There seems to exist an increasing interest for industry in the field of fullerenes, which accounts for a good economic perspective. The proposed treatment strategy was already discussed with competent partners and potential investors from Pfizer Innovative Health and Boehringer Ingelheim. The preliminary agreement states of the requirement to deliver results of animal studies, after what the partnering cooperation could be developed. So, successful completion of the animal project has a potential to establish a transferred technology to be tested in the human clinical trials. The scale-up of the proposed treatment technology will require escalation of the product manufacturing in closer cooperation with existing national companies.

VI. REFERENCES

- Abd El-Wahab A.E., Ghareeb D.A., Sarhan E.E.M., Abu-Serie M.M. & El Demellawy M.A. 2013. *In vitro* biological assessment of *Berberis vulgaris* and its active constituent, Berberine: antioxidants, anti-acetylcholinesterase, anti-diabetic and anticancer effects. *BMC Complement Altern Med.* 13: 218.
- Agostinis P., Berg K., Cengel K.A., Foster T.H., Girotti A.W., Gollnick S.O., Hahn S.M., Hamblin M.R., Juzeniene A., Kessel D., Korbelik M., Moan J., Mroz P., Nowis D., Piette J., Wilson B.C. & Golab J. 2011. Photodynamic therapy of cancer: an update. *CA Cancer J Clin.* 61: 250–281.
- Akiyama M., Ikeda A., Shintani T., Doi Y., Kikuchi J., Ogawa T., Yogo K., Takeya T. & Yamamoto N. 2008. Solubilisation of [60]fullerenes using block copolymers and evaluation of their photodynamic activities. *Org. Biomol. Chem.* 6: 1015–1019.
- Akter M., Sikder Md.T., Rahman Md.M., Ullah A.K.M.A., Hossain K.F.B., Banik S., Hosokawa T., Saito T. & Kurasaki M. 2018. A systematic review on silver nanoparticles-induced cytotoxicity: Physicochemical properties and perspectives. *Journal of Advanced Research.* 9: 1–16.
- Albring K.F., Weidemüller J., Mittag S., Weiske J., Friedrich K., Geroni M.C., Lombardi P. & Huber O. 2013. Berberine acts as a natural inhibitor of Wnt/ β -catenin signaling – Identification of more active 13-arylalkyl derivatives. *BioFactors.* 39: 652–662.
- Ali S.S., Hardt J.I., Quick K.L., Sook Kim-Han J., Erlanger B.F., Huang T., Epstein C.J. & Dugan L.L. 2004. A biologically effective fullerene (C₆₀) derivative with superoxide dismutase mimetic properties. *Free Radical Biology and Medicine.* 37: 1191–1202.
- Amoêdo N.D., Valencia J.P., Rodrigues M.F., Galina A. & Rumjanek F.D. 2013. How does the metabolism of tumour cells differ from that of normal cells. *Biosci Rep.* 33: e00080.
- Andrievsky G., Klochkov V. & Derevyanchenko L. 2005. Is the C₆₀ Fullerene Molecule Toxic?! Fullerenes, Nanotubes and Carbon Nanostructures. 13: 363–376.
- Aniogo E.C., George B.P.A. & Abrahamse H. 2017. *In vitro* combined effect of Doxorubicin and sulfonated zinc Phthalocyanine-mediated photodynamic therapy on MCF-7 breast cancer cells. *Tumour Biol.* 39: 1010428317727278.
- Arora A., Balasubramanian C., Kumar N., Agrawal S., Ojha R.P. & Maiti S. 2008. Binding of Berberine to human telomeric quadruplex – spectroscopic, calorimetric and molecular modeling studies. *The FEBS Journal.* 275: 3971–3983.
- Arruebo M., Vilaboa N., Sáez-Gutierrez B., Lambea J., Tres A., Valladares M. & González-Fernández Á. 2011. Assessment of the evolution of cancer treatment therapies. *Cancers (Basel).* 3: 3279–3330.
- Arya N., Arora A., Vasu K.S., Sood A.K. & Katti D.S. 2013. Combination of single walled carbon nanotubes/graphene oxide with paclitaxel: a reactive oxygen species mediated synergism for treatment of lung cancer. *Nanoscale.* 5: 2818–2829.
- Asada R., Liao F., Saitoh Y. & Miwa N. 2014. Photodynamic anti-cancer effects of fullerene [C₆₀]-PEG complex on fibrosarcomas preferentially over normal fibroblasts in terms of fullerene uptake and cytotoxicity. *Mol. Cell. Biochem.* 390: 175–184.
- Aschberger K., Johnston H.J., Stone V., Aitken R.J., Tran C.L., Hankin S.M., Peters S.A.K. & Christensen F.M. 2010. Review of fullerene toxicity and exposure – appraisal of a human health risk assessment, based on open literature. *Regulatory Toxicology and Pharmacology.* 58: 455–473.
- Baati T., Bourasset F., Gharbi N., Njim L., Abderrabba M., Kerkeni A., Szwarc H. & Moussa F. 2012. The prolongation of the lifespan of rats by repeated oral administration of [60]fullerene. *Biomaterials.* 33: 4936–4946.

- Bao J., Huang B., Zou L., Chen S., Zhang C., Zhang Y., Chen M., Wan J.-B., Su H., Wang Y. & He C. 2015. Hormetic effect of Berberine attenuates the anticancer activity of chemotherapeutic agents. *PLoS One*. 10: e0139298.
- Barenholz Y. (Chezy) 2012. Doxil® – The first FDA-approved nano-drug: lessons learned. *Journal of Controlled Release*. 160: 117–134.
- Bedrov D., Smith G.D., Davande H. & Li L. 2008. Passive Transport of C₆₀ Fullerenes through a Lipid Membrane: A Molecular Dynamics Simulation Study. *J. Phys. Chem. B*. 112: 2078–2084.
- Bharali D.J., Khalil M., Gurbuz M., Simone T.M. & Mousa S.A. 2009. Nanoparticles and cancer therapy: A concise review with emphasis on dendrimers. *Int J Nanomedicine*. 4: 1–7.
- Bhowmick N.A., Neilson E.G. & Moses H.L. 2004. Stromal fibroblasts in cancer initiation and progression. *Nature*. 432: 332–337.
- Biju V. 2014. Chemical modifications and bioconjugate reactions of nanomaterials for sensing, imaging, drug delivery and therapy. *Chem. Soc. Rev.* 43: 744–764.
- Bilobrov V., Sokolova V., Prylutska S., Panchuk R., Litsis O., Osetskyi V., Evstigneev M., Prylutsky Yu., Epple M., Ritter U. & Rohr J. 2019. A novel nanoconjugate of Landomycin A with C₆₀ fullerene for cancer targeted therapy: *in vitro* studies. *Cel. Mol. Bioeng.* 12: 41–51.
- Blazkova I., Viet Nguyen H., Kominkova M., Konecna R., Chudobova D., Krejcova L., Kopel P., Hynek D., Zitka O., Beklova M., Adam V. & Kizek R. 2014. Fullerene as a transporter for Doxorubicin investigated by analytical methods and *in vivo* imaging. *Electrophoresis*. 35: 1040–1049.
- Bochvar, D. A. & E. G. Galpern 1973. Hypothetical systems-carbododecahedron, s-icosahedron and carbo-s-icosahedron. *Dokl. Akad. Nauk SSSR*. 209: 610-612 (in Russian).
- Borowik A., Prylutsky Y., Kawelski Ł., Kyzyma O., Bulavin L., Ivankov O., Cherepanov V., Wyrzykowski D., Kaźmierkiewicz R., Gołński G., Woźniowiczka A., Evstigneev M., Ritter U. & Piosik J. 2018. Does C₆₀ fullerene act as a transporter of small aromatic molecules?. *Colloids Surf B Biointerfaces*. 164: 134–143.
- Boyd P.D.W., Hodgson M.C., Rickard C.E.F., Oliver A.G., Chaker L., Brothers P.J., Bolskar R.D., Tham F.S. & Reed C.A. 1999. Selective supramolecular porphyrin/fullerene interactions 1. *J. Am. Chem. Soc.* 121: 10487–10495.
- Braden B.C., Goldbaum F.A., Chen B.-X., Kirschner A.N., Wilson S.R. & Erlanger B.F. 2000. X-ray crystal structure of an anti-Buckminsterfullerene antibody Fab fragment: Biomolecular recognition of C₆₀. *Proceedings of the National Academy of Sciences*. 97: 12193–12197.
- Bradford M.M. 1976. A rapid and sensitive method for the quantitation of microgram quantities of protein utilizing the principle of protein-dye binding. *Anal. Biochem.* 72: 248–254.
- Bray F., Ferlay J., Soerjomataram I., Siegel R.L., Torre L.A. & Jemal A. 2018. Global cancer statistics 2018: GLOBOCAN estimates of incidence and mortality worldwide for 36 cancers in 185 countries. *CA: A Cancer Journal for Clinicians*. 68: 394–424.
- Brücher B.L.D.M. & Jamall I.S. 2014. Cell-cell communication in the tumor microenvironment, carcinogenesis, and anticancer treatment. *CPB*. 34: 213–243.
- Burlaka A.P., Sidorik Y.P., Prylutska S.V., Matyshevska O.P., Golub O.A., Prylutsky Y.I. & Scharff P. 2004. Catalytic system of the reactive oxygen species on the C₆₀ fullerene basis. *Exp. Oncol.* 26: 326–327.
- Buytaert E., Dewaele M. & Agostinis P. 2007. Molecular effectors of multiple cell death pathways initiated by photodynamic therapy. *Biochimica et Biophysica Acta (BBA) - Reviews on Cancer*. 1776: 86–107.
- Buzea C., Pacheco I.I. & Robbie K. 2007. Nanomaterials and nanoparticles: Sources and toxicity. *Biointerphases*. 2: MR17–MR71.
- Cai Y., Xia Q., Luo R., Huang P., Sun Y., Shi Y. & Jiang W. 2014. Berberine inhibits the growth of human colorectal adenocarcinoma *in vitro* and *in vivo*. *J Nat Med*. 68: 53–62.
- Cai Z., Lin M., Wuchter C., Ruppert V., Dörken B., Ludwig W.D. & Karawajew L. 2001. Apoptotic response to homoharringtonine in human wt p53 leukemic cells is independent of reactive oxygen species generation and implicates Bax translocation, mitochondrial cytochrome c release and caspase activation. *Leukemia*. 15: 567–574.

- Candido N.M., de Melo M.T., Franchi L.P., Primo F.L., Tedesco A.C., Rahal P. & Calmon M.F. 2018. Combining photodynamic therapy and chemotherapy: improving breast cancer treatment with nanotechnology. *J Biomed Nanotechnol.* 14: 994–1008.
- Capek I. 2017. Polymer decorated gold nanoparticles in nanomedicine conjugates. *Adv Colloid Interface Sci.* 249: 386–399.
- Carmichael J., DeGraff W.G., Gazdar A.F., Minna J.D. & Mitchell J.B. 1987. Evaluation of a tetrazolium-based semiautomated colorimetric assay: assessment of chemosensitivity testing. *Cancer Res.* 47: 936–942.
- Castano A.P., Demidova T.N. & Hamblin M.R. 2004. Mechanisms in photodynamic therapy: part one - photosensitizers, photochemistry and cellular localization. *Photodiagnosis Photodyn Ther.* 1: 279–293.
- Castro E., Hernandez Garcia A., Zavala G. & Echegoyen L. 2017. Fullerenes in Biology and Medicine. *J Mater Chem B Mater Biol Med.* 5: 6523–6535.
- Cernáková M., Kost'álová D., Kettmann V., Plodová M., Tóth J. & Drímal J. 2002. Potential antimutagenic activity of Berberine, a constituent of *Mahonia aquifolium*. *BMC Complement Altern Med.* 2: 2.
- Chabner B.A. & Roberts T.G. 2005. Timeline: chemotherapy and the war on cancer. *Nat. Rev. Cancer.* 5: 65–72.
- Changenet-Barret P., Gustavsson T., Markovitsi D., Manet I. & Monti S. 2013. Unravelling molecular mechanisms in the fluorescence spectra of Doxorubicin in aqueous solution by femtosecond fluorescence spectroscopy. *Physical Chemistry Chemical Physics.* 15: 2937–2944.
- Chaudhuri P., Paraskar A., Soni S., Mashelkar R.A. & Sengupta S. 2009. Fullerenol-cytotoxic conjugates for cancer chemotherapy. *ACS Nano.* 3: 2505–2514.
- Chen B.-X., Wilson S.R., Das M., Coughlin D.J. & Erlanger B.F. 1998. Antigenicity of fullerenes: antibodies specific for fullerenes and their characteristics. *Proceedings of the National Academy of Sciences.* 95: 10809–10813.
- Chen EH L.D. & Xu B D.J. 2015. Anticancer drug combinations, a big momentum is needed. *Journal of Postgenomics Drug & Biomarker Development.* 5: 3.
- Chen G., Roy I., Yang C. & Prasad P.N. 2016a. Nanochemistry and nanomedicine for nanoparticle-based diagnostics and therapy. *Chem. Rev.* 116: 2826–2885.
- Chen Q., Wang X., Wang C., Feng L., Li Y. & Liu Z. 2015. Drug-induced self-assembly of modified albumins as nano-theranostics for tumor-targeted combination therapy. *ACS Nano.* 9: 5223–5233.
- Chen Y.-W., Hwang K.C., Yen C.-C. & Lai Y.-L. 2004. Fullerene derivatives protect against oxidative stress in RAW 264.7 cells and ischemia-reperfused lungs. *American Journal of Physiology-Regulatory, Integrative and Comparative Physiology.* 287: R21–R26.
- Chen Y.-W., Liu T.-Y., Chang P.-H., Hsu P.-H., Liu H.-L., Lin H.-C. & Chen S.-Y. 2016b. A theranostic nrGO@MSN-ION nanocarrier developed to enhance the combination effect of sonodynamic therapy and ultrasound hyperthermia for treating tumor. *Nanoscale.* 8: 12648–12657.
- Cheng N., Chytil A., Shyr Y., Joly A. & Moses H.L. 2008. TGF- β signaling deficient fibroblasts enhance Hepatocyte Growth Factor signaling in mammary carcinoma cells to promote scattering and invasion. *Mol Cancer Res.* 6: 1521–1533.
- Cheng R. & Xue Y. 2016. Carbon nanomaterials for drug delivery. In: Zhang M., Naik R.R., & Dai L. (eds), *Carbon Nanomaterials for Biomedical Applications*, Springer International Publishing, Cham. 31–80.
- Cheng W., Haedicke I.E., Nofiele J., Martinez F., Beera K., Scholl T.J., Cheng H.-L.M. & Zhang X.-A. 2014. Complementary strategies for developing Gd-free high-field T₁ MRI contrast agents based on Mn(III) porphyrins. *J. Med. Chem.* 57: 516–520.
- Chirico F., Fumelli C., Marconi A., Tinari A., Straface E., Malorni W., Pellicciari R. & Pincelli C. 2007. Carboxyfullerenes localize within mitochondria and prevent the UVB-induced intrinsic apoptotic pathway. *Exp. Dermatol.* 16: 429–436.
- Chistyakov V.A., Prazdnova E.V., Soldatov A.V., Smirnova Y.O. & Alperovich I. 2014. Can C₆₀ fullerene demonstrate properties of mitochondria-targeted antioxidant from the computational point of view?. *8: 4.*
- Chitkara D. 2018. *Molecular medicines for cancer: concepts and applications of nanotechnology.* CRC Press.

- Chou T.-C. 2006. Theoretical basis, experimental design, and computerized simulation of synergism and antagonism in drug combination studies. *Pharmacol. Rev.* 58: 621–681.
- Choudhary N., Hwang S. & Choi W. 2014. Carbon Nanomaterials: A Review. In: Bhushan B., Luo D., Schricker S.R., Sigmund W., & Zauscher S. (eds), *Handbook of Nanomaterials Properties*, Springer Berlin Heidelberg, Berlin, Heidelberg. 709–769.
- Cleary A.S., Leonard T.L., Gestl S.A. & Gunther E.J. 2014. Tumour cell heterogeneity maintained by cooperating subclones in Wnt-driven mammary cancers. *Nature.* 508: 113–117.
- Cooper G.M. 2000. *The development and causes of cancer. The cell: a molecular approach.* 2nd edition.
- Cortés-Funes H. & Coronado C. 2007. Role of anthracyclines in the era of targeted therapy. *Cardiovasc Toxicol.* 7: 56–60.
- Costley D., Mc Ewan C., Fowley C., McHale A.P., Atchison J., Nomikou N. & Callan J.F. 2015. Treating cancer with sonodynamic therapy: a review. *International Journal of Hyperthermia.* 31: 107–117.
- Curl R.F. & Smalley R.E. 1988. Probing C₆₀. *Science.* 242: 1017–1022.
- Dagogo-Jack I. & Shaw A.T. 2017. Tumour heterogeneity and resistance to cancer therapies. *Nature Reviews Clinical Oncology.* 15: 81–94.
- Danhier F., Feron O. & Préat V. 2010. To exploit the tumor microenvironment: Passive and active tumor targeting of nanocarriers for anti-cancer drug delivery. *J Control Release.* 148: 135–146.
- Davidson R.A. 1981. Spectral analysis of graphs by cyclic automorphism subgroups. *Theoret. Chim. Acta.* 58: 193–231.
- Davies M. & Samuels Y. 2010. Analysis of the genome to personalize therapy for melanoma. *Oncogene.* 29: 5545–5555.
- Delgado J.L., Filippone S., Giacalone F., Herranz M.A., Illescas B., Pérez E.M. & Martín N. 2014. Buckyballs. *Top Curr Chem.* 350: 1–64.
- Dellinger A.L., Cunin P., Lee D., Kung A.L., Brooks D.B., Zhou Z., Nigrovic P.A. & Kepley C.L. 2015. Inhibition of inflammatory arthritis using fullerene nanomaterials. *PLOS ONE.* 10: e0126290.
- Didenko Y.T. & Pugach S.P. 1994. Spectra of water sonoluminescence. *The Journal of Physical Chemistry.* 98: 9742–9749.
- Dolmans D.E.J.G.J., Fukumura D. & Jain R.K. 2003. Photodynamic therapy for cancer. *Nat. Rev. Cancer.* 3: 380–387.
- Dong H. & Cao Y. 2018. *Carbon nanomaterials for optical bioimaging and phototherapy. Carbon Nanomaterials for Bioimaging, Bioanalysis, and Therapy*, John Wiley & Sons, Ltd. 43–62.
- Dorsey J.G. & Dill K.A. 1989. The molecular mechanism of retention in reversed-phase liquid chromatography. *Chem. Rev.* 89: 331–346.
- Dougherty T.J. 1974. Activated dyes as antitumor agents. *JNCI: Journal of the National Cancer Institute.* 52: 1333–1336.
- Dougherty T.J. 1996. A brief history of clinical photodynamic therapy development at Roswell Park Cancer Institute. *Journal of Clinical Laser Medicine & Surgery.* 14: 219–221.
- Dutta R. 2007. Drug carriers in pharmaceutical design: promises and progress. *CPD.* 13: 761–769.
- Edmondson R., Broglie J.J., Adcock A.F. & Yang L. 2014. Three-dimensional cell culture systems and their applications in drug discovery and cell-based biosensors. *Assay Drug Dev Technol.* 12: 207–218.
- Emelyantsev S., Prazdnova E., Chistyakov V. & Alperovich I. 2019. Biological effects of C₆₀ fullerene revealed with bacterial biosensor – toxic or rather antioxidant? *Biosensors.* 9: 81.
- Erkiert-Polguj A., Halbina A., Polak-Pacholczyk I. & Rotsztein H. 2016. Light-emitting diodes in photodynamic therapy in non-melanoma skin cancers--own observations and literature review. *J Cosmet Laser Ther.* 18: 105–110.
- Eruslanov E. & Kusmartsev S. 2010. Identification of ROS using oxidized DCFDA and flow-cytometry. *Methods Mol. Biol.* 594: 57–72.
- Evstigneev M.P., Buchelnikov A.S., Voronin D.P., Rubin Y.V., Belous L.F., Prylutsky Y.I. & Ritter U. 2013. Complexation of C₆₀ fullerene with aromatic drugs. *Chemphyschem.* 14: 568–578.

- Fan J., Fang G., Zeng F., Wang X. & Wu S. 2013. Water-dispersible fullerene aggregates as a targeted anticancer prodrug with both chemo- and photodynamic therapeutic actions. *Small*. 9: 613–621.
- Fan W., Yung B., Huang P. & Chen X. 2017. Nanotechnology for multimodal synergistic cancer therapy. *Chemical Reviews*. 117: 13566–13638.
- Fang F.C. & Casadevall A. 2010. Lost in translation – basic science in the era of translational research. *Infection and Immunity*. 78: 563–566.
- Fesik S.W. 2005. Promoting apoptosis as a strategy for cancer drug discovery. *Nat. Rev. Cancer*. 5: 876–885.
- Feynman R.P. 1960. There's plenty of room at the bottom. *Engineering and Science*. 23: 22–36.
- Fiaschi T. & Chiarugi P. 2012. Oxidative stress, tumor microenvironment, and metabolic reprogramming: a diabolic liaison. *Int J Cell Biol*. 2012: 762825.
- Finn N.A., Findley H.W. & Kemp M.L. 2011. A switching mechanism in Doxorubicin bioactivation can be exploited to control Doxorubicin toxicity. *PLoS Comput. Biol*. 7: e1002151.
- Flusberg B.A., Cocker E.D., Piyawattanametha W., Jung J.C., Cheung E.L.M. & Schnitzer M.J. 2005. Fiberoptic fluorescence imaging. *Nat Methods*. 2: 941–950.
- Fojtu M., Gumulec J., Stracina T., Raudenska M., Skotakova A., Vaculovicova M., Adam V., Babula P., Novakova M. & Masarik M. 2017. Reduction of Doxorubicin-induced cardiotoxicity using nanocarriers: a review. *Curr. Drug Metab*. 18: 237–263.
- Franceschin M., Rossetti L., D'Ambrosio A., Schirripa S., Bianco A., Ortaggi G., Savino M., Schultes C. & Neidle S. 2006. Natural and synthetic G-quadruplex interactive Berberine derivatives. *Bioorganic & Medicinal Chemistry Letters*. 16: 1707–1711.
- Franskevych D., Palyvoda K., Petukhov D., Prylutska S., Grynyuk I., Schuetze C., Drobot L., Matyshevskaya O. & Ritter U. 2017. Fullerene C₆₀ Penetration into leukemic cells and its photoinduced cytotoxic effects. *Nanoscale Res Lett*. 12: 40.
- Frezza C., Cipolat S. & Scorrano L. 2007. Organelle isolation: functional mitochondria from mouse liver, muscle and cultured fibroblasts. *Nature Protocols*. 2: 287–295.
- Friedman S.H., DeCamp D.L., Sijbesma R.P., Srdanov G., Wudl F. & Kenyon G.L. 1993. Inhibition of the HIV-1 protease by fullerene derivatives: model building studies and experimental verification. *J. Am. Chem. Soc*. 115: 6506–6509.
- Gaitan D.F., Atchley A.A., Lewia S.D., Carlson J.T., Maruyama X.K., Moran M. & Sweider D. 1996. Spectra of single-bubble sonoluminescence in water and glycerin-water mixtures. *Physical Review E*. 54: 525–528.
- Gao F., He G., Yin H., Chen J., Liu Y., Lan C., Zhang S. & Yang B. 2019. Titania-coated 2D gold nanoplates as nanoagents for synergistic photothermal/sonodynamic therapy in the second near-infrared window. *Nanoscale*. 11: 2374–2384.
- Gao J., Wang Y., Folta K.M., Krishna V., Bai W., Indeglia P., Georgieva A., Nakamura H., Koopman B. & Moudgil B. 2011. Polyhydroxy fullerenes (fullerols or fullerlenols): beneficial effects on growth and lifespan in diverse biological models. *PLoS ONE*. 6: e19976.
- Georghiou P.E. 2016. Calixarenes and Fullerenes. In: Neri P., Sessler J.L., & Wang M.-X. (eds), *Calixarenes and beyond*, Springer International Publishing, Cham. 879–919.
- Gharbi N., Pressac M., Hadchouel M., Szwarc H., Wilson S.R. & Moussa F. 2005. [60]Fullerene is a powerful antioxidant *in vivo* with no acute or subacute toxicity. *Nano Lett*. 5: 2578–2585.
- Giancotti F.G. 2014. Deregulation of cell signaling in cancer. *FEBS Letters*. 588: 2558–2570.
- Gollwitzer C., Bartczak D., Goenaga-Infante H., Kestens V., Krumrey M., Minelli C., Pálmai M., Ramaye Y., Roebben G., Sikora A. & Varga Z. 2016. A comparison of techniques for size measurement of nanoparticles in cell culture medium. *Anal. Methods*. 8: 5272–5282.
- Golombek S.K., May J.-N., Theek B., Appold L., Drude N., Kiessling F. & Lammers T. 2018. Tumor targeting via EPR: strategies to enhance patient responses. *Adv Drug Deliv Rev*. 130: 17–38.
- Goodarzi S., Da Ros T., Conde J., Sefat F. & Mozafari M. 2017. Fullerene: biomedical engineers get to revisit an old friend. *Materials Today*. 20: 460–480.

- Grebinyk S.M., Palyvoda K.O., Prylutska S.V., Grynyuk I.I., Samoylenko A.A., Drobot L.B. & Matyshevska O.P. 2012a. Photoactivated fullerene C₆₀ induces store-operated Ca²⁺ entry and cytochrome c release in Jurkat cells. *Ukr Biokhim Zh.* 84: 58–63.
- Grinholc M., Nakonieczna J., Fila G., Taraszkiwicz A., Kawiak A., Szewczyk G., Sarna T., Lilge L. & Bielawski K.P. 2015. Antimicrobial photodynamic therapy with fulleropyrrolidine: photoinactivation mechanism of *Staphylococcus aureus*, *in vitro* and *in vivo* studies. *Appl Microbiol Biotechnol.* 99: 4031–4043.
- Grynyuk I., Grebinyk S., Prylutska S., Mykhailova A., Franskevich D., Matyshevska O., Schütze C. & Ritter U. 2013. Photoexcited fullerene C₆₀ disturbs prooxidant-antioxidant balance in leukemic L1210 cells. *Mat.-wiss. u. Werkstofftech.* 44: 139–143.
- Gumbiner B.M. 1996. Cell Adhesion: The molecular basis of tissue architecture and morphogenesis. *Cell.* 84: 345–357.
- Gumenyuk V.G., Bashmakova N.V., Kutovyy S.Y., Yashchuk V.M. & Zaika L.A. 2012. Binding parameters of alkaloids Berberine and sanguinarine with DNA. *Ukr J Phys.* 56: 524–533.
- Guo Q., Huang F., Goncalves C., Del Rincón S.V. & Miller W.H. 2019. Translation of cancer immunotherapy from the bench to the bedside. *Adv. Cancer Res.* 143: 1–62.
- Guo X., Ding R., Zhang Y., Ye L., Liu X., Chen C., Zhang Z. & Zhang Y. 2014. Dual role of photosensitizer and carrier material of fullerene in micelles for chemo–photodynamic therapy of cancer. *Journal of Pharmaceutical Sciences.* 103: 3225–3234.
- Gupta A.K. & Gupta M. 2005. Cytotoxicity suppression and cellular uptake enhancement of surface modified magnetic nanoparticles. *Biomaterials.* 26: 1565–1573.
- Gupta S.C., Hevia D., Patchva S., Park B., Koh W. & Aggarwal B.B. 2012. Upsides and downsides of reactive oxygen species for cancer: the roles of reactive oxygen species in tumorigenesis, prevention, and therapy. *Antioxid Redox Signal.* 16: 1295–1322.
- Hait W.N. 2010. Anticancer drug development: the grand challenges. *Nature Reviews Drug Discovery.* 9: 253–254.
- Hamblin M.R. 2018. Fullerenes as photosensitizers in photodynamic therapy: pros and cons. *Photochem Photobiol Sci.* 17: 1515–1533.
- Hanahan D. & Weinberg R.A. 2011. Hallmarks of cancer: the next generation. *Cell.* 144: 646–674.
- Harush-Frenkel O., Debotton N., Benita S. & Altschuler Y. 2007. Targeting of nanoparticles to the clathrin-mediated endocytic pathway. *Biochem. Biophys. Res. Commun.* 353: 26–32.
- Hassan M., Watari H., AbuAlmaaty A., Ohba Y. & Sakuragi N. 2014. Apoptosis and molecular targeting therapy in cancer. *Biomed Res Int.* 2014: 150845.
- Hassanpour S.H. & Dehghani M. 2017. Review of cancer from perspective of molecular. *Journal of Cancer Research and Practice.* 4: 127–129.
- Hempstead J., Jones D.P., Ziouche A., Cramer G.M., Rizvi I., Arnason S., Hasan T. & Celli J.P. 2015. Low-cost photodynamic therapy devices for global health settings: characterization of battery-powered LED performance and smartphone imaging in 3D tumor models. *Sci Rep.* 5: 10093.
- Herst P.M., Rowe M.R., Carson G.M. & Berridge M.V. 2017. Functional mitochondria in health and disease. *Front Endocrinol (Lausanne).* 8: 296.
- Hirshburg J., Choi B., Nelson J.S. & Yeh A.T. 2007. *Zhu. Lasers Surg Med.* 39: 140–144.
- Holohan C., Van Schaeybroeck S., Longley D.B. & Johnston P.G. 2013. Cancer drug resistance: an evolving paradigm. *Nat Rev Cancer.* 13: 714–726.
- Honary S. & Zahir F. 2013. Effect of zeta potential on the properties of nano-drug delivery systems - a review (Part 2). *Trop. J. Pharm Res.* 12: 265–273.
- Horie M., Nishio K., Kato H., Shinohara N., Nakamura A., Fujita K., Kinugasa S., Endoh S., Yamamoto K., Yamamoto O., Niki E., Yoshida Y. & Iwahashi H. 2010. *In vitro* evaluation of cellular responses induced by stable fullerene C₆₀ medium dispersion. *J. Biochem.* 148: 289–298.
- Hu Z. & Lu X. 2014. Chapter 8 - mechanical properties of carbon nanotubes and graphene. in: tanaka k. & iijima s. (eds), carbon nanotubes and graphene (second edition), Elsevier, Oxford. 165–200.

- Huang Y., Xie P., Yang S.-T., Zhang X., Zeng G., Xin Q. & Tang X.-H. 2018. Carbon nanoparticles suspension injection for the delivery of Doxorubicin: Comparable efficacy and reduced toxicity. *Mater Sci Eng C Mater Biol Appl.* 92: 416–423.
- Huang Y.-Y., Sharma S.K., Yin R., Agrawal T., Chiang L.Y. & Hamblin M.R. 2014. Functionalized fullerenes in photodynamic therapy. *J Biomed Nanotechnol.* 10: 1918–1936.
- Hussain S., Vanoirbeek J.A.J. & Hoet P.H.M. 2012. Interactions of nanomaterials with the immune system: Interactions of nanomaterials with the immune system. *WIREs Nanomed Nanobiotechnol.* 4: 169–183.
- Husseini G.A., Kanan S. & Al-Sayah M. 2016. Investigating the fluorescence quenching of Doxorubicin in folic acid solutions and its relation to ligand-targeted nanocarriers. *J Nanosci Nanotechnol.* 16: 1410–1414.
- Iannazzo D., Piperno A., Pistone A., Grassi G. & Galvagno S. 2013. Recent advances in carbon nanotubes as delivery systems for anticancer drugs. *Curr. Med. Chem.* 20: 1333–1354.
- Iijima S. 1980. Direct observation of the tetrahedral bonding in graphitized carbon black by high resolution electron microscopy. *Journal of Crystal Growth.* 50: 675–683.
- Innocenti A., Durdagi S., Doostdar N., Strom T.A., Barron A.R. & Supuran C.T. 2010. Nanoscale enzyme inhibitors: fullerenes inhibit carbonic anhydrase by occluding the active site entrance. *Bioorg. Med. Chem.* 18: 2822–2828.
- Inui S., Aoshima H., Nishiyama A. & Itami S. 2011. Improvement of acne vulgaris by topical fullerene application: unique impact on skin care. *Nanomedicine: Nanotechnology, Biology and Medicine.* 7: 238–241.
- Isaacson C.W., Usenko C.Y., Tanguay R.L. & Field J.A. 2007. Quantification of fullerenes by LC/ESI-MS and its application to *in vivo* toxicity assays. *Anal. Chem.* 79: 9091–9097.
- Issa B. & Obaidat I.M. 2019. Magnetic nanoparticles as MRI contrast agents. *Magnetic Resonance Imaging.*
- Iuga C., Ortíz E. & Vivier-Bunge A. 2011. Antioxidant activity of fullerene C₆₀ against OH free radicals: A quantum chemistry and computational kinetics study. 3: 4.
- Iwase Y., Nishi K., Fujimori J., Fukai T., Yumita N., Ikeda T., Chen F., Momose Y. & Umemura S. 2016. Antitumor effect of sonodynamically activated pyrrolidine tris-acid fullerene. *Japanese Journal of Applied Physics.* 55: 07KF02.
- Jeelani P.G., Mulay P., Venkat R. & Ramalingam C. 2019. Multifaceted application of silica nanoparticles. *A Review. Silicon.* 12: 1337–1354.
- Jeevanandam J., Barhoum A., Chan Y.S., Dufresne A. & Danquah M.K. 2018. Review on nanoparticles and nanostructured materials: history, sources, toxicity and regulations. *Beilstein J Nanotechnol.* 9: 1050–1074.
- Jiang B.-H. & Liu L.-Z. 2009. PI3K/PTEN Signaling in angiogenesis and tumorigenesis. *Adv Cancer Res.* 102: 19–65.
- Jiang G. & Li G. 2012. Preparation, characterization, and properties of fullerene-vinylpyrrolidone copolymers. *Biotechnology Progress.* 28: 215–222.
- Jiao Q., Li L., Mu Q. & Zhang Q. 2014. Immunomodulation of nanoparticles in nanomedicine applications. *Biomed Res Int.* 2014: 762825.
- Johnston H.J., Hutchison G.R., Christensen F.M., Aschberger K. & Stone V. 2010. The biological mechanisms and physicochemical characteristics responsible for driving fullerene Toxicity. *Toxicol Sci.* 114: 162–182.
- Jung K. & Reszka R. 2001. Mitochondria as subcellular targets for clinically useful anthracyclines. *Adv. Drug Deliv. Rev.* 49: 87–105.
- Kalluru P., Vankayala R., Chiang C.-S. & Hwang K.C. 2016. Unprecedented “all-in-one” lanthanide-doped mesoporous silica frameworks for fluorescence/mr imaging and combination of NIR light triggered chemo-photodynamic therapy of tumors. *Advanced Functional Materials.* 26: 7908–7920.
- Kar T., Bettinger H.F., Scheiner S. & Roy A.K. 2008. Noncovalent π - π stacking and CH \cdots π interactions of aromatics on the surface of single-wall carbon nanotubes: an MP2 study. *J. Phys. Chem. C.* 112: 20070–20075.

- Kato S., Kikuchi R., Aoshima H., Saitoh Y. & Miwa N. 2010. Defensive effects of fullerene-C₆₀/liposome complex against UVA-induced intracellular reactive oxygen species generation and cell death in human skin keratinocytes HaCaT, associated with intracellular uptake and extracellular excretion of fullerene-C₆₀. *J. Photochem. Photobiol. B, Biol.* 98: 144–151.
- Ke M.-R., Chen S.-F., Peng X.-H., Zheng Q.-F., Zheng B.-Y., Yeh C.-K. & Huang J.-D. 2017. A tumor-targeted activatable phthalocyanine-tetrapeptide-Doxorubicin conjugate for synergistic chemophotodynamic therapy. *Eur J Med Chem.* 127: 200–209.
- Keahey P., Ramalingam P., Schmeler K. & Richards-Kortum R.R. 2016. Differential structured illumination microendoscopy for *in vivo* imaging of molecular contrast agents. *Proc Natl Acad Sci U S A.* 113: 10769–10773.
- Keasling J. 2008. From yeast to alkaloids. *Nature Chemical Biology.* 4: 524–525.
- Kepley C. 2012. Fullerenes in medicine; Will it ever Occur?. *J Nanomedic Nanotechnol.* 3: e111.
- Khaliq N.U., Park D.Y., Lee H.J., Oh K.S., Seo J.H., Kim S.Y., Hwang C.S., Lim T.-H. & Yuk S.H. 2018. Pluronic/Heparin nanoparticles for chemo-photodynamic combination cancer therapy through photoinduced caspase-3 activation. *ACS Appl. Nano Mater.* 1: 2943–2952.
- Khdair A., Chen D., Patil Y., Ma L., Dou Q.P., Shekhar M.P.V. & Panyam J. 2010. Nanoparticle-mediated combination chemotherapy and photodynamic therapy overcomes tumor drug resistance. *J Control Release.* 141: 137–144.
- Kim D., Lee M., Suh Y.D. & Kim S.K. 1992. Observation of fluorescence emission from solutions of C₆₀ and C₇₀ fullerenes and measurement of their excited-state lifetimes. *J. Am. Chem. Soc.* 114: 4429–4430.
- Kizek R., Adam V., Hrabeta J., Eckschlager T., Smutny S., Burda J.V., Frei E. & Stiborova M. 2012. Anthracyclines and ellipticines as DNA-damaging anticancer drugs: recent advances. *Pharmacol. Ther.* 133: 26–39.
- Kolosnjaj J., Szwarc H. & Moussa F. 2007. Toxicity Studies of Fullerenes and Derivatives. In: Chan W.C.W. (eds), *Bio-Applications of Nanoparticles*, Springer, New York, NY. 168–180
- Kolp B. 2018. Investigation of fullerene anticancer activity in combination with carbacylamidophosphates. Technical University of Applied Sciences Wildau, Wildau.
- Kong Q., Beel J.A. & Lillehei K.O. 2000. A threshold concept for cancer therapy. *Medical Hypotheses.* 55: 29–35.
- Koruga D., Simic-Krstic J., Matija L. & Ratkaj Z. 2002. Molecular nanotechnology: golden mean as a driving force of self-assembly. 7: 14765892.
- Koshland D.E.J. 1991. Molecule of the year. *Science.* 254: 1705.
- Kou L., Sun J., Zhai Y. & He Z. 2013. The endocytosis and intracellular fate of nanomedicines: Implication for rational design. *Asian Journal of Pharmaceutical Sciences.* 8: 1–10.
- Kratschmer W., Lambt L.D. & Fostiropoulos K. 1990. Solid C₆₀: a new form of carbon. 347: 354–358.
- Kroto H. 1988. Space, stars, C₆₀, and soot. *Science.* 242: 1139–1145.
- Kroto H. 1993. The Birth of C₆₀: Buckminsterfullerene. In: Kuzmany H., Fink J., Mehring M., & Roth S. (eds), *Electronic properties of fullerenes*, Springer Berlin Heidelberg, Berlin, Heidelberg. 1–7.
- Kroto H.W., Heath J.R., O'Brien S.C., Curl R.F. & Smalley R.E. 1985. C₆₀: Buckminsterfullerene. *Nature.* 318: 162–163.
- Kumar M. & Raza K. 2017. C₆₀-fullerenes as drug delivery carriers for anticancer agents: promises and hurdles. *Pharm Nanotechnol.* 5: 169–179.
- Kumari S., Singh S. & Das P. 2018. Carbon dots as a nanotool for integrated photodynamic therapy and chemotherapy. *Indian J. Chem.* 57B: 265–270.
- Kuo C.-L., Chi C.-W. & Liu T.-Y. 2005. Modulation of apoptosis by Berberine through inhibition of cyclooxygenase-2 and mcl-1 expression in oral cancer cells. *In vivo.* 19: 247–252.
- Labille J., Masion A., Ziarelli F., Rose J., Brant J., Villiéras F., Pelletier M., Borschneck D., Wiesner M.R. & Bottero J.-Y. 2009. Hydration and dispersion of C₆₀ in Aqueous systems: the nature of water–fullerene interactions. *Langmuir.* 25: 11232–11235.

- Lai P.-S., Lou P.-J., Peng C.-L., Pai C.-L., Yen W.-N., Huang M.-Y., Young T.-H. & Shieh M.-J. 2007. Doxorubicin delivery by polyamidoamine dendrimer conjugation and photochemical internalization for cancer therapy. *J Control Release*. 122: 39–46.
- Lee C.-M., Huang S.-T., Huang S.-H., Lin H.-W., Tsai H.-P., Wu J.-Y., Lin C.-M. & Chen C.-T. 2011. C₆₀ fullerene-pentoxifylline dyad nanoparticles enhance autophagy to avoid cytotoxic effects caused by the β -amyloid peptide. *Nanomedicine*. 7: 107–114.
- Lee D.J., Ahn Y.S., Youn Y.S. & Lee E.S. 2013. Poly(ethylene glycol)-crosslinked fullerenes for high efficient phototherapy: Multimeric Fullerenes. *Polymers for Advanced Technologies*. 24: 220–227.
- Lee Y.-H. & Ma Y.-T. 2017. Synthesis, characterization, and biological verification of anti-HER2 indocyanine green-Doxorubicin-loaded polyethyleneimine-coated perfluorocarbon double nanoemulsions for targeted photochemotherapy of breast cancer cells. *J Nanobiotechnology*. 15: 41.
- Levi N., Hantgan R.R., Lively M.O., Carroll D.L. & Prasad G.L. 2006. C₆₀-Fullerenes: detection of intracellular photoluminescence and lack of cytotoxic effects. *J Nanobiotechnology*. 4: 14.
- Li E., Sun Y., Lv G., Li Y., Zhang Z., Hu Z. & Cao W. 2019. Sinoporphyrin sodium based sonodynamic therapy induces anti-tumor effects in hepatocellular carcinoma and activates p53/caspase 3 axis. *Int. J. Biochem. Cell Biol*. 113: 104–114.
- Li L., Xie J., Zhang X., Chen J., Luo Y., Zhang L. & Luo R. 2010a. Retrospective study of photodynamic therapy vs photodynamic therapy combined with chemotherapy and chemotherapy alone on advanced esophageal cancer. *Photodiagnosis Photodyn Ther*. 7: 139–143.
- Li M.-M., Wang Y.-B., Zhang Y. & Wang W. 2016. The nature of the noncovalent interactions between benzene and C₆₀ fullerene. *J. Phys. Chem. A*. 120: 5766–5772.
- Li X., Zhang C., Le Guyader L. & Chen C. 2010b. “Smart” nanomaterials for cancer therapy. *Sci. China Chem*. 53: 2241–2249.
- Li X., Zhao X., Pardhi D., Wu Q., Zheng Y., Zhu H. & Mao Z. 2018. Folic acid modified cell membrane capsules encapsulating Doxorubicin and indocyanine green for highly effective combinational therapy *in vivo*. *Acta Biomater*. 74: 374–384.
- Li X.-L., Hu Y.-J., Wang H., Yu B.-Q. & Yue H.-L. 2012. molecular spectroscopy evidence of Berberine binding to DNA: Comparative Binding and Thermodynamic Profile of Intercalation. *Biomacromolecules*. 13: 873–880.
- Li Y., Zhou Q., Hu Z., Yang B., Li Q., Wang J., Zheng J. & Cao W. 2015. 5-Aminolevulinic acid-based sonodynamic therapy induces the apoptosis of osteosarcoma in mice. *PLoS One*. 10: e0132074.
- Li Z., Pan L.-L., Zhang F.-L., Zhu X.-L., Liu Y. & Zhang Z.-Z. 2014. 5-Aminolevulinic acid-loaded fullerene nanoparticles for *in vitro* and *in vivo* photodynamic therapy. *Photochem. Photobiol*. 90: 1144–1149.
- Liao F., Saitoh Y. & Miwa N. 2011. Anticancer effects of fullerene [C₆₀] included in polyethylene glycol combined with visible light irradiation through ROS generation and DNA fragmentation on fibrosarcoma cells with scarce cytotoxicity to normal fibroblasts. *Oncol. Res*. 19: 203–216.
- Liu H.-Q., An Y.-W., Hu A.-Z., Li M.-H. & Cui G.-H. 2019. Photodynamic therapy enhanced the antitumor effects of Berberine on HeLa cells. *Open Chemistry*. 17: 413–421.
- Liu J. & Tabata Y. 2010. Photodynamic therapy of fullerene modified with pullulan on hepatoma cells. *J Drug Target*. 18: 602–610.
- Liu J.-H., Cao L., Luo P.G., Yang S.-T., Lu F., Wang H., Meziani M.J., Haque Sk.A., Liu Y., Lacher S. & Sun Y.-P. 2010a. Fullerene-conjugated Doxorubicin in cells. *ACS Appl. Mater. Interfaces*. 2: 1384–1389.
- Liu T. & Troisi A. 2013. What makes fullerene acceptors special as electron acceptors in organic solar cells and how to replace them. *Adv. Mater. Weinheim*. 25: 1038–1041.
- Liu W., Zhang X., Liu P., Shen X., Lan T., Li W., Jiang Q., Xie X. & Huang H. 2010b. Effects of Berberine on matrix accumulation and NF-kappa B signal pathway in alloxan-induced diabetic mice with renal injury. *European Journal of Pharmacology*. 638: 150–155.
- Lu F., Haque Sk.A., Yang S.-T., Luo P.G., Gu L., Kitaygorodskiy A., Li H., Lacher S. & Sun Y.-P. 2009. Aqueous compatible fullerene-Doxorubicin conjugates. *J Phys Chem C Nanomater Interfaces*. 113: 17768.

- Luiza Andrezza N., Vevert-Bizet C., Bourg-Heckly G., Sureau F., José Salvador M. & Bonneau S. 2016. Berberine as a photosensitizing agent for antitumoral photodynamic therapy: Insights into its association to low density lipoproteins. *Int J Pharm.* 510: 240–249.
- Luksiene Z. 2003. Photodynamic therapy: mechanism of action and ways to improve the efficiency of treatment. *Medicina (Kaunas).* 39: 1137–1150.
- Ma A., Chen H., Cui Y., Luo Z., Liang R., Wu Z., Chen Z., Yin T., Ni J., Zheng M. & Cai L. 2019. Metalloporphyrin complex-based nanosensitizers for deep-tissue tumor theranostics by noninvasive sonodynamic therapy. *Small.* 15: e1804028.
- Maeda H., Sawa T. & Konno T. 2001. Mechanism of tumor-targeted delivery of macromolecular drugs, including the EPR effect in solid tumor and clinical overview of the prototype polymeric drug SMANCSq. *Journal of Controlled Release.* 15.
- Magoulas G.E., Bantzi M., Messari D., Voulgari E., Gialeli C., Barbouri D., Giannis A., Karamanos N.K., Papaioannou D. & Avgoustakis K. 2015. Synthesis and evaluation of anticancer activity in cells of novel stoichiometric pegylated fullerene-Doxorubicin conjugates. *Pharm. Res.* 32: 1676–1693.
- Mann J. 2002. Natural products in cancer chemotherapy: past, present and future. *Nat. Rev. Cancer.* 2: 143–148.
- Martinez Z.S., Castro E., Seong C.-S., Cerón M.R., Echegoyen L. & Llano M. 2016. Fullerene derivatives strongly inhibit hiv-1 replication by affecting virus maturation without impairing protease activity. *antimicrobial agents and chemotherapy.* 60: 5731–5741.
- Matsumura Y. & Maeda H. 1986. A new concept for macromolecular therapeutics in cancer chemotherapy: mechanism of tumorotropic accumulation of proteins and the antitumor agent smancs. *Cancer Res.* 46: 6387–6392.
- McDonald J.H. & University of Delaware 2009. Handbook of biological statistics. Sparky House Publishing, Baltimore, Maryland.
- McKenzie K., Maclean M., Grant M.H., Ramakrishnan P., MacGregor S.J. & Anderson J.G. 2016. The effects of 405 nm light on bacterial membrane integrity determined by salt and bile tolerance assays, leakage of UV-absorbing material and SYTOX green labelling. *Microbiology (Reading, Engl.).* 162: 1680–1688.
- Meeran S.M., Katiyar S. & Katiyar S.K. 2008. Berberine-induced apoptosis in human prostate cancer cells is initiated by reactive oxygen species generation. *Toxicology and Applied Pharmacology.* 229: 33–43.
- Mendes R.G., Bachmatiuk A., Büchner B., Cuniberti G. & Rummeli M.H. 2012. Carbon nanostructures as multi-functional drug delivery platforms. *J. Mater. Chem. B.* 1: 401–428.
- Min Y., Caster J.M., Eblan M.J. & Wang A.Z. 2015. Clinical translation of nanomedicine. *Chem. Rev.* 115: 11147–11190.
- Mirhadi E., Rezaee M. & Malaekheh-Nikouei B. 2018. Nano strategies for Berberine delivery, a natural alkaloid of Berberis. *Biomed. Pharmacother.* 104: 465–473.
- Mizuno K., Zhiyentayev T., Huang L., Khalil S., Nasim F., Tegos G.P., Gali H., Jahnke A., Wharton T. & Hamblin M.R. 2011. Antimicrobial Photodynamic Therapy with Functionalized Fullerenes: Quantitative Structure-activity Relationships. *Journal of nanomedicine & nanotechnology.* 2: 1–9.
- Montellano A., Da Ros T., Bianco A. & Prato M. 2011. Fullerene C₆₀ as a multifunctional system for drug and gene delivery. *Nanoscale.* 3: 4035–4041.
- Moore L. T., Rodriguez-Lorenzo L., Hirsch V., Balog S., Urban D., Jud C., Rothen-Rutishauser B., Lattuada M. & Petri-Fink A. 2015. Nanoparticle colloidal stability in cell culture media and impact on cellular interactions. *Chemical Society Reviews.* 44: 6287–6305.
- Moreno I. & Sun C.-C. 2008. Modeling the radiation pattern of LEDs. *Opt. Express, OE.* 16: 1808–1819.
- Motlagh N.S.H., Parvin P., Ghasemi F. & Atyabi F. 2016. Fluorescence properties of several chemotherapy drugs: Doxorubicin, paclitaxel and bleomycin. *Biomed Opt Express.* 7: 2400–2406.
- Mroz P., Tegos G.P., Gali H., Wharton T., Sarna T. & Hamblin M.R. 2007. Photodynamic therapy with fullerenes. *Photochem Photobiol Sci.* 6: 1139–1149.
- Mroz P., Xia Y., Asanuma D., Konopko A., Zhiyentayev T., Huang Y.-Y., Sharma S.K., Dai T., Khan U.J., Wharton T. & Hamblin M.R. 2011a. Intraperitoneal photodynamic therapy mediated by a fullerene in a mouse model of abdominal dissemination of colon adenocarcinoma. *Nanomedicine.* 7: 965–974.

- Mroz P., Yaroslavsky A., Kharkwal G.B. & Hamblin M.R. 2011b. Cell Death Pathways in Photodynamic Therapy of Cancer. *Cancers (Basel)*. 3: 2516–2539.
- Myhre O., Andersen J.M., Aarnes H. & Fonnum F. 2003. Evaluation of the probes 2',7'-dichlorofluorescein diacetate, luminol, and lucigenin as indicators of reactive species formation. *Biochem. Pharmacol.* 65: 1575–1582.
- Nagata S., Obana A., Gohto Y. & Nakajima S. 2003. Necrotic and apoptotic cell death of human malignant melanoma cells following photodynamic therapy using an amphiphilic photosensitizer, ATX-S10(Na). *Lasers Surg Med.* 33: 64–70.
- Navya P.N. & Daima H.K. 2016. Rational engineering of physicochemical properties of nanomaterials for biomedical applications with nanotoxicological perspectives. *Nano Converg.* 3: 1.
- Neag M.A., Mocan A., Echeverría J., Pop R.M., Bocsan C.I., Crişan G. & Buzoianu A.D. 2018. Berberine: Botanical Occurrence, Traditional Uses, Extraction Methods, and Relevance in Cardiovascular, Metabolic, Hepatic, and Renal Disorders. *Front Pharmacol.* 9: 557.
- Nielsen G.D., Roursgaard M., Jensen K.A., Poulsen S.S. & Larsen S.T. 2008. *In vivo* biology and toxicology of fullerenes and their derivatives. *Basic Clin. Pharmacol. Toxicol.* 103: 197–208.
- Ohmura T., Fukushima T., Shibaguchi H., Yoshizawa S., Inoue T., Kuroki M., Sasaki K. & Umemura S.-I. 2011. Sonodynamic Therapy with 5-Aminolevulinic Acid and Focused Ultrasound for Deep-seated Intracranial Glioma in Rat. *Anticancer Research.* 7: 2527–2533.
- Orlova M. 2013. Perspectives of Fullerene Derivatives in PDT and Radiotherapy of Cancers. *BJMMR.* 3: 1731–1756.
- Ortiz L.M.G., Lombardi P., Tillhon M. & Scovassi A.I. 2014. Berberine, an epiphany against cancer. *Molecules.* 19: 12349–12367.
- Osawa E. 1970. Superaromaticity. *Kagaku (Science)*. 25: 854–863 (in Japanese).
- Otake E., Sakuma S., Torii K., Maeda A., Ohi H., Yano S. & Morita A. 2010. Effect and mechanism of a new photodynamic therapy with glycoconjugated fullerene. *Photochem. Photobiol.* 86: 1356–1363.
- Palyvoda K.O., Grynyuk I.I., Prylutska S.V., Samoylenko A.A., Drobot L.B. & Matyshevska O.P. 2010. Apoptosis photoinduction by C₆₀ fullerene in human leukemic T cells. *Ukr Biokhim Zh.* 82: 121–127.
- Pan G., Wang G.-J., Liu X.-D., Fawcett J.P. & Xie Y.-Y. 2002. The involvement of P-glycoprotein in Berberine absorption. *Pharmacol. Toxicol.* 91: 193–197.
- Panchuk R.R., Prylutska S.V., Chumakl V.V., Skorokhyd N.R., Lehka L.V., Evstigneev M.P., Prylutsky Y.I., Berger W., Heffeter P., Scharff P., Ritter U. & Stoika R.S. 2015. Application of C₆₀ Fullerene-Doxorubicin Complex for Tumor Cell Treatment *in vitro* and *in vivo*. *J Biomed Nanotechnol.* 11: 1139–1152.
- Park S.H., Sung J.H., Kim E.J., Chung N., Park S.H., Sung J.H., Kim E.J. & Chung N. 2015. Berberine induces apoptosis via ROS generation in PANC-1 and MIA-PaCa2 pancreatic cell lines. *Brazilian Journal of Medical and Biological Research.* 48: 111–119.
- Patil J.B., Kim J. & Jayaprakasha G.K. 2010. Berberine induces apoptosis in breast cancer cells (MCF-7) through mitochondrial-dependent pathway. *European Journal of Pharmacology.* 645: 70–78.
- Peng C.-L., Lai P.-S., Lin F.-H., Yueh-Hsiu Wu S. & Shieh M.-J. 2009. Dual chemotherapy and photodynamic therapy in an HT-29 human colon cancer xenograft model using SN-38-loaded chlorin-core star block copolymer micelles. *Biomaterials.* 30: 3614–3625.
- Pennington R.J. 1961. Biochemistry of dystrophic muscle. Mitochondrial succinate–tetrazolium reductase and adenosine triphosphatase. *Biochem J.* 80: 649–654.
- Pereira G.C., Branco A.F., Matos J.A.C., Pereira S.L., Parke D., Perkins E.L., Serafim T.L., Sardão V.A., Santos M.S., Moreno A.J.M., Holy J. & Oliveira P.J. 2007. Mitochondrially Targeted Effects of Berberine [Natural Yellow 18, 5,6-dihydro-9,10-dimethoxybenzo(g)-1,3-benzodioxolo(5,6-a) quinolizinium] on K1735-M2 Mouse Melanoma Cells: Comparison with Direct Effects on Isolated Mitochondrial Fractions. *J Pharmacol Exp Ther.* 323: 636–649.
- Pérez E.M. & Martín N. 2015. π - π interactions in carbon nanostructures. *Chem. Soc. Rev.* 44: 6425–6433.
- Perry J.L., Reuter K.G., Luft J.C., Pecot C.V., Zamboni W. & DeSimone J.M. 2017. Mediating Passive Tumor Accumulation through Particle Size, Tumor Type, and Location. *Nano Lett.* 17: 2879–2886.

- Perumal O.P., Inapagolla R., Kannan S. & Kannan R.M. 2008. The effect of surface functionality on cellular trafficking of dendrimers. *Biomaterials*. 29: 3469–3476.
- Piotrovsky L.B. 2006. Chapter 9 - Biological activity of pristine fullerene C₆₀. In: Dai L. (eds), *Carbon Nanotechnology*, Elsevier, Amsterdam. 235–253.
- Pollock R.E. & Morton D.L. 2003. *Principles of Surgical Oncology*. Holland-Frei Cancer Medicine. 6th edition.
- Porporato P.E., Filigheddu N., Pedro J.M.B.-S., Kroemer G. & Galluzzi L. 2018. Mitochondrial metabolism and cancer. *Cell Res*. 28: 265–280.
- Porter A.E., Gass M., Muller K., Skepper J.N., Midgley P. & Welland M. 2007. Visualizing the Uptake of C₆₀ to the Cytoplasm and Nucleus of Human Monocyte-Derived Macrophage Cells Using Energy-Filtered Transmission Electron Microscopy and Electron Tomography. *Environ. Sci. Technol*. 41: 3012–3017.
- Prabhakar P.K. & Doble M. 2011. Effect of Natural Products on Commercial Oral Antidiabetic Drugs in Enhancing 2-Deoxyglucose Uptake by 3T3-L1 Adipocytes. *Ther Adv Endocrinol Metab*. 2: 103–114.
- Price P.M., Mahmoud W.E., Al-Ghamdi A.A. & Bronstein L.M. 2018. Magnetic Drug Delivery: Where the Field Is Going. *Front. Chem*. 6: 619.
- Prylutska S., Panchuk R., Gołuński G., Skivka L., Prylutsky Y., Hurmach V., Skorohyd N., Borowik A., Woziwodzka A., Piosik J., Kyzyma O., Garamus V., Bulavin L., Evstigneev M., Buchelnikov A., Stoika R., Berger W., Ritter U. & Scharff P. 2017a. C₆₀ fullerene enhances cisplatin anticancer activity and overcomes tumor cell drug resistance. *Nano Res*. 10: 652–671.
- Prylutska S., Politenkova S., Afanasieva K., Korolovych V., Bogutska K., Sivolob A., Skivka L., Evstigneev M., Kostjukov V., Prylutsky Y. & Ritter U. 2017c. A nanocomplex of C₆₀ fullerene with cisplatin: design, characterization and toxicity. *Beilstein J. Nanotechnol*. 8: 1494–1501.
- Prylutska S.V., Grebinyk A.G., Lynchak O.V., Byelinska I.V., Cherepanov V.V., Tauscher E., Matyshevska O.P., Prylutsky Y.I., Rybalchenko V.K., Ritter U. & Frohme M. 2019. *In vitro* and *in vivo* toxicity of pristine C₆₀ fullerene aqueous colloid solution. *Fullerenes, Nanotubes and Carbon Nanostructures*. 9: 715–728.
- Prylutska S.V., Grynyuk I.I., Grebinyk S.M., Matyshevska O.P., Prylutsky Y.I., Ritter U., Siegmund C. & Scharff P. 2009. Comparative study of biological action of fullerenes C₆₀ and carbon nanotubes in thymus cells. *Materialwissenschaft und Werkstofftechnik*. 40: 238–241.
- Prylutska S.V., Grynyuk I.I., Palyvoda K.O. & Matyshevska O.P. 2010a. Photoinduced cytotoxic effect of fullerenes C₆₀ on transformed T-lymphocytes. *Exp. Oncol*. 32: 29–32.
- Prylutska S.V., Matyshevska O.P., Golub A.A., Prylutsky Y.I., Potebnya G.P., Ritter U. & Scharff P. 2007. Study of C₆₀ fullerenes and C₆₀-containing composites cytotoxicity in vitro. *Materials Science and Engineering: C*. 27: 1121–1124.
- Prylutska S.V., Skivka L.M., Didenko G.V., Prylutsky Y.I., Evstigneev M.P., Potebnya G.P., Panchuk R.R., Stoika R.S., Ritter U. & Scharff P. 2015b. Complex of C₆₀ Fullerene with Doxorubicin as a Promising Agent in Antitumor Therapy. *Nanoscale Res Lett*. 10: 499.
- Prylutsky Y.I., Cherepanov V.V., Kostjukov V.V., Evstigneev M.P., Kyzyma O.A., Bulavin L.A., Ivankov O., Davidenko N.A. & Ritter U. 2016. Study of the complexation between Landomycin A and C₆₀ fullerene in aqueous solution. *RSC Adv*. 6: 81231–81236.
- Prylutsky Y.I., Evstigneev M.P., Pashkova I.S., Wyrzykowski D., Woziwodzka A., Gołuński G., Piosik J., Cherepanov V.V. & Ritter U. 2014a. Characterization of C₆₀ fullerene complexation with antibiotic Doxorubicin. *Phys Chem Chem Phys*. 16: 23164–23172.
- Prylutsky Yu.I., Evstigneev M.P., Cherepanov V.V., Kyzyma O.A., Bulavin L.A., Davidenko N.A. & Scharff P. 2015. Structural organization of C₆₀ fullerene, Doxorubicin, and their complex in physiological solution as promising antitumor agents. *J Nanopart Res*. 17: 45.
- Prylutsky Yu.I., Petrenko V.I., Ivankov O.I., Kyzyma O.A., Bulavin L.A., Litsis O.O., Evstigneev M.P., Cherepanov V.V., Naumovets A.G. & Ritter U. 2014b. On the origin of C₆₀ fullerene solubility in aqueous solution. *Langmuir*. 30: 3967–3970.
- Putterman S.J. & Weninger K.R. 2000. Sonoluminescence: how bubbles turn sound into light. *Annual review of fluid mechanics*. 32: 445–476.

- Qiao R., Roberts A.P., Mount A.S., Klaine S.J. & Ke P.C. 2007. Translocation of C₆₀ and its derivatives across a lipid bilayer. *Nano Lett.* 7: 614–619.
- Ramakrishnan P., Maclean M., MacGregor S.J., Anderson J.G. & Grant M.H. 2014. Differential sensitivity of osteoblasts and bacterial pathogens to 405-nm light highlighting potential for decontamination applications in orthopedic surgery. *J Biomed Opt.* 19: 105001.
- Ramakrishnan P., Maclean M., MacGregor S.J., Anderson J.G. & Grant M.H. 2016. Cytotoxic responses to 405 nm light exposure in mammalian and bacterial cells: Involvement of reactive oxygen species. *Toxicol In Vitro.* 33: 54–62.
- Ribeiro J.N., Silva A.R. da & Jorge R.A. 2004. Involvement of mitochondria in apoptosis of cancer cells induced by photodynamic therapy. *Jornal Brasileiro de Patologia e Medicina Laboratorial.* 40: 383–390.
- Ritter U., Prylutskyy Y.I., Evstigneev M.P., Davidenko N.A., Cherepanov V.V., Senenko A.I., Marchenko O.A. & Naumovets A.G. 2015. Structural features of highly stable reproducible C₆₀ fullerene aqueous colloid solution probed by various techniques. *fullerenes, nanotubes and carbon nanostructures.* 23: 530–534.
- Rizvi S.A.A. & Saleh A.M. 2018. Applications of nanoparticle systems in drug delivery technology. *Saudi Pharmaceutical Journal.* 26: 64–70.
- Rohlfing E.A., Cox D.M. & Kaldor A. 1984. Production and characterization of supersonic carbon cluster beams. *The Journal of Chemical Physics.* 81: 3322–3330.
- Rossi G., Barnoud J. & Monticelli L. 2013. Partitioning and solubility of C₆₀ fullerene in lipid membranes. *Phys. Scr.* 87: 058503.
- Russ K.A., Elvati P., Parsonage T.L., Dews A., Jarvis J.A., Ray M., Schneider B., Smith P.J.S., Williamson P.T.F., Violi A. & Philbert M.A. 2016. C₆₀ fullerene localization and membrane interactions in RAW 264.7 immortalized mouse macrophages. *Nanoscale.* 8: 4134–4144.
- Rustin P. 2002. Mitochondria, from cell death to proliferation. *Nat. Genet.* 30: 352–353.
- Ryan J.J., Bateman H.R., Stover A., Gomez G., Norton S.K., Zhao W., Schwartz L.B., Lenk R. & Kepley C.L. 2007. Fullerene nanomaterials inhibit the allergic response. *The Journal of Immunology.* 179: 665–672.
- Sabuncu A.C., Grubbs J., Qian S., Abdel-Fattah T.M., Stacey M.W. & Beskok A. 2012. Probing nanoparticle interactions in cell culture media. *Colloids Surf B Biointerfaces.* 95: 96–102.
- Sahay G., Kim J.O., Kabanov A.V. & Bronich T.K. 2010. The exploitation of differential endocytic pathways in normal and tumor cells in the selective targeting of nanoparticulate chemotherapeutic agents. *Biomaterials.* 31: 923–933.
- Saini R. & Poh C.F. 2013. Photodynamic therapy: a review and its prospective role in the management of oral potentially malignant disorders. *Oral Dis.* 19: 440–451.
- Samanta P.N. & Das K.K. 2017. Noncovalent interaction assisted fullerene for the transportation of some brain anticancer drugs: A theoretical study. *Journal of Molecular Graphics and Modelling.* 72: 187–200.
- Sano K., Nakajima T., Choyke P.L. & Kobayashi H. 2013. Markedly enhanced permeability and retention effects induced by photo-immunotherapy of tumors. *ACS Nano.* 7: 717–724.
- Santos S.M., Dinis A.M., Peixoto F., Ferreira L., Jurado A.S. & Videira R.A. 2014. Interaction of fullerene nanoparticles with biomembranes: from the partition in lipid membranes to effects on mitochondrial bioenergetics. *Toxicol. Sci.* 138: 117–129.
- Schafer F.Q. & Buettner G.R. 2001. Redox environment of the cell as viewed through the redox state of the glutathione disulfide/glutathione couple. *Free Radical Biology and Medicine.* 30: 1191–1212.
- Scharff P., Ritter U., Matyshevska O.P., Prylutskyy S.V., Grynyuk I.I., Golub A.A., Prylutskyy Y.I. & Burlaka A.P. 2008. Therapeutic reactive oxygen generation. *Tumori.* 94: 278–283.
- Schrand A.M., Hens S.A.C. & Shenderova O.A. 2009. Nanodiamond particles: properties and perspectives for bioapplications. *Critical Reviews in Solid State and Materials Sciences.* 34: 18–74.
- Schumacker P.T. 2006. Reactive oxygen species in cancer cells: Live by the sword, die by the sword. *Cancer Cell.* 10: 175–176.
- Schütz C.A., Juillerat-Jeanneret L., Mueller H., Lynch I. & Riediker M. 2013. Therapeutic nanoparticles in clinics and under clinical evaluation. *Nanomedicine.* 8: 449–467.

- Scott C.A., Westmacott D., Broadhurst M.J., Thomas G.J. & Hall M.J. 1986. 9-alkyl anthracyclines. Absence of cross-resistance to adriamycin in human and murine cell cultures. *Br J Cancer*. 53: 595–600.
- Scrivens W.A., Tour J.M., Creek K.E. & Pirisi L. 1994. Synthesis of ^{14}C -Labeled C_{60} , Its Suspension in Water, and Its Uptake by Human Keratinocytes. *J. Am. Chem. Soc.* 116: 4517–4518.
- Senapati S., Mahanta A.K., Kumar S. & Maiti P. 2018. Controlled drug delivery vehicles for cancer treatment and their performance. *Signal Transduction and Targeted Therapy*. 3: 7.
- Seo Y.-S., Yim M.-J., Kim B.-H., Kang K.-R., Lee S.-Y., Oh J.-S., You J.-S., Kim S.-G., Yu S.-J., Lee G.-J., Kim D.K., Kim C.S., Kim J.-S. & Kim J.-S. 2015. Berberine-induced anticancer activities in FaDu head and neck squamous cell carcinoma cells. *Oncology Reports*. 34: 3025–3034.
- Sepúlveda D., Guan Y., Rangel U. & Wheeler S.E. 2017. Stacked homodimers of substituted contorted hexabenzocoronenes and their complexes with C_{60} fullerene. *Org. Biomol. Chem.* 15: 6042–6049.
- Serafim T.L., Oliveira P.J., Sardao V.A., Perkins E., Parke D. & Holy J. 2008. Different concentrations of Berberine result in distinct cellular localization patterns and cell cycle effects in a melanoma cell line. *Cancer Chemother Pharmacol.* 61: 1007–1018.
- Sever R. & Brugge J.S. 2015. Signal Transduction in Cancer. *Cold Spring Harb Perspect Med.* 5: a006098.
- Sharma S.K., Chiang L.Y. & Hamblin M.R. 2011. Photodynamic therapy with fullerenes *in vivo*: reality or a dream?. *Nanomedicine (Lond)*. 6: 1813–1825.
- Shen H. 2007. The compressive mechanical properties of C_n ($n=20, 60, 80, 180$) and endohedral M@C_{60} ($\text{M}=\text{Na}, \text{Al}, \text{Fe}$) fullerene molecules. *Molecular Physics*. 105: 2405–2409.
- Shen Y., Shuhendler A.J., Ye D., Xu J.-J. & Chen H.-Y. 2016. Two-photon excitation nanoparticles for photodynamic therapy. *Chem Soc Rev.* 45: 6725–6741.
- Shewach D.S. & Kuchta R.D. 2009. Introduction to cancer chemotherapeutics. *Chem Rev.* 109: 2859–2861.
- Shi J., Kantoff P.W., Wooster R. & Farokhzad O.C. 2017. Cancer nanomedicine: progress, challenges and opportunities. *Nat Rev Cancer*. 17: 20–37.
- Shi J., Liu Y., Wang L., Gao J., Zhang J., Yu X., Ma R., Liu R. & Zhang Z. 2014. A tumoral acidic pH-responsive drug delivery system based on a novel photosensitizer (fullerene) for *in vitro* and *in vivo* chemo-photodynamic therapy. *Acta Biomater.* 10: 1280–1291.
- Shi J., Wang B., Wang L., Lu T., Fu Y., Zhang H. & Zhang Z. 2016. Fullerene (C_{60})-based tumor-targeting nanoparticles with “off-on” state for enhanced treatment of cancer. *Journal of Controlled Release*. 235: 245–258.
- Shrivastava A. & Gupta V. 2011. Methods for the determination of limit of detection and limit of quantitation of the analytical methods. *Chronicles of Young Scientists*. 2: 21.
- Slepička P., Hubáček T., Kolská Z., Trostová S., Kasálková N.S., Bačáková L. & Švorčík V. 2013. The properties and application of carbon nanostructures. *Polymer Science*.
- Spencer D.S., Puranik A.S. & Peppas N.A. 2015. Intelligent nanoparticles for advanced drug delivery in cancer treatment. *Curr Opin Chem Eng.* 7: 84–92.
- Sperandio F.F., Sharma S.K., Wang M., Jeon S., Huang Y.-Y., Dai T., Nayka S., de Sousa S.C.O.M., Chiang L.Y. & Hamblin M.R. 2013. Photoinduced electron-transfer mechanisms for radical-enhanced photodynamic therapy mediated by water-soluble decacationic C_{70} and C_{84}O_2 fullerene derivatives. *Nanomedicine*. 9: 570–579.
- Spesia M.B., Milanese M.E. & Durantini E.N. 2017. Chapter 18 - fullerene derivatives in photodynamic inactivation of microorganisms. In: Fikai A. & Grumezescu A.M. (eds), *Nanostructures for Antimicrobial Therapy*, Elsevier. 413–433
- Stueckle T.A., Sargent L., Rojasasakul Y. & Wang L. 2016. Genotoxicity and carcinogenic potential of carbon nanomaterials. *Biomedical Applications and Toxicology of Carbon Nanomaterials*, John Wiley & Sons, Ltd. 267–332.
- Sun C.-Y., Cao Z., Zhang X.-J., Sun R., Yu C.-S. & Yang X. 2018. Cascade-amplifying synergistic effects of chemo-photodynamic therapy using ROS-responsive polymeric nanocarriers. *Theranostics*. 8: 2939–2953.
- Sun T., Zhang Y.S., Pang B., Hyun D.C., Yang M. & Xia Y. 2014. Engineered nanoparticles for drug delivery in cancer therapy. *Angew. Chem. Int. Ed.* 53:12320–12364.

- Suzuki J., Denning D.P., Imanishi E., Horvitz H.R. & Nagata S. 2013. Xk-related protein 8 and CED-8 promote phosphatidylserine exposure in apoptotic cells. *Science*. 341: 403–406.
- Tabata Y., Ishii T., Aoyama T., Oki R., Hirano Y., Ogawa O. & Ikada Y. 2002. Sonodynamic effect of polyethylene glycol-conjugated fullerene on tumor. In: Ōsawa E. (eds), *Perspectives of Fullerene Nanotechnology*, Springer Netherlands, Dordrecht. 185–196.
- Tabata Y., Murakami Y. & Ikada Y. 1997. Photodynamic effect of polyethylene glycol–modified fullerene on tumor. *Jpn J Cancer Res*. 88: 1108–1116.
- Tacar O., Sriamornsak P. & Dass C.R. 2013. Doxorubicin: an update on anticancer molecular action, toxicity and novel drug delivery systems. *J. Pharm. Pharmacol.* 65: 157–170.
- Tang S. & Zheng J. 2018. Antibacterial activity of silver nanoparticles: structural effects. *Advanced Healthcare Materials*. 7: 1701503.
- Tanimoto S., Sakai S., Kudo E., Okada S., Matsumura S., Takahashi D. & Tushima K. 2012. Target-selective photodegradation of HIV-1 protease and inhibition of HIV-1 Replication in living cells by designed fullerene-sugar hybrids. *Chem. Asian J.* 7: 911–914.
- Thompson L.C., Urankar R.N., Holland N.A., Vidanapathirana A.K., Pitzer J.E., Han L., Sumner S.J., Lewin A.H., Fennell T.R., Lust R.M., Brown J.M. & Wingard C.J. 2014. C₆₀ exposure augments cardiac ischemia/reperfusion injury and coronary artery contraction in sprague dawley rats. *Toxicol Sci*. 138: 365–378.
- Thorn C.F., Oshiro C., Marsh S., Hernandez-Boussard T., McLeod H., Klein T.E. & Altman R.B. 2011. Doxorubicin pathways: pharmacodynamics and adverse effects. *Pharmacogenet. Genomics*. 21: 440–446.
- Thrower P. 1999. Editorial. *Carbon*. 37: 1677–1678.
- Tong J., Zimmerman M.C., Li S., Yi X., Luxenhofer R., Jordan R. & Kabanov A.V. 2011. Neuronal uptake and intracellular superoxide scavenging of a fullerene (C₆₀)-poly(2-oxazoline)s nanoformulation. *Biomaterials*. 32: 3654–3665.
- Tran S., DeGiovanni P.-J., Piel B. & Rai P. 2017. Cancer nanomedicine: a review of recent success in drug delivery. *Clin Transl Med*. 6: 44.
- Truong N.P., Whittaker M.R., Mak C.W. & Davis T.P. 2015. The importance of nanoparticle shape in cancer drug delivery. *Expert Opinion on Drug Delivery*. 12: 129–142.
- Turajlic S., Sottoriva A., Graham T. & Swanton C. 2019. Resolving genetic heterogeneity in cancer. *Nature Reviews Genetics*. 20: 404–416.
- Tziortzioti R. 2016. Induction of apoptosis by functionalized fullerene-based sonodynamic therapy in HL-60 cells. *Anticancer Research*. 36: 2665–2674.
- Uhrich K.E., Cannizzaro S.M., Langer R.S. & Shakesheff K.M. 1999. Polymeric Systems for Controlled Drug Release. *Chem. Rev.* 99: 3181–3198.
- Ventola C.L. 2017. Progress in nanomedicine: approved and investigational nanodrugs. *P T*. 42: 742–755.
- Vogelstein B., Papadopoulos N., Velculescu V.E., Zhou S., Diaz L.A. & Kinzler K.W. 2013. Cancer genome landscapes. *Science*. 339: 1546–1558.
- Wagner T., Magill C.R. & Herrle J.O. 2018. Carbon Isotopes. In: White W.M. (eds), *Encyclopedia of Geochemistry: A comprehensive reference source on the chemistry of the Earth*, Springer International Publishing, Cham. 194–204.
- Wallace D.C. 2012. Mitochondria and cancer. *Nat Rev Cancer*. 12: 685–698.
- Wang J., Byrne J.D., Napier M.E. & DeSimone J.M. 2011a. More effective nanomedicines through particle design. *Small*. 7: 1919–1931.
- Wang J., Jiao Y. & Shao Y. 2018. Mesoporous silica nanoparticles for dual-mode chemo-sonodynamic therapy by low-energy ultrasound. *Materials*. 11: 2041.
- Wang N., Zhu M., Wang X., Tan H.-Y., Tsao S. & Feng Y. 2014. Berberine-induced tumor suppressor p53 up-regulation gets involved in the regulatory network of MIR-23a in hepatocellular carcinoma. *Biochimica et Biophysica Acta (BBA) - Gene Regulatory Mechanisms*. 1839: 849–857.
- Wang X., Meng G., Zhang S. & Liu X. 2016. A Reactive ¹O₂ - Responsive combined treatment system of photodynamic and chemotherapy for cancer. *Sci Rep*. 6: 29911.

- Wang Y., Kheir M.M., Chai Y., Hu J., Xing D., Lei F. & Du L. 2011b. Comprehensive study in the inhibitory effect of Berberine on gene transcription, including TATA Box. *Plos One*. 6: e23495.
- Weinberg R. A. 2007. *The biology of cancer*. Garland science, New York.
- Weyandt J.D., Thompson C.B., Giaccia A.J. & Rathmell W.K. 2017. Metabolic alterations in cancer and their potential as therapeutic targets. *Am Soc Clin Oncol Educ Book*. 37: 825–832.
- van Wezel A.P., Morinière V., Emke E., ter Laak T. & Hogenboom A.C. 2011. Quantifying summed fullerene nC₆₀ and related transformation products in water using LC LTQ Orbitrap MS and application to environmental samples. *Environ Int*. 37: 1063–1067.
- Wielinga P.R., Westerhoff H.V. & Lankelma J. 2000. The relative importance of passive and P-glycoprotein mediated anthracycline efflux from multidrug-resistant cells. *Eur. J. Biochem*. 267: 649–657.
- Wu C., He Q., Zhu A., Li D., Xu M., Yang H. & Liu Y. 2014. Synergistic anticancer activity of photo- and chemoresponsive nanoformulation based on polylysine-functionalized graphene. *ACS Appl Mater Interfaces*. 6: 21615–21623.
- Wu H.L., Hsu C.Y., Liu W.H. & Yung B.Y.M. 1999. Berberine-induced apoptosis of human leukemia HL-60 cells is associated with down-regulation of nucleophosmin/B23 and telomerase activity. *International Journal of Cancer*. 81: 923–929.
- Xiao L., Aoshima H., Saitoh Y. & Miwa N. 2010. Fullerene-polyvinylpyrrolidone clathrate localizes in the cytoplasm to prevent ultraviolet-A ray-induced DNA-fragmentation and activation of the transcriptional factor NF-kappaB. *J. Cell. Biochem*. 111: 955–966.
- Xiao N., Chen S., Ma Y., Qiu J., Tan J.-H., Ou T.-M., Gu L.-Q., Huang Z.-S. & Li D. 2012. Interaction of Berberine derivative with protein POT1 affect telomere function in cancer cells. *Biochemical and Biophysical Research Communications*. 419: 567–572.
- Xu X., Li R., Ma M., Wang X., Wang Y. & Zou H. 2012. Multidrug resistance protein P-glycoprotein does not recognize nanoparticle C₆₀: experiment and modeling. *Soft Matter*. 8: 2915.
- Yadav B.C. & Kumar R. 2008. Structure, properties and applications of fullerenes. *Internat. J. Nanotech. Appl*. 2: 15–24.
- Yamago S., Tokuyama H., Nakamura E., Kikuchi K., Kananishi S., Sueki K., Nakahara H., Enomoto S. & Ambe F. 1995. *In vivo* biological behavior of a water-miscible fullerene: ¹⁴C labeling, absorption, distribution, excretion and acute toxicity. *Chemistry & Biology*. 2: 385–389.
- Yamakoshi Y., Umezawa N., Ryu A., Arakane K., Miyata N., Goda Y., Masumizu T. & Nagano T. 2003. Active Oxygen Species Generated from Photoexcited Fullerene (C₆₀) as Potential Medicines: O^{2•-} versus ¹O₂. *J. Am. Chem. Soc*. 125: 12803–12809.
- Yang D., Gao S., Fang Y., Lin X., Jin X., Wang X., Ke L. & Shi K. 2018. The π - π stacking-guided supramolecular self-assembly of nanomedicine for effective delivery of antineoplastic therapies. *Nanomedicine*. 13: 3159–3177.
- Yang S.H., Pettiette C.L., Conceicao J., Cheshnovsky O. & Smalley R.E. 1987. Ups of buckminsterfullerene and other large clusters of carbon. *Chemical Physics Letters*. 139: 233–238.
- Yang Y., Karakhanova S., Hartwig W., D’Haese J.G., Philippov P.P., Werner J. & Bazhin A.V. 2016. Mitochondria and mitochondrial ROS in cancer: Novel Targets for Anticancer Therapy. *J. Cell. Physiol*. 231: 2570–2581.
- Yano S., Hirohara S., Obata M., Hagiya Y., Ogura S., Ikeda A., Kataoka H., Tanaka M. & Joh T. 2011. Current states and future views in photodynamic therapy. *Journal of Photochemistry and Photobiology C: Photochemistry Reviews*. 12: 46–67.
- Yin R., Wang M., Huang Y.-Y., Huang H.-C., Avci P., Chiang L.Y. & Hamblin M.R. 2014. Photodynamic therapy with decacationic [60]fullerene monoadducts: effect of a light absorbing electron-donor antenna and micellar formulation. *Nanomedicine*. 10: 795–808.
- Yingchoncharoen P., Kalinowski D.S. & Richardson D.R. 2016. Lipid-based drug delivery systems in cancer therapy: what is available and what is yet to come. *Pharmacol Rev*. 68: 701–787.
- Yip K.W. & Reed J.C. 2008. Bcl-2 family proteins and cancer. *Oncogene*. 27: 6398–6406.

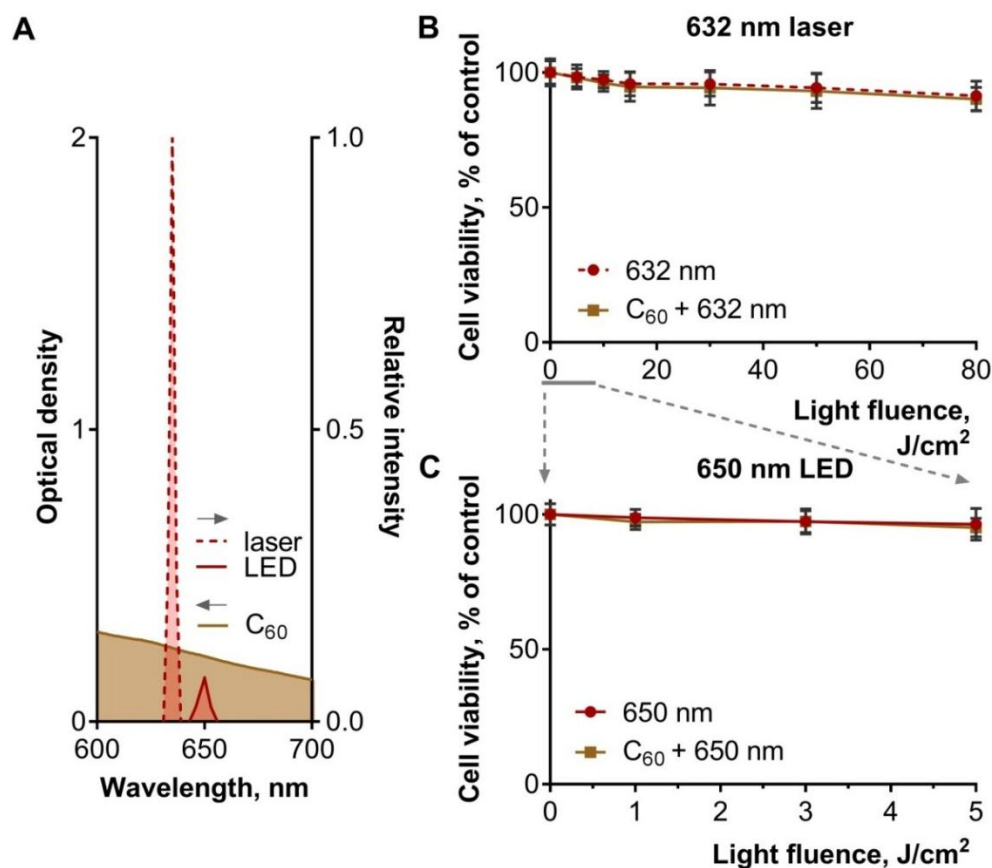
- You D.G., Deepagan V.G., Um W., Jeon S., Son S., Chang H., Yoon H.I., Cho Y.W., Swierczewska M., Lee S., Pomper M.G., Kwon I.C., Kim K. & Park J.H. 2016. ROS-generating TiO₂ nanoparticles for non-invasive sonodynamic therapy of cancer. *Scientific Reports*. 6: 23200.
- Yu C., Avci P., Canteenwala T., Chiang L.Y., Chen B.J. & Hamblin M.R. 2016. Photodynamic Therapy with Hexa(sulfo-n-butyl)[60]Fullerene Against Sarcoma *in vitro* and *in vivo*. *J Nanosci Nanotechnol*. 16: 171–181.
- Yu C.-H., Lin H.-P., Chen H.-M., Yang H., Wang Y.-P. & Chiang C.-P. 2009. Comparison of clinical outcomes of oral erythroleukoplakia treated with photodynamic therapy using either light-emitting diode or laser light. *Lasers Surg Med*. 41: 628–633.
- Yumita N., Iwase Y., Nishi K., Ikeda T., Komatsu H., Fukai T., Onodera K., Nishi H., Takeda K., Umemura S.-I., Okudaira K. & Momose Y. 2011. Sonodynamically-induced Antitumor Effect of Mono-l-aspartyl Chlorin e6 (NPe6). *Anticancer Research*. 31: 501–506.
- Zhang J., Cao H., Zhang B., Cao H., Xu X., Ruan H., Yi T., Tan L., Qu R., Song G., Wang B. & Hu T. 2013. Berberine potently attenuates intestinal polyps growth in ApcMin mice and familial adenomatous polyposis patients through inhibition of Wnt signalling. *Journal of Cellular and Molecular Medicine*. 17: 1484–1493.
- Zhang L.W., Yang J., Barron A.R. & Monteiro-Riviere N.A. 2009. Endocytic mechanisms and toxicity of a functionalized fullerene in human cells. *Toxicol. Lett*. 191: 149–157.
- Zhang Q.L., O'Brien S.C., Heath J.R., Liu Y., Curl R.F., Kroto H.W. & Smalley R.E. 1986. Reactivity of large carbon clusters: spheroidal carbon shells and their possible relevance to the formation and morphology of soot. *J. Phys. Chem*. 90: 525–528.
- Zhang X., Gu L., Li J., Shah N., He J., Yang L., Hu Q. & Zhou M. 2010. Degradation of MDM2 by the Interaction between Berberine and DAXX Leads to Potent Apoptosis in MDM2-Overexpressing Cancer Cells. *Cancer Res*. 70: 9895–9904.
- Zhang Y., Huang F., Ren C., Yang L., Liu J., Cheng Z., Chu L. & Liu J. 2017. Targeted chemo-photodynamic combination platform based on the DOX prodrug nanoparticles for enhanced cancer therapy. *ACS Appl Mater Interfaces*. 9: 13016–13028.
- Zhou F., Wu S., Wu B., Chen W.R. & Xing D. 2011. Mitochondria-targeting single-walled carbon nanotubes for cancer photothermal therapy. *Small*. 7: 2727–2735.
- Zhou F., Wu S., Yuan Y., Chen W.R. & Xing D. 2012. Mitochondria-targeting photoacoustic therapy using single-walled carbon nanotubes. *Small*. 8: 1543–1550.
- Zhou F., Xing D., Wu B., Wu S., Ou Z. & Chen W.R. 2010. New insights of transmembranal mechanism and subcellular localization of noncovalently modified single-walled carbon nanotubes. *Nano Lett*. 10: 1677–1681.
- Zhou L., Zhou L., Wei S., Ge X., Zhou J., Jiang H., Li F. & Shen J. 2014. Combination of chemotherapy and photodynamic therapy using graphene oxide as drug delivery system. *J. Photochem. Photobiol. B, Biol*. 135: 7–16.
- Zhou Z., Song J., Nie L. & Chen X. 2016. Reactive oxygen species generating systems meeting challenges of photodynamic cancer therapy. *Chem Soc Rev*. 45: 6597–6626.
- Zhu D., Larin K.V., Luo Q. & Tuchin V.V. 2013. Recent progress in tissue optical clearing. *Laser Photon Rev*. 7: 732–757.
- Zhu M., Wang R. & Nie G. 2014. Applications of nanomaterials as vaccine adjuvants. *Hum Vaccin Immunother*. 10: 2761–2774.
- Zolfagharpour F., Khalilabad M.H.R., Nikkhoo N.S., Mousavi M.H. & Hatampanah S. 2013. Spectrum of emitted light from sonoluminescence bubbles. *Advances in Applied Physics*. 1: 93–103.
- Zuckerman S.T. & Kao W.J. 2009. Nanomaterials and Biocompatibility: Carbon nanotubes and fullerenes. In: de Villiers M.M., Aramwit P., & Kwon G.S. (eds), *Nanotechnology in Drug Delivery*, Springer, New York, NY. 229–266.

VII. APPENDIX

Appendix 1

Red light sources for C₆₀ photodynamic treatment of cells

The possible induction of C₆₀'s toxicity with red light was studied after treatment of CCRF-CEM cells with 20 μ M C₆₀ for 24 h and consequent irradiation with LED and laser light sources. At 24 h after light irradiation, cell viability was assessed with the MTT assay. No significant effect on the viability of leukemic cells, incubated with or without C₆₀ was detected under 650 nm LED light irradiation. The increased intensities up to 80 J/cm², allowed with the use of 632 nm helium-neon 30 mW laser, caused no cytotoxicity that could be linked with low C₆₀'s absorbance of longwavelength light.



A1 Figure 1. Red light sources for C₆₀ photodynamic treatment of leukemic cells: A – Correlation between absorption spectrum of C₆₀ and exposure spectrums of red light sources; CCRF-CEM cells viability under action of 20 μ M C₆₀, excited with: B – 632 nm laser, C – 650 nm LED.

Appendix 2

Spectroscopic and fluorometric analysis of Berberine

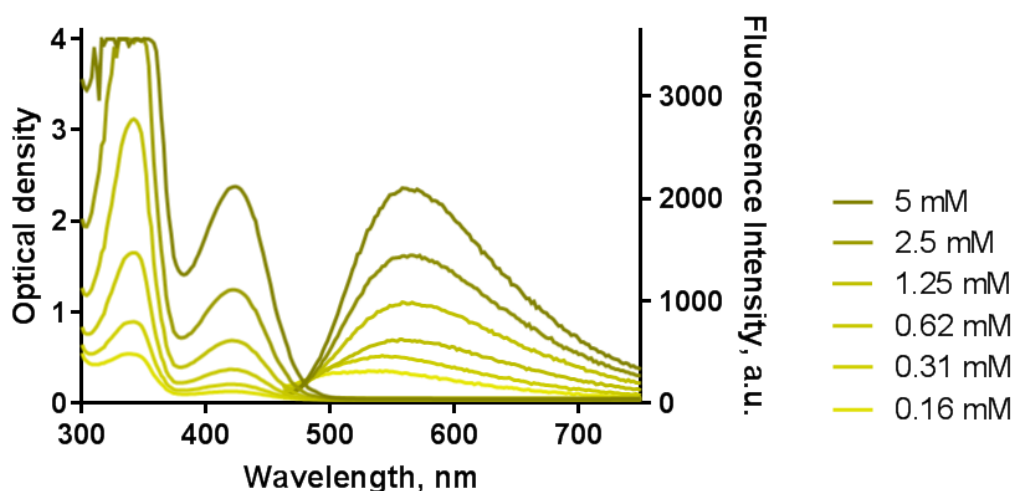
In order to study accumulation of Berberine in leukemic cells, firstly, its optical spectra were recorded and its absorption and fluorescence maxima were determined.

Methods

The absorption and fluorescence spectra of Berberine aqueous solutions were measured at the following parameters: 1. Absorption – wavelength range: 300-750 nm, wavelength step size: 2 nm, number of flashes per well: 25; 2. Fluorescence – $\lambda_{\text{ex}} = 424$ nm, wavelength range: 462-750 nm, wavelength step size: 2 nm, number of flashes per well: 25. A volume of 100 μL of the studied solutions was measured in the 96-well plates with a multimode microplate spectrometer Tecan Infinite M200 PRO.

Results

Berberine's absorption was found in the spectral range of $\lambda < 500$ nm, consisting two bands with the maxima at 424 and 334 nm (Appendix 2 Fig. 1). The fluorescence of Berberine contained one band with a maximum at 560 nm upon excitation at $\lambda = 424$ nm (Appendix 2 Fig. 1). Optical density and fluorescence spectra were recorded for Berberine aqueous solutions and found to be in accordance with the literature data (Gumenyuk et al., 2012).



A2 Figure 1. Optical density and fluorescence spectra of Berberine.

Appendix 3

C₆₀ sonodynamic treatment of cancer cells

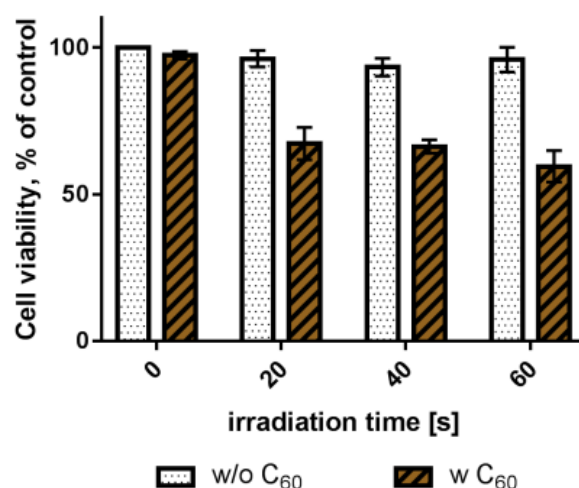
Pristine C₆₀ application as a possible sonosensitizer for treatment of human cervix carcinoma HeLa cells was studied in combination with 1 MHz ultrasound (US).

Methods

HeLa cells were seeded in 6- (2×10^5 /well) or 96- (1×10^4 /well) well plates. After 24 h, cells were incubated with 20 μ M C₆₀. After another 24 h cells were prepared for US treatment. In every empty well on each plate, filtered water was added as well as into the spaces between the wells to prevent excessive heating during US treatment. The water in the water tank was previously degassed with vacuum pump SpeedVac. The US transducer was driven at resonance frequency of 950 kHz (\sim 1 MHz) with a performance of 500 W. HeLa cells were exposed to US for 0, 20, 40 and 60 s. During the US treatment, temperature was continuously monitored to be under 37°C. After treatment with US, the cells were incubated for 48 h before analysis of viability with the MTT assay (96-well plates) or differentiation of cell death type by flow cytometry analysis (6-well plates).

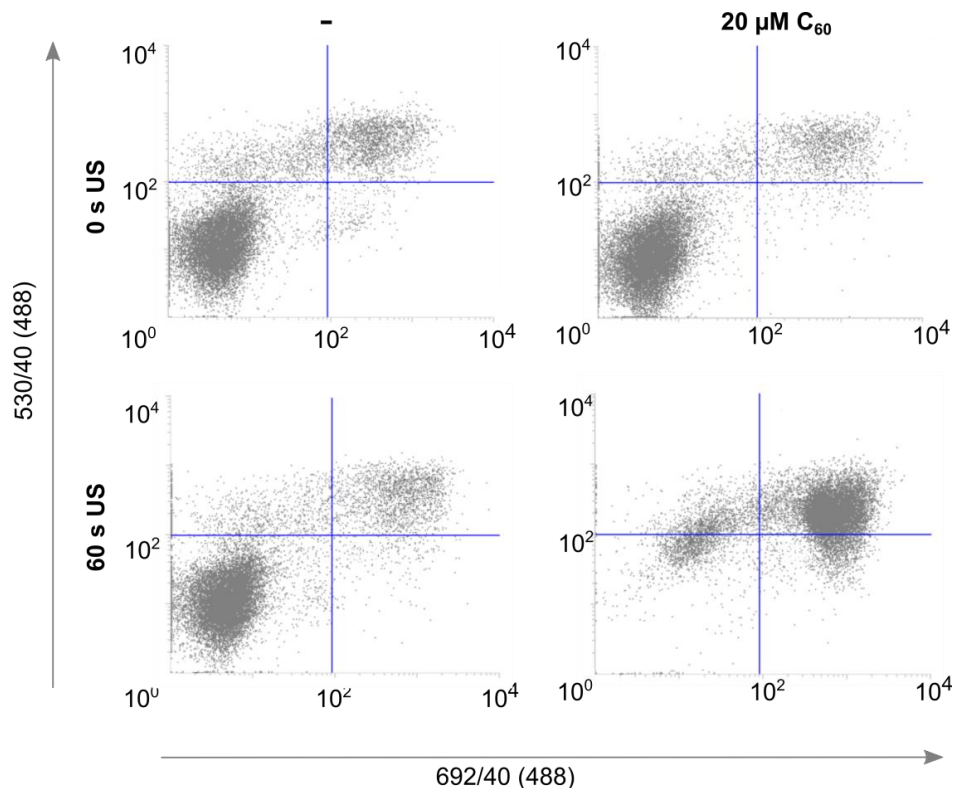
Results

No influence of high frequency US irradiation used alone on HeLa cell viability was detected. However, US in the presence of C₆₀ rapidly decreased cell viability (Appendix 3 Fig 1). This conclusion also correlated with microscopic analysis. As is presented on the Appendix 3 Fig. 2, the content of apoptotic cells in the control group accounted 8% of all cells that demonstrated pretty low apoptotic rate in the cell culture under basic conditions. The addition of 20 μ M C₆₀ had no significant effect on the cell distribution – the apoptotic cell content was estimated to be 8.2%. Therefore, C₆₀ was proven to be not toxic to HeLa cells under used concentration during incubation up to 72 h. US alone caused neither apoptosis nor necrosis induction in the cells as well.



A3 Figure 1. C₆₀ sonodynamic treatment of HeLa cells: viability of HeLa cells treated with high frequency US alone and in combination with 20 μM C₆₀; image by Benjamin Kolp (Kolp, 2018).

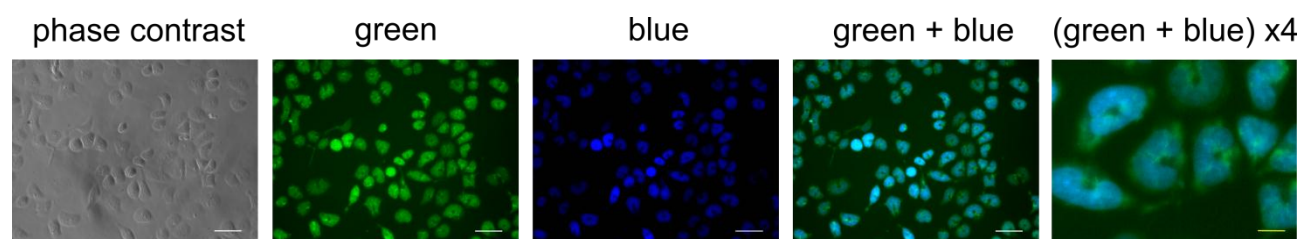
In contrast, once cells were treated with 20 μM C₆₀ and irradiated with US, the content of apoptotic cells was significantly increased (Appendix 3 Fig. 2). US treatment for 20 s induced apoptosis in $79 \pm 4\%$ of cells in the presence of C₆₀. The increase of 1 MHz US treatment to 60 s resulted in apoptotic cell content on the level of $83 \pm 4\%$ in the presence of C₆₀ (Appendix 3 Fig. 2).



A3 Figure 2. Apoptosis detection in HeLa cells, treated with 20 μM C₆₀ and 1 MHz ultrasound with Annexin V-FITC/PI staining and flow cytometry; image by Benjamin Kolp (Kolp, 2018).

Appendix 4*Berberine (0.5 μ M) localization in CCRF-CEM cells*

Since the study testified Berberine intranuclear localization in leukemic CCRF-CEM cells at high concentration (50 μ M), it was interesting to check additionally Berberine intracellular distribution in the lower concentrations. Thus, CCRF-CEM cells, incubated for 24 h with 0.5 μ M Berberine, were subjected to the fluorescence microscopy, that demonstrated its efficient intracellular accumulation. Double staining with DNA-binding dye Hoechst 33342 evidenced Berberine accumulation in the cell nucleus. However, on the contrary to the 50 μ M Berberine in the studied cells green fluorescence was detected in the extranuclear space as well (Appendix 4 Fig. 1).

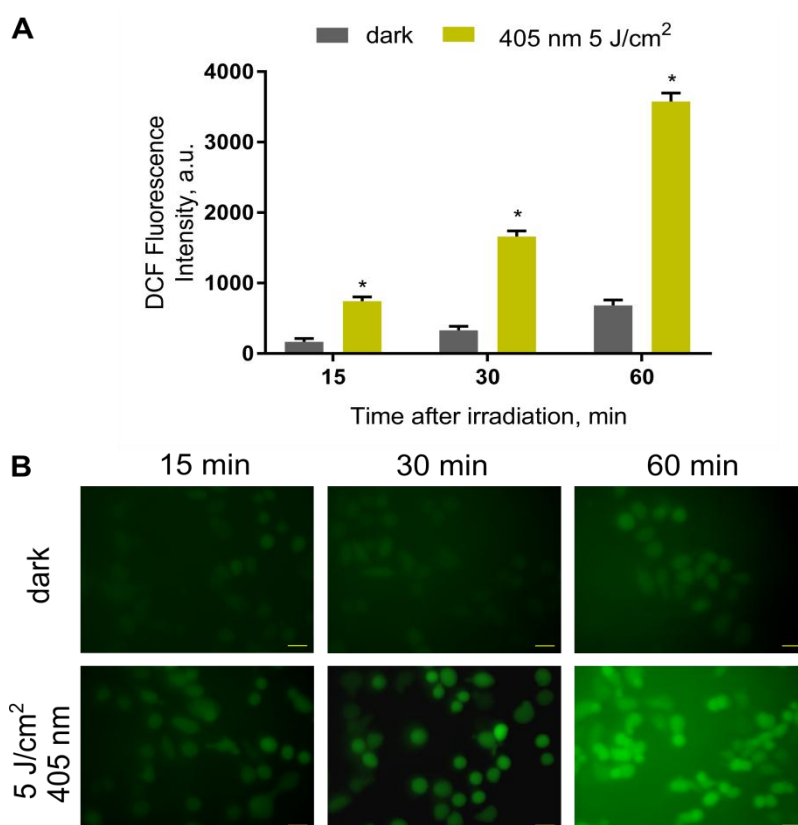


A4 Figure 1. Phase contrast and fluorescence images of CCRF-CEM cells, incubated for 24 h with 0.5 μ M Berberine (green – $\lambda_{\text{ex}} = 435$ nm, $\lambda_{\text{em}} > 515$ nm) and co-stained with DNA-binding dye Hoechst 33342 (blue – $\lambda_{\text{ex}} = 377$ nm, $\lambda_{\text{em}} = 447$ nm); the white scale bar 40 μ m, the yellow scale bar on image “(green + blue) $\times 4$ ” corresponds to 10 μ m.

Appendix 5

Intracellular reactive oxygen species generation in CCRF-CEM cells treated with photoexcited Berberine

To study whether free Berberine had any prooxidant effect on CCRF-CEM cells under light irradiation, reactive oxygen species (ROS) generation in cells was evaluated with the use of the fluorescent dye DCFH-DA (Eruslanov & Kusmartsev, 2010). The minor increase of fluorescence signal was detected during the incubation of cells in dark (Appendix 5 Fig. 1), that corresponded to initial prooxidant activity of Berberine (Park et al., 2015). However, once CCRF-CEM cells, incubated with 0.5 μM Berberine, were exposed to the 5 J/cm^2 405 nm LED, the intense ROS generation was detected. Thus, ROS level exceeded the control on 4.4, 5.0 and 5.2 times at 15, 30 and 60 min after light irradiation correspondingly. The detected oxidant stress evidenced the prooxidant activity of Berberine excited with 5 J/cm^2 405 nm LED light.



A5 Figure 1. Prooxidant effect of Berberine in CCRF-CEM cells under 405 nm light irradiation: A – Intracellular ROS generation level of CCRF-CEM cells, exposed to 0.5 μM Berberine and 5 J/cm^2 405 nm LED, * $p \leq 0.01$ in comparison with the dark control; B – Fluorescence microscopy of CCRF-CEM cells after 15, 30 and 60 min incubation with DCFH-DA (green – $\lambda_{\text{ex}} = 472 \text{ nm}$, $\lambda_{\text{em}} = 520 \text{ nm}$), scale bar 20 μm .

ABBREVIATIONS

ATP – Adenosine Triphosphate

BSA – Bovine Serum Albumin

CDDP – Cis-Diamminedichloridoplatinum

CI – Combination Index

C₆₀ – C₆₀ Fullerene

C₆₀-Ber – C₆₀ Fullerene-Berberine nanocomplex/es

C₆₀-Dox – C₆₀ Fullerene- Doxorubicin nanocomplex/es

CT – Chemotherapy

DAPI – 4',6-Diamidino-2-phenylindole dihydrochloride

DCFH-DA – 2,7-Dichlorofluorescein Diacetate

DMEM – Dulbecco's Modified Eagle Medium

DMSO – Dimethylsulfoxide

EGTA – Ethylene Glycol-bis(β-aminoethyl ether)-N,N,N',N'-Tetraacetic Acid

ESI – Electro Spray Ionization

FACS – Fluorescence Activated Cell Sorting

FBS – Fetal Bovine Serum

FITC – Fluorescein Isothiocyanate

FRET – Fluorescence Resonance Energy Transfer

HIV – Human Immunodeficiency Viruses

HPLC – High Performance Liquid Chromatography

IB – Isolation Buffer

IC₅₀ – Half-Maximal Inhibitory Concentration

INT – 2-(4-Iodophenyl)-3-(4-Nitrophenyl)-5-Phenyl-2H-Tetrazolium

LED – Light-Emitting Diode

LoD – Limit of Detection

LoQ – Limit of Quantification

MALDI-TOF – Matrix Assisted Laser Desorption Ionization-Time of Flight

MOPS – 3-(*N*-Morpholino)propanesulphonic Acid

MRM – Multiple Reactions Monitoring

MS – Mass Spectrometry

MS/MS – Tandem Mass Spectrometry

MTT – 3-(4,5-Dimethylthiazol-2-Yl)-2,5-Diphenyl Tetrazolium Bromide

PBS – Phosphate Buffered Saline

PEG – Polyethylene Glycol

PDT – Photodynamic Therapy

PI – Propidium Iodide

ROS – Reactive Oxygen Species

RPMI – Roswell Park Memorial Institute Medium

RT – Room Temperature

SIM – Selected Ion Monitoring

SR – Succinate-Reductase

TEM – Transmission Electron Microscopy

Tris – Tris(hydroxymethyl)aminomethane

UV-vis – Ultraviolet-Visible

λ_{ex} – excitation wavelength

λ_{em} – emission wavelength

LIST OF FIGURES

<i>Figure</i>	<i>Page</i>
Figure 1. Discovery of C ₆₀ fullerene.	25
Figure 2. Structure-determined properties of C ₆₀ .	28
Figure 3. Schematic mechanism of photodynamic treatment of cancer cells with C ₆₀ .	30
Figure 4. C ₆₀ -Dox nanocomplex for photodynamic cancer chemotherapy.	38
Figure 5. The workflow plan for the development of C ₆₀ -based photodynamic treatment and drug delivery to cancer cells.	39
Figure 6. Developed HPLC-ESI-MS method for C ₆₀ detection and quantification.	48
Figure 7. Developed HPLC-ESI-MS method for Doxorubicin detection and quantification.	50
Figure 8. Parts of LED light source designed in 3D software SOLIDWorks.	52
Figure 9. LED light system scheme.	52
Figure 10. MALDI-TOF-MS spectrum of C ₆₀ colloid solution.	63
Figure 11. Intracellular localization of C ₆₀ in CCRF-CEM cells.	64
Figure 12. Intracellular uptake of C ₆₀ in CCRF-CEM cells.	65
Figure 13. Quantitative analysis of C ₆₀ content in mitochondria of leukemic cells.	66
Figure 14. <i>In vitro</i> C ₆₀ photodynamic treatment of human leukemic cells.	67
Figure 15. Reactive oxygen species generation in CCRF-CEM cells (A) and fluorescence microscopy images (B) at 1 h and 3 h after treatment with either C ₆₀ or irradiation at 405 nm 10 J/cm ² alone or their combination.	69

Figure 16. ATP level in CCRF-CEM cells under treatment with 20 μM C_{60} in dark (A) or after irradiation with 10 J/cm^2 405 nm light (B).	70
Figure 17. Induction of leukemic cells apoptosis by light irradiation of accumulated C_{60} .	71
Figure 18. Multiple reaction monitoring chromatograms of free Doxorubicin, C_{60} -Dox 1:1 and 2:1 (1 μM Doxorubicin-equivalent concentration).	72
Figure 19. Optical characterization of C_{60} -Dox nanocomplexes.	74
Figure 20. Hydrodynamic size (diameter, nm) of C_{60} -Dox in RPMI cell culture medium.	75
Figure 21. Fluorescence microscopy images of CCRF-CEM cells, stained with DAPI (Blue), FITC-based immunostaining for C_{60} (Green) and Doxorubicin (Red) after treatment with: 450 and 900 nM C_{60} , 450 nM Doxorubicin (Dox), 1:1 or 2:1 C_{60} -Dox.	77
Figure 22. Intracellular uptake of 1 μM free or C_{60} -complexated Doxorubicin in a drug-equivalent concentration.	78
Figure 23. Viability of leukemic cells after treatment with Doxorubicin or its C_{60} -nanocomplexes.	80
Figure 24. Berberine intracellular localization.	83
Figure 25. Viability of CCRF-CEM cells, treated with 1-200 μM Berberine during 24, 48 and 72 h.	84
Figure 26. Berberine proapoptotic effects on CCRF-CEM cells.	85
Figure 27. Detection of apoptotic CCRF-CEM cells, treated with Berberine, with Annexin V-FITC/PI double staining.	86
Figure 28. Intracellular accumulation of free Berberine and C_{60} -Ber in a Berberine-equivalent concentration.	88
Figure 29. Viability of CCRF-CEM cells, treated with a free or C_{60} -complexated Berberine.	89

Figure 30. Cell cycle analysis in CCRF-CEM cells, incubated for 24 h after treatment with either free 10 μ M Berberine or C ₆₀ -Ber at Berberine-equivalent concentration.	91
Figure 31. Caspase 3/7 activity in CCRF-CEM cells, incubated for 24 h under treatment with either free or C ₆₀ -complexed Berberine at 10 μ M equivalent concentration.	92
Figure 32. Viability of CCRF-CEM cells under action of photoexcited C ₆₀ -Dox.	93
Figure 33. ROS generation in CCRF-CEM cells treated with C ₆₀ -Dox and light irradiation.	96
Figure 34. ATP level and caspase 3/7 activity in CCRF-CEM cells at 3 h after treatment. Treatment was done with either free C ₆₀ and Doxorubicin or C ₆₀ -Dox in dark or after irradiation with 10 J/cm ² 405 nm LED light.	97
Figure 35. Cell death differentiation in CCRF-CEM treated with C ₆₀ -Dox and light irradiation.	98
Figure 36. Viability of CCRF-CEM cells under action of photoexcited C ₆₀ -Ber.	100
Figure 37. Research workflow with delivered results (in brown) towards C ₆₀ -drug nanocomplex-based photodynamic cancer chemotherapy.	127
Figure 38. The workflow for studies towards C ₆₀ -based anticancer photodynamic chemotherapy.	129
A1 Figure 1. Red light sources for C ₆₀ photodynamic treatment of leukemic cells.	i
A2 Figure 1. Optical density and fluorescence spectra of Berberine.	ii
A3 Figure 1. C ₆₀ sonodynamic treatment of HeLa cells.	iv
A3 Figure 2. Apoptosis detection in HeLa cells, treated with 20 μ M C ₆₀ and 1 MHz ultrasound.	iv
A4 Figure 1. Phase contrast and fluorescence images of CCRF-CEM cells, incubated for 24 h with 0.5 μ M Berberine.	v

A5 Figure 1. Prooxidant effect of Berberine in CCRF-CEM cells under 405 nm light irradiation.	vi
---	----

LIST OF TABLES

<i>Table</i>	<i>Page</i>
Table 1. The rational design for nanosystem as a carrier of anticancer drug	22
Table 2. Nanocarbon-mediated photodynamic cancer chemotherapy	36
Table 3. Chemicals used in the work	41
Table 4. Media and buffers used in the work	42
Table 5. Cell lines used in the work	42
Table 6. Kits used in the work	43
Table 7. Consumables used in the work	43
Table 8. Light sources used in the work	43
Table 9. Equipment used in the work	44
Table 10. Software used in the work	45
Table 11. Stock concentrations of C ₆₀ and Doxorubicin/Berberine in nanocomplexes	45
Table 12. HPLC-ESI-MS conditions for analysis of C ₆₀	48
Table 13. HPLC-ESI-MS/MS conditions for analysis of Doxorubicin	49
Table 14. Mean fluorescence intensity (FI) of intracellular accumulated Doxorubicin estimated by FACS histograms	79
Table 15. Half-maximal inhibitory concentration (IC ₅₀ , nM) of free and C ₆₀ -bound Doxorubicin in human leukemic cell lines	81
Table 16. Mean fluorescence intensity (FI) of the intracellular accumulated Berberine	88
Table 17. Half-maximal inhibitory concentration (IC ₅₀) of the free Berberine and C ₆₀ -Ber towards CCRF-CEM cells	90

Table 18. IC ₅₀ (nM) values for the photoexcited free and C ₆₀ -complexated Doxorubicin	94
Table 19. Combination index of interaction between phototoxic effects of C ₆₀ and non-irradiated C ₆₀ -Dox	94
Table 20. IC ₅₀ (nM) values for the photoexcited free free and C ₆₀ -complexated Berberine	101
Table 21. Combination index of interaction between phototoxic effects of C ₆₀ and Berberine and non-irradiated C ₆₀ -Ber.	101
Table 22. The rational design of C ₆₀ -Dox nanocomplexes	114

LIST OF FORMULAE

<i>Formula</i>	<i>Page</i>
Formula 1. Limit of detection and limit of quantification	47
Formula 2. Linear regression equation for C ₆₀ fullerene quantification	47
Formula 3. Linear regression equation for Doxorubicin quantification	50
Formula 4. Succinate-reductase activity calculation	56
Formula 5. Combination index calculation	61

Curriculum Vitae

Anna Grebinyk, M.Sc.

A dynamic and creative young scientist with a wide international network and a strong background in cancer nanotechnology

Address: Niederlausitzstr. 35, 15738 Zeuthen, Germany
Affiliation: Technical University of Applied Sciences Wildau
E-mail: grebinyk@th-wildau.de
LinkedIn: <https://www.linkedin.com/in/anna-grebinyk-186a8245/>
ResearchGate: https://www.researchgate.net/profile/Anna_Grebinyk

PUBLICATIONS

11 Original Peer-Reviewed Papers in international journals (+ 2 in national journals)

> 20 oral and poster presentations at the international scientific conferences

RECIEVED FUNDING

- Branderburg programme “Strengthening technological and supplication-oriented research at scientific institutions (StaF Directive, 13% success rate) for Post-Doc study	350 000 Eur
- German Academic Exchange Service (DAAD, 20% success rate) for PhD study	60 000 Eur
- Travel grants and awards (in total)	5 000 Eur

EDUCATION and RESEARCH EXPERIENCE

Research fellow , supervisor: Prof. Dr. Marcus Frohme Molecular Biotechnology and Functional Genomics Technical University of Applied Sciences (TUAS) Wildau, Germany	since 2020
--	-------------------

PhD student , supervisor: Prof. Dr. Thomas Dandekar / Prof. Dr. Marcus Frohme Faculty of Biology, University of Würzburg / TUAS Wildau, Germany Thesis: “Synergistic Chemo- and Photodynamic Treatment of Cancer Cells with C ₆₀ Fullerene Nanocomplexes”	since 2015
--	-------------------

Focus of research: - *synthesis and characterization of anticancer nanocomplexes*
 - *proof-of-concept for photodynamic chemotherapy on various cancer models*
 - *clarification of apoptosis induction mechanisms in cancer cells*

Maternity leave	2014-2015
------------------------	------------------

Master of Biochemistry with High Distinction, top ranked: 97/100 score Taras Shevchenko National University (TSNU) of Kyiv, Ukraine, supervisor: Prof. Dr. Olga Matyshevskaya Thesis: “Reactive oxygen species production and antioxidant enzymes activity of leukemic cells under action of hydrogen peroxide and C ₆₀ fullerene”	2011-2013
---	------------------

Bachelor of Biology with High Distinction, 92/100 score Taras Shevchenko National University of Kyiv, Ukraine, supervisor: Prof. Dr. Olga Matyshevskaya	2007-2011
---	------------------

Focus of research: - *modulation of redox balance with C₆₀ fullerene in leukemic and normal cells*

ADDITIONAL EXPIERENCE

- Head of the Ethics Commission of the TUAS Wildau	since 2019
- Teaching of M.Sc. Biomaterials (attended by 15, 2016), B.Sc. Practice Cell Culture (attended by 15) and Fluorescence Microscopy (attended by 50), TUAS Wildau	since 2016
- Teaching of B.Sc. and M.Sc. Biochemistry (attended by 25), TSNU Kyiv	2010-2012

EDITORIAL EXPIERENCE

Reviewer for Sci Rep, RSC Advan, J Biomed Nanotechnol, Diam Relat Mater, BMC Bioinform, Front Microbiol, Toxins and J Integr Neurosci	since 2017
Assistant Editor and Graphic Designer (on a voluntary basis) German-Ukrainian Academic Society / The UKRAINE Network	since 2016
- Contribution to the web-page (300+ Posts) and Newsletter (x24; 600+ Subscribes) publication	
- Design of promotional materials (posters, programs, logotypes, etc.)	

ADDITIONAL EDUCATION

- Basic module **Management Skills for Research and University** **2017-2018**
Academy for Postdoctoral Career Development, University of Potsdam, Germany
- Courses **Spectroscopy, Biohotonics**, Prof. Dr. Yashchuk, Department of Physics TSNU Kyiv **2012-2014**
- Course **Optics**, Prof. Dr. Slobodyanyuk, Department of Physics TSNU Kyiv **2011-2012**
- Full training **Desktop Publishing Operator** **2004-2006**
International Educational-Scientific UNESCO Center “Information Technology and Systems”
National Academy of Sciences and Ministry of Education of Ukraine

INTERCULTURAL SKILLS

English	Fluent
German and Polish	Intermediate
Ukrainian and Russian	Native speaker

Cooperation with scientists from Poland, Azerbaijan and China (contact establishment, joint experiments, funding acquisition)

Scientific event organization: Annual Meetings and PhD-thesis presentation contest of German-Ukrainian Academic Society (2017-2018, attended by 100+), German-Ukrainian Summer School 2021 “Lessons in Biomedicine learnt from Nanotechnology and Artificial Intelligence”, Kyiv & Kharkiv

RECOGNITIONS**Scholarships:**

- “Research Grant – **Doctoral Programme in Germany**” (DAAD) **2015-2019**
- Three one-year Scholarships of Victor Pinchuk’s Nationwide Initiative to support **Gifted Pro-active Youth** “Zavtra.UA (Tomorrow.UA)” **2011-2014**

Awards:

- **3rd Speed Lecture Award**, BIONNALE 2019, Berlin, Germany
- **1st place in communication challenge**, the 18th Federation of European Biochemical Societies (FEBS) Young Scientists’ Forum, Prague, Czech Republic, 2018
- **1st place excellent oral presentation**, the International Academy of rating technology and sociology “Golden Fortune” at the 4th German-Ukrainian Symposium “Physics and Chemistry of Nanostructure and Nanobiotechnology”, Ilmenau, Germany, 2013
- **2nd place oral presentation**, the 8th International scientific conference “Youth and Progress in Biology”, Lviv, Ukraine, 2011
- **Best poster**, the 19th International School-Seminar “Spectroscopy of molecules and crystals” Crimea, Ukraine, 2009

Travel grants:

- FEBS for the 18th FEBS Young Scientists’ Forum and the 43rd FEBS Congress “Biochemistry forever”, Prague, Czech Republic, 2018
- Biotechnology Business Institute for the 1st European Symposium “Breaking Down Complexity: Innovative models and techniques in biomedicine”, Barcelona, Spain, 2017
- FEBS for the 41st Congress “Molecular and Systems Biology for a Better Life” scheduled for Kuşadası, Turkey, 2017 (cancelled)
- German Cell Biology Society for the 12th International Congress of Cell Biology, Prague, Czech Republic, 2016
- DAAD and German Ministry of Foreign Affairs for the Summer-School “Perspectives for Young Scientists in Life Sciences”, Ivano-Frankivsk, Ukraine, 2016

MEMBERSHIPS

- since 2017: Gesellschaft für Biochemie und Molekularbiologie
- since 2016: All-Ukrainian Public Organization Ukrainian Society of Cell Biology, International Federation for Cell Biology, International Union of Biochemistry and Molecular Biology, German-Ukrainian Academic Society / The UKRAINE Network
- since 2012: Ukrainian Biochemical Society, Federation of European Biochemical Societies
- since 2004: Minor Academy of Sciences of Ukraine – **twice 1st (2006, 2007) and 2nd (2005) place at the all-Ukrainian Research Paper Defense Competition among High School Students**

PUBLICATIONS

Original peer-reviewed publications derived from the Thesis

1.	<u>Grebinyk A.</u> , Grebinyk S., Prylutska S., Ritter U., Matyshevskaya O., Dandekar T. & Frohme M. 2018. C ₆₀ fullerene accumulation in human leukemic cells and perspectives of LED-mediated photodynamic therapy. <i>Free Radic Biol Med.</i> 124: 319–327.
2.	<u>Grebinyk A.</u> , Grebinyk S., Prylutska S., Ritter U., Matyshevskaya O., Dandekar T. & Frohme M. 2018. HPLC-ESI-MS method for C ₆₀ fullerene mitochondrial content quantification. <i>Data Brief.</i> 19: 2047–2052.
3.	<u>Grebinyk A.</u> , Prylutska S., Grebinyk S., Prylutsky Y., Ritter U., Matyshevskaya O., Dandekar T. & Frohme M. 2019. Complexation with C ₆₀ Fullerene Increases Doxorubicin Efficiency against Leukemic Cells In Vitro. <i>Nanoscale Res Lett.</i> 14: 61.
4.	<u>Grebinyk A.</u> , Yashchuk V., Bashmakova N., Gryn D., Hagemann T., Naumenko A., Kutsevol N., Dandekar T. & Frohme M. 2019. A new triple system DNA-Nanosilver-Berberine for cancer therapy. <i>Appl Nanosci.</i> 9: 945–956.
5.	<u>Grebinyk A.</u> , Prylutska S., Buchelnikov A., Tverdokhle N., Grebinyk S., Evstigneev M., Matyshevskaya O., Cherepanov V., Prylutsky Y., Yashchuk V., Naumovets A., Ritter U., Dandekar T. & Frohme M. 2019. C ₆₀ Fullerene as an Effective Nanoplatfrom of Alkaloid Berberine Delivery into Leukemic Cells. <i>Pharmaceutics.</i> 11: 586.
6.	<u>Grebinyk A.</u> , Prylutska S., Chepurna O., Grebinyk S., Prylutsky Y., Ritter U., Ohulchansky T.Y., Matyshevskaya O., Dandekar T. & Frohme M. 2019. Synergy of Chemo- and Photodynamic Therapies with C ₆₀ Fullerene-Doxorubicin Nanocomplex. <i>Nanomaterials.</i> 9: 1540.

Other publications derived from the Thesis

1.	<u>Grebinyk A.</u> , Prylutska S., Matyshevskya O., Dandekar T. & Frohme M. Fullerene C ₆₀ -Doxorubicin Conjugate for Effective Drug Delivery <i>in vitro</i> . 9 th Meeting of Engineering of Functional Interfaces, 03-05.07.2016, P. 36, Wildau, Germany – Oral and Poster presentations
2.	<u>Grebinyk A.</u> , Prylutska S., Matyshevskya O., Dandekar T. & Frohme M. Fullerene C ₆₀ increases Doxorubicin Efficiency in Leukemic Cells. 12 th International Congress of Cell Biology in Czech Republic, 21-25.07.2016 (with Travel grant from the German Cell Biology Society's), P. 283, Prague, Czech Republic– Poster presentation
3.	<u>Grebinyk A.</u> , Prylutska S., Matyshevskya O., Dandekar T. & Frohme M. Fullerene C ₆₀ as a Nanocarrier of Doxorubicin for Cancer Treatment. 41 st Federation of European Biochemical Societies (FEBS) Congress, 03-08.09.2016, (with FEBS Bursary), FEBS Journal 283, Supplement 1, 2016, P. 177, scheduled for Kuşadası, Turkey, but the live event was cancelled – online poster presentation
4.	<u>Grebinyk A.</u> Nanofootball against Cancer. Final of the PhD Thesis Presentation Contest, German-Ukrainian Academic Society “The UKRAINIAN Academic International Network”, in cooperation with the MitOst e.V. and supported by the Embassy of Ukraine in Germany at the Forum “UkraineLab: Playing Polyphony of the Society. Exploring the European Identity” 19-22.09.2016, Berlin, Germany – Oral presentation
5.	<u>Grebinyk A.</u> , Yashchuk V., Bashmakova N., Gryn D., Naumenko A., Kutsevol N., Dandekar T. & Frohme M. Berberine Anticancer Activity through Nanocomplex with DNA and Nanoparticles. 5 th International research and practice Conference "Nanotechnology and Nanomaterials", 23-26.08.2017, P. 605, Chernivtsi, Ukraine – Oral presentation
6.	<u>Grebinyk A.</u> , Prylutska S., Grebinyk S., Matyshevskya O., Prylutskyyy Y.,

	Dandekar T. & Frohme M. LEDs as excitation source for fullerene C ₆₀ photodynamic cancer therapy. 1 st European PhD and Postdoc Symposium “Breaking Down Complexity: Innovative models and techniques in biomedicine” of the European Academy for Biomedical science (ENABLE), 15-17.11.2017, (with travel grant from biotechnology Business Institute), P. 68, Barcelona, Spain – Oral and poster presentations
7.	Gamaleia N., Yashchuk V., <u>Grebinyk A.</u> , Bashmakova N., Gryn D., Naumenko A., Kutsevol N., Dandekar T. & Frohme M. DNA-Ag Nanoparticle-Berberine System for Cancer Chemo- and Photodynamic Therapy. 47 th International conference “Lasers Application in Biology”, 12-14.10.2017, P. 165-166, Charkiw, Ukraine – Thesis
8.	<u>Grebinyk A.</u> , Prylutska S., Grebinyk S., Matyshevskaya O., Dandekar T. & Frohme M. Mitochondrial fullerene C ₆₀ accumulation in human leukemic cells for LED-mediated photodynamic therapy. 18 th FEBS Young Scientists' Forum, 04-07.07.2018, (with FEBS Travel Grant), Prague, Czech Republic – Oral and poster presentation
9.	<u>Grebinyk A.</u> , Prylutska S., Grebinyk S., Matyshevskaya O., Dandekar T. & Frohme M. Mitochondrial fullerene C ₆₀ accumulation in human leukemic cells for LED-mediated photodynamic therapy. 43 rd FEBS Congress, 07-12.07.2018, (with FEBS Travel Grant), P. 472, Prague, Czech Republic – Poster presentation
10.	<u>Grebinyk A.</u> Nanofootball against Cancer. 3 rd Speed Lecture Award at the BIONNALE 2019, 07-05. 2019, Berlin, Germany – Oral presentation
11.	Chepurina O., <u>Grebinyk A.</u> , Petrushko Y., Prylutska S., Grebinyk S., Yashchuk V.M., Matyshevskaya O., Ritter U., Dandekar T., Frohme M., Qu J. & Ohulchanskyy T.Y. LED-based portable light source for photodynamic therapy. Optics in Health Care and Biomedical Optics IX, 12-16.07.2020, 11190, 111901A, Shenzhen, China – Thesis

Other peer-reviewed publications

1.	Prylutska S., Grynyuk I., <u>Grebinyk A.</u> , Hurmach V., Shatrava I., Sliva T., Amirkhanov V., Prylutsky Y., Matyshevskaya O., Slobodyanik M., Frohme M. & Ritter U. 2017. Cytotoxic Effects of Dimorfolido-N-Trichloroacetylphosphorylamide and Dimorfolido-N-Benzoylphosphorylamide in Combination with C ₆₀ Fullerene on Leukemic Cells and Docking Study of Their Interaction with DNA. <i>Nanoscale Res Lett.</i> 12: 124.
2.	<u>Grebinyk A.</u> , Prylutska S., Grynyuk I., Kolp B., Hurmach V., Sliva T., Amirkhanov V., Trush V., Matyshevskaya O., Slobodyanik M., Prylutsky Y., Frohme M. & Ritter U. 2018. C ₆₀ Fullerene Effects on Diphenyl-N-(trichloroacetyl)-amidophosphate Interaction with DNA In Silico and Its Cytotoxic Activity Against Human Leukemic Cell Line In Vitro. <i>Nanoscale Res Lett.</i> 13: 81.
3.	Prylutska S., Grynyuk I., Skaterna T., Horak I., <u>Grebinyk A.</u> , Drobot L., Matyshevskaya O., Senenko A., Prylutsky Y., Naumovets A., Ritter U. & Frohme M. 2019. Toxicity of C ₆₀ fullerene-cisplatin nanocomplex against Lewis lung carcinoma cells. <i>Arch. Toxicol.</i> 93: 1213–1226.
4.	Prylutska S.V., <u>Grebinyk A.G.</u> , Lynchak O.V., Byelinska I.V., Cherepanov V.V., Tauscher E., Matyshevskaya O.P., Prylutsky Y.I., Rybalchenko V.K., Ritter U. & Frohme M. 2019. In vitro and in vivo toxicity of pristine C ₆₀ fullerene aqueous colloid solution. <i>Fullerenes, Nanotubes and Carbon Nanostructures.</i> 27: 715–728.